Exciton Dynamics and Anisotropy in 2D Metal Organochalcogenolate Semiconductors

by

Woo Seok Lee

B.S., Materials Science and Engineering, Korea University, 2017
M.S., Materials Science and Engineering, Korea University, 2019

Submitted to the Department of Materials Science and Engineering

in partial fulfillment of the requirements for the degree of

DOCTOR OF PHILOSOPHY IN MATERIALS SCIENCE AND ENGINEERING

at the

MASSACHUSETTS INSTITUTE OF TECHNOLOGY

September 2024

Authored by: _____
Woo Seok Lee
Department of Materials Science and Engineering
August 12, 2024

Certified by: _____
William A. Tisdale
Warren K. Lewis Professor of Chemical Engineering
Thesis Supervisor

Accepted by: _____
Robert J. Macfarlane
Associate Professor of Materials Science and Engineering
Chair, Department of Committee on Graduate Studies

Exciton Dynamics and Anisotropy in 2D Metal Organochalcogenolate Semiconductors

By

Woo Seok Lee

Submitted to the Department of Materials Science and Engineering on August 12, 2024, in partial fulfillment of the requirements for the degree of Doctor of Philosophy in Materials Science and Engineering

Abstract

Silver phenylselenolate (AgSePh) is a novel hybrid organic-inorganic two-dimensional (2D) semiconductor that belongs to the broader class of metal organochalcogenolates (MOCs). Since its blue-emitting excitonic properties were discovered in 2018, AgSePh has attracted attention from the scientific community. From a fundamental science perspective, AgSePh provides an excellent platform for exploring many-body interactions among quasiparticles (such as excitons, phonons, and photons) due to its large exciton binding energy, strong exciton-lattice interactions, and natural photonic cavity structure. From a technological standpoint, its narrow blue emission, a tunable bandgap through composition control, chemical robustness, in-plane anisotropy, and low-cost, scalable synthetic methods make AgSePh promising candidate for photonic and optoelectronic applications. However, we do not yet fully understand how its excitonic properties arise at a fundamental level. *The central aim of this thesis is to elucidate the correlation between structure, inorganic composition, organic ligands, and excitonic properties in these novel hybrid 2D semiconductors.*

First, we present the synthesis, structural and optical properties of 2D AgEPh (E = S, Se, Te) single crystals, colloidal nanocrystals, and thin films. Importantly, the growth of millimeter-sized single crystalline 2D AgEPh (E = S, Se, Te) enables their crystal structure determination via single crystal X-ray diffraction: AgSPh in $P2_1$, AgSePh in $P2_1/c$, and AgTePh in $P2_1/c$.

Second, we explore the underlying mechanism of light emission in AgSePh and AgTePh. Despite having the same crystal structure, these compounds exhibit strikingly different excitonic properties: AgSePh shows narrow photoluminescence (PL) with a minimal Stokes shift, while AgTePh exhibits broad PL with a large Stokes shift. Using time-resolved and temperature dependent optical spectroscopy, combined with sub-gap photoexcitation studies, we demonstrate that the exciton dynamics in AgSePh films are dominated by the interaction of free-excitons with extrinsic defect states, whereas the dynamics in AgTePh are dominated by intrinsic exciton self-trapping behavior.

Third, we study alloying between AgEPh. we demonstrate that AgSePh and AgTePh form homogeneous alloys with tunable excitonic properties across all compositions, whereas AgSPh and AgSePh/AgTePh exhibit a miscibility gap. These observations are elucidated by density functional theory calculations and correlated with crystallographic information.

Fourth, using polarization-resolved micro-absorption, reflectance, and photoluminescence spectroscopy, combined with the GW plus Bethe-Salpeter equation calculations, we reveal multiple low-lying excitons with in-plane anisotropy in AgSePh and AgTePh. This showcases the richness of excitonic physics in these materials, which arises from their low-symmetry crystal structures.

Finally, we show that the electronic and excitonic structure of AgSePh can be engineered through organic functionalization, resulting in giant excitonic anisotropy and a completely different absorption spectrum in 2D AgSePh-F_2(2,3). This divergence in excitonic properties is attributed to the semi 1D Ag chains in AgSePh-F_2(2,3), in contrast to hexagonal 2D Ag network in AgSePh. This finding can be generalized to other blue-emitting 2D AgSePh-R compounds which exhibit either AgSePh-like or AgSePh-F_2(2,3)-like absorption spectra.

Overall, this thesis advances the understanding of the structure-composition-excitonic property relationships in these emerging hybrid semiconductors, paving the way for future investigations into this exciting material family.

Thesis supervisor: William A. Tisdale
Title: Warren K. Lewis Professor of Chemical Engineering

Acknowledgements

Looking back on my Ph.D., it was the most humbling experience that made me realize how unpredictable and unplanned life and research can be. Despite the unpredictability that often made me nervous and sometimes frustrated, I have been able to reach this point thanks to the many people who have helped me along the way.

Firstly, and most importantly, I would like to thank my thesis advisor, Prof. William Tisdale. I appreciate his emphasis during my early Ph.D. years on understanding and analyzing experimental observations through textbook knowledge rather than relying on descriptions from previously published papers. Although I did not initially grasp the importance of having a strong fundamental background, I followed his advice and this approach has become an invaluable asset to me as a scientist. I also appreciate that Will has always been supportive of my career development, not only by mentoring my research and writing multiple recommendation letters but also by providing sincere career advice. He has been a great role model for me, both in my career and in life.

I would also like to thank my two other thesis committee members: Professors Rafael Jaramillo and Ju Li. They provided valuable feedback and comments during every committee meeting, enabling me to move forward in my Ph.D. I particularly thank Prof. Jaramillo for providing sincere career advice when I visited him to ask about the Rowland program and for writing a recommendation letter for me for the Kadanoff-Rice fellowship.

I would not have been able to complete my Ph.D. without the support of the wonderful former and current members of the Tisdale group. Two former members who were especially important are Dr. Watcharaphol (Oat) Paritmonkol and Tomoaki Sakurada. I was lucky to work with and learn from both of you during my early Ph.D. years. I enjoyed the time we spent working together as an MOC team, and I am grateful that we still keep in touch and continue to collaborate since we are all in academia. Thank you for being my mentors, colleagues, and friends.

Along with Oat, Dr. Wenbi Shcherbakov-Wu taught me various spectroscopic techniques including diffusion imaging, low frequency Raman, cryogenic measurements, and more. I appreciate you both for being my great spectroscopy teachers.

I also thank Dr. Eric Powers and Dr. Seung Kyun (SK) Ha for helping me with TA and ICP-OES. Eric became the person to discuss MOC with after Oat and Tomoaki left, as MOC became the primary material system in his later Ph.D. I actually got to know the Tisdale group thanks to SK, whom I met at the 2019 Nano Korea conference. Thank you for introducing the Tisdale group to me.

I also thank Dr. Ruomeng Wan for her help and discussions on TEM, ED, diffuse-reflectance, organic ligand synthesis, and H-NMR. Thomas Sheehan also helped me with organic ligand synthesis and diffusion imaging. Thank you both for being my organic chemistry teachers since Tomoaki left.

I was also lucky to lead the second generation of the MOC team with Nicholas Samulewicz and Tejas (TJ) Desphande. I thank you both for contributing to my thesis in my later Ph.D. with your efforts on TA, TEM, ED, SEM, and AFM.

I am also grateful for two amazing UROP students, Annlin Su and Daniela Alaron, who contributed to the optimization of MOC synthesis.

Furthermore, I have had the privilege to work with and learn from talented scientists in the group: Dr. Kris Williams, Dr. Sam Winslow, Dr. Fabio Marangi, Dr. Nannan Mao, Dr. Chana Honick, Dr. Seryio Saris, Narumi Nagaya, Abigail Taussig, Eliza Price, Niamh Brown, Maya

Chattoraj, Jimin Kwag, Justin Griffith, Guilia Lo Gerfo Morganti, Guilherme Bejar, and Angelina Rogatch. Thank you all for being wonderful labmates.

I would also like to thank Barbara Balkwill for being our amazing group administrator who always helped our research go smoothly.

All past and current groups mentioned above were always supportive and welcoming, making me feel that the Tisdale group is my home. I sincerely appreciate you all.

During my Ph.D., I have also been fortunate to collaborate with many great scientists outside of the Tisdale lab. I thank Dr. Peter Müller for his help with X-ray techniques and structural refinement. He was also very generous and kind in answering my endless questions about crystallography. I also thank Dr. Yeongsu Cho and Prof. Heather Kulik for DFT and GW-BSE calculations, which form an important part of my thesis. Your theoretical calculations have helped me deeply understand the underlying mechanisms in my experimental observations. I also thank Dr. Katarzyna Posmyk, Dr. Paulina Peksa, Prof. Michał Baranowski and Prof. Paulina Płochocka for the cryogenic reflectance measurements, which helped reconcile the inconsistency between room temperature observation and GW-BSE calculations. Additionally, I thank Prof. Soong Ju Oh, my Master's degree advisor, for welcoming me to work in his lab in Korea when MIT shut down during COVID. Thanks to his support, I was able to investigate the optoelectronic properties of MOCs.

I want to also thank all the friends I met at MIT for making my Ph.D. life happier. I first thank the friends who started their Ph.D. the same year as me, particularly Byunghun Lee, Hyunwon Chu, Eunsoo Cho, Sungyun Yang, and Heejung Roh. I also thank my friends in MIT KGMSE, especially Soyeon Kim, Misong Ju, and Changhwan Oh. Additionally, I thank other friends at MIT, including the 2020-21 KGSA board members, and more.

I would like to extend my gratitude to my friends in Korea. Friends from Osan High School, particularly Heeseung Jo, Joopil Jang, and Sungjoon Moon. Friends from Korea University, especially Dohee Kim, Chowoon Bong, Gilsub Kim, and the College-ID-228 members. Friends I met during military service, particularly Daehyun Choi, Changsoo Kim, Gabpil Yang, and Jaesung Huh. Friends from my Master's group, especially Hyungmok Joh, Donggyu Kim, Haneun Kim, and Junhyun Ahn.

I thank my family - my parents and sister, brother-in-law, and my adorable niece - for their endless love, support and trust to me. Although being far away from family was tough for my Ph.D., it made me realize how important you are to me.

Last but not least, to my amazing partner and my best friend, Claire, thank you for filling my life with unconditional support, love, and joy. You have made and continue to make me a better person. I cannot thank you enough.

Contents

List of Figures

List of Tables

Chapter 1

Introduction

1.1 Motivation and introduction

The creation, manipulation, and detection of photons using semiconductors enables a wide range of optoelectronic and photonic applications, including light emitting diodes, solar cells, image sensors, photonic communication and computing. In semiconductors, a photon is absorbed by promoting an electron from the valence band to the conduction band, leaving behind a positive charge, a hole, in the valence band. The photogenerated electron and hole travel through semiconductors for a finite time as uncorrelated separate states (free charge carriers) or as a bound electron-hole pair known as an exciton before they recombine to reemit a photon. Because semiconductors consist of repetitive atomic structure, the collective motions of lattices known as phonons affect absorption, transport, and emission processes mentioned above. Therefore, the performance of optoelectronic and photonic devices is governed by the interplay between these quasiparticles (electrons, excitons, phonons, and photons).

Advances in these technologies have been driven by the discovery and development of two-dimensional (2D) semiconductors. A prominent subfamily of 2D semiconductors is the transition metal dichalcogenides (TMDs).[1] They consist of stacks of 2D inorganic sheets that interact directly through van der Waals forces, exhibiting a layer-dependent tunable bandgap. In their monolayer form, the combined effects of quantum confinement and reduced dielectric screening result in excitons with binding energies up to hundreds of meV.[2,3] These robust excitons dominate the optical response at room temperature, leading to strong absorption, emission, and nonlinear excitonic phenomena due to enhanced light-matter interaction. However, preparing monolayer samples typically involves mechanical exfoliation and layer transfer, processes that are prone to causing sample damage or contamination.[4,5]

Another promising subfamily of 2D semiconductors is the hybrid organic-inorganic 2D lead halide perovskites (LHPs).[6,7] Similar to monolayer TMDs, 2D LHPs possess robust excitons that remain stable at the room temperature. However, unlike TMDs, 2D LHPs feature organic

ligands on top and bottom of inorganic sheets, which decouple electronic coupling between layers, resulting in a layer-independent bandgap. The solution processability and tunable bandgap across visible range via composition control make them even more promising. Additionally, the soft ionic lattices, combined with a hybrid organic-inorganic structure, lead to strong electron (or exciton)-phonon interaction.[8] This interaction causes the crystal lattice surrounding charges (or excitons) to become polarized or distorted, protecting them from external defects or trap states, which contributes to their defect tolerance.[9] However, due to their ionic bonding, 2D LHPs are sensitive to water and polar solvents, limiting their long-term stability. Furthermore, the presence of lead in their composition raises concerns regarding environmental and health issues during the operation and the recycling of 2D LHP devices.[10]

2D metal organochalcogenolates (MOCs) are a novel class of hybrid organic-inorganic 2D semiconductors.[11–13] Similar to TMDs and 2D LHPs, 2D MOCs crystallize in the form of three-dimensional (3D) solids consisting of 2D layers stacked by van der Waals forces. However, 2D MOCs are fundamentally distinguished from other 2D semiconductors by the presence of organic ligands *covalently* bonded to the inorganic sheet. This covalent bonding across organic and inorganic components provides them with chemical stability and electronic band gap tunability through organic ligand modification.[14] Among 2D MOCs, silver phenylchalcogenolate (AgSePh) has gained the most interest. Although first discovered by John Corrigan & co-workers in 2002,[15] its importance was not widely recognized until 2018, when Hohman & co-workers at Lawrence Berkeley Lab demonstrated that AgSePh (dubbed "mithrene") is an excitonic 2D semiconductor emitting blue (~467 nm) photoluminescence (PL).[12,13] Following studies from multiple groups have showed its many promising properties such as strong exciton binding energy, in-plane optical anisotropy, low-cost and scalable synthetic methods, air stability, chemical robustness, and heavy metal-free composition.[16,17]

Though AgSePh has shown significant potential that could surpass rival excitonic semiconductors such as TMDs and 2D LHPs, many outstanding questions remain unanswered to further enhance its performance and expand its functionality. What is the mechanism behind light emission in AgSePh? What factors affect exciton dynamics in AgSePh? How does its excitonic characteristics relate to its in-plane anisotropic crystal structure? Can we replace Se to other chalcogens like S and Te? Would AgSPh and AgTePh exhibit the same crystal structure and

excitonic property as AgSePh? Can we create an alloy between them? How do the exciton-phonon interactions change with variations in chalcogen ratio? How do the structure and excitonic properties change when we functionalize organic ligands?

The aim of this thesis is to experimentally investigate the fundamental aspects of these questions. The ultimate goal is to establish a relationship between a structure-composition-optical property in in this emerging class of hybrid organic-inorganic semiconductors, from the perspective of interactions among quasiparticles (electrons, excitons, phonons, and photons). The following chapters will provide the background knowledge necessary to address these issues. Chapter 2 introduces excitons and other exciton-associated complex quasiparticles and how they are influenced by the dimension of host materials from a fundamental point of view. Chapter 3 summarizes the historical development of MOCs that host these quasiparticles and existing knowledge gap in structure-composition-optical property relationship in these emerging materials.

Chapters 4 through 8 will address these knowledge gaps using evidence from experimental observations and theoretical calculations. Chapter 4 will present the advanced synthesis of single crystalline 2D AgEPh (E = S, Se, Te) with sufficient size and quality for single-crystal X-ray diffraction that reveals their microscopic crystal structures. Chapter 5 will explore the light emission mechanisms in AgSePh and AgTePh thin films through various spectroscopic studies. Chapter 6 will investigate the thermodynamic stability and tunable excitonic properties of $AgX_{1-n}Y_nPh$ (X, Y = S, Se, Te) thin films achieved through alloying. Chapter 7 will examine the excitonic anisotropy of single crystalline AgEPh crystals, arising from their anisotropic crystal structures, based on both spectroscopic observations and theoretical calculations. Finally, Chapter 8 will demonstrate giant excitonic anisotropy in 2D AgSePh-F_2(2,3) enabled by its semi-1D Ag-Ag chain structure.

1.2 References

(1) Novoselov, K. S.; Mishchenko, A.; Carvalho, A.; Castro Neto, A. H. 2D Materials and van Der Waals Heterostructures. *Science (1979)* **2016**, *353* (6298). https://doi.org/10.1126/science.aac9439.

(2) He, K.; Kumar, N.; Zhao, L.; Wang, Z.; Mak, K. F.; Zhao, H.; Shan, J. Tightly Bound Excitons in Monolayer WSe_2. *Phys Rev Lett* **2014**, *113* (2), 026803. https://doi.org/10.1103/PhysRevLett.113.026803.

(3) Chernikov, A.; Berkelbach, T. C.; Hill, H. M.; Rigosi, A.; Li, Y.; Aslan, B.; Reichman, D. R.; Hybertsen, M. S.; Heinz, T. F. Exciton Binding Energy and Nonhydrogenic Rydberg Series in Monolayer WS_2. *Phys Rev Lett* **2014**, *113* (7), 076802. https://doi.org/10.1103/PhysRevLett.113.076802.

(4) Goodman, A. J.; Lien, D.-H.; Ahn, G. H.; Spiegel, L. L.; Amani, M.; Willard, A. P.; Javey, A.; Tisdale, W. A. Substrate-Dependent Exciton Diffusion and Annihilation in Chemically Treated MoS_2 and WS_2. *The Journal of Physical Chemistry C* **2020**, *124* (22), 12175–12184. https://doi.org/10.1021/acs.jpcc.0c04000.

(5) Kang, K.; Lee, K.-H.; Han, Y.; Gao, H.; Xie, S.; Muller, D. A.; Park, J. Layer-by-Layer Assembly of Two-Dimensional Materials into Wafer-Scale Heterostructures. *Nature* **2017**, *550* (7675), 229–233. https://doi.org/10.1038/nature23905.

(6) Weidman, M. C.; Seitz, M.; Stranks, S. D.; Tisdale, W. A. Highly Tunable Colloidal Perovskite Nanoplatelets through Variable Cation, Metal, and Halide Composition. *ACS Nano* **2016**, *10* (8), 7830–7839. https://doi.org/10.1021/acsnano.6b03496.

(7) Paritmongkol, W.; Dahod, N. S.; Stollmann, A.; Mao, N.; Settens, C.; Zheng, S.-L.; Tisdale, W. A. Synthetic Variation and Structural Trends in Layered Two-Dimensional Alkylammonium Lead Halide Perovskites. *Chemistry of Materials* **2019**, *31* (15), 5592–5607. https://doi.org/10.1021/acs.chemmater.9b01318.

(8) Ghosh, D.; Welch, E.; Neukirch, A. J.; Zakhidov, A.; Tretiak, S. Polarons in Halide Perovskites: A Perspective. *J Phys Chem Lett* **2020**, *11* (9), 3271–3286. https://doi.org/10.1021/acs.jpclett.0c00018.

(9) Miyata, K.; Meggiolaro, D.; Trinh, M. T.; Joshi, P. P.; Mosconi, E.; Jones, S. C.; De Angelis, F.; Zhu, X.-Y. Large Polarons in Lead Halide Perovskites. *Sci Adv* **2017**, *3* (8). https://doi.org/10.1126/sciadv.1701217.

(10) Su, P.; Liu, Y.; Zhang, J.; Chen, C.; Yang, B.; Zhang, C.; Zhao, X. Pb-Based Perovskite Solar Cells and the Underlying Pollution behind Clean Energy: Dynamic Leaching of Toxic Substances from Discarded Perovskite Solar Cells. *J Phys Chem Lett* **2020**, *11* (8), 2812–2817. https://doi.org/10.1021/acs.jpclett.0c00503.

(11) Veselska, O.; Demessence, A. D10 Coinage Metal Organic Chalcogenolates: From Oligomers to Coordination Polymers. *Coord Chem Rev* **2018**, *355*, 240–270. https://doi.org/10.1016/j.ccr.2017.08.014.

(12) Trang, B.; Yeung, M.; Popple, D. C.; Schriber, E. A.; Brady, M. A.; Kuykendall, T. R.; Hohman, J. N. Tarnishing Silver Metal into Mithrene. *J Am Chem Soc* **2018**, *140* (42), 13892–13903. https://doi.org/10.1021/jacs.8b08878.

(13) Schriber, E. A.; Popple, D. C.; Yeung, M.; Brady, M. A.; Corlett, S. A.; Hohman, J. N. Mithrene Is a Self-Assembling Robustly Blue Luminescent Metal–Organic Chalcogenolate Assembly for 2D Optoelectronic Applications. *ACS Appl Nano Mater* **2018**, *1* (7), 3498–3508. https://doi.org/10.1021/acsanm.8b00662.

(14) Li, Y.; Jiang, X.; Fu, Z.; Huang, Q.; Wang, G.-E.; Deng, W.-H.; Wang, C.; Li, Z.; Yin, W.; Chen, B.; Xu, G. Coordination Assembly of 2D Ordered Organic Metal Chalcogenides with Widely Tunable Electronic Band Gaps. *Nat Commun* **2020**, *11* (1), 261. https://doi.org/10.1038/s41467-019-14136-8.

(15) Cuthbert, H. L.; Wallbank, A. I.; Taylor, N. J.; Corrigan, J. F. Synthesis and Structural Characterization of [Cu20Se4(M3-SePh)12(PPh3)6] and [Ag(SePh)]∞. *Z Anorg Allg Chem* **2002**, *628* (11), 2483–2488. https://doi.org/10.1002/1521-3749(200211)628:11<2483::AID-ZAAC2483>3.0.CO;2-U.

(16) Yao, K.; Collins, M. S.; Nell, K. M.; Barnard, E. S.; Borys, N. J.; Kuykendall, T.; Hohman, J. N.; Schuck, P. J. Strongly Quantum-Confined Blue-Emitting Excitons in Chemically Configurable Multiquantum Wells. *ACS Nano* **2021**, *15* (3), 4085–4092. https://doi.org/10.1021/acsnano.0c08096.

(17) Maserati, L.; Refaely-Abramson, S.; Kastl, C.; Chen, C. T.; Borys, N. J.; Eisler, C. N.; Collins, M. S.; Smidt, T. E.; Barnard, E. S.; Strasbourg, M.; Schriber, E. A.; Shevitski, B.; Yao, K.; Hohman, J. N.; Schuck, P. J.; Aloni, S.; Neaton, J. B.; Schwartzberg, A. M. Anisotropic 2D Excitons Unveiled in Organic–Inorganic Quantum Wells. *Mater Horiz* **2021**, *8* (1), 197–208. https://doi.org/10.1039/C9MH01917K.

Chapter 2

Excitons, polarons, and polaritons.

The basis of this chapter has been adapted from several books[1–4] that I relied on to gain fundamental knowledge throughout my Ph.D.

2.1 Excitons

In semiconductors, a photon is absorbed by promoting an electron from the valence band to the conduction band, leaving behind a positive charge, a hole, in the valence band. If interactions between the photogenerated electron and hole are negligible, they behave as two independent quasiparticles, known as free charge carriers. On the other hand, if they are attracted to each other via Coulomb forces and behave together as a bound pair, such a bound electron-hole pair no longer represent two uncorrelated quasiparticles. Instead, the electron-hole pair bound by Coulomb forces is considered a neutral quasiparticle called an exciton, which represents the lowest excitation in semiconductors. In this section, we will fundamentally review the types and properties of excitons and how dimensionality affects them.

2.1.1 Excitons in bulk semiconductors

In a simplified way, an exciton can be conceived as an electron and a hole orbiting round each other with the attractive force arising from the Coulomb potential:

$$U(r) = -\frac{e^2}{4\pi\varepsilon_o\varepsilon\, r}, \tag{2.1}$$

where r is the electron-hole distance and ε is the dielectric constant of the semiconductor. This is resembled to the Coulomb potential in hydrogen atom, allowing us to apply the Bohr model of the hydrogen atom to establish an exciton model with some modifications:

The exciton Bohr radius can be expressed as:

$$r_n = \frac{\varepsilon}{(m_r/m_o)} n^2 a_B, \tag{2.2}$$

where n = 1, 2, 3, … is the principal quantum orbit number, $m_r = (m_e m_h)/(m_e + m_h)$ is the reduced mass of the exciton, m_o is the free electron mass, and a_B is the Bohr radius of the hydrogen atom (≈ 5×10^{-2} nm).

In a similar way, the exciton binding energy can be expressed as:

$$E_{b(n)} = \frac{(m_r/m_o)}{\varepsilon^2} \frac{1}{n^2} Ry(H) = \frac{Ry^*}{n^2}, \tag{2.3}$$

where $Ry(H)$ represents the binding energy (or ionization) energy of the ground state hydrogen atom, commonly known as one Rydberg (13.6 eV), and Ry^* represents the effective Rydberg constant.

Therefore, semiconductors with larger dielectric constants typically have excitons with larger radius and weaker exciton binding energy. This is because the attractive Coulomb force between the electrons and hole is more strongly shielded in a semiconductor with a larger dielectric constant. Depending on the degree of exciton radius, there exist three basic types of excitons:

- *Frenkel excitons (or small radius excitons)*: These excitons are typically observed molecular crystal semiconductors with low dielectric constants. The spatial extension of this exciton is approximately confined to a single unit cell or molecule and it usually exhibits exciton binding energy in the range of 0.1~1 eV.
- *Wannier-Mott excitons (or large radius excitons)*: These excitons are mainly observed in inorganic semiconductors with high dielectric constants. In this case, the electron and hole are separated over many lattice constants, and the exciton wavefunction is strongly delocalized over many unit cells, with the exciton binding energy on the order of ~0.01 eV.
- *Charge transfer excitons*: This intermediate case involves the electron and hole being located on adjacent unit cells. These excitons are primarily observed in ionic crystals or semiconductor interfaces.

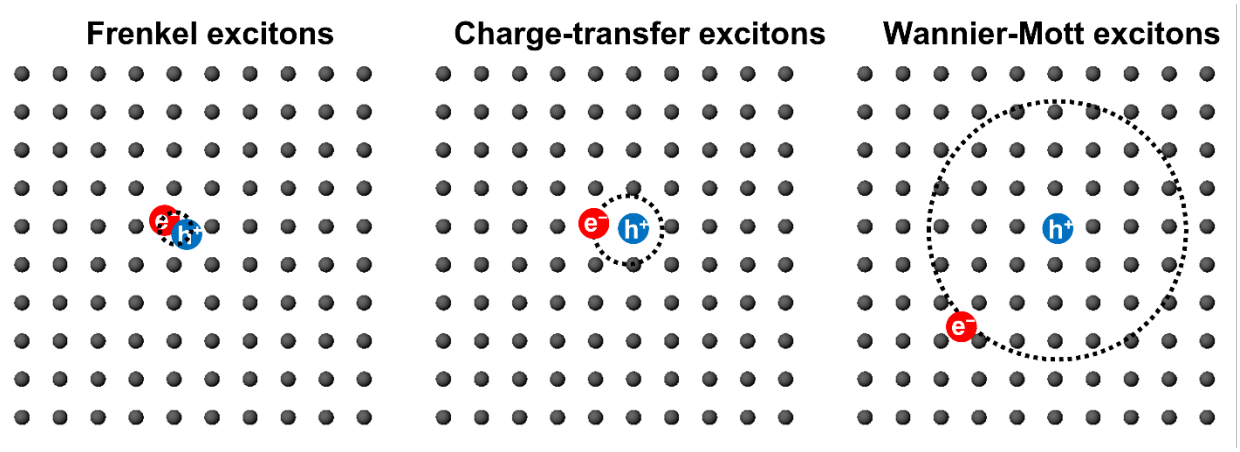

Figure 2.1 Schematics of Frenkel excitons (left), charge-transfer excitons (center), and Wannier-Mott excitons (right).

In an ideal pure semiconductor, delocalized Wannier-mott excitons can travel *freely* through the semiconductor for a finite time before they recombine. In this thesis, such delocalized excitons are referred to as *free-excitons*. The total energy of these free-excitons propagating through the semiconductor can be expressed as:

$$E_n(K) = E_g - E_{b(n)} + E_{kin} = E_g - \frac{(m_r/m_o)}{\varepsilon^2}\frac{1}{n^2}Ry(H) + \frac{\hbar^2 K^2}{2(m_e + m_h)}, \tag{2.4}$$

where E_g is the electronic bandgap, K is the exciton wavevector, $\hbar$ is the reduced Plank constant, $E_{kin} = \hbar^2 K^2/2(m_e + m_h)$ is the kinetic energy of the exciton. When there are impurities acting as trap states for the free-excitons in semiconductors, the free-excitons become localized at the impurities and lose their kinetic energy. Additionally, if the excitons strongly interact with surrounding lattices, they can also become localized through a process known as exciton self-trapping (which will be discussed in detail in the section 2.2). In this thesis, these localized excitons are referred to as *bound excitons*.

2.1.2 Charge carriers (electrons or holes) in two-dimensional semiconductors

The properties of excitons are strongly dependent on the dimensionality of semiconductors. Given the vast scope of this topic, we will focus on the theoretical frameworks of excitons in 2D semiconductors, which are the most relevant to this thesis.

The simplest system of 2D semiconductors is a quantum well with infinite energy barriers. Imagine a layer (a 2D semiconductor) lying on the *x*-*y* plane, with a thickness of L_z along the *z*-axis. The excitons can move freely within *x*-*y* plane, but their motion along *z*-axis will be confined within the layer's thickness due to the potential energy barrier (V) outside of it:

$$\begin{aligned} V(z) &= 0 \text{ for } 0 < z < L_z, \\ V(z) &= \infty \text{ for } z < 0 \text{ and for } L_z < z. \end{aligned} \tag{2.5}$$

First, we will examine how spatial confinement affects the wavefunction and energy of a charge carrier (an electron or a hole). Then, we will extend our analysis to excitons in the next section, taking into account the Coulomb interactions between the electron and the hole.

The time-independent Schrödinger equation for a charge carrier confined in the quantum well $V(z)$ can be expressed as:

$$\left[-\frac{\hbar^2}{2m}\left(\frac{\partial^2}{\partial x^2}+\frac{\partial^2}{\partial y^2}+\frac{\partial^2}{\partial z^2}\right)+V(z)\right]\psi(x,y,z)=E\psi(x,y,z), \tag{2.6}$$

where ψ and E is the wavefunction and energy of a charge carrier, respectively. For convenience, we can separate the equation into two parts: one describing the motion in the x-y plane, where the charge carrier moves freely, and the other describing the motion along the z-axis, where the spatial confinement occurs:

$$\begin{aligned} \frac{\partial^2}{\partial x^2}+\frac{\partial^2}{\partial y^2}+\frac{\partial^2}{\partial z^2} &= \nabla_{xy}{}^2+\frac{\partial^2}{\partial z^2}, \\ \psi(x,y,z) &= \phi(x,y)\zeta(z), \\ E &= E_{xy}+E_z. \end{aligned} \tag{2.7}$$

Thus, instead of the original wave equation (2.6), we solve two separate equations:

$$\begin{aligned} -\frac{\hbar^2}{2m}\nabla_{xy}{}^2\phi(x,y) &= E_{xy}\phi(x,y), \\ \left[-\frac{\hbar^2}{2m}\frac{\partial^2}{\partial z^2}+V(z)\right]\zeta(z) &= E_z\zeta(z). \end{aligned} \tag{2.8}$$

The first equation corresponds to the free motion of a charge carrier within the x-y plane. As a result, its eigenfunctions are plane waves, and the dispersion relation take the well-known form of parabolic bands:

$$E_{xy} = \frac{\hbar^2}{2m}\left({k_x}^2 + {k_y}^2\right) = \frac{\hbar^2}{2m}{k_{xy}}^2. \tag{2.9}$$

The second equation describes the motion of a charge carrier along z-axis where spatial confinement occurs. Because of the infinite energy barriers, a charge carrier cannot escape outside of the well, which gives the boundary conditions of:

$$\zeta(0) = \zeta(L_z) = 0. \tag{2.10}$$

By applying these boundary conditions along with the normalization condition (the total probability of finding a charge carrier is equal to one), we can determine the wavefunctions and the corresponding energies of a charge carrier in a quantum well along z-axis as:

$$\zeta(z) = \sqrt{\frac{2}{L_z}} sin\left(\frac{n\pi}{L_z}z\right), E_z = \frac{\hbar^2\pi^2 n^2}{2m{L_z}^2}, n = 1, 2, 3, \ldots \tag{2.11}$$

Thus, the overall energy of a charge carrier in an ideal quantum well with infinite potential barriers can be expressed as:

$$E = E_{xy} + E_z = \frac{\hbar^2}{2m}\left({k_{xy}}^2 + \frac{\pi^2 n^2}{{L_z}^2}\right), n = 1, 2, 3, \ldots \tag{2.12}$$

Consequently, the energy of a charge carrier can be adjusted by the thickness, L_z, of a quantum well, and this phenomenon is known as *quantum confinement effect*. It is important to note that in a real quantum well, the potential barriers have finite values. While the solution to the wave equation inside such a quantum well remains largely unchanged, the solution outside takes the form of an evanescent (exponentially decaying) wave instead of being zero. Additionally, to observe the quantum confinement effect, the potential barrier, V_o, must be equal to or larger than

$$V_o > \frac{\hbar^2\pi^2}{2m{L_z}^2}. \tag{2.13}$$

2.1.3 Excitons in two-dimensional semiconductors

In the previous section, we discussed single-particle wave equations in a quantum well and explained how spatial confinement quantizes the energies of individual charge carriers (electrons and holes). However, to address excitons, where an electron and a hole are bound by the Coulomb

interaction, we need to use a two-particle Hamiltonian which includes the kinetic energies of the electron and hole, the quantum well potential, V_{well}, and the Coulomb interaction potential, V_{Coul}:

$$H = -\frac{\hbar^2}{2m_e}\left(\frac{\partial^2}{\partial {x_e}^2}+\frac{\partial^2}{\partial {y_e}^2}+\frac{\partial^2}{\partial {z_e}^2}\right)-\frac{\hbar^2}{2m_h}\left(\frac{\partial^2}{\partial {x_h}^2}+\frac{\partial^2}{\partial {y_h}^2}+\frac{\partial^2}{\partial {z_h}^2}\right)+V_{well}+V_{Coul},$$
$$V_{well} = \Delta E_C + \Delta E_V = V_o(z_{e,h}), \tag{2.14}$$
$$V_{Coulomb} = -\frac{e^2}{4\pi\varepsilon_o\varepsilon\, r},$$

where ΔE_C is the potential barrier for an electron, ΔE_V is the potential barrier for a hole, and $r = |r_e - r_h|$ depends on the formulation of the electron and hole motion in the x-y plane in the frame of the exciton center of mass. We can significantly simply this Hamiltonian by assuming *strong quantum confinement limit*. Under this assumption, effect of Coulomb interaction on the exciton energy along z-axis is considered negligible, so excitonic effects manifest only in the x-y plane:

$$H = -\frac{\hbar^2}{2m_e}\frac{\partial^2}{\partial {z_e}^2}-\frac{\hbar^2}{2m_h}\frac{\partial^2}{\partial {z_h}^2}-\frac{\hbar^2}{2M_{xy}}\left(\frac{\partial^2}{\partial X^2}+\frac{\partial^2}{\partial X^2}\right)-\frac{\hbar^2}{2m_{xy}}\left(\frac{\partial^2}{\partial x^2}+\frac{\partial^2}{\partial y^2}\right)+V_o(z_{e,h}) - \frac{e^2}{4\pi\varepsilon_o\varepsilon\, r} \tag{2.15}$$

where $M_{xy} = m_e + m_h$ is the total exciton mass and m_{xy} $(= m_r)$ is the reduced exciton mass. The capital letters (X, Y) represent the coordinates of the exciton center of mass, while the lower-case letters (x, y) represent the relative coordinates of the electron and the hole. The time-independent Schrödinger equation with the above Hamiltonian can then be divided into two parts describing separately the motion in the x-y plane and along the z-axis. The wavefunction is thus separated into three parts:

$$\psi(r) = {\phi_n}^{xy}(r_{xy})\zeta_{e,i}(z_e)\zeta_{h,j}(z_h), \tag{2.16}$$

where the second and third terms represent the motions of the electron and the hole along the z-axis. In contrast, the first term describes the (quasi-) free motion of the exciton with principal quantum number n in the x-y plane. The associated exciton binding energies in the 2D quantum well are:

$$E_{b(n)}{}^{2D} = \frac{Ry^*}{\left(n-\frac{1}{2}\right)^2}, n = 1, 2, 3, \ldots \tag{2.17}$$

We can now directly compare the binding energy of excitons in 3D bulk semiconductors and 2D semiconductors. For the ground state exciton ($n = 1$), exciton binding energy in 2D system is four times larger than in the 3D bulk system. Additionally, because the squared exciton Bohr radius is inversely proportional to the exciton binding energy (${a_B}^2 \propto 1/E_b$), the exciton Bohr radius in 2D system is half the size of that in the 3D bulk case. This can be understood as the electron and hole being 'squeezed' closer together in a narrow well, leading to a decrease in the exciton radius and an increase of the electron-hole binding interaction. Another important characteristic of an exciton is its *oscillator strength* (f), which is defined as the radiative transition probability between two energy levels. Therefore, a stronger oscillator strength of exciton indicates stronger absorption and emission from its excitonic transition. The oscillator strength of an exciton is inversely proportional to the cube of its Bohr radius ($f \propto 1/{a_B}^3$). Consequently, the oscillator strength of an exciton in 2D semiconductors is eight times stronger than in 3D bulk semiconductors.

Until now, we have discussed how the quantum confinement effect impacts the properties of excitons using 2D hydrogen atom models, assuming a constant dielectric environment. However, in addition to the quantum confinement effect, the discontinuity of dielectric constants in 2D systems also significantly influences excitons. When the dielectric constant outside of 2D semiconductors is smaller than that inside, the dielectric screening of excitons is reduced (Figure 2.2). This is because the electric field lines connecting the electron and hole extend outside of the 2D semiconductors. As a result, the Coulomb interactions between the electron and hole become stronger, leading to higher exciton binding energy. This phenomenon is known as the *dielectric confinement effect*. Consequently, excitons become more robust, stable, and stronger in 2D semiconductors due to both quantum confinement and dielectric confinement effects, dominating the optical properties of the material.

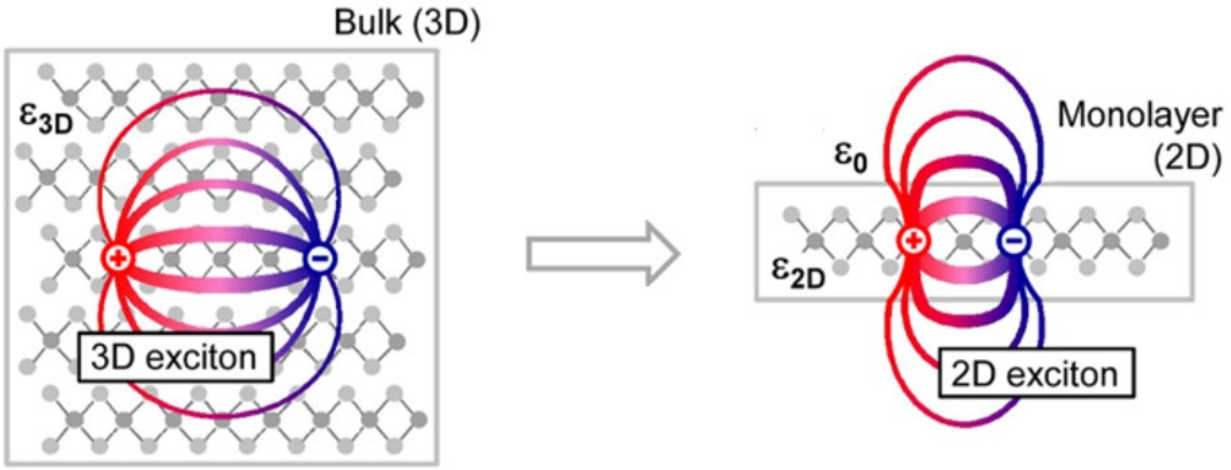

Figure 2.2 Real-space representation of excitons in a 3D bulk and a 2D monolayer semiconductor, showing reduced dielectric screening on an exciton in 2D system. Figure adapted from [5].

2.2 Polarons

A charge carrier (or an exciton) in a deformable lattice can create an attractive potential well through short-range and/or long-range electron (or an exciton)-lattice interactions, where it can be temporarily trapped. This state, where a charge (or an exciton) is trapped in a potential well created by an electron (or an exciton)-lattice interaction is known as a quasiparticle called a *polaron*. Depending on the type of species trapped in the potential well, it can be referred to as an electron-polaron, hole-polaron, or exciton polaron. Polarons play a crucial role in photophysical properties of semiconductors, particularly low-dimensional semiconductors with polarizable and soft lattices. In this section, we will briefly discuss the electron-phonon interactions involved in polaron formation, types and properties of polarons depending on the strength of these interactions, and how dimensionality affects polarons. While our primary focus will be on electron-polarons to explain the concept, we will also briefly touch on exciton-polarons which are more relevant to this thesis.

2.2.1 Electron-phonon interactions

Electron-phonon interactions describe how the energy of an electronic charge is affected by displacement of atoms around the charge. There are two types of electron-phonon interactions: *Long-range interactions* and *short-range interactions*.

Long-range electron-phonon interactions occurs in polarizable (ionic and polar) materials. Pairing anions with cations allows the Coulomb potential of these materials to be represented as an array of electric dipoles. Changing the separation between the ions alters the potential experienced by an electron. The displacement of ions induced by the point charge of an electron provides a Coulomb-like potential well ${V_{eq}}^{LR}$ to the electron at r:

$$ {V_{eq}}^{LR}(r) = -\left(\frac{1}{\varepsilon_\infty} - \frac{1}{\varepsilon_o}\right)\frac{e^2}{|r|}, \tag{2.18} $$

where ε_∞ and ε_o are the material's optical and static dielectric constants. The magnitude of this Coulomb potential quantifies the strength of the long-range electron-phonon interaction. This interaction is typically associated with longitudinal optical (LO) phonons which can generate net electric field to the electron.

Short-range electron-phonon interactions occur when the energy of an electron depends on the strain where it resides. This interaction is typically associated with acoustic phonons and can occur in any semiconductors regardless of whether they are polar or nonpolar. Strain-induced shifts of the energies of bonding and-antibonding states (or electronic energies in semiconductors) generate a potential well ${V_{eq}}^{SR}$ to the electron, which, within the continuum treatment, can be expressed as:

$$ {V_{eq}}^{SR} = -\frac{F^2}{k}, \tag{2.19} $$

where F has dimensions of a force and k is the continuum's stiffness constant.

The potential wells formed by long-range and short-range electron-phonon interactions for a confined carrier of radius R are shown in Figure 2.3.

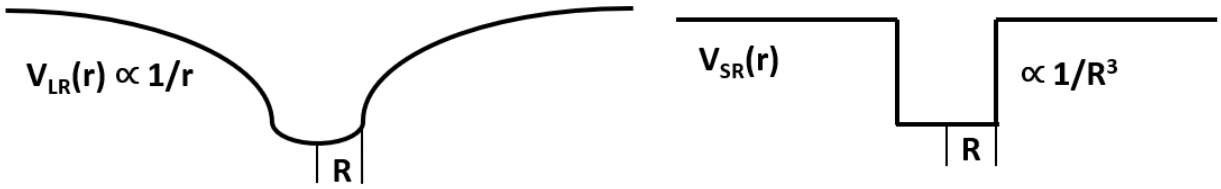

Figure 2.3 Potential wells formed through long-range electron-optical phonon (left) and short-range electron-acoustic phonon (right) interactions.

Depending on the degree or strength of electron-phonon interactions, we define two types of polarons: *Large polarons (or weak-coupling polarons)* and *small polarons (strong-coupling polarons)*.

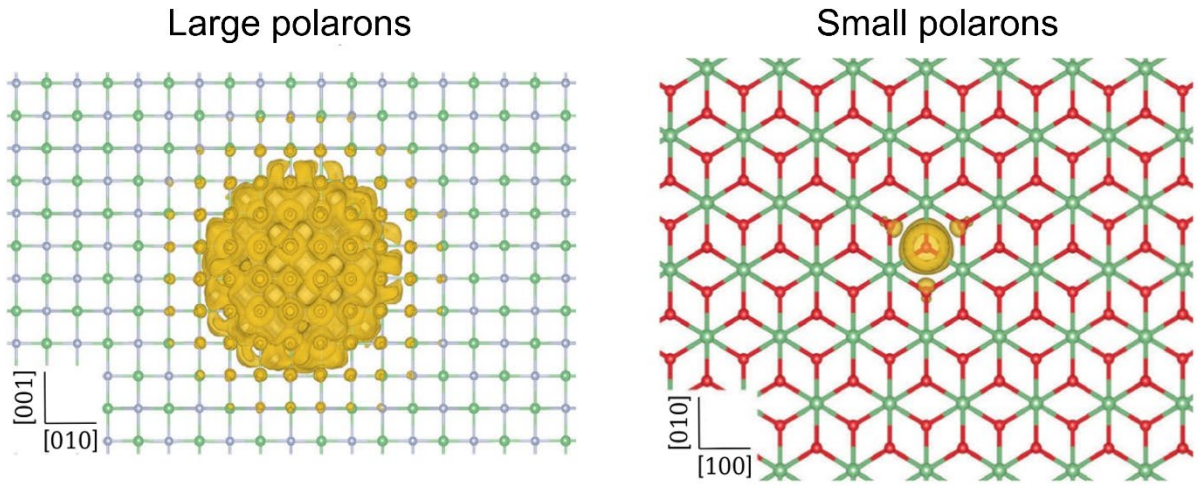

Figure 2.4 A large polaron in NiF (left) and a small polaron in Li_2O (right). Figure adapted from [6].

- *Large polarons (or weak-coupling polarons)*: Large polarons involve moderate lattice deformation around an electron, extending over several unit cells. This is typically due to the electrostatic polarization of an ionic lattice, with ion displacements much smaller than the lattice constant. In this case, the trapping time is extremely short, so the large polaron can be expressed as an increase of the effective mass of the electron. Therefore, its transport can be modeled as a free-electron transport with an increased effective mass.
- *Small polarons (or strong-coupling polarons)*: Small polarons involve stronger lattice distortion confined to about one unit cell. This often results from short-range potentials, though

long-range electrostatic polarization with significant ion displacements can also be a factor. This results in much longer trapping times, so the transport of small polarons is typically described by a hopping mechanism. The extreme case of small polaron is sometimes referred to as *self-trapped electron*, where the transfer time scale exceeds the observation period.

In the following sections, we will first review large polarons that exist in the weak-coupling regime and extend our discussion to small polarons, self-trapping, and the effects of material dimension on polaron formation.

2.2.2 Large polarons (or weak-coupling polarons)

With sufficiently weak electron-phonon interaction, an electron in semiconductors form a large polaron or weak-coupling polaron. The energies and the effective masses associated with the quasiparticles are then slightly shifted from the free-electron values. These effects can be calculated by treating the electron-phonon interaction as a small perturbation.

In this weak-coupling scheme, the conduction band is shifted through long-range electron-phonon Coulomb interaction by:

$$\Delta {E_{WC}}^{LR} = -\frac{e^2}{2R_p}\left(\frac{1}{\varepsilon_\infty}-\frac{1}{\varepsilon_o}\right) = -\alpha\hbar w, \tag{2.20}$$

where the large polaron radius R_p and Fröhlich coupling constant α are expressed as:

$$R_p \equiv \left(\frac{\hbar}{2mw}\right)^{1/2} = \left(\frac{t}{\hbar w}\right)^{1/2} a, \tag{2.21}$$

$$\alpha = \frac{e^2}{\hbar}\left(\frac{1}{\varepsilon_\infty}-\frac{1}{\varepsilon_o}\right)\sqrt{\frac{m}{2\hbar w}} \tag{2.22}$$

where m is the effective mass of a free-electron, w is the phonon frequency, $t \equiv \hbar^2/2ma^2$ is the associated electronic band parameter, a is the lattice constant. This radius represents a distance that an electron can diffuse during the period of an atomic vibration. Fröhlich coupling constant α represents the strength of the long-range electron-phonon Coulomb interaction. Then, the corresponding effective mass m^* for a large polaron can be expressed as:

$$m^* = m\left(1 + \frac{\alpha}{6}\right). \tag{2.23}$$

Since $\alpha < 1$, m^* is only slightly heavier than m. Thus, a large polaron can be considered as a free-electron-like particle with an increased effective mass and relaxed energy, and its transport can still be described as a free-electron model (metallic or bandlike transport). The weak-coupling regime of the long-range electron-phonon Coulomb interaction remains valid as long as the potential well depth is less than the characteristic optical phonon energy.

Although it is less significant for the formation of a large polaron, the short-range electron-acoustic phonon interaction also reduces the energy of an electron at the conduction band minimum in the weak-coupling regime:

$$\Delta {E_{WC}}^{LR} = -\frac{F^2/k}{12(R_p/a)^2}. \tag{2.24}$$

The weak-coupling regime of the short-range electron-acoustic phonon interaction breaks down when the product of the force exerted by an electron on adjacent atoms and the time an electron can spend a site exceeds the momentum of these atoms' vibrations.

2.2.3 Small polarons (or strong-coupling polarons) and self-trapping

In the strong electron-phonon coupling regime where small polarons form, the descriptions of electron-phonon interactions for large polarons no longer apply, and a different formalism is required. In this section, we will discuss the self-trapping of an electron in a continuum model, which represents the extreme case of small polarons.

The adiabatic energy of an electron with wavefunction $\psi(r)$ interacting with a field of elastic dilation $\Delta(r)$ and Coulomb potential $\phi(r)$ can be expressed as:

$$\begin{aligned} E[\psi, \Delta, \phi] = \frac{\hbar^2}{2m}\int (\nabla\psi)^2 d\tau + E_d \int |\psi(r)|^2 \Delta(r) d\tau + e\int |\psi(r)|^2 \phi(r) d\tau \\ + \frac{C}{2}\int |\psi(r)|^2 \phi(r) d\tau + \frac{\varepsilon'}{8\pi}\int |\nabla\phi(r)|^2 d\tau, \end{aligned} \tag{2.25}$$

where E_d is the deformation potential, C is the elastic constant, and $\varepsilon'$is given by $1/\varepsilon' = 1/\varepsilon_\infty - 1/\varepsilon_o$. Here, the first term is the energy kinetic energy. The second and third terms are associated

with the strength of the short-range electron-acoustic phonon interaction and the strength of the long-range electron-LO phonon interaction, respectively. The fourth and fifth terms represent the elastic and dielectric polarization energies of the medium, respectively. Our interest in on the minimum of E with respective to ψ, Δ, ϕ. To solve this, a trial wavefunction $\psi(r)$ in the form of a Gaussian of radial extent a is assumed:

$$\psi(r) = (\sqrt{2}/a)^{3/2}\exp[-\pi(r/a)^2], \tag{2.26}$$

where the radius of localization a is the variational parameter in the range between a_o(the lattice constant) and ∞(free-electron). Minimizing $E[\psi, \Delta, \phi]$ sequentially with respect to Δ and ϕ while keeping $\psi(r, a)$ fixed yields:

$$\Delta(r) = (-E_d/C)|\psi(r, a)|^2 \tag{2.27}$$

and

$$\nabla^2\phi(r) = (4\pi e/\varepsilon')|\psi(r, a)|^2. \tag{2.28}$$

Integrating over the volume of the medium after substituting (2,26), (2.27) and (2.28) into (2.25), the energy as a function of a_o/a can be obtained:

$$E[\psi] = B(a_o/a)^2 - E^{ac}(a_o/a)^3 - E^{op}(a_o/a), \tag{2.29}$$

where $B \equiv 3\pi\hbar^2/2m{a_o}^2$, $E^{ac} \equiv {E_d}^2/2C{a_o}^3$, and $E^{op} \equiv e^2/\varepsilon' a_o$ are associated with the kinetic energy of the electron, lattice relaxation energies contributed by the electron-acoustic phonon and LO phonon interactions, respectively. For efficient discussion, we introduce two dimensionless electron-phonon coupling parameters $g_s = E^{ac}/B$ and $g_l = E^{op}/B$. Then, (2.29) becomes:

$$E(a_o/a)^{3D} = B[(a_o/a)^2 - g_s(a_o/a)^3 - g_l(a_o/a)] \tag{2.30}$$

Figure 2.5 exhibits example plots of E vs. a_o/a depending on the values of g_s and g_l. Note that $a_o/a \to 0$ corresponds to a free-electron (or a large polaron) whereas $a_o/a \to 1$ corresponds to a self-trapped electron (or a small polaron).

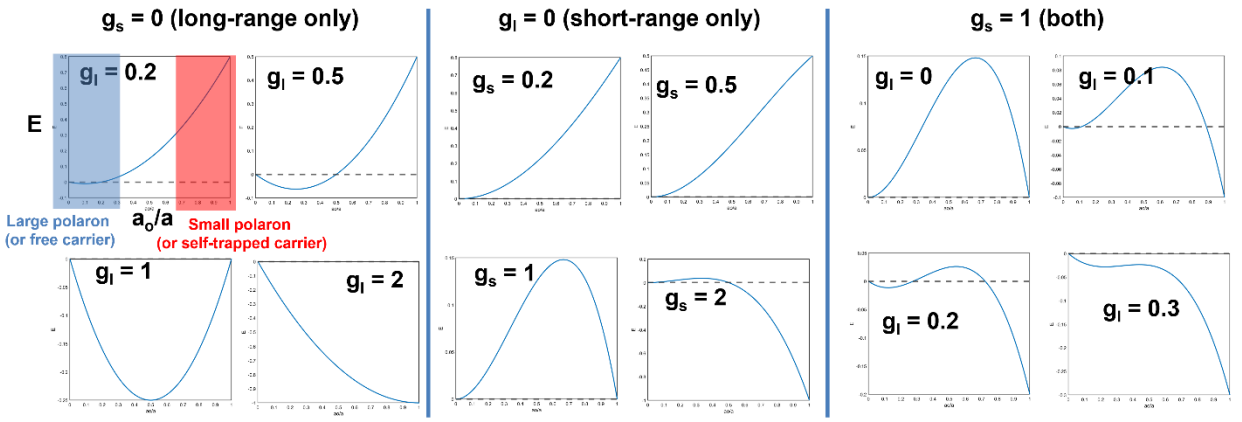

Figure 2.5 Adiabatic energy of a charge carrier vs. a_o/a in 3D semiconductors as a function of g_s and g_l.

It is clearly shown that small polaron state becomes the most stable state, and the activation energy barrier from free-electron to self-trapped exciton decreases as electron-phonon coupling becomes stronger. Because the energy of small polarons or self-trapped electrons are highly relaxed compared to their surroundings, their wavefunctions are localized within a single unit cell and they become almost immobile. When they do transport (with extremely low mobility), it typically occurs through hopping mechanisms.

2.2.4 Self-trapping in low-dimensional semiconductors

Small polaron formation and self-trapping has been discussed so far for three dimensions. In this section, we will discuss how the dimensionality of semiconductors affect self-trapping of charge carriers. We will also briefly extend our discussion to exciton-phonon interactions and exciton self-trapping.

Short-range electron-acoustic phonon interactions occur in three-dimensions. Thus, when the material is reduced to 2D or 1D, these interactions are also reduced to 2D and 1D, respectively. In contrast, long-range electron-phonon Coulomb interaction results from the interaction between an electron and LO-phonons. Since LO-phonons are only relevant in the 1D longitudinal direction, reducing the material dimension from 3D to 2D or 1D does not affect the electron-LO phonon

interaction in the previous formalism. Therefore, $E(a_o/a)$ for 2D and 1D cases can be expressed as:

$$E(a_o/a)^{2D} = B[(a_o/a)^2 - g_s(a_o/a)^2 - g_l(a_o/a)] \tag{2.31}$$

and

$$E(a_o/a)^{1D} = B[(a_o/a)^2 - g_s(a_o/a) - g_l(a_o/a)]. \tag{2.32}$$

Figure 2.6 exhibits example plots of E vs. a_o/a depending on the values of g_s and g_l.

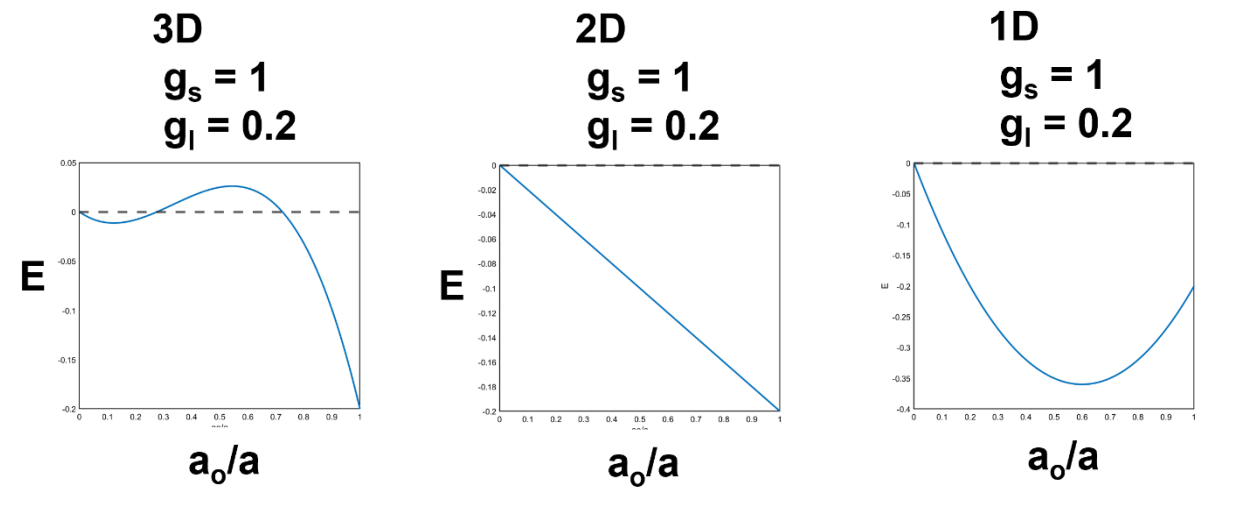

Figure 2.6 Adiabatic energy of a charge carrier vs. a_o/a in 1D, 2D, and 3D semiconductors with $g_s = 1$ and $g_l = 0.2$.

It is shown that reducing material dimension lowers the activation energy barrier from free-electron (large polaron) to self-trapped electron (small polaron). Therefore, small polarons are more easily observed in low-dimensional semiconductors compared to their 3D bulk counterparts.

So far, we have focused on electron-phonon interactions and electron-phonon polarons. The same formalism and description can be applied to hole-phonon interactions and hole-phonon polarons. However, how can we describe exciton-phonon interactions and exciton-polarons?

There are two simplified ways to describe exciton-phonon interactions and exciton-polarons. One approach is to consider the exciton as a charge-neutral particle and assume that only short-range exciton-acoustic phonon interactions are present, while long-range Coulomb

interactions are absent. The other approach is to assume that one charge carrier (either an electron or a hole) is dominant in the exciton and apply previous formalism only to the dominant charge carrier. This situation arises when the effective masses of an electron and a hole are significantly different. In such case, heavy carrier can dominate the motion of the exciton. However, I would like to emphasize that neither approach is perhaps the best way to describe the exciton-phonon interactions and exciton-polarons. There is still much room for improvement in our understanding and description of these interactions. The advancement of theory is accompanied by the experimental observations and confirmations. In this regard, spectroscopic observations of exciton-phonon interactions and self-trapped excitons in novel low-dimensional hybrid semiconductors, which we will discuss in the following chapters of this thesis, may contribute to the advancement of this field in condensed matter physics.

2.3 Exciton-polaritons

As explained in the previous section of 2.1.3, excitons in low-dimensional semiconductors exhibit strong oscillator strength, resulting in strong absorption and emission. Consequently, when a photon is created through exciton recombination, it can be re-absorbed within the material, creating an exciton once again. If this process is efficiently repeated, the distinction between excitons and photons inside the material becomes ambiguous. Although this is a simplified description, this state, where an exciton and a photon are strongly coupled, is known as an *exciton-polariton*. When a semiconductor containing excitons with strong binding energy and oscillator strength is placed inside an optical cavity with photon energy close to that of the exciton, the exciton-photon interaction can enter the *strong coupling regime*. This results in the formation of strongly-coupled exciton-polaritons, which alter and dominate the optical and optoelectronic properties of semiconductors. Although this topic is beyond the primary scope of this thesis, we will provide a brief review of this subject here, because some 2D MOCs have the potential to host strong exciton-polaritons (as we will show in Chapter 7). One of the requirements for exciton-polariton formation is a robust photonic state in the semiconductor. We will begin by discussing optical cavity that can support strongly-confined photonic modes.

2.3.1 Fabry-Perot cavity and standing-wave photon modes

The Fabry-Perot (FP) interferometer, also known as the *etalon*, is a typical optical cavity consisting of two parallel reflection surfaces. Constructive and destructive interferences occur when the phase change of a photon during a round trip inside the cavity corresponds to an even or odd integer multiple of π, respectively. The phase change can be expressed as:

$$\varphi = \frac{2\pi}{\lambda}\delta \tag{2.33}$$

where λ is the wavelength of the photon and δ is the path difference ($\delta = 2L$ where L is the length of the cavity). Consequently, the conditions for constructive and destructive interference are:

$$\begin{aligned} &\text{Constructive: } \varphi = \frac{4\pi L}{\lambda} = 2m\pi \rightarrow L = \frac{\lambda}{2}m, \\ &\text{Destructive: } \varphi = \frac{4\pi L}{\lambda} = m\pi \rightarrow L = \frac{\lambda}{4}m, \\ &\text{where, } m = 1,2,3, \ldots \end{aligned} \tag{2.34}$$

When the constructive interference occurs, the cavity is in resonance, supporting the standing-wave photon modes whose energies can be tuned by adjusting the length of the cavity.

2.3.2 Exciton-polaritons in 2D semiconductors inside the cavity

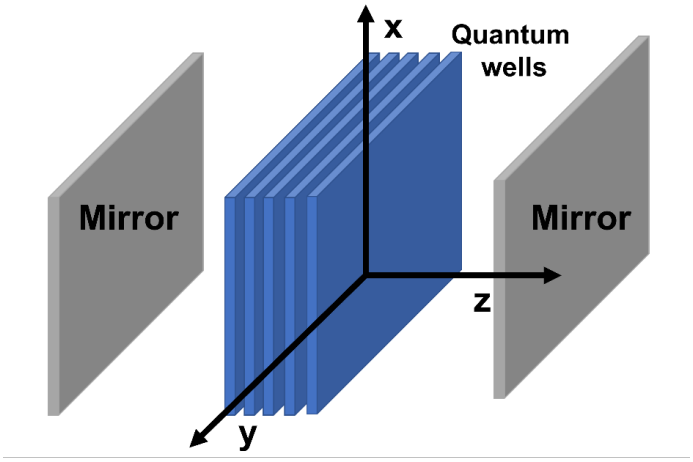

Figure 2.7 2D Quantum well semiconductors placed in reflective mirrors. Excitons and photons are confined along the z-axis.

Now, imagine a 2D semiconductor is placed inside the FP cavity where both excitons and photons are confined along z-axis, as shown in Figure 2.7. When the energies of exciton and cavity are close enough, excitons in the semiconductor and photons confined within the cavity begin to exchange their energies, forming exciton-polaritons. In this section, we will discuss how an exciton-polariton is formed and what factors affect the formation of this quasiparticle. To describe the interactions of exciton and photon, we will begin with the dispersion of a photon which is expressed:

$$E_P(k) = \hbar c|k|, \tag{2.35}$$

where k is the light velocity and $|k| = \sqrt{{k_x}^2 + {k_y}^2 + {k_z}^2}$ is the wave vector. Since the photon is confined along z-axis, the dispersion of photon becomes:

$$E_P(k) = \frac{\hbar c}{n}\sqrt{\left(\frac{2\pi}{L}\right)^2 + {k_{||}}^2}, \tag{2.36}$$

where L is the length between two mirrors, n is the refractive index of the semiconductor, and $k_{||}$ is equal to $\sqrt{{k_x}^2 + {k_y}^2}$. The first order approximation of Taylor expansion gives:

$$E_P(k_{||}) \approx E_{Po} + \frac{\hbar^2 {k_{||}}^2}{2{m_P}^*} \tag{2.37}$$

where $E_{Po} = 2\pi\hbar c/Ln$ is the photon energy at $k_{||} = 0$ and ${m_P}^* \approx \hbar n/cL$ is the effective mass of the cavity photon. As we described in the previous section of 2.1.2, the dispersion of the exciton in 2D semiconductors can be expressed as:

$$E_X(k) = E_{Xo} + \frac{\hbar^2 {k_{||}}^2}{2{m_X}^*} \tag{2.38}$$

where E_{Xo} is the exciton energy at $k_{||} = 0$ and ${m_X}^*$ is the effective mass of the exciton. Using a simplified model of two oscillators, the Hamiltonian for the exciton-photon system can be expressed as:

$$H = \sum_k E_P(k){p_k}^\dagger p_k + \sum_k E_X(k){x_k}^\dagger x_k + \sum_k \hbar\Omega({x_k}^\dagger p_k + {p_k}^\dagger x_k) \tag{2.39}$$

where $\hbar\Omega$ represents the interaction energy (also known as Rabi splitting), ${p_k}^{\dagger}p_k$ and ${x_k}^{\dagger}x_k$ are the operators of creation and annihilation for photons and excitons, respectively. The eigen states of this system can be derived as a solution of the linear polariton system with the following eigen values:

$$E_{UP}(k_{||}) = \frac{E_P(k_{||}) + E_X(k_{||})}{2} + \frac{1}{2}\sqrt{\Delta(k_{||})^2 + 4\hbar^2\Omega^2}, \tag{2.40}$$

$$E_{LP}(k_{||}) = \frac{E_P(k_{||}) + E_X(k_{||})}{2} - \frac{1}{2}\sqrt{\Delta(k_{||})^2 + 4\hbar^2\Omega^2}, \tag{2.41}$$

where $E_{UP}(k_{||})$ and $E_{LP}(k_{||})$ represent the energies of the upper and lower branches of the exciton-polariton state, and $\Delta(k_{||})$ is $E_P(k_{||}) - E_X(k_{||})$. The schematic of $E_{UP}(k_{||})$ and $E_{LP}(k_{||})$ when $E_{Po} = E_{Xo}$ is shown in Figure 2.8.

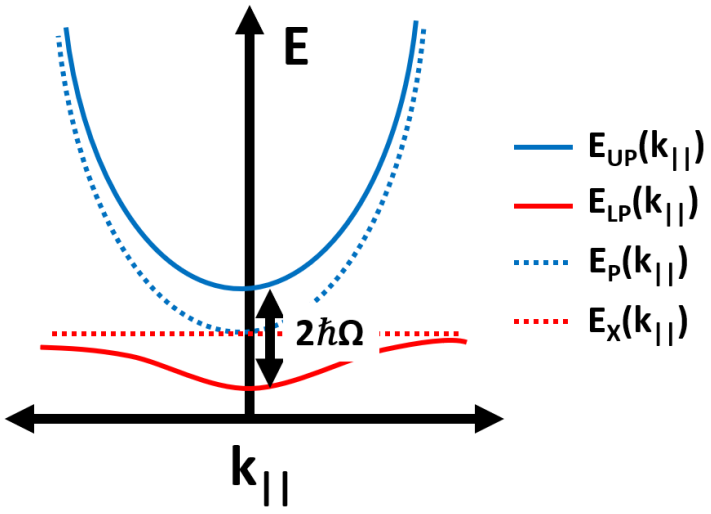

Figure 2.8 Exciton-polariton dispersions in a quantum well-FP cavity.

It is worth noting that the effective mass of the exciton ${m_X}^*$ is much greater than the effective mass of the photon ${m_P}^*$, resulting in a nearly flat slope for $E_X(k_{||})$ compared to others.

In reality, in addition to $\Delta(k_{||})$ and $\hbar\Omega$, the lifetimes of the individual components (photon and exciton) significantly impact the dynamics and energies of the system. Taking lifetimes into account:

$$E_{LP,UP}(k_{||}) = \frac{E_P(k_{||}) + E_X(k_{||}) + i(\gamma_P + \gamma_X)}{2} \pm \frac{1}{2}\sqrt{\left(\Delta(k_{||}) + i(\gamma_P - \gamma_X)\right)^2 + 4\hbar^2\Omega^2}, \qquad (2.42)$$

where γ_P and γ_X represents the homogenous linewidth of the photonic and excitonic modes, respectively, which are directly related to their corresponding lifetimes via Heisenberg's uncertainty principle, $\tau \cdot \gamma \geq \hbar$. The decay rate of the photons is determined by the cavity losses (absorption and leakage) and the decay rate of the excitons is governed by radiative and non-radiative decay processes. Typical lifetimes are τ_P~1-10ps and τ_X~1ns . Therefore, the requirement for strong exciton-photon coupling is $\hbar\Omega > |\gamma_P - \gamma_X/2|$. Qualitatively, this means having strongly confined photons with minimal leakage and excitons with strong oscillator strength.

Some semiconductors, including 2D LHPs, have a natural flat FP optical cavity structure and 2D excitons with strong oscillator strength. One example is 2D AgSePh. It has flat top and bottom surfaces and a high refractive index, allowing these surfaces to act as mirrors. Additionally, it features excitons lying in 2D plane parallel to the flat surfaces, with strong binding energy and strong oscillator strength. Consequently, when its thickness is within the range of excitons' wavelength, it can exhibit exciton-polariton features.

2.4 References

(1) Pelant, I.; Valenta, J. *Luminescence Spectroscopy of Semiconductors*; Oxford University Press, 2012. https://doi.org/10.1093/acprof:oso/9780199588336.001.0001.

(2) Emin, D. *Polarons*; Cambridge University Press, 2012. https://doi.org/10.1017/CBO9781139023436.

(3) Song, K. S.; Williams, R. T. *Self-Trapped Excitons*; Springer Berlin Heidelberg: Berlin, Heidelberg, 1993; Vol. 105. https://doi.org/10.1007/978-3-642-97432-8.

(4) Rahimi-Iman, A. *Polariton Physics*; Springer International Publishing: Cham, 2020; Vol. 229. https://doi.org/10.1007/978-3-030-39333-5.

(5) Chernikov, A.; Berkelbach, T. C.; Hill, H. M.; Rigosi, A.; Li, Y.; Aslan, B.; Reichman, D. R.; Hybertsen, M. S.; Heinz, T. F. Exciton Binding Energy and Nonhydrogenic Rydberg Series in Monolayer WS_2. *Phys Rev Lett* **2014**, *113* (7), 076802. https://doi.org/10.1103/PhysRevLett.113.076802.

(6) Franchini, C.; Reticcioli, M.; Setvin, M.; Diebold, U. Polarons in Materials. *Nat Rev Mater* **2021**, *6* (7), 560–586. https://doi.org/10.1038/s41578-021-00289-w

Chapter 3

Low-dimensional metal organochalcogenolates

A key material system in this thesis is metal organochalcogenolates (MOCs),[1] also known as metal-organic chalcogenides and organic metal chalcogenides (OMCs).[2] MOCs are a novel class of low-dimensional hybrid organic-inorganic materials with the chemical formula of $[M(ER)]_n$. Here, M stands for metals, E stands for chalcogen elements (S, Se, Te), and R denotes an organic hydrocarbon. Coinage metals [Cu(I), Ag(I), Au(I)] are commonly used in these materials due to their favorable soft base-soft acid interaction, but metals such as Cd, Pb, Zn, In, Sn and Fe can also be used.[3–5]

Depending on the steric hinderance and/or Vander Waals interactions between organic ligands as well as electronic interactions between organic and inorganic components, there exists 0D, 1D, 2D MOCs. OD MOCs exhibit the properties of molecular complexes, whereas 1D and 2D MOCs can exhibit semiconductor properties with delocalized electronic bands along the direction or plane where inorganic components are extended.

Although the history of this material family began in 1980s, MOCs were not widely recognized as a platform for studying novel exciton physics and developing innovative excitonic devices until 2018. This recognition came when a silver phenylchalcogenolate (AgSePh, also known as “mithrene”) was rediscovered as a blue-emitting excitonic semiconductor.[6,7] Since then, multiple groups have reported promising properties of AgSePh, such as strong exciton binding energy, a tunable bandgap via the control of organic and inorganic components, in-plane optical anisotropy, and more.

In this chapter, I will briefly review the history and progress of AgSePh and its derivatives (AgSPh, AgTePh, and AgSeR), and highlight a knowledge gap in the community that I will address in the following chapters based on my Ph.D. research.

3.1 Synthesis and structure of 2D AgEPh (E = S, Se, Te)

The synthesis and structure of AgSePh was first reported in 2002 by John Corrigan & co-workers (Figure 3.1).[8] Briefly, AgSePh single crystals were obtained by adding a solution of lithium phenylselenolate (PhSeLi) to a solution of silver chloride (AgCl) and triphenylphosphine in tetrahydrofuran (THF). The crystal structure was determined to be monoclinic C2/c using single-crystal X-ray diffraction (SCXRD) measurement at 180 K. Unfortunately, no further studies were conducted on this material until 2018.

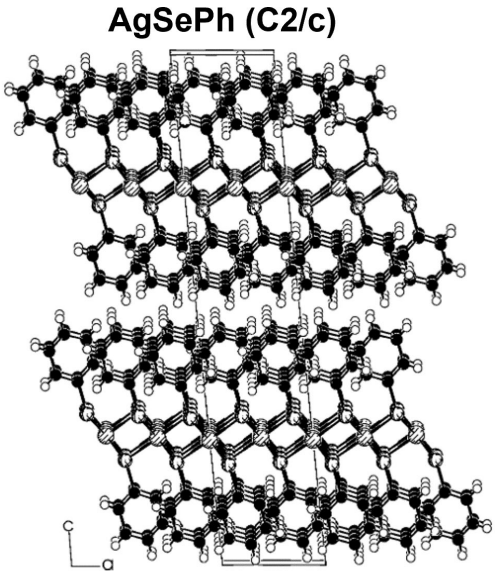

Figure 3.1 Crystal structure of AgSePh in C2/c, reported in [8].

In 2018, Hohman and co-workers rediscovered AgSePh as a blue-emitting excitonic semiconductors by developing two new synthetic methods (Figure 3.2). One method, known as biphasic method,[7] involves layering toluene containing diphenyl diselenide (Ph_2Se_2) on top of a water containing silver nitrate ($AgNO_3$). AgSePh microcrystals are then formed at the interface. The other method, known as tarnishing method,[6] involves reacting a metallic Ag film is reacted with Ph_2Se_2 vapor at elevated temperatures, transforming it into polycrystalline AgSePh films with a domain size of a few hundreds of nanometers. Similar results can be obtained upon the reaction between silver (I) oxide (Ag_2O) and benzeneselenol (PhSeH) vapor.

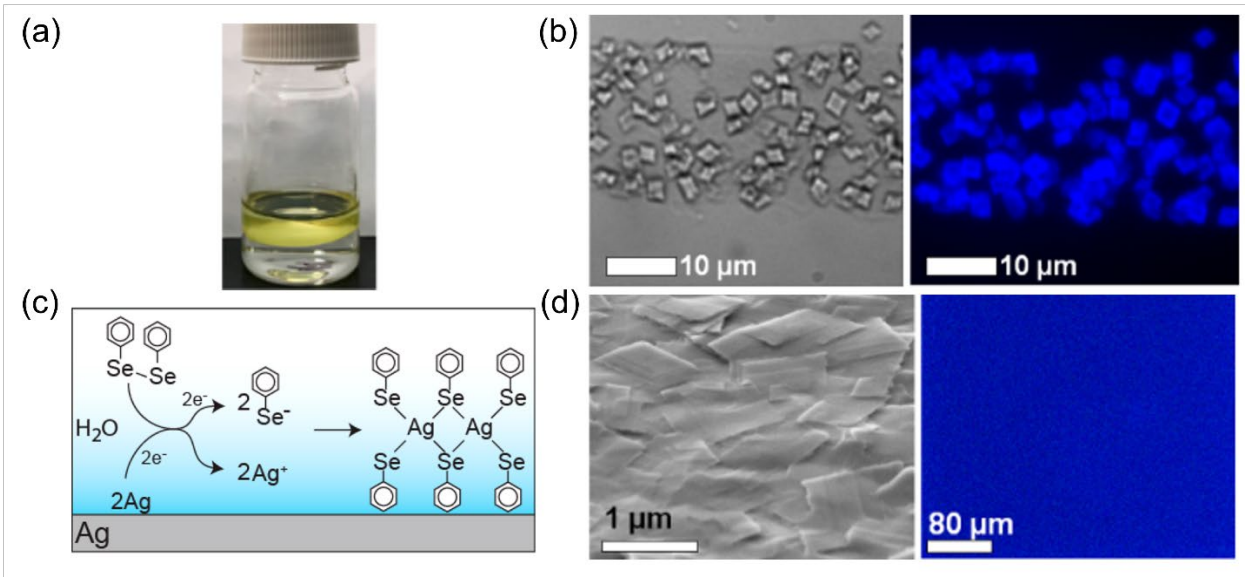

Figure 3.2 Biphasic and tarnishing methods. (a) A photo of reaction vial for the biphasic method. (b) Optical and confocal emission micrographs of AgSePh crystals from the biphasic method. (c) Schematic overview of the tarnishing method. (d) Optical and confocal emission micrographs of AgSePh thin films from the tarnishing method. Panels (a,b) adapted from [7]. Panels (c,d) adapted from [6].

In 2021, Paritmongkol in the Tisdale group and co-workers developed an amine-assisted reaction method (Figure 3.3).[9] This method involves mixing amine solution (e.g., propylamine) containing AgNO3 and toluene containing Ph_2Se_2, resulting in millimeter-sized AgSePh single crystals. The SCXRD measurement at 100 K determined the structure of obtained AgSePh single crystal to be monoclinic $P2_1/c$.

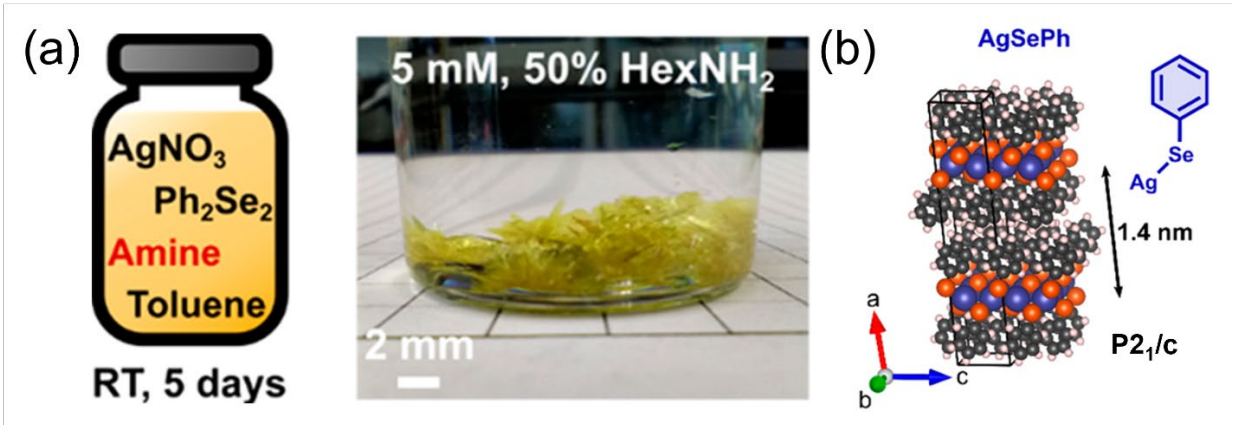

Figure 3.3 Amine-assisted single-phase method. (a) Schematic illustration of the method (left) and image of the resulting product (right). (b) Crystal structure of AgSePh in $P2_1/c$. Figure adapted from [9].

In 2022, Nate Hohman & co-workers developed small molecule serial femtosecond X-ray crystallography (smSFX) to determine the structure of small molecules (Figure 3.4).[10] As a proof of concept, they synthesized nanometer-sized AgSePh crystals by directly reacting Ag_2O powders with a PhSeH solution, and determined the structure of AgSePh to be monoclinic C2/c using this new method at room temperature. Additionally, using similar methods, they synthesized nanometer-sized AgSPh and AgTePh, and determined the structures of AgSPh to be monoclinic Cc and AgTePh to be monoclinic C2/c.

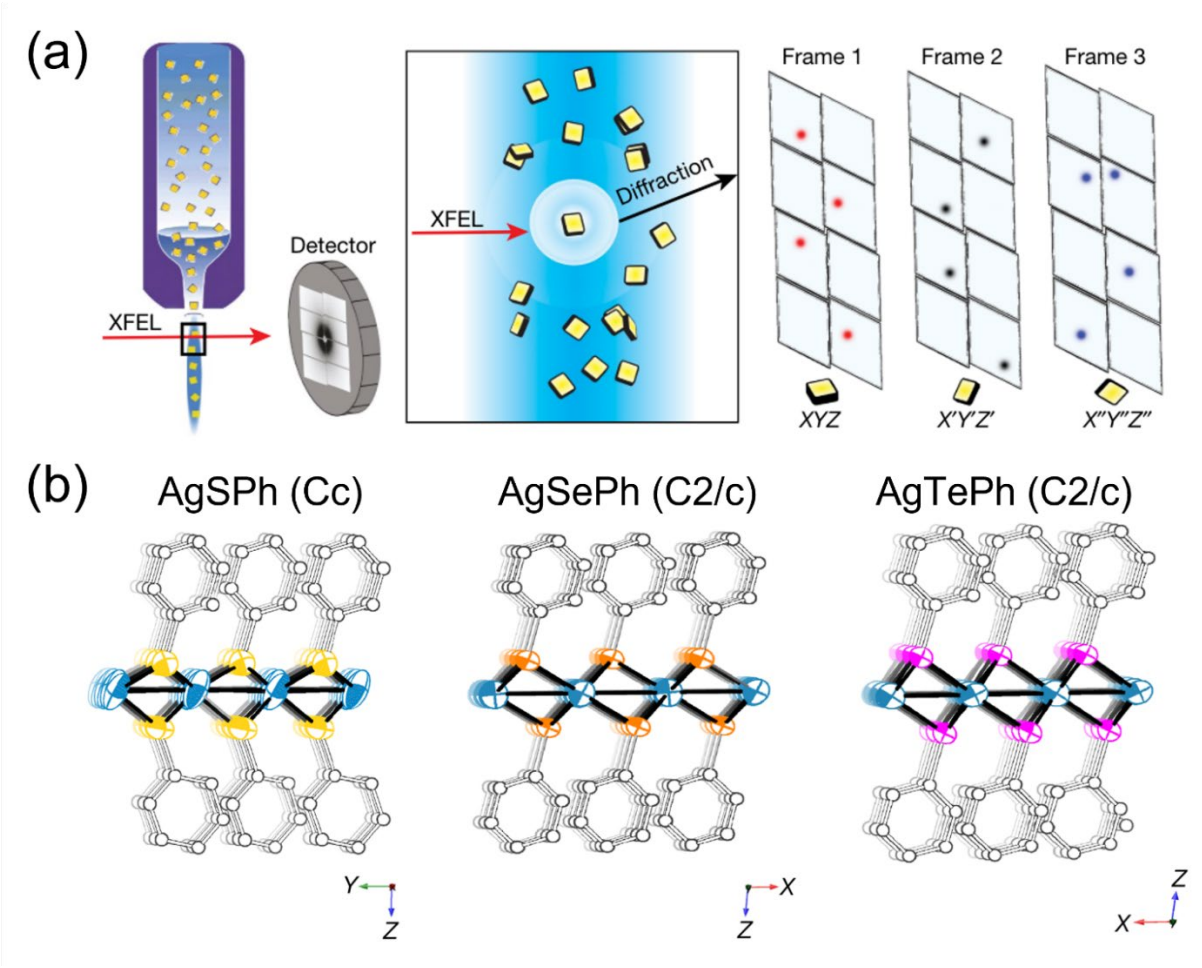

Figure 3.4 Small-molecule serial femtosecond X-ray crystallography (smSFX). (a) Schematic illustration of the smSFX experiment. (b) Crystal structures of AgSPh in Cc, AgSePh in C2/c, and AgTePh in C2/c, determined by smSFX. Figure adapted from [10].

Indeed, there is a clear debate regarding the crystal structure of AgSePh ($P2_1/c$ vs. C2/c). Since knowing the correct structure is the first step in understanding and optimizing material

properties, it is crucial and time-urgent to address this issue. Possible scenarios for this discrepancy include: 1) a phase transition from $P2_1/c$ (at 100K) to C2/c (at 180K and room temperature), 2) polymorphism at the same temperature, or 3) incorrect structure determination due to factors such as low crystal quality of instrument limitations. Additionally, the crystal sizes of AgSPh and AgTePh reported so far are limited to below a few micrometers, restricting both fundamental studies and practical applications. Indeed, there are remaining questions:

- What is the correct crystallographic description for AgSePh, between $P2_1/c$ and C2/c?
- Can we synthesize single crystalline AgSPh and AgTePh with sufficient size and quality?

This thesis will address these issues in Chapter 4.

3.2 Excitons and exciton-phonon interactions in 2D AgEPh (E=S, Se, Te)

Since the rediscovery of AgSePh as a blue-emitting semiconductor in 2018, this material has begun to attract attention from the scientific community as a novel 2D hybrid organic-inorganic excitonic semiconductor for both fundamental and applied research. This interest arises from four unique features of AgSePh:

- *Natural quantum well structures.* AgSePh crystallizes in the form of a 3D solid consisting of 2D layers stacked by interlayer van der Waals interactions. Each 2D layer consists of an inorganic AgSe sheet sandwiched between phenyl rings. Consequently, AgSePh has natural hybrid quantum well structures that can support robust excitons inside inorganic sheets due to quantum and dielectric confinement effects.
- *In-plane anisotropy*. In both P21/c and C2/c structures, AgSePh exhibit in-plane anisotropy in its structure. Since material properties are governed by its structure, it is likely that excitons confined within the 2D layers in AgSePh may also exhibit in-plane anisotropy. Moreover, AgSePh may exhibit in-plane anisotropic electrical, thermal, and optical properties that can unlock novel devices for directional electron, exciton, photon, and heat transport.
- *Covalent bonding*. AgSePh features covalent bonding not only within organic and inorganic components but also between them. This covalent bonding makes AgSePh stable in air and

polar solvents, unlike 2D LHPs. More importantly, because of the covalent bonding between inorganic and organic components, excitons in AgSePh may exhibit a hybrid nature of Wannier excitons (commonly observed in inorganic semiconductors) and Frenkel excitons (commonly observed in organic molecular semiconductors) or even new types of excitons.

- *Tunable bandgap*. Another potential advantage of the covalent bonding between inorganic sheet and organic ligands is the tunability of the bandgap through organic modification, which is unachievable in other 2D van der Waals semiconductors, including TMDs and 2D LHPs. In addition to organic group modification, substituting inorganic components such as metals or chalcogens can control the bandgap of AgSePh, enabling application-specific properties and functionalities.

Inspired by these potentials of AgSePh, multiple groups have investigated exciton physics and dynamics in this material. The following is the important findings regarding excitonic properties in AgSePh and its analogues.

Schwartzberg and co-workers first demonstrated that absorption feature in AgSePh consists of three distinct excitonic resonances (labelled as X_1, X_2, and X_3 excitons, from lower energy to higher energy) (Figure 3.5a).[11] Using pump energy-dependent transient absorption spectroscopy, they determined exciton binding energy of X_1 exciton to be ~380 meV (Figure 3.5b), which was in good agreement with the lowest-lying exciton binding energy (~350 meV) predicted by GW and Bethe-Salpeter equation (GW-BSE) calculations. The lowest exciton binding energy was also measured to be ~400 meV by Schuck and co-workers using low-temperature PL excitation spectroscopy (Figure 3.5c).[12] Indeed, it was experimentally and theoretically confirmed that AgSePh possesses robust excitons with binding energy of 300~400 meV, comparable to those of monolayer TMDs and 2D LHPs.

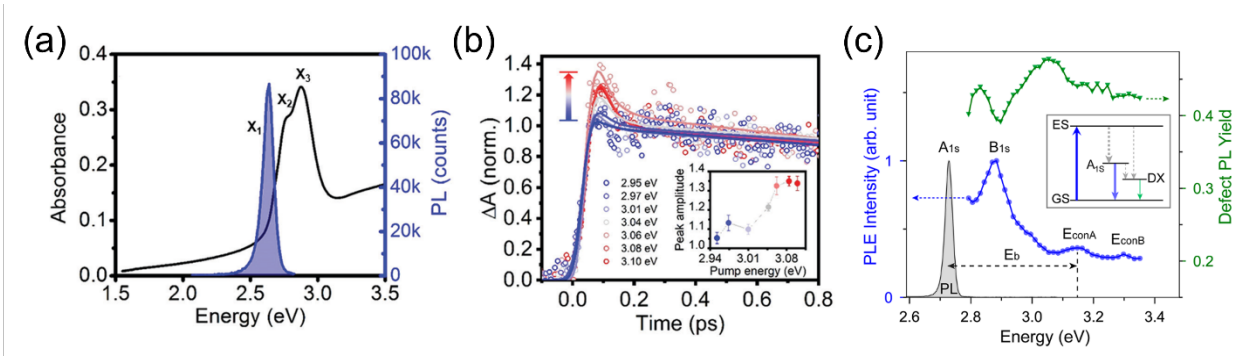

Figure 3.5 Three distinct excitons and exciton binding energy of the lowest exciton in AgSePh. (a) Excitonic absorption resonances of X_1, X_2 and X_3 excitons and photoluminescence from X_1 exciton recombination. (b) Detection of band-edge absorption onset using pump energy-dependent transient absorption spectroscopy. (c) Probing exciton binding energy using low-temperature photoluminescence excitation spectroscopy. Panels (a,b) adapted from [11]. Panel (c) adapted from [12].

Schwartzberg and co-workers also first revealed the anisotropy of X_1, X_2 and X_3 excitons.[11] Using spectroscopic ellipsometry, they showed that the extinction coefficient in the in-plane direction is much larger than the that in the out-of-plane direction, indicating that the excitonic dipole moments lie in the 2D plane (Figure 3.6a). Additionally, using polarization-resolved absorption spectroscopy, they revealed in-plane anisotropy of these excitons: X_1 and X_3 excitons are polarized along [010] direction, while the X_2 exciton is polarized along [100] direction (Figure 3.6b,c). Two low-lying excitons with strong oscillator strength and orthogonal polarization were also predicted by GW-BSE calculations (Figure 3.6d,e). However, there was some inconsistency between experimental observations and theoretical calculations: 1) three distinct excitons were observed in experiments, whereas two excitons were predicted in calculations, and 2) the absorption intensity of the lowest exciton is lower than that of the second-lowest exciton in experiments, whereas the opposite was predicted in calculations. Consequently, more investigations are required to fill this knowledge gap.

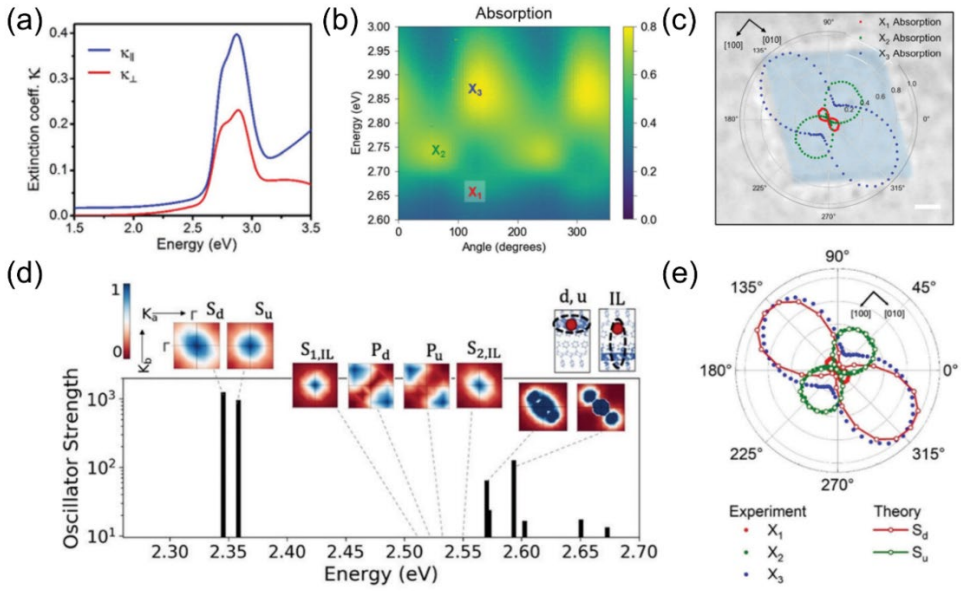

Figure 3.6 Anisotropic excitons in AgSePh. (a) Optical extinction coefficient for the in-plane and out-of-plane components, calculated from ellipsometry fit. (b,c) The in-plane anisotropy of excitons in AgSePh, revealed by polarization-resolved absorption spectroscopy. (d,e) exciton energy, oscillator strength, and anisotropy in AgSePh, predicted by the GW-BSE calculations. Figure adapted from [11].

While only narrow-blue emission, primarily arising from the recombination of the X_1 exciton, is observed at room temperature, multiple groups have reported largely Stokes-shifted and broad emission in addition to the narrow-blue emission in AgSePh at low temperatures (Figure 3.7). Schwartzberg and co-workers attributed this broad emission to the defect-derived emission, as it became saturated with increased excitation power (Figure 3.7a,b).[12] Paritmongkol in the Tisdale group and co-workers also assigned it to defects based on the observation that this emission was suppressed in high-quality single crystals (Figure 3.7c).[9] On the other hand, using ultrafast transient absorption spectroscopy, Maserati and co-workers suggested the possibility that this broadband emission might arise from exciton self-trapping (Figure 3.7d,e).[13] Indeed, it is still unclear whether this broad emission arises from defects, defect-aided self-trapped excitons, or intrinsic self-trapped excitons.

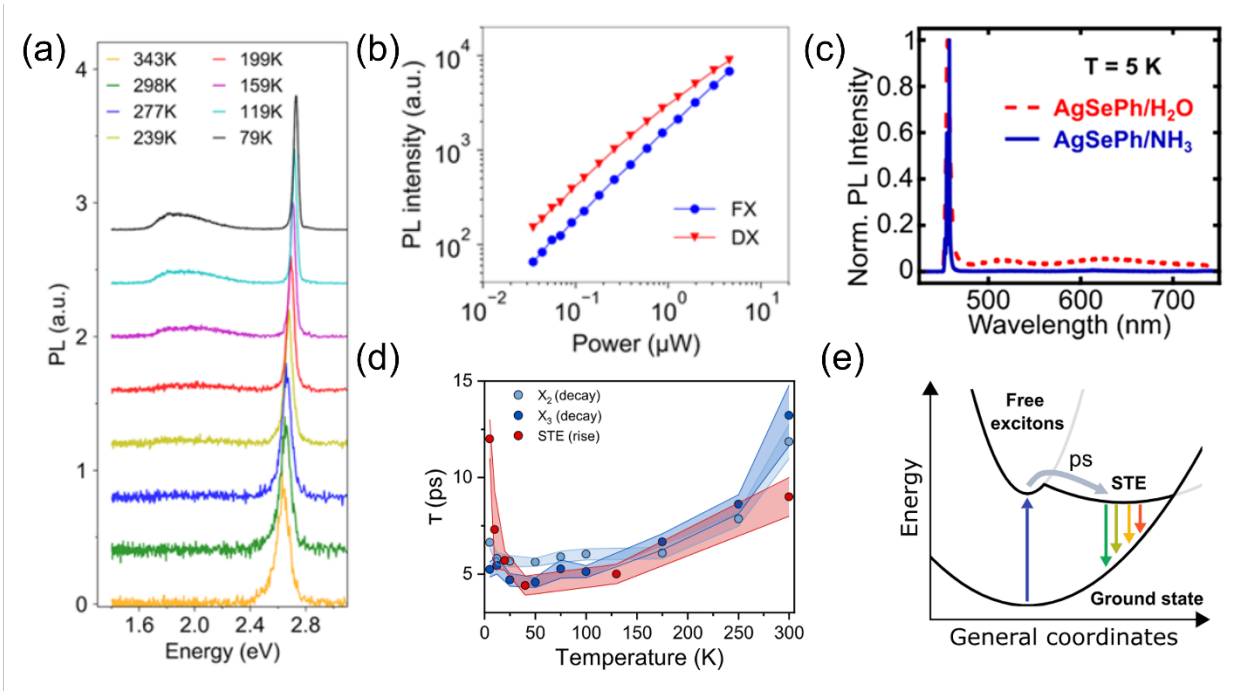

Figure 3.7 Largely Stokes-shifted and broad emission in AgSePh. (a) Temperature-dependent photoluminescence spectra of AgSePh. (b) Power-dependent intensities of narrow emission and broad emission in AgSePh. (c) Suppressed broad emission in high-quality AgSePh single crystal. (d) Temperature-dependent exciton dynamics revealed by ultrafast transient absorption spectroscopy. (e) Schematic diagram showing exciton self-trapping process. The colored arrows indicate possible radiative recombination of the self-trapped exciton. Panels (a,b) adapted from [12]. Panel c adapted from [9]. Panels (d,e) adapted from [13].

The requirement for exciton self-trapping is strong exciton-lattice interactions. These strong exciton-lattice interactions can lead to other interesting excitonic features beyond self-trapping. Powers in the Tisdale group and co-workers revealed coherent exciton-lattice dynamics in AgSePh (Figure 3.8).[14] Using femtosecond resonant impulsive vibrational spectroscopy (IVS), multiple hybrid organic-inorganic vibrational modes that strongly couple to the excited electronic states were identified (Figure 3.8a,b). Moreover, analysis of temperature-dependent PL peak shifts and linewidth broadening, combined with IVS analysis and density functional theory calculations, revealed that the excitonic light emission in AgSePh is strongly influenced by a coupling with a phonon mode (99 cm^{-1}) involving the wagging motion of phenyl rings and metal-chalcogen stretching (figure 3.8c-e). These findings demonstrate hybrid nature of vibrational modes and strong exciton-phonon interactions in AgSePh.

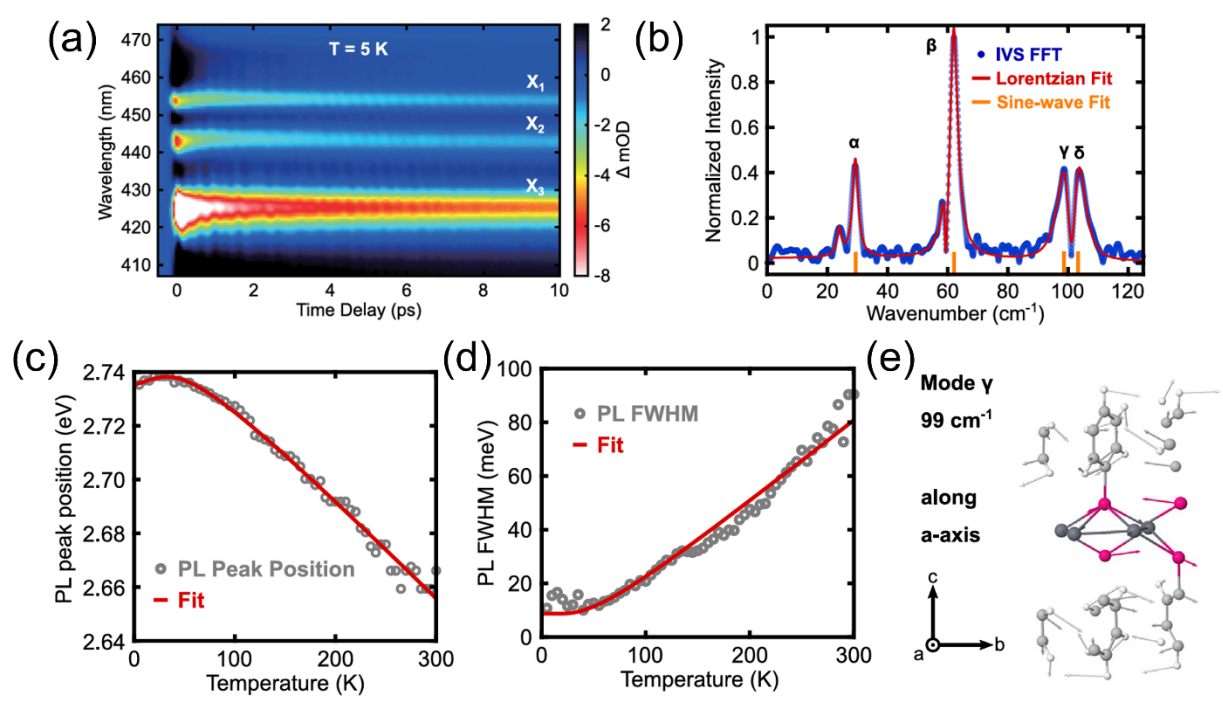

Figure 3.8 Coherent exciton-lattice dynamics and its effect on light emission in AgSePh. (a) Impulsive vibrational spectroscopy (IVS) color map of AgSePh at 5 K. (b) Vibrational frequencies obtained from IVS data. Temperature-dependent photoluminescence (c) peak shifts and (d) linewidth broadening. (e) Density functional theory (DFT)-simulated atomic displacements for 99 cm^{-1} mode. Figure adapted from [14].

Researchers have also investigated the possibility of tunable excitonic properties through chalcogen substitution (Figure 3.9). Hohman and co-workers introduced thiophenol and diphenyl ditelluride instead of benzeneselenol or diphenyl diselenide for the tarnishing method to synthesize 2D silver phenylthioloate (AgSPh, also known as "thiorene") and 2D silver phenyltellurolate (AgTePh, also known as "tethrene"), respectively. The obtained AgSPh exhibited single absorption peak at ~3.45 eV and no PL, whereas AgTePh showed two broad excitonic absorption resonances with large energetic separation and largely Stokes-shifted broad PL (Figure 3.9a and b). Norris and co-workers also explored the chalcogen substitution by developing new synthetic methods (Figure 3.9c-f).[15] They demonstrated tunable emission across the ultraviolet (UV) to visible range through chalcogen substitution or mixing. Interestingly, they observed that AgSPh exhibited PL centered at ~380 nm, although its efficiency was extremely low (~0.0004%).

Additionally, they found that 1D AgTePh formed instead of 2D AgTePh, implying that the microscopic crystal structure or even the chemical formula of AgTePh synthesized by their method is likely different from the 2D AgTePh obtained by Hohman and co-workers.

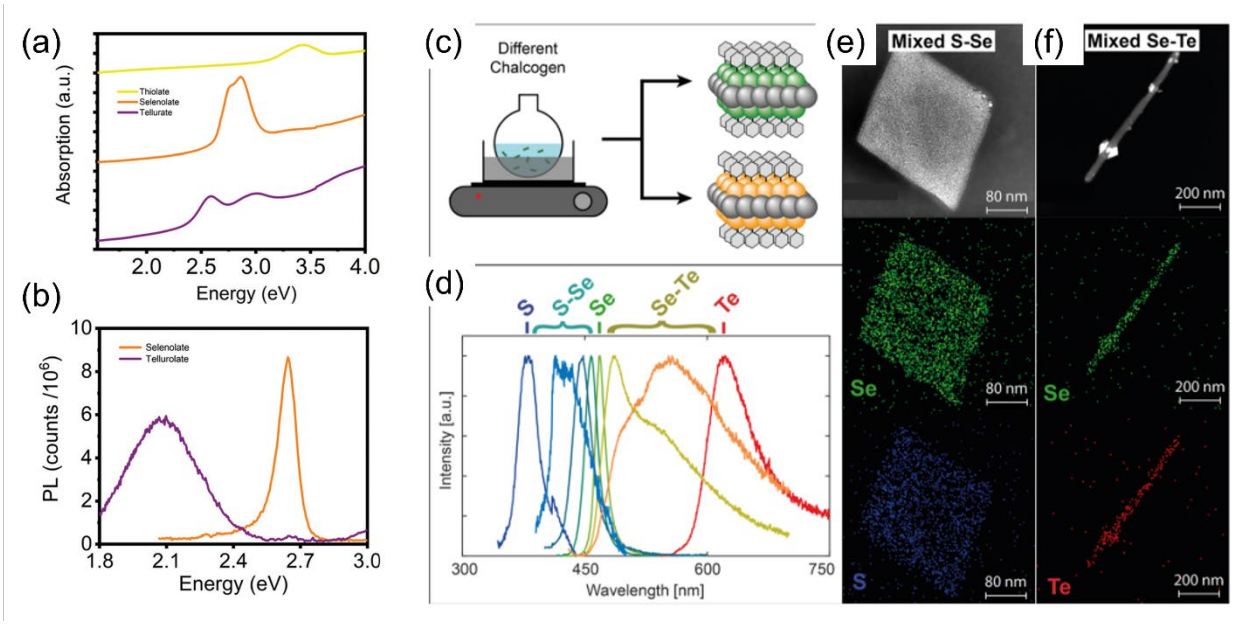

Figure 3.9 Effects of chalcogen substitution in AgSePh on its absorption and photoluminescence. (a) Absorption and (b) Photoluminescence spectra of AgEPh (E = S, Se, Te) obtained by the tarnishing method. (c) Schematic showing the synthesis of AgEPh (E = S, Se, Te) and their alloys (or mixtures), developed by Norris and coworkers. (d) Photoluminescence spectra and (e,f) scanning transmission electron microscopy and energy-dispersive X-ray measurements of AgEPh (E = S, Se, Te) and their alloys (or mixtures). Panels (a,b) adapted from ref. [11]. Panels (c-f) adapted from [15].

Indeed, there has been significant progress in understanding the excitonic properties of AgSePh and tuning its properties via chalcogen substitution. However, several questions remain:

- Why are the excitonic states and their anisotropy in experimental observations and theoretical calculations inconsistent?
- Why do the absorption spectra of AgEPh (E=S,Se,Te) differ so significantly?
- What is the origin of the absence of PL (or PL with extremely low efficiency) in AgSPh?
- What is the light emission mechanism in AgSePh and AgTePh, respectively?
- Are the alloys between AgEPh homogeneous? Do they form a complete solid-solution system? If not, why?
- How does the chalcogen substitution affect exciton-phonon interactions in AgEPh?

- Do AgSPh and AgTePh exhibit optical anisotropy like AgSePh?
- Can we tune the optical properties of AgEPh by controlling their thickness through photonic effects?

This thesis will address these questions from Chapter 5 to Chapter 7.

3.3 0D, 1D and 2D silver organochalcogenolates (AgSeR)

As I highlighted in the previous section, one of the unique features of AgSePh or MOCs in general is the covalent bonding between organic and inorganic components. This could potentially allow bandgap tuning via organic modification even in the absence of atomic displacement in inorganic components. However, depending on the steric hindrance between organic ligands and/or electronic interaction between inorganic components and organic ligands, one can even control the structure or dimension of the materials.

As a proof of concept, Paritmongkol, Tisdale, and co-workers demonstrated a new material design strategy by introducing a heteroatom (N) into the phenylselenide ligands, which transformed 2D AgSePh into 0D silver pyridinylselenide (AgSePy) (Figure 3.10a-c).[16] AgSePy exhibited strong and broad orange PL with a quantum yield of ~64%. While it crystallizes into a 1D rod shape in bulk, density functional theory calculations confirmed its 0D electronic structure. Sakurada in the Tisdale group and co-workers also demonstrated the transformation of 2D AgSePh into yellow-emissive 1D silver 2,6-difluorophenylselenolate – $AgSePhF_2(2,6)$ – through fluorination of the phenyl ligands at the ortho-positions (Figure 3.10d-f).[17] The $AgSePhF_2(2,6)$ exhibited broad PL centered at ~574 nm with a quantum yield of ~2.5%. Density functional theory calculations confirmed its 1D electronic structure, where the conduction and valence band edges are strongly dispersive along the 1D crystal axis.

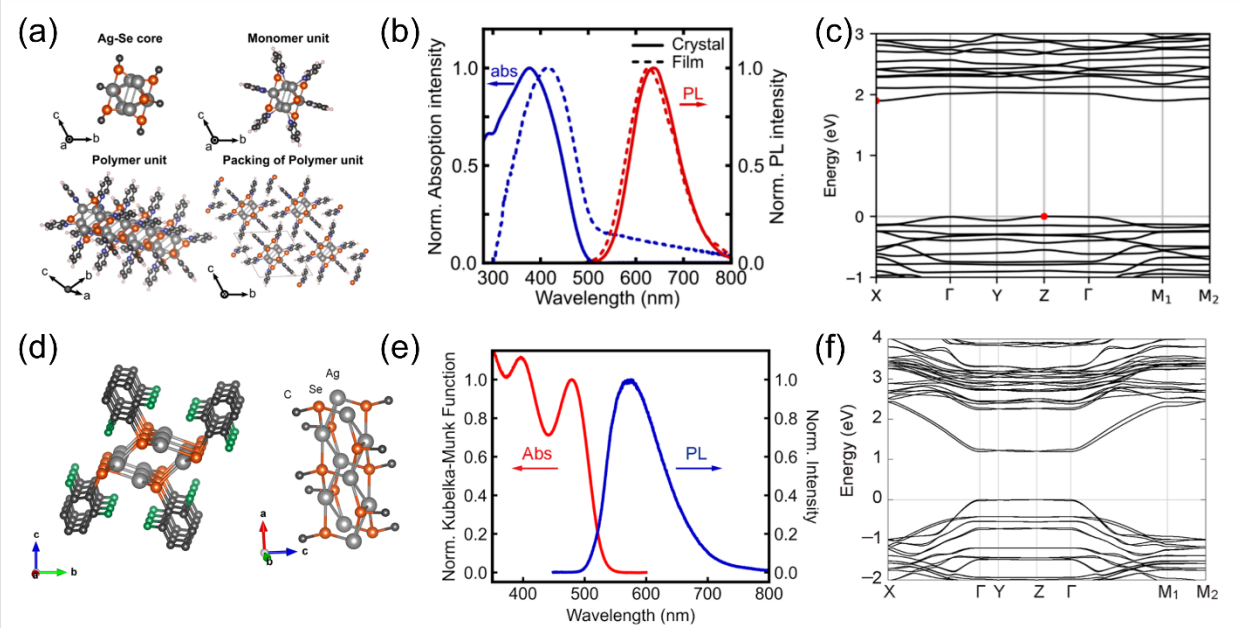

Figure 3.10 0D AgSePy and 1D $AgSePhF_2(2,6)$. (a) The crystal structure of AgSePy. (b) Absorption and photoluminescence spectra of AgSePy. (c) Electronic band structure of AgSePy. (d) Crystal structure of $AgSePhF_2(2,6)$. (e) Absorption and photoluminescence spectra of $AgSePhF_2(2,6)$. (f) Electronic band structure of $AgSePhF_2(2,6)$. Panels (a-c) adapted from [16]. Panels (d-f) adapted from ref. [17].

Sakurada in the Tisdale group and co-workers also demonstrated an organic ligand modification strategy that enables fine-tuning of emission wavelengths while maintaining 2D quantum well structures with blue emission (Figure 3.11). Interestingly, among blue-emitting 2D AgSe-R, two types of absorption spectra were observed: Excitonic absorption peaks crowded near 450 nm, like AgSePh (Figure 3.11a) or excitonic absorption peaks separated by a large energetic gap, like $AgSePhF_2(2,3)$ (Figure 3.11b). Despite its significance for band structure optimization and improving emission efficiency, the origin of these different absorption spectra is unknown.

- What governs electronic and excitonic band structure in 2D AgSe-R?

This thesis will address this question in Chapter 8.

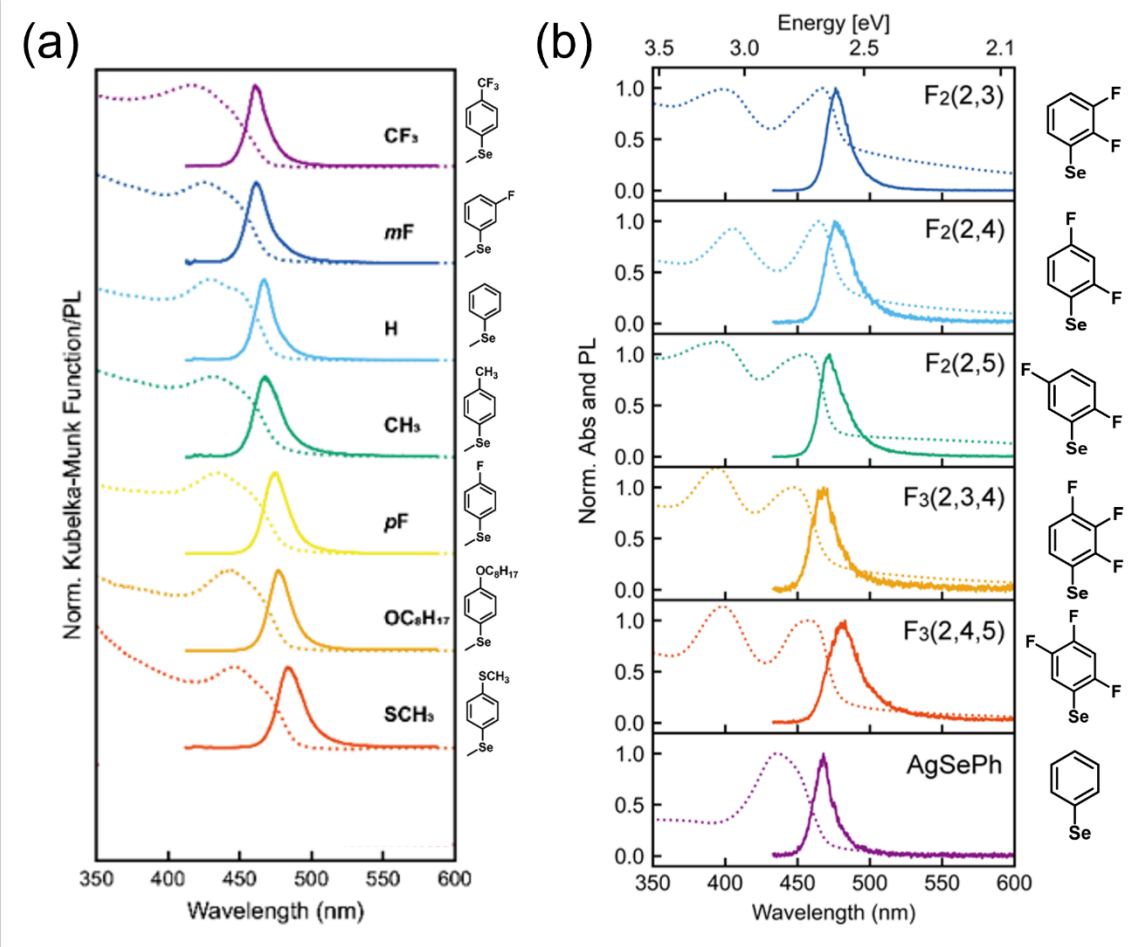

Figure 3.11 Absorption and photoluminescence spectra of 2D AgSe-R where R is a functionalized benzene. Two types of absorption spectra are observed: (a) excitonic absorption peaks crowded near 450 nm, like AgSePh or (b) excitonic absorption peaks separated by a large energetic gap, like AgSePhF_2(2,3). Unpublished data from the Tisdale group, with Tomoaki Sakurada as the lead person for the projects.

3.4 References

(1) Veselska, O.; Demessence, A. D10 Coinage Metal Organic Chalcogenolates: From Oligomers to Coordination Polymers. *Coord Chem Rev* **2018**, *355*, 240–270. https://doi.org/10.1016/j.ccr.2017.08.014.

(2) Wang, G.; Luo, S.; Di, T.; Fu, Z.; Xu, G. Layered Organic Metal Chalcogenides (OMCs): From Bulk to Two-Dimensional Materials. *Angewandte Chemie International Edition* **2022**, *61* (27). https://doi.org/10.1002/anie.202203151.

(3) Yeung, M.; Popple, D. C.; Schriber, E. A.; Teat, S. J.; Beavers, C. M.; Demessence, A.; Kuykendall, T. R.; Hohman, J. N. Corrosion of Late- and Post-Transition Metals into Metal–Organic Chalcogenolates and Implications for Nanodevice Architectures. *ACS Appl Nano Mater* **2020**, *3* (4), 3568–3577. https://doi.org/10.1021/acsanm.0c00057.

(4) Yang, H.; Mandal, S.; Lee, Y. H.; Park, J. Y.; Zhao, H.; Yuan, C.; Huang, L.; Chen, M.; Dou, L. Dimensionality Engineering of Lead Organic Chalcogenide Semiconductors. *J Am Chem Soc* **2023**, *145* (44), 23963–23971. https://doi.org/10.1021/jacs.3c05745.

(5) Yan, H.; Hohman, J. N.; Li, F. H.; Jia, C.; Solis-Ibarra, D.; Wu, B.; Dahl, J. E. P.; Carlson, R. M. K.; Tkachenko, B. A.; Fokin, A. A.; Schreiner, P. R.; Vailionis, A.; Kim, T. R.; Devereaux, T. P.; Shen, Z.-X.; Melosh, N. A. Hybrid Metal–Organic Chalcogenide Nanowires with Electrically Conductive Inorganic Core through Diamondoid-Directed Assembly. *Nat Mater* **2017**, *16* (3), 349–355. https://doi.org/10.1038/nmat4823.

(6) Trang, B.; Yeung, M.; Popple, D. C.; Schriber, E. A.; Brady, M. A.; Kuykendall, T. R.; Hohman, J. N. Tarnishing Silver Metal into Mithrene. *J Am Chem Soc* **2018**, *140* (42), 13892–13903. https://doi.org/10.1021/jacs.8b08878.

(7) Schriber, E. A.; Popple, D. C.; Yeung, M.; Brady, M. A.; Corlett, S. A.; Hohman, J. N. Mithrene Is a Self-Assembling Robustly Blue Luminescent Metal–Organic Chalcogenolate Assembly for 2D Optoelectronic Applications. *ACS Appl Nano Mater* **2018**, *1* (7), 3498–3508. https://doi.org/10.1021/acsanm.8b00662.

(8) Cuthbert, H. L.; Wallbank, A. I.; Taylor, N. J.; Corrigan, J. F. Synthesis and Structural Characterization of [Cu20Se4(M3-SePh)12(PPh3)6] and [Ag(SePh)]∞. *Z Anorg Allg Chem* **2002**, *628* (11), 2483–2488. https://doi.org/10.1002/1521-3749(200211)628:11<2483::AID-ZAAC2483>3.0.CO;2-U.

(9) Paritmongkol, W.; Sakurada, T.; Lee, W. S.; Wan, R.; Müller, P.; Tisdale, W. A. Size and Quality Enhancement of 2D Semiconducting Metal–Organic Chalcogenolates by Amine Addition. *J Am Chem Soc* **2021**, *143* (48), 20256–20263. https://doi.org/10.1021/jacs.1c09106.

(10) Schriber, E. A.; Paley, D. W.; Bolotovsky, R.; Rosenberg, D. J.; Sierra, R. G.; Aquila, A.; Mendez, D.; Poitevin, F.; Blaschke, J. P.; Bhowmick, A.; Kelly, R. P.; Hunter, M.; Hayes, B.; Popple, D. C.; Yeung, M.; Pareja-Rivera, C.; Lisova, S.; Tono, K.; Sugahara, M.; Owada, S.; Kuykendall, T.; Yao, K.; Schuck, P. J.; Solis-Ibarra, D.; Sauter, N. K.; Brewster, A. S.; Hohman, J. N. Chemical Crystallography by Serial Femtosecond X-Ray Diffraction. *Nature* **2022**, *601* (7893), 360–365. https://doi.org/10.1038/s41586-021-04218-3.

(11) Maserati, L.; Refaely-Abramson, S.; Kastl, C.; Chen, C. T.; Borys, N. J.; Eisler, C. N.; Collins, M. S.; Smidt, T. E.; Barnard, E. S.; Strasbourg, M.; Schriber, E. A.; Shevitski, B.; Yao, K.; Hohman, J. N.; Schuck, P. J.; Aloni, S.; Neaton, J. B.; Schwartzberg, A. M. Anisotropic 2D Excitons Unveiled in Organic–Inorganic Quantum Wells. *Mater Horiz* **2021**, *8* (1), 197–208. https://doi.org/10.1039/C9MH01917K.

(12) Yao, K.; Collins, M. S.; Nell, K. M.; Barnard, E. S.; Borys, N. J.; Kuykendall, T.; Hohman, J. N.; Schuck, P. J. Strongly Quantum-Confined Blue-Emitting Excitons in Chemically Configurable Multiquantum Wells. *ACS Nano* **2021**, *15* (3), 4085–4092. https://doi.org/10.1021/acsnano.0c08096.

(13) Kastl, C.; Schwartzberg, A. M.; Maserati, L. Picoseconds-Limited Exciton Recombination in Metal–Organic Chalcogenides Hybrid Quantum Wells. *ACS Nano* **2022**, *16* (3), 3715–3722. https://doi.org/10.1021/acsnano.1c07281.

(14) Powers, E. R.; Paritmongkol, W.; Yost, D. C.; Lee, W. S.; Grossman, J. C.; Tisdale, W. A. Coherent Exciton-Lattice Dynamics in a 2D Metal Organochalcogenolate Semiconductor. *Matter* **2024**, *7* (4), 1612–1630. https://doi.org/10.1016/j.matt.2024.01.033.

(15) Hernandez Oendra, A. C.; Aspect, M. A.; Jaeggi, J. L.; Baumann, J.; Lightner, C. R.; Pun, A. B.; Norris, D. J. Tunable Synthesis of Metal–Organic Chalcogenide Semiconductor Nanocrystals. *Chemistry of Materials* **2023**, *35* (21), 9390–9398. https://doi.org/10.1021/acs.chemmater.3c02275.

(16) Khamlue, R.; Sakurada, T.; Cho, Y.; Lee, W. S.; Leangtanom, P.; Taylor, M. G.; Naewthong, W.; Sripetch, P.; Na Ranong, B.; Autila, T.; Rungseesumran, T.; Kaewkhao, J.; Sudyoadsuk, T.; Kopwitthaya, A.; Müller, P.; Promarak, V.; Kulik, H. J.; Tisdale, W. A.; Paritmongkol, W. Heterocyclic Modification Leading to Luminescent 0D Metal Organochalcogenide with Stable X-Ray Scintillating Properties. *Chemistry of Materials* **2024**, *36* (10), 5238–5240. https://doi.org/10.1021/acs.chemmater.4c00653.

(17) Sakurada, T.; Cho, Y.; Paritmongkol, W.; Lee, W. S.; Wan, R.; Su, A.; Shcherbakov-Wu, W.; Müller, P.; Kulik, H. J.; Tisdale, W. A. 1D Hybrid Semiconductor Silver 2,6-Difluorophenylselenolate. *J Am Chem Soc* **2023**, *145* (9), 5183–5190. https://doi.org/10.1021/jacs.2c11896.

Chapter 4

Synthesis and Structural Anisotropy of Single Crystalline 2D AgEPh (E=S, Se, Te)

The basis of this chapter has been adapted from:
Woo Seok Lee, Peter Müller, Nicholas Samulewicz, Tejas Deshpande, Ruomeng Wan, William A. Tisdale. "Synthesis and Structural Anisotropy of Single Crystalline 2D AgEPh (E=S, Se, Te)" *In manuscript* (2024).

4.1 Abstract

Silver phenylchalcogenides (AgEPh; E = S, Se, Te) are emerging two-dimensional (2D) semiconductors belonging to a broader class of hybrid organic-inorganic materials, known as metal organochalcogenides (MOCs). However, the size of AgSPh and AgTePh crystals has been limited to less than 5 μm, presenting challenges for both fundamental and applied research. Moreover, despite its significance for theoretical calculations as well as the understanding and further optimization of material properties, the accurate description of the crystal structure of AgSePh (C2/c or $P2_1/c$) is debated. In this chapter, we report the growth of millimeter-sized single crystalline 2D AgEPh (E = S, Se, Te) with a unique macroscopic parallelogram shape. Transmission electron microscopy and electron diffraction studies reveal the relationship between their macroscopic morphology and microscopic crystal structure. More importantly, we determine three new crystal structures through single crystal X-ray diffraction: 2D AgSPh in $P2_1$ and 2D AgTePh in $P2_1/c$ as well as 1D $AgTeC_{6.27}H_{5.62}N_{0.09}$ (1D AgTePh + $0.089C_3H_7N$) in P-1. Strikingly, our space group assignment of 2D AgEPh in primitive lattices is different from the previously reported C-centered lattices (AgSPh in Cc, AgSePh and AgTePh in C2/c). Using temperature-dependent powder X-ray diffraction, absorption and photoluminescence spectroscopy of 2D AgEPh prepared from different synthetic methods, we explore and discuss potential causes for the discrepancies in crystal structure descriptions, such as phase transitions, polymorphism, and variations in crystal size and quality.

4.2 Introduction

Metal organochalcogenolates (MOCs) are an emerging class of low-dimensional hybrid organic-inorganic semiconductors with a chemical formula of $[M(ER)]_n$ where M typically stands for coinage metals [Cu(I), Ag(I), and Au(I)]; E for chalcogen elements (S, Se, Te); and R for an organic hydrocarbon.[1–3] Unlike other low-dimensional hybrid materials such as colloidal nanocrystals[4] or halide perovskites,[5] MOCs are distinguished by the covalent bonds between their inorganic and organic components. This covalent bonding enables structural, dimensional and electronic tunability through both organic functionalization[6–14] and inorganic component manipulations.[3,8,14–21] Consequently, MOC find applications across a broad range of fields, including catalysis,[17,20] sensing,[10,22–25] light emission,[11,15,21,26] and electronic devices.[27,28]

Silver phenylthiolate (AgSPh, also known as "thiorene"),[17–20] silver phenylselenolate (AgSePh, also known as "mithrene"),[17,18,20,26,29–31] silver phenyltellurolate (AgTePh, also known as "tethrene")[17–19,21] are prototypical members of two-dimensional (2D) MOCs. These compounds form layered van der Waals solids where inorganic silver chalcogenide layers are sandwiched by benzene rings. Among these, AgSePh has received the most attention due to its narrow blue (~467 nm) emission,[8,18,19,21,23,24,26,29–35] while AgSPh exhibits no photoluminescence[18,19] and AgTePh shows a broad emission centered at ~600 nm with a significant Stokes shift.[18,19,21] Initially, the crystal structures of these compounds were refined to monoclinic C-centered lattices (AgSPh in Cc,[18] AgSePh[18,31] and AgTePh[18] in C2/c). Recently, our group developed an amine-assisted reaction method, enabling the growth of millimeter-sized single crystalline AgSePh whose structure was refined to $P2_1/c$ space group.[30] However, whether this amine-assisted method can be extended to grow large, high-quality crystals of other chalcogen analogues remains unproven. More importantly, despite its significance for theoretical calculations and further material property optimization, the accurate description of the crystal structure of AgSePh (C2/c *vs.* $P2_1/c$) remains a subject of debate.[18,30,31]

Here, we report the growth of millimeter-sized single crystalline AgEPh (E = S, Se, Te) with a unique macroscopic parallelogram shape. Through transmission electron microscopy and electron diffraction studies, we reveal the relationship between macroscopic morphology of 2D AgEPh and their microscopic crystal structure. Furthermore, we determine three new crystal structures through single crystal X-ray diffraction: 2D AgSPh in $P2_1$ and 2D AgTePh in $P2_1/c$ as

well as 1D $AgTeC_{6.27}H_{5.62}N_{0.09}$ (1D AgTePh + $0.089C_3H_7N$) in P-1. We explore and discuss potential causes for the discrepancies in crystal structure descriptions of 2D AgEPh (Primitive lattices in this work *vs.* C-centered lattices in previous works), such as phase transitions, polymorphism, and variations in crystal size and quality, by employing temperature-dependent powder X-ray diffraction, absorption and photoluminescence spectroscopy of 2D AgEPh prepared from different synthetic methods.

4.3 Results and Discussion

4.3.1 Synthesis, structural and optical characterization of AgEPh (E = S, Se, Te)

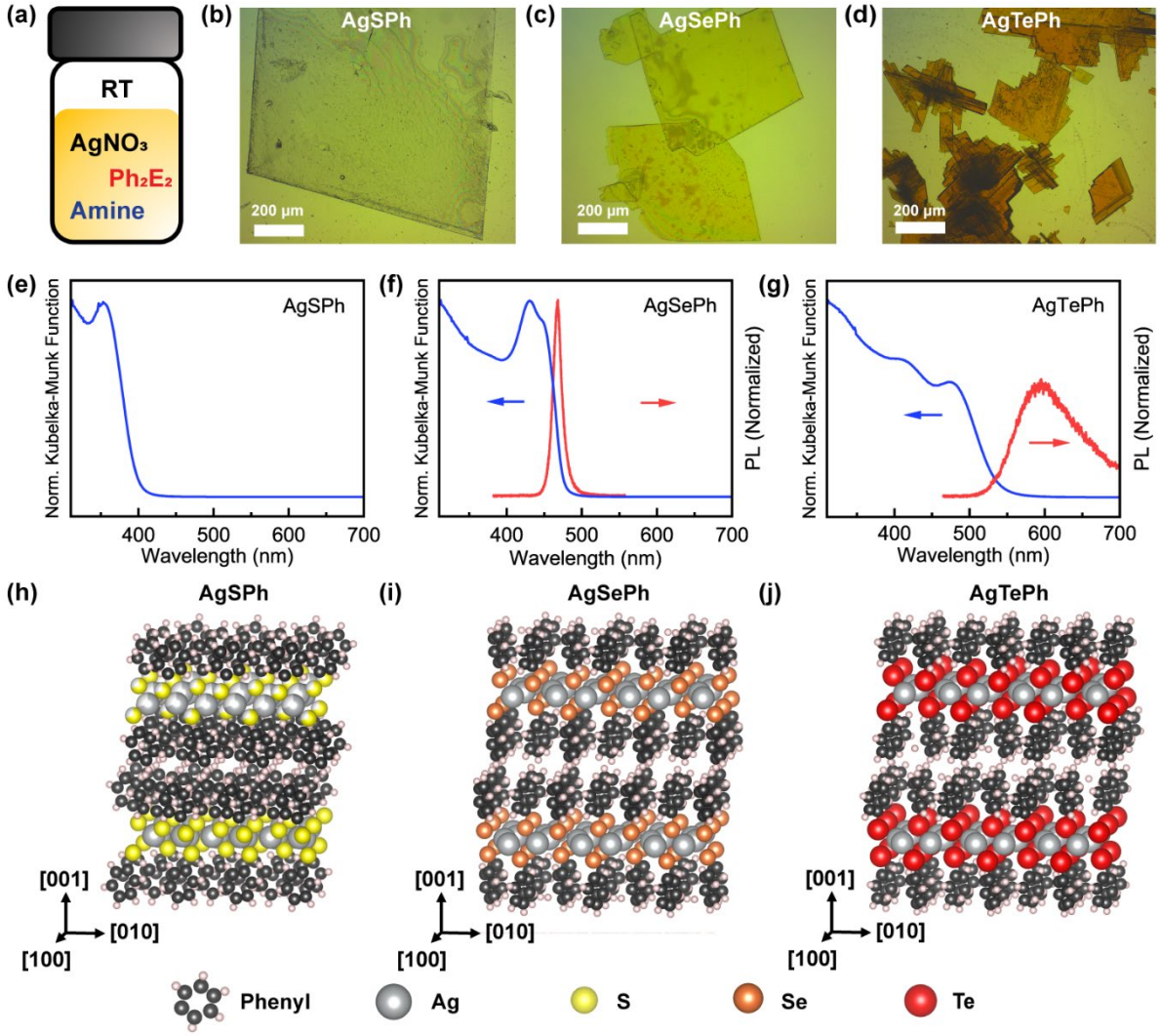

Figure 4.1 Structural and optical properties of AgEPh (E = S, Se, Te) crystals synthesized by (a) the amine-assisted solution phase reaction method. Optical micrographs of (b) AgSPh, (c) AgSePh, and (d) AgTePh crystals. Diffuse reflectance UV-vis absorption and photoluminescence spectra of (e) AgSPh, (f) AgSePh, and (g) AgTePh crystals. Crystal structures of (h) AgSPh (monoclinic $P2_1$), (i) AgSePh (monoclinic $P2_1/c$),[30] and (j) AgTePh (monoclinic $P2_1/c$) determined by single-crystal X-ray diffraction. Disordered atoms in AgSPh are omitted for clarity.

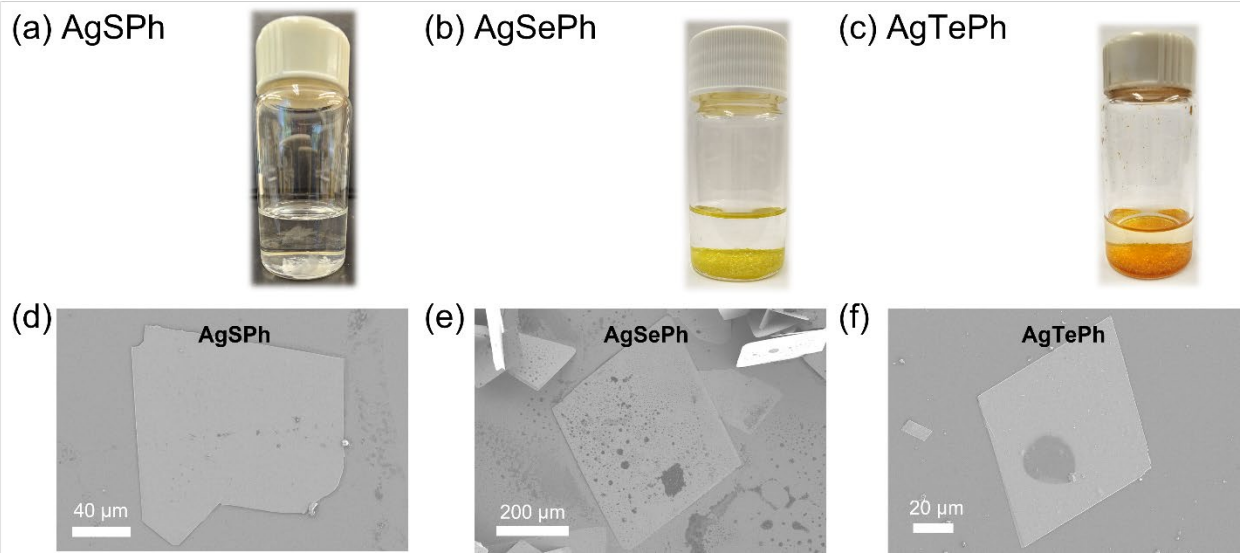

Figure 4.2 Photographs of the vial upon the completion of reaction and the scanning electron micrographs of the AgEPh (E = S, Se, Te) crystals.

Two-dimensional (2D) AgEPh (E = S, Se, Te) crystals were synthesized by the amine-assisted solution phase method with a slight modification (Figure 4.1a).[30] Briefly, a 20 mM solution of silver nitrate ($AgNO_3$) in 1-butylamine ($BuNH_2$) and a 20 mM solution of diphenyl dichalcogenide (Ph_2E_2; E = S, Se, Te) in $BuNH_2$ were mixed in a sealed vial. The vial was then stored under dark at room temperature for 2 weeks to obtain AgSPh crystals, 3 days for AgSePh crystals, and 2 months for AgTePh crystals. The lateral sizes of the AgEPh crystals vary from ~10 μm to even larger than ~1 mm (Figures 4.1b-d and 4.2). For AgSPh and AgSePh, no byproduct or intermediate phase was observed during the synthesis process, and similar results were obtained when propylamine ($PrNH_2$) and hexylamine ($HexNH_2$) were used instead of $BuNH_2$.

However, intermediate phases or byproducts such as 1D fibers or 1D crystals (1D AgTePh + 0.089 C_3H_7N) were observed during the synthesis of 2D AgTePh (Figure 4.3). When $BuNH_2$ was used, after one day, 1D fibers emerged and started to grow. After one week to a month, 2D AgTePh crystals began to appear and grow, accompanied by a reduction of 1D fibers, implying a chemical transformation of 1D fibers to 2D AgTePh. After 2-3 months, only 2D AgTePh crystals were observed. Similar results were observed when propylamine ($PrNH_2$) and $HexNH_2$ were used instead of $BuNH_2$. On the other hand, when mixing a solution of $AgNO_3$ in $PrNH_2$ with a solution of Ph_2Te_2 in toluene, 1D crystals were observed after a week in the absence of 1D fibers and 2D

AgTePh (Figure 4.3b). The 1D fibers, 1D crystals and 2D crystals of AgTePh exhibited distinct photoluminescence spectra (Figure 4.3c), suggesting differences in their crystal structures or possibly even in their chemical formula. For example, the crystal structure of 1D crystals was determined through single-crystal X-ray diffraction, revealing a triclinic P-1 space group with a chemical formula of $AgTeC_{6.27}H_{5.62}N_{0.09}$ (1D AgTePh + 0.089 C_3H_7N), where the amine solvent was trapped within a channel between chains of 1D AgTePh (Figure 4.3d-g and Table 4.1). Therefore, careful attention and choice of solvent are needed to obtain 2D AgTePh crystals.

Diffuse reflectance UV-vis absorption and photoluminescence (PL) spectra of AgEPh crystals at room temperature are shown in Figure 4.1e-g. The AgSPh crystals exhibited an absorption centered around 355 nm (~3.49 eV), but no PL was observed when excited by 355 nm light. The AgSePh crystals exhibited two "apparent" overlapping absorption peaks at 431 nm and 452 nm (~2.87 and ~2.74 eV). Upon excitation with 405 nm light, the AgSePh crystals displayed PL centered at 467 nm (~2.65 eV) with a full-with-at-half-maximum (FWHM) of ~76 meV. The AgTePh crystals revealed two "apparent" absorption peaks, with large energetic separation, centered at 417 nm and 477 nm (~2.97 and ~2.59 eV). When excited by 405 nm light, the AgTePh crystals exhibited a significantly red-shifted and broad PL centered at 597 nm (~2.04 eV) with a FWHM of ~382 meV.

The AgEPh crystals exhibit excellent crystallinity sufficient for single-crystal X-ray diffraction (SCXRD). In our previous work, we reported the crystal structure of AgSePh in monoclinic $P2_1/c$ space group determined through SCXRD at 100 K (Figure 4.1i).[30] In this work, we additionally report the new crystal structures of AgSPh in monoclinic $P2_1$ space group and AgTePh in monoclinic $P2_1/c$ space group determined through SCXRD at 100 K, confirming their in-plane anisotropic 2D layered structures consisting of inorganic AgE layers sandwiched with benzene rings like AgSePh (Figure 4.1h,j, and Tables 4.1-4.4). Additional crystallographic information of 2D AgSPh, 2D AgTePh, and 1D $AgTeC_{6.27}H_{5.62}N_{0.09}$ (1D AgTePh + 0.089C_3H_7N) are:

- 2D AgSPh crystallizes in the monoclinic chiral space group $P2_1$ with four AgSPh subunits in the asymmetric unit. The structure is a 2D polymer and application of crystallographic symmetry gives rise to infinite sheets extending parallel to the a-b-plane and stacking along the crystallographic c-axis with the phenyl rings from adjacent planes pointing towards one

another. The structure shows significant disorder of the Ag—S chains that could be modelled only partially. The corresponding phenyl rings should also be disordered; however, this could not be parameterized. The high maxima and minima in the difference electron density, mostly located near Ag and S atoms, suggest that the disorder is not modelled perfectly; however, no better model could be established. Unfortunately, owing to this massive and only partially resolved disorder, the value of this structure is limited.

- 2D AgTePh crystallizes in the monoclinic centrosymmetric space group $P2_1/c$ with two AgTePh subunits in the asymmetric unit. Just like in the case of 2D AgSPh, the structure is a 2D polymer and application of crystallographic symmetry gives rise to infinite sheets extending parallel to the a-b-plane and stacking along the crystallographic c-axis with the phenyl rings from adjacent planes pointing towards one another.
- 1D $AgTeC_{6.27}H_{5.62}N_{0.09}$ (1D AgTePh + $0.089C_3H_7N$) crystallizes in the triclinic centrosymmetric space group P-1 with three AgTePh subunits as well as one disordered and only partially occupied molecule of n-propylamine in the asymmetric unit. In this structure, the molecules form a 1D polymer with infinite strands extending along the crystallographic a-direction. Those strands have an AgTe core and the phenyl rings are displayed radially to the outside. In the crystal packing, solvent accessible channels along the a-direction are formed which are filled with disordered n-propylamine. The propylamine was found to be partially disordered and only partially occupied (the asymmetric unit contains just 27% of one solvent molecule, corresponding to 9% of solvent per AgTePh subunit). All three phenyl rings were refined as 50:50 disordered with respect to a rotation about the C1-C4 axis.

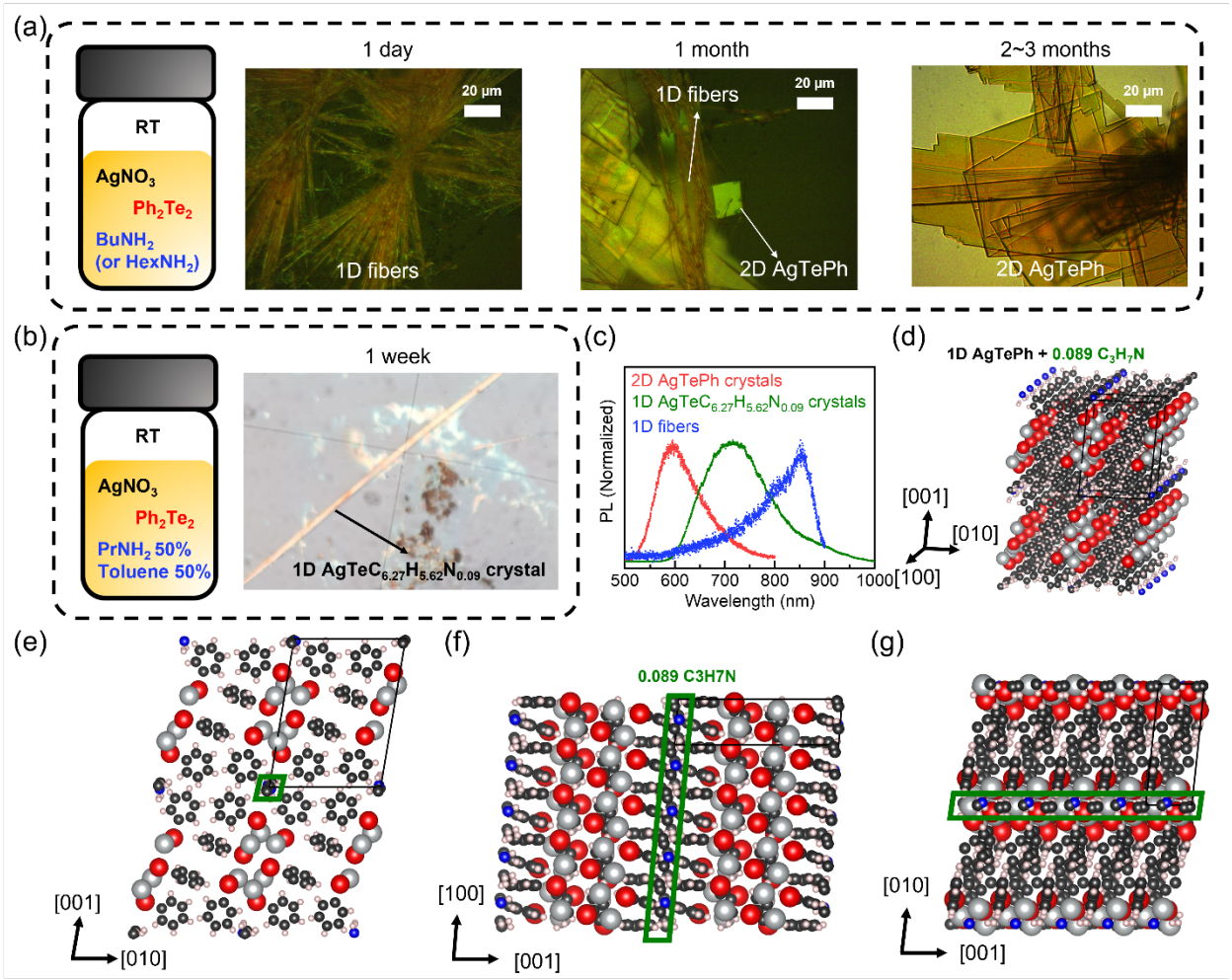

Figure 4.3 (a) Schematic illustration of a reaction vial with precursors in $BuNH_2$ (or $HexNH_2$), and images of the reaction products over time. (b) Schematic illustration of a reaction vial with precursors in a mixture of $PrNH_2$ and toluene, and an image of the reaction product after a week. (c) Photoluminescence spectra of 1D fibers, 1D crystals, and 2D crystals generated during the synthesis process of (a) and (b). Crystal structures of 1D $AgTeC_{6.27}H_{5.62}N_{0.09}$ crystal (1D AgTePh + 0.089 C_3H_7N) depicted from (d) the perspective view, and along crystallographic (e) [100], (f) [010], and (g) [001] directions. The black solid line represents a single unit cell, and the green solid line represents the region where the amine solvent (C_3H_7N) was trapped between chains of 1D AgTePh.

Table 4.1 Crystal data and structure refinement of 2D AgSPh, 2D AgTePh, and 1D $AgTeC_{6.27}H_{5.62}N_{0.09}$ (1D AgTePh + $0.089C_3H_7N$)

	2D AgSPh	2D AgTePh	1D AgTePh + $0.089C_3H_7N$
Identification code	P23051	P23058	P21094
Empirical formula	C_6H_5AgS	C_6H_5AgTe	$C_{6.27}H_{5.62}AgN_{0.09}Te$
Formula weight	217.03	312.57	317.64
Temperature	100(2) K	100(2) K	100(2) K
Wavelength	0.71073 Å	0.71073 Å	0.71073 Å
Crystal system	Monoclinic	Monoclinic	Triclinic
Space group	$P2_1$	$P2_1/c$	P-1
Unit cell dimensions	a = 7.3481(10) Å, α = 90°	a = 5.8218(2) Å, α = 90°	a = 4.81028(10) Å, α = 79.9448(10)°
	b = 5.8045(7) Å, β = 94.111(4)°	b = 7.4781(3) Å, β = 92.9041(15)°	b = 12.8426(3) Å, β = 84.5318(9)°
	c = 28.134(4) Å, γ = 90°	c = 30.1349(13) Å, γ = 90°	c = 17.2883(4) Å, γ = 83.1369(9)°
Volume	1196.9(3) $Å^3$	1310.27(9) $Å^3$	1041.04(4) $Å^3$
Z	8	8	6
Density (calculated)	2.409 Mg/m^3	3.169 Mg/m^3	3.040 Mg/m^3
Absorption coefficient	3.585 mm^{-1}	7.322 mm^{-1}	6.915 mm^{-1}
F(000)	832	1120	857
Crystal size	0.415 x 0.355 x 0.035 mm^3	0.235 x 0.070 x 0.010 mm^3	0.200 x 0.015 x 0.005 mm^3
Theta range for data collection	1.451 to 31.587°.	2.707 to 31.551°.	1.619 to 31.583°.
Index ranges	-10<=h<=10, -8<=k<=8, -41<=l<=41	-8<=h<=8, -10<=k<=11, -44<=l<=44	-7<=h<=6, -18<=k<=18, -25<=l<=25
Reflections collected	61611	69667	91707
Independent reflections	7992 [R(int) = 0.0518]	4361 [R(int) = 0.0389]	6924 [R(int) = 0.0434]
Completeness to theta = 25.242°	99.70%	99.80%	99.90%
Absorption correction	Semi-empirical from equivalents	Semi-empirical from equivalents	Semi-empirical from equivalents
Refinement method	Full-matrix least-squares on F^2	Full-matrix least-squares on F^2	Full-matrix least-squares on F^2
Data / restraints / parameters	7992 / 669 / 328	4361 / 0 / 145	6924 / 1409 / 429
Goodness-of-fit on F2	1.117	1.03	1.1
Final R indices [I>2sigma(I)]	R1 = 0.0879, wR2 = 0.2489	R1 = 0.0252, wR2 = 0.0581	R1 = 0.0203, wR2 = 0.0325
R indices (all data)	R1 = 0.0978, wR2 = 0.2591	R1 = 0.0370, wR2 = 0.0655	R1 = 0.0279, wR2 = 0.0349
Absolute structure parameter	0.43(14)	n/a	n/a
Extinction coefficient	0.0060(13)	n/a	n/a
Largest diff. peak and hole	6.749 and -8.434 $e.Å^{-3}$	1.345 and -1.217 $e.Å^{-3}$	1.045 and -0.947 $e.Å^{-3}$

Table 4.2 Bond lengths [Å] and angles [°] for 2D AgSPh.

Ag(1)-S(1)	2.471(3)
Ag(1)-S(2)#1	2.543(3)
Ag(1)-S(2)#2	2.579(4)
Ag(1)-Ag(2)#3	2.923(2)
Ag(1)-Ag(2)#2	2.924(2)
S(1)-C(11)	1.789(11)
S(1)-Ag(2)	2.534(4)
S(1)-Ag(2)#3	2.606(4)
C(11)-C(16)	1.389(13)
C(11)-C(12)	1.403(13)
C(12)-C(13)	1.389(14)
C(12)-H(12)	0.9500
C(13)-C(14)	1.405(14)
C(13)-H(13)	0.9500
C(14)-C(15)	1.398(14)
C(14)-H(14)	0.9500
C(15)-C(16)	1.397(13)
C(15)-H(15)	0.9500
C(16)-H(16)	0.9500
Ag(2)-S(2)	2.489(4)
S(2)-C(21)	1.789(11)
C(21)-C(26)	1.397(14)
C(21)-C(22)	1.409(13)
C(22)-C(23)	1.395(13)
C(22)-H(22)	0.9500
C(23)-C(24)	1.395(14)
C(23)-H(23)	0.9500
C(24)-C(25)	1.394(14)
C(24)-H(24)	0.9500
C(25)-C(26)	1.384(15)
C(25)-H(25)	0.9500
C(26)-H(26)	0.9500
Ag(3)-S(3)	2.480(6)
Ag(3)-S(4)#4	2.551(7)
Ag(3)-S(4)#5	2.564(6)
Ag(3)-Ag(4)#6	2.924(3)
Ag(3)-Ag(4)#4	2.930(4)
S(3)-C(31)	1.788(13)
S(3)-Ag(4)	2.522(6)
S(3)-Ag(4)#6	2.625(7)
C(31)-C(32)	1.393(16)
C(31)-C(36)	1.408(16)
C(32)-C(33)	1.385(16)
C(32)-H(32)	0.9500
C(33)-C(34)	1.394(17)
C(33)-H(33)	0.9500
C(34)-C(35)	1.395(17)
C(34)-H(34)	0.9500
C(35)-C(36)	1.384(17)
C(35)-H(35)	0.9500
C(36)-H(36)	0.9500
Ag(4)-S(4)	2.497(6)
S(4)-C(41)	1.788(13)
C(41)-C(46)	1.390(16)
C(41)-C(42)	1.401(15)
C(42)-C(43)	1.385(15)
C(42)-H(42)	0.9500
C(43)-C(44)	1.401(17)
C(43)-H(43)	0.9500
C(44)-C(45)	1.395(17)
C(44)-H(44)	0.9500
C(45)-C(46)	1.383(16)
C(45)-H(45)	0.9500
C(46)-H(46)	0.9500
Ag(3A)-S(3A)	2.505(12)
Ag(3A)-S(4A)#4	2.53(3)
Ag(3A)-S(4A)#1	2.79(4)
Ag(3A)-S(3A)#7	2.85(2)
Ag(3A)-Ag(3A)#7	2.923(2)
Ag(3A)-Ag(3A)#8	2.923(2)
S(3A)-Ag(4A)#6	2.47(3)
S(3A)-Ag(4A)	2.519(12)
Ag(4A)-S(4A)	2.507(11)
Ag(4A)-S(4A)#4	2.66(3)
Ag(4A)-Ag(4A)#4	2.9112(18)
Ag(4A)-Ag(4A)#6	2.9112(18)
S(1)-Ag(1)-S(2)#1	123.76(15)
S(1)-Ag(1)-S(2)#2	133.81(11)
S(2)#1-Ag(1)-S(2)#2	95.58(7)
S(1)-Ag(1)-Ag(2)#3	57.03(10)
S(2)#1-Ag(1)-Ag(2)#3	67.97(10)
S(2)#2-Ag(1)-Ag(2)#3	139.77(10)
S(1)-Ag(1)-Ag(2)#2	111.46(10)
S(2)#1-Ag(1)-Ag(2)#2	120.71(10)
S(2)#2-Ag(1)-Ag(2)#2	53.33(9)
Ag(2)#3-Ag(1)-Ag(2)#2	166.04(5)
C(11)-S(1)-Ag(1)	103.7(5)
C(11)-S(1)-Ag(2)	115.8(4)
Ag(1)-S(1)-Ag(2)	95.93(13)
C(11)-S(1)-Ag(2)#3	124.7(4)
Ag(1)-S(1)-Ag(2)#3	70.25(9)
Ag(2)-S(1)-Ag(2)#3	119.57(13)
C(16)-C(11)-C(12)	120.8(10)
C(16)-C(11)-S(1)	119.5(8)
C(12)-C(11)-S(1)	119.7(9)
C(13)-C(12)-C(11)	120.0(11)
C(13)-C(12)-H(12)	120.0
C(11)-C(12)-H(12)	120.0
C(12)-C(13)-C(14)	119.9(12)
C(12)-C(13)-H(13)	120.1
C(14)-C(13)-H(13)	120.1
C(15)-C(14)-C(13)	119.4(11)

C(15)-C(14)-H(14)	120.3
C(13)-C(14)-H(14)	120.3
C(16)-C(15)-C(14)	121.1(11)
C(16)-C(15)-H(15)	119.4
C(14)-C(15)-H(15)	119.4
C(11)-C(16)-C(15)	118.8(11)
C(11)-C(16)-H(16)	120.6
C(15)-C(16)-H(16)	120.6
S(2)-Ag(2)-S(1)	124.13(15)
S(2)-Ag(2)-S(1)#2	131.63(12)
S(1)-Ag(2)-S(1)#2	96.53(8)
S(2)-Ag(2)-Ag(1)#2	110.42(10)
S(1)-Ag(2)-Ag(1)#2	122.36(10)
S(1)#2-Ag(2)-Ag(1)#2	52.72(9)
S(2)-Ag(2)-Ag(1)#3	56.22(10)
S(1)-Ag(2)-Ag(1)#3	69.35(10)
S(1)#2-Ag(2)-Ag(1)#3	137.88(10)
Ag(1)#2-Ag(2)-Ag(1)#3	166.04(5)
C(21)-S(2)-Ag(2)	102.8(5)
C(21)-S(2)-Ag(1)#5	116.5(4)
Ag(2)-S(2)-Ag(1)#5	95.30(13)
C(21)-S(2)-Ag(1)#3	122.5(4)
Ag(2)-S(2)-Ag(1)#3	70.45(9)
Ag(1)#5-S(2)-Ag(1)#3	120.95(13)
C(26)-C(21)-C(22)	120.4(11)
C(26)-C(21)-S(2)	120.4(9)
C(22)-C(21)-S(2)	119.2(9)
C(23)-C(22)-C(21)	119.1(11)
C(23)-C(22)-H(22)	120.4
C(21)-C(22)-H(22)	120.4
C(22)-C(23)-C(24)	120.5(11)
C(22)-C(23)-H(23)	119.8
C(24)-C(23)-H(23)	119.8
C(25)-C(24)-C(23)	119.7(12)
C(25)-C(24)-H(24)	120.2
C(23)-C(24)-H(24)	120.2
C(26)-C(25)-C(24)	120.8(12)
C(26)-C(25)-H(25)	119.6
C(24)-C(25)-H(25)	119.6
C(25)-C(26)-C(21)	119.6(12)
C(25)-C(26)-H(26)	120.2
C(21)-C(26)-H(26)	120.2
S(3)-Ag(3)-S(4)#4	136.1(2)
S(3)-Ag(3)-S(4)#5	123.1(3)
S(4)#4-Ag(3)-S(4)#5	94.95(12)
S(3)-Ag(3)-Ag(4)#6	57.43(19)
S(4)#4-Ag(3)-Ag(4)#6	141.12(17)
S(4)#5-Ag(3)-Ag(4)#6	66.96(17)
S(3)-Ag(3)-Ag(4)#4	112.27(18)
S(4)#4-Ag(3)-Ag(4)#4	53.67(15)
S(4)#5-Ag(3)-Ag(4)#4	119.34(18)
Ag(4)#6-Ag(3)-Ag(4)#4	165.15(10)
C(31)-S(3)-Ag(3)	101.8(7)

C(31)-S(3)-Ag(4)	114.8(6)
Ag(3)-S(3)-Ag(4)	96.2(2)
C(31)-S(3)-Ag(4)#6	126.0(6)
Ag(3)-S(3)-Ag(4)#6	69.81(15)
Ag(4)-S(3)-Ag(4)#6	119.1(2)
C(32)-C(31)-C(36)	118.4(13)
C(32)-C(31)-S(3)	122.5(11)
C(36)-C(31)-S(3)	118.8(12)
C(33)-C(32)-C(31)	120.9(15)
C(33)-C(32)-H(32)	119.6
C(31)-C(32)-H(32)	119.6
C(32)-C(33)-C(34)	119.6(16)
C(32)-C(33)-H(33)	120.2
C(34)-C(33)-H(33)	120.2
C(33)-C(34)-C(35)	120.7(15)
C(33)-C(34)-H(34)	119.6
C(35)-C(34)-H(34)	119.6
C(36)-C(35)-C(34)	118.9(16)
C(36)-C(35)-H(35)	120.6
C(34)-C(35)-H(35)	120.6
C(35)-C(36)-C(31)	121.4(16)
C(35)-C(36)-H(36)	119.3
C(31)-C(36)-H(36)	119.3
S(4)-Ag(4)-S(3)	123.6(3)
S(4)-Ag(4)-S(3)#4	130.80(19)
S(3)-Ag(4)-S(3)#4	97.06(12)
S(4)-Ag(4)-Ag(3)#4	109.82(18)
S(3)-Ag(4)-Ag(3)#4	124.1(2)
S(3)#4-Ag(4)-Ag(3)#4	52.76(16)
S(4)-Ag(4)-Ag(3)#6	55.38(18)
S(3)-Ag(4)-Ag(3)#6	69.86(18)
S(3)#4-Ag(4)-Ag(3)#6	135.93(17)
Ag(3)#4-Ag(4)-Ag(3)#6	165.15(10)
C(41)-S(4)-Ag(4)	102.2(7)
C(41)-S(4)-Ag(3)#6	121.5(6)
Ag(4)-S(4)-Ag(3)#6	70.96(16)
C(41)-S(4)-Ag(3)#1	116.5(6)
Ag(4)-S(4)-Ag(3)#1	94.6(2)
Ag(3)#6-S(4)-Ag(3)#1	121.9(2)
C(46)-C(41)-C(42)	118.7(13)
C(46)-C(41)-S(4)	121.7(11)
C(42)-C(41)-S(4)	119.6(11)
C(43)-C(42)-C(41)	121.1(15)
C(43)-C(42)-H(42)	119.5
C(41)-C(42)-H(42)	119.5
C(42)-C(43)-C(44)	119.0(15)
C(42)-C(43)-H(43)	120.5
C(44)-C(43)-H(43)	120.5
C(45)-C(44)-C(43)	120.7(15)
C(45)-C(44)-H(44)	119.6
C(43)-C(44)-H(44)	119.6
C(46)-C(45)-C(44)	119.1(16)
C(46)-C(45)-H(45)	120.4

C(44)-C(45)-H(45)	120.4
C(45)-C(46)-C(41)	121.4(15)
C(45)-C(46)-H(46)	119.3
C(41)-C(46)-H(46)	119.3
S(3A)-Ag(3A)-S(4A)#4	91.6(9)
Ag(4A)#6-S(3A)-Ag(3A)	127.6(11)
Ag(4A)#6-S(3A)-Ag(4A)	71.4(5)
Ag(3A)-S(3A)-Ag(4A)	91.9(6)
S(3A)#4-Ag(4A)-S(4A)	97.8(10)
S(3A)#4-Ag(4A)-S(3A)	172.9(9)
S(4A)-Ag(4A)-S(3A)	88.1(10)

S(3A)#4-Ag(4A)-S(4A)#4	85.8(7)
S(4A)-Ag(4A)-S(4A)#4	176.2(7)
S(3A)-Ag(4A)-S(4A)#4	88.3(7)

Symmetry transformations used to generate equivalent atoms: #1 x-1,y,z #2 -x,y-1/2,-z #3 -x,y+1/2,-z

#4 -x+2,y+1/2,-z+1 #5 x+1,y,z #6 -x+2,y-1/2,-z+1 #7 -x+1,y+1/2,-z+1 #8 -x+1,y-1/2,-z+1

Table 4.3 Bond lengths [Å] and angles [°] for 2D AgTePh.

Ag(1)-Te(1)	2.8055(3)
Ag(1)-Te(2)	2.8336(3)
Ag(1)-Ag(2)	2.8630(4)
Ag(1)-Te(1)#1	2.9107(3)
Ag(1)-Te(2)#2	2.9373(3)
Ag(1)-Ag(2)#1	3.0156(4)
Ag(1)-Ag(2)#2	3.0654(3)
Te(1)-C(11)	2.133(3)
Te(1)-Ag(2)	2.8334(3)
Te(1)-Ag(2)#1	2.9652(3)
C(11)-C(12)	1.390(4)
C(11)-C(16)	1.393(4)
C(12)-C(13)	1.394(4)
C(12)-H(12)	0.9500
C(13)-C(14)	1.387(5)
C(13)-H(13)	0.9500
C(14)-C(15)	1.394(5)
C(14)-H(14)	0.9500
C(15)-C(16)	1.393(4)
C(15)-H(15)	0.9500
C(16)-H(16)	0.9500
Ag(2)-Te(2)	2.8126(3)
Ag(2)-Te(2)#3	2.8698(3)
Te(2)-C(21)	2.124(3)
C(21)-C(22)	1.390(4)
C(21)-C(26)	1.397(4)
C(22)-C(23)	1.389(4)
C(22)-H(22)	0.9500
C(23)-C(24)	1.391(5)
C(23)-H(23)	0.9500
C(24)-C(25)	1.389(4)
C(24)-H(24)	0.9500
C(25)-C(26)	1.396(4)
C(25)-H(25)	0.9500
C(26)-H(26)	0.9500
Te(1)-Ag(1)-Te(2)	119.139(10)
Te(1)-Ag(1)-Ag(2)	59.969(8)
Te(2)-Ag(1)-Ag(2)	59.170(8)
Te(1)-Ag(1)-Te(1)#1	118.207(9)
Te(2)-Ag(1)-Te(1)#1	109.250(9)
Ag(2)-Ag(1)-Te(1)#1	142.260(11)
Te(1)-Ag(1)-Te(2)#2	113.155(10)
Te(2)-Ag(1)-Te(2)#2	113.890(8)
Ag(2)-Ag(1)-Te(2)#2	142.062(11)
Te(1)#1-Ag(1)-Te(2)#2	75.451(8)
Te(1)-Ag(1)-Ag(2)#1	61.120(8)
Te(2)-Ag(1)-Ag(2)#1	142.762(11)
Ag(2)-Ag(1)-Ag(2)#1	108.279(9)
Te(1)#1-Ag(1)-Ag(2)#1	57.089(7)
Te(2)#2-Ag(1)-Ag(2)#1	96.766(9)
Te(1)-Ag(1)-Ag(2)#2	143.141(11)
Te(2)-Ag(1)-Ag(2)#2	58.062(8)
Ag(2)-Ag(1)-Ag(2)#2	105.242(9)
Te(1)#1-Ag(1)-Ag(2)#2	94.233(9)
Te(2)#2-Ag(1)-Ag(2)#2	55.831(7)
Ag(2)#1-Ag(1)-Ag(2)#2	146.418(12)
C(11)-Te(1)-Ag(1)	104.22(8)
C(11)-Te(1)-Ag(2)	104.13(8)
Ag(1)-Te(1)-Ag(2)	61.023(8)
C(11)-Te(1)-Ag(1)#4	128.01(8)
Ag(1)-Te(1)-Ag(1)#4	109.947(7)
Ag(2)-Te(1)-Ag(1)#4	63.320(8)
C(11)-Te(1)-Ag(2)#1	126.84(8)
Ag(1)-Te(1)-Ag(2)#1	62.939(8)
Ag(2)-Te(1)-Ag(2)#1	110.506(8)
Ag(1)#4-Te(1)-Ag(2)#1	103.560(9)
C(12)-C(11)-C(16)	120.3(3)
C(12)-C(11)-Te(1)	117.9(2)
C(16)-C(11)-Te(1)	121.8(2)
C(11)-C(12)-C(13)	119.5(3)
C(11)-C(12)-H(12)	120.2
C(13)-C(12)-H(12)	120.2
C(14)-C(13)-C(12)	120.6(3)
C(14)-C(13)-H(13)	119.7
C(12)-C(13)-H(13)	119.7
C(13)-C(14)-C(15)	119.7(3)
C(13)-C(14)-H(14)	120.2
C(15)-C(14)-H(14)	120.2
C(16)-C(15)-C(14)	120.1(3)
C(16)-C(15)-H(15)	119.9
C(14)-C(15)-H(15)	119.9
C(11)-C(16)-C(15)	119.8(3)
C(11)-C(16)-H(16)	120.1
C(15)-C(16)-H(16)	120.1
Te(2)-Ag(2)-Te(1)	118.903(10)
Te(2)-Ag(2)-Ag(1)	59.895(8)
Te(1)-Ag(2)-Ag(1)	59.008(8)
Te(2)-Ag(2)-Te(2)#3	116.695(9)
Te(1)-Ag(2)-Te(2)#3	111.341(10)
Ag(1)-Ag(2)-Te(2)#3	143.147(11)
Te(2)-Ag(2)-Te(1)#4	111.208(10)
Te(1)-Ag(2)-Te(1)#4	115.529(9)
Ag(1)-Ag(2)-Te(1)#4	141.208(11)
Te(2)#3-Ag(2)-Te(1)#4	75.629(8)
Te(2)-Ag(2)-Ag(1)#4	141.716(11)
Te(1)-Ag(2)-Ag(1)#4	59.590(8)
Ag(1)-Ag(2)-Ag(1)#4	105.530(9)
Te(2)#3-Ag(2)-Ag(1)#4	95.957(9)
Te(1)#4-Ag(2)-Ag(1)#4	55.941(7)
Te(2)-Ag(2)-Ag(1)#3	59.779(8)
Te(1)-Ag(2)-Ag(1)#3	144.181(11)
Ag(1)-Ag(2)-Ag(1)#3	108.003(9)

Te(2)#3-Ag(2)-Ag(1)#3	56.919(7)
Te(1)#4-Ag(2)-Ag(1)#3	95.179(9)
Ag(1)#4-Ag(2)-Ag(1)#3	146.418(12)
C(21)-Te(2)-Ag(2)	104.82(8)
C(21)-Te(2)-Ag(1)	102.92(8)
Ag(2)-Te(2)-Ag(1)	60.935(8)
C(21)-Te(2)-Ag(2)#2	125.08(8)
Ag(2)-Te(2)-Ag(2)#2	112.051(8)
Ag(1)-Te(2)-Ag(2)#2	65.018(8)
C(21)-Te(2)-Ag(1)#3	127.23(8)
Ag(2)-Te(2)-Ag(1)#3	64.389(8)
Ag(1)-Te(2)-Ag(1)#3	112.462(8)
Ag(2)#2-Te(2)-Ag(1)#3	105.295(9)
C(22)-C(21)-C(26)	120.0(3)
C(22)-C(21)-Te(2)	118.8(2)
C(26)-C(21)-Te(2)	121.2(2)
C(23)-C(22)-C(21)	120.0(3)
C(23)-C(22)-H(22)	120.0
C(21)-C(22)-H(22)	120.0
C(22)-C(23)-C(24)	120.2(3)
C(22)-C(23)-H(23)	119.9
C(24)-C(23)-H(23)	119.9
C(25)-C(24)-C(23)	120.0(3)
C(25)-C(24)-H(24)	120.0
C(23)-C(24)-H(24)	120.0
C(24)-C(25)-C(26)	120.0(3)
C(24)-C(25)-H(25)	120.0
C(26)-C(25)-H(25)	120.0
C(25)-C(26)-C(21)	119.7(3)
C(25)-C(26)-H(26)	120.1
C(21)-C(26)-H(26)	120.1
_____	
Symmetry transformations used to generate equivalent atoms: #1 -x+1,y+1/2,-z+1/2 #2 -x+2,y+1/2,-z+1/2 #3 -x+2,y-1/2,-z+1/2	
#4 -x+1,y-1/2,-z+1/2	

Table 4.4 Bond lengths [Å] and angles [°] for 1D $AgTeC_{6.27}H_{5.62}N_{0.09}$ (1D AgTePh + $0.089C_3H_7N$).

Ag(1)-Te(1)	2.7059(3)
Ag(1)-Te(1)#1	2.7073(3)
Ag(1)-Te(2)	2.7887(3)
Ag(1)-Ag(2)	2.9393(3)
Ag(1)-Ag(3)	2.9870(3)
Ag(2)-Te(2)#2	2.7946(2)
Ag(2)-Te(2)#3	2.8152(2)
Ag(2)-Te(3)	2.8189(3)
Ag(2)-Ag(3)#4	2.9541(3)
Ag(2)-Ag(3)	3.0098(3)
Ag(3)-Te(3)	2.7978(3)
Ag(3)-Te(3)#1	2.8310(3)
Ag(3)-Te(1)#1	2.8674(3)
Ag(3)-Te(2)#3	3.1954(3)
Te(1)-C(11A)	2.078(8)
Te(1)-C(11)	2.195(8)
C(11)-C(16)	1.406(9)
C(11)-C(12)	1.436(9)
C(12)-C(13)	1.396(7)
C(12)-H(12)	0.9500
C(13)-C(14)	1.379(9)
C(13)-H(13)	0.9500
C(14)-C(15)	1.383(10)
C(14)-H(14)	0.9500
C(15)-C(16)	1.400(7)
C(15)-H(15)	0.9500
C(16)-H(16)	0.9500
C(11A)-C(16A)	1.350(8)
C(11A)-C(12A)	1.382(8)
C(12A)-C(13A)	1.378(7)
C(12A)-H(12A)	0.9500
C(13A)-C(14A)	1.383(10)
C(13A)-H(13A)	0.9500
C(14A)-C(15A)	1.388(10)
C(14A)-H(14A)	0.9500
C(15A)-C(16A)	1.388(7)
C(15A)-H(15A)	0.9500
C(16A)-H(16A)	0.9500
Te(2)-C(21A)	2.138(8)
Te(2)-C(21)	2.141(8)
C(21)-C(22)	1.368(9)
C(21)-C(26)	1.422(8)
C(22)-C(23)	1.391(7)
C(22)-H(22)	0.9500
C(23)-C(24)	1.393(11)
C(23)-H(23)	0.9500
C(24)-C(25)	1.384(11)
C(24)-H(24)	0.9500
C(25)-C(26)	1.386(6)
C(25)-H(25)	0.9500
C(26)-H(26)	0.9500
C(21A)-C(26A)	1.386(8)
C(21A)-C(22A)	1.399(9)
C(22A)-C(23A)	1.396(6)
C(22A)-H(22A)	0.9500
C(23A)-C(24A)	1.386(11)
C(23A)-H(23A)	0.9500
C(24A)-C(25A)	1.382(11)
C(24A)-H(24A)	0.9500
C(25A)-C(26A)	1.397(6)
C(25A)-H(25A)	0.9500
C(26A)-H(26A)	0.9500
Te(3)-C(31)	2.078(8)
Te(3)-C(31A)	2.183(8)
C(31)-C(32)	1.353(8)
C(31)-C(36)	1.392(8)
C(32)-C(33)	1.389(7)
C(32)-H(32)	0.9500
C(33)-C(34)	1.387(10)
C(33)-H(33)	0.9500
C(34)-C(35)	1.376(10)
C(34)-H(34)	0.9500
C(35)-C(36)	1.390(7)
C(35)-H(35)	0.9500
C(36)-H(36)	0.9500
C(31A)-C(32A)	1.420(9)
C(31A)-C(36A)	1.422(9)
C(32A)-C(33A)	1.401(7)
C(32A)-H(32A)	0.9500
C(33A)-C(34A)	1.382(10)
C(33A)-H(33A)	0.9500
C(34A)-C(35A)	1.373(9)
C(34A)-H(34A)	0.9500
C(35A)-C(36A)	1.384(7)
C(35A)-H(35A)	0.9500
C(36A)-H(36A)	0.9500
N(1S)-C(1S)	1.459(17)
C(1S)-C(2S)	1.497(15)
C(1S)-H(1S1)	0.9900
C(1S)-H(1S2)	0.9900
C(2S)-C(3S)	1.600(17)
C(2S)-H(2S1)	0.9900
C(2S)-H(2S2)	0.9900
C(3S)-H(3S1)	0.9800
C(3S)-H(3S2)	0.9800
C(3S)-H(3S3)	0.9800
N(1T)-C(1T)	1.474(19)
C(1T)-C(2T)	1.469(18)
C(1T)-H(1T1)	0.9900
C(1T)-H(1T2)	0.9900
C(2T)-C(3T)	1.509(19)

C(2T)-H(2T1)	0.9900
C(2T)-H(2T2)	0.9900
C(3T)-H(3T1)	0.9800
C(3T)-H(3T2)	0.9800
C(3T)-H(3T3)	0.9800
Te(1)-Ag(1)-Te(1)#1	125.400(10)
Te(1)-Ag(1)-Te(2)	105.717(8)
Te(1)#1-Ag(1)-Te(2)	112.327(9)
Te(1)-Ag(1)-Ag(2)	106.378(9)
Te(1)#1-Ag(1)-Ag(2)	119.850(8)
Te(2)-Ag(1)-Ag(2)	75.487(7)
Te(1)-Ag(1)-Ag(3)	137.962(9)
Te(1)#1-Ag(1)-Ag(3)	60.234(7)
Te(2)-Ag(1)-Ag(3)	108.602(8)
Ag(2)-Ag(1)-Ag(3)	61.037(7)
Te(2)#2-Ag(2)-Te(2)#3	118.069(8)
Te(2)#2-Ag(2)-Te(3)	120.683(8)
Te(2)#3-Ag(2)-Te(3)	118.282(8)
Te(2)#2-Ag(2)-Ag(1)	112.947(8)
Te(2)#3-Ag(2)-Ag(1)	100.335(8)
Te(3)-Ag(2)-Ag(1)	73.054(7)
Te(2)#2-Ag(2)-Ag(3)#4	67.475(7)
Te(2)#3-Ag(2)-Ag(3)#4	172.269(9)
Te(3)-Ag(2)-Ag(3)#4	58.677(6)
Ag(1)-Ag(2)-Ag(3)#4	72.091(7)
Te(2)#2-Ag(2)-Ag(3)	173.035(9)
Te(2)#3-Ag(2)-Ag(3)	66.441(7)
Te(3)-Ag(2)-Ag(3)	57.259(6)
Ag(1)-Ag(2)-Ag(3)	60.264(6)
Ag(3)#4-Ag(2)-Ag(3)	107.522(9)
Te(3)-Ag(3)-Te(3)#1	117.426(9)
Te(3)-Ag(3)-Te(1)#1	110.024(8)
Te(3)#1-Ag(3)-Te(1)#1	98.440(8)
Te(3)-Ag(3)-Ag(2)#1	147.958(9)
Te(3)#1-Ag(3)-Ag(2)#1	58.277(6)
Te(1)#1-Ag(3)-Ag(2)#1	101.919(8)
Te(3)-Ag(3)-Ag(1)	72.614(7)
Te(3)#1-Ag(3)-Ag(1)	152.789(9)
Te(1)#1-Ag(3)-Ag(1)	55.043(6)
Ag(2)#1-Ag(3)-Ag(1)	127.300(9)
Te(3)-Ag(3)-Ag(2)	57.938(6)
Te(3)#1-Ag(3)-Ag(2)	148.506(9)
Te(1)#1-Ag(3)-Ag(2)	112.515(8)
Ag(2)#1-Ag(3)-Ag(2)	107.523(9)
Ag(1)-Ag(3)-Ag(2)	58.699(7)
Te(3)-Ag(3)-Te(2)#3	107.421(8)
Te(3)#1-Ag(3)-Te(2)#3	107.932(8)
Te(1)#1-Ag(3)-Te(2)#3	115.772(8)
Ag(2)#1-Ag(3)-Te(2)#3	53.886(6)
Ag(1)-Ag(3)-Te(2)#3	91.203(7)
Ag(2)-Ag(3)-Te(2)#3	53.859(6)
C(11A)-Te(1)-Ag(1)	115.4(2)

C(11)-Te(1)-Ag(1)	114.33(19)
C(11)-Te(1)-Ag(1)#4	105.07(18)
Ag(1)-Te(1)-Ag(1)#4	125.400(10)
C(11)-Te(1)-Ag(3)#4	92.6(2)
Ag(1)-Te(1)-Ag(3)#4	76.896(7)
Ag(1)#4-Te(1)-Ag(3)#4	64.724(7)
C(16)-C(11)-C(12)	115.7(6)
C(16)-C(11)-Te(1)	126.1(5)
C(12)-C(11)-Te(1)	118.2(5)
C(13)-C(12)-C(11)	121.5(6)
C(13)-C(12)-H(12)	119.2
C(11)-C(12)-H(12)	119.2
C(14)-C(13)-C(12)	120.5(6)
C(14)-C(13)-H(13)	119.7
C(12)-C(13)-H(13)	119.7
C(13)-C(14)-C(15)	119.6(8)
C(13)-C(14)-H(14)	120.2
C(15)-C(14)-H(14)	120.2
C(14)-C(15)-C(16)	120.5(6)
C(14)-C(15)-H(15)	119.7
C(16)-C(15)-H(15)	119.7
C(15)-C(16)-C(11)	122.0(5)
C(15)-C(16)-H(16)	119.0
C(11)-C(16)-H(16)	119.0
C(16A)-C(11A)-C(12A)	124.1(7)
C(16A)-C(11A)-Te(1)	119.8(5)
C(12A)-C(11A)-Te(1)	116.1(5)
C(13A)-C(12A)-C(11A)	117.5(5)
C(13A)-C(12A)-H(12A)	121.3
C(11A)-C(12A)-H(12A)	121.3
C(12A)-C(13A)-C(14A)	120.6(6)
C(12A)-C(13A)-H(13A)	119.7
C(14A)-C(13A)-H(13A)	119.7
C(13A)-C(14A)-C(15A)	119.6(8)
C(13A)-C(14A)-H(14A)	120.2
C(15A)-C(14A)-H(14A)	120.2
C(14A)-C(15A)-C(16A)	120.6(6)
C(14A)-C(15A)-H(15A)	119.7
C(16A)-C(15A)-H(15A)	119.7
C(11A)-C(16A)-C(15A)	117.5(5)
C(11A)-C(16A)-H(16A)	121.2
C(15A)-C(16A)-H(16A)	121.2
C(21A)-Te(2)-Ag(1)	97.3(2)
C(21)-Te(2)-Ag(1)	95.9(2)
C(21)-Te(2)-Ag(2)#2	101.7(2)
Ag(1)-Te(2)-Ag(2)#2	122.542(8)
C(21)-Te(2)-Ag(2)#3	91.90(19)
Ag(1)-Te(2)-Ag(2)#3	115.406(8)
Ag(2)#2-Te(2)-Ag(2)#3	118.069(8)
C(21)-Te(2)-Ag(3)#3	108.42(19)
Ag(1)-Te(2)-Ag(3)#3	155.048(8)
Ag(2)#2-Te(2)-Ag(3)#3	58.640(6)
Ag(2)#3-Te(2)-Ag(3)#3	59.700(6)

C(22)-C(21)-C(26)	119.5(6)
C(22)-C(21)-Te(2)	123.0(5)
C(26)-C(21)-Te(2)	117.5(5)
C(21)-C(22)-C(23)	120.4(5)
C(21)-C(22)-H(22)	119.8
C(23)-C(22)-H(22)	119.8
C(22)-C(23)-C(24)	120.4(6)
C(22)-C(23)-H(23)	119.8
C(24)-C(23)-H(23)	119.8
C(25)-C(24)-C(23)	119.7(8)
C(25)-C(24)-H(24)	120.2
C(23)-C(24)-H(24)	120.2
C(24)-C(25)-C(26)	120.3(6)
C(24)-C(25)-H(25)	119.9
C(26)-C(25)-H(25)	119.9
C(25)-C(26)-C(21)	119.7(5)
C(25)-C(26)-H(26)	120.1
C(21)-C(26)-H(26)	120.1
C(26A)-C(21A)-C(22A)	120.4(6)
C(26A)-C(21A)-Te(2)	121.3(5)
C(22A)-C(21A)-Te(2)	118.3(5)
C(23A)-C(22A)-C(21A)	119.4(5)
C(23A)-C(22A)-H(22A)	120.3
C(21A)-C(22A)-H(22A)	120.3
C(24A)-C(23A)-C(22A)	120.0(6)
C(24A)-C(23A)-H(23A)	120.0
C(22A)-C(23A)-H(23A)	120.0
C(25A)-C(24A)-C(23A)	120.4(9)
C(25A)-C(24A)-H(24A)	119.8
C(23A)-C(24A)-H(24A)	119.8
C(24A)-C(25A)-C(26A)	120.2(6)
C(24A)-C(25A)-H(25A)	119.9
C(26A)-C(25A)-H(25A)	119.9
C(21A)-C(26A)-C(25A)	119.5(5)
C(21A)-C(26A)-H(26A)	120.3
C(25A)-C(26A)-H(26A)	120.3
C(31)-Te(3)-Ag(3)	99.33(19)
C(31A)-Te(3)-Ag(3)	103.3(2)
C(31)-Te(3)-Ag(2)	96.6(2)
C(31A)-Te(3)-Ag(2)	97.91(19)
Ag(3)-Te(3)-Ag(2)	64.804(7)
C(31)-Te(3)-Ag(3)#4	118.4(2)
Ag(3)-Te(3)-Ag(3)#4	117.426(9)
Ag(2)-Te(3)-Ag(3)#4	63.046(7)
C(32)-C(31)-C(36)	123.6(7)
C(32)-C(31)-Te(3)	120.6(5)
C(36)-C(31)-Te(3)	115.7(5)
C(31)-C(32)-C(33)	118.1(5)
C(31)-C(32)-H(32)	120.9
C(33)-C(32)-H(32)	120.9
C(34)-C(33)-C(32)	120.4(6)
C(34)-C(33)-H(33)	119.8
C(32)-C(33)-H(33)	119.8

C(35)-C(34)-C(33)	119.9(8)
C(35)-C(34)-H(34)	120.1
C(33)-C(34)-H(34)	120.1
C(34)-C(35)-C(36)	120.9(6)
C(34)-C(35)-H(35)	119.6
C(36)-C(35)-H(35)	119.6
C(35)-C(36)-C(31)	117.0(5)
C(35)-C(36)-H(36)	121.5
C(31)-C(36)-H(36)	121.5
C(32A)-C(31A)-C(36A)	116.0(6)
C(32A)-C(31A)-Te(3)	124.6(6)
C(36A)-C(31A)-Te(3)	119.4(5)
C(33A)-C(32A)-C(31A)	120.9(6)
C(33A)-C(32A)-H(32A)	119.6
C(31A)-C(32A)-H(32A)	119.6
C(34A)-C(33A)-C(32A)	121.0(6)
C(34A)-C(33A)-H(33A)	119.5
C(32A)-C(33A)-H(33A)	119.5
C(35A)-C(34A)-C(33A)	119.3(8)
C(35A)-C(34A)-H(34A)	120.4
C(33A)-C(34A)-H(34A)	120.4
C(34A)-C(35A)-C(36A)	121.1(6)
C(34A)-C(35A)-H(35A)	119.5
C(36A)-C(35A)-H(35A)	119.5
C(35A)-C(36A)-C(31A)	121.7(5)
C(35A)-C(36A)-H(36A)	119.1
C(31A)-C(36A)-H(36A)	119.1
N(1S)-C(1S)-C(2S)	113.5(14)
N(1S)-C(1S)-H(1S1)	108.9
C(2S)-C(1S)-H(1S1)	108.9
N(1S)-C(1S)-H(1S2)	108.9
C(2S)-C(1S)-H(1S2)	108.9
H(1S1)-C(1S)-H(1S2)	107.7
C(1S)-C(2S)-C(3S)	109.6(14)
C(1S)-C(2S)-H(2S1)	109.7
C(3S)-C(2S)-H(2S1)	109.7
C(1S)-C(2S)-H(2S2)	109.7
C(3S)-C(2S)-H(2S2)	109.7
H(2S1)-C(2S)-H(2S2)	108.2
C(2S)-C(3S)-H(3S1)	109.5
C(2S)-C(3S)-H(3S2)	109.5
H(3S1)-C(3S)-H(3S2)	109.5
C(2S)-C(3S)-H(3S3)	109.5
H(3S1)-C(3S)-H(3S3)	109.5
H(3S2)-C(3S)-H(3S3)	109.5
C(2T)-C(1T)-N(1T)	116.0(19)
C(2T)-C(1T)-H(1T1)	108.3
N(1T)-C(1T)-H(1T1)	108.3
C(2T)-C(1T)-H(1T2)	108.3
N(1T)-C(1T)-H(1T2)	108.3
H(1T1)-C(1T)-H(1T2)	107.4
C(1T)-C(2T)-C(3T)	120(2)
C(1T)-C(2T)-H(2T1)	107.4

C(3T)-C(2T)-H(2T1)	107.4
C(1T)-C(2T)-H(2T2)	107.4
C(3T)-C(2T)-H(2T2)	107.4
H(2T1)-C(2T)-H(2T2)	106.9
C(2T)-C(3T)-H(3T1)	109.5
C(2T)-C(3T)-H(3T2)	109.5
H(3T1)-C(3T)-H(3T2)	109.5
C(2T)-C(3T)-H(3T3)	109.5
H(3T1)-C(3T)-H(3T3)	109.5
H(3T2)-C(3T)-H(3T3)	109.5

Symmetry transformations used to generate equivalent atoms: #1 x+1,y,z #2 -x,-y+2,-z+1 #3 -x+1,-y+2,-z+1 #4 x-1,y,

4.3.2 Relationship between the macroscopic morphology and microscopic structure

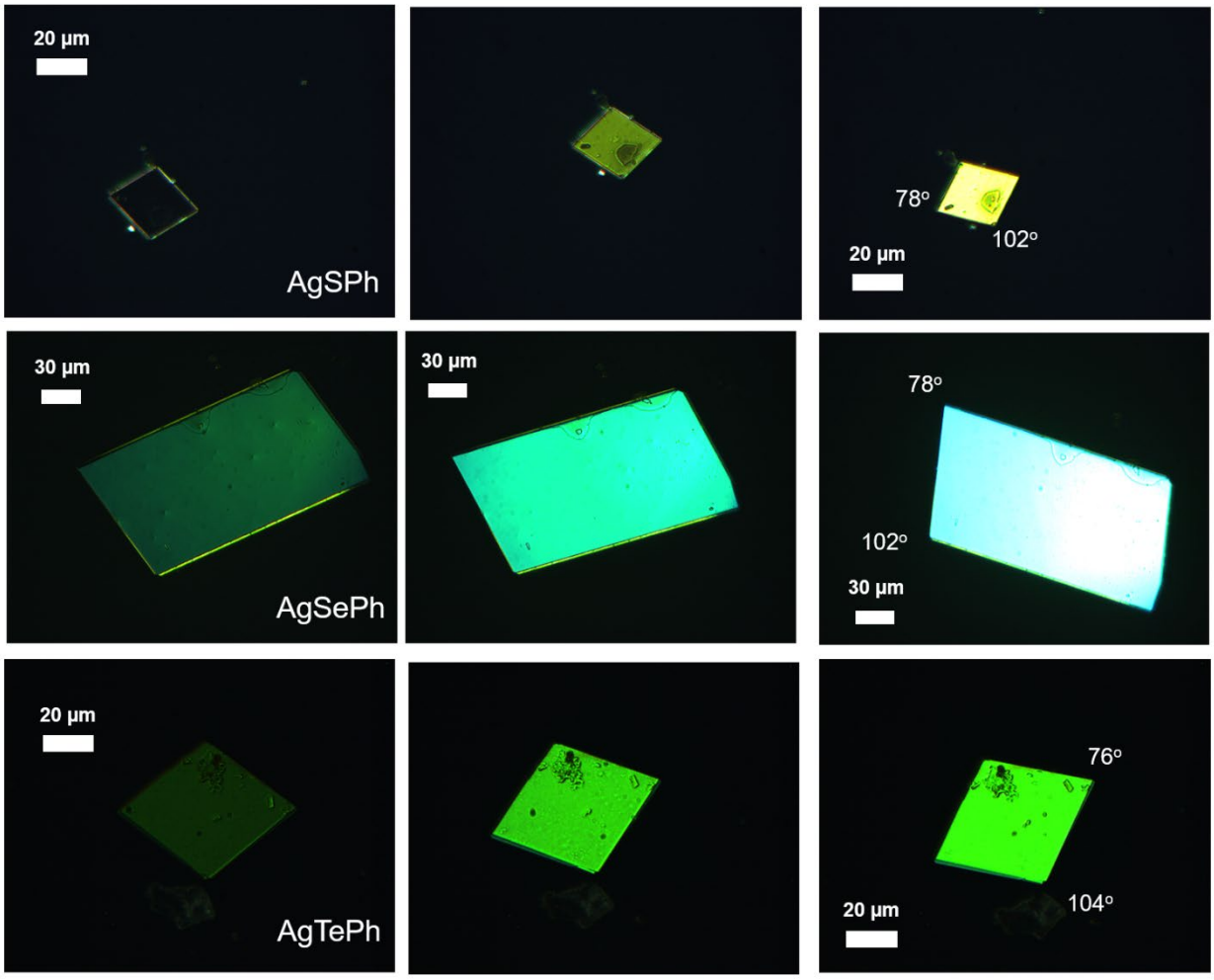

Figure 4.4 Polarized optical micrographs of single crystal of AgSPh, AgSePh, and AgTePh taken at different angles relative to light polarization. The uniform brightness change throughout the crystal at each rotation angle indicates that the crystal is single.

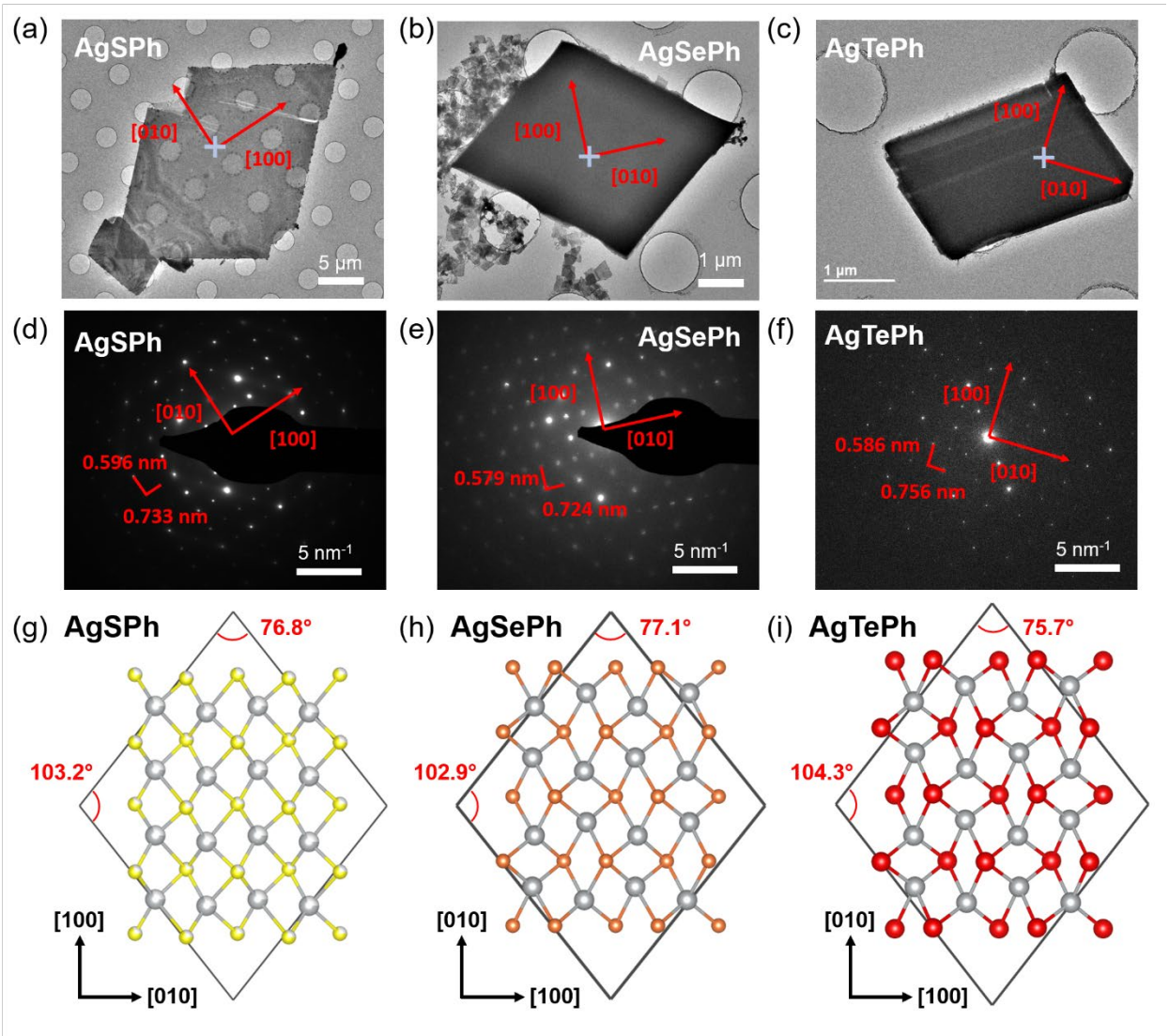

Figure 4.5 Transmission electron microscopy (TEM) images of (a) AgSPh, (b) AgSePh, and (c) AgTePh crystals. Single crystal electron diffraction (ED) patterns of (d) AgSPh, (e) AgSePh, and (f) AgTePh at marked locations in (a-c). The red arrows indicate the in-plane crystallographic axes determined through a comparison between experimental ED patterns (d-f) and simulated ED patterns based on crystallographic information. Crystal structures of (g) AgSPh in $P2_1$, (h) AgSePh in $P2_1/c$, and (i) AgTePh in $P2_1/c$, depicted along crystallographic [001] orientation. Phenyl rings are omitted for clarity. The parallelograms outlined with a black solid line depict artificial crystals terminated by {110} planes.

The AgEPh single crystals tend to exhibit a unique parallelogram shape, featuring acute angles of 76-78° and obtuse angles of 102-104° (Figures 4.1b-d, 4.2, and 4.4). To explore the relationship between macroscopic morphology and microscopic crystal structure, we performed

transmission electron microscopy (TEM) and electron diffraction (ED) analysis on AgEPh single crystals (Figure 4.5). Briefly, we obtained ED patterns of AgEPh single crystal with a parallelogram shape. The diffraction spots were subsequently indexed with (*hkl*) values by comparing them with simulated ED patterns based on the crystallographic information (Figure 4.6). The crystallographic [100] and [010] axes were then presented by drawing lines from the origin towards (*h*00) and (0*k*0) diffraction spots, respectively. By superimposing these crystallographic axes onto the TEM images corresponding to the ED patterns, we found that, for AgSPh, the [100] and [010] axes align with directions toward acute and obtuse angles, respectively. Conversely, for AgSePh and AgTePh, the [010] and [100] axes align with directions toward acute and obtuse angles, respectively (Figure 4.5a-f).

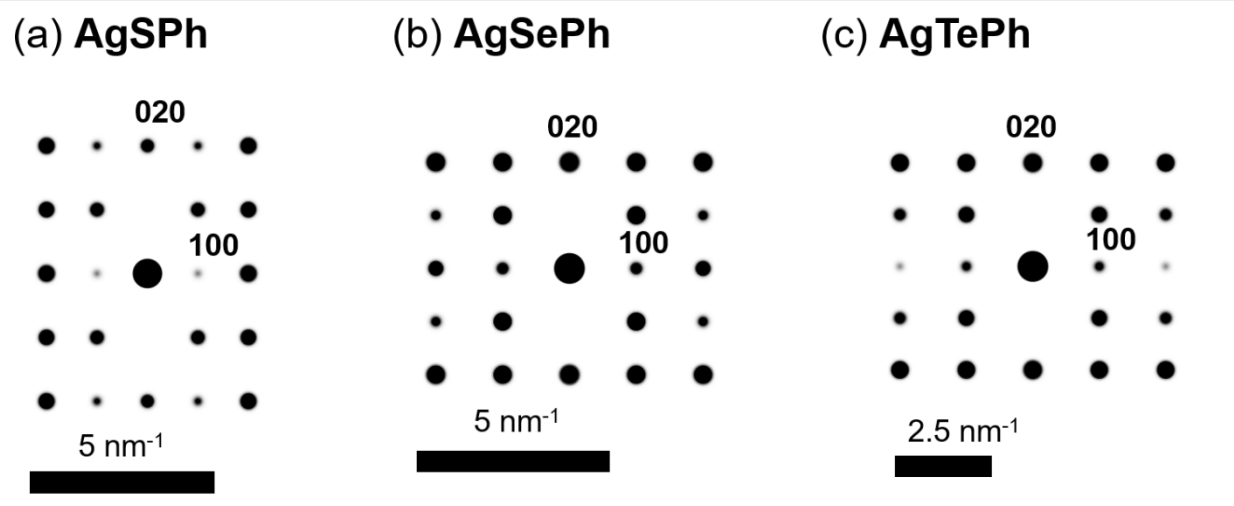

Figure 4.6 Simulated electron diffraction patterns of (a) AgSPh in $P2_1$, (b) AgSePh in $P2_1/c$,[30] and (c) AgTePh in $P2_1/c$ when the incident electron beam aligns with crystallographic [001] axis. The absence of (0l0) reflections in simulations, where l is an odd integer, is due to systematic absence. The appearance of (0l0) reflections (l is an odd integer) in experimental electron diffraction patterns could be attributed to the strong interaction between electrons and atoms, leading to multiple diffractions as electron beam passes through the sample. For example, the intensity observed at the (010) reflection can arise from the (100) reflection followed by the (-110) reflection.

It should be noted that care must be taken when comparing TEM images and ED patterns to determine crystal orientation. In crystallography, crystal lattice parameters (a, b, c, α, β, γ) and reciprocal lattice parameters (a^*, b^*, c^*, α^*, β^*, γ^*) are related by the following equations:

$$a = \frac{b^* \times c^*}{a^* \cdot b^* \times c^*}, b = \frac{c^* \times a^*}{a^* \cdot b^* \times c^*}, c = \frac{a^* \times b^*}{a \cdot b^* \times c^*}, \alpha = 180° - \alpha^*, \beta = 180° - \beta^*, \gamma$$

$$= 180° - \gamma^*, or \quad (4.1)$$

$$a^* = \frac{b \times c}{a \cdot b \times c}, b^* = \frac{c \times a}{a \cdot b \times c}, c^* = \frac{a \times b}{a \cdot b \times c}, \alpha^* = 180° - \alpha, \beta^* = 180° - \beta, \gamma^* = 180° - \gamma$$

Therefore, in cubic, orthorhombic, and tetragonal systems where crystal lattice vectors are all orthogonal to each other ($\alpha = \beta = \gamma = 90°$), the directions of crystal lattice vectors and reciprocal lattice vectors are identical ($a \| a^*$, $b \| b^*$, $c \| c^*$). However, in other Bravais lattice systems, the directions of crystal lattice vectors and reciprocal lattice vectors may not be the same, requiring a careful consideration when extracting crystal orientation in transmission electron microscopy (TEM) images from their electron diffraction (ED) patterns.

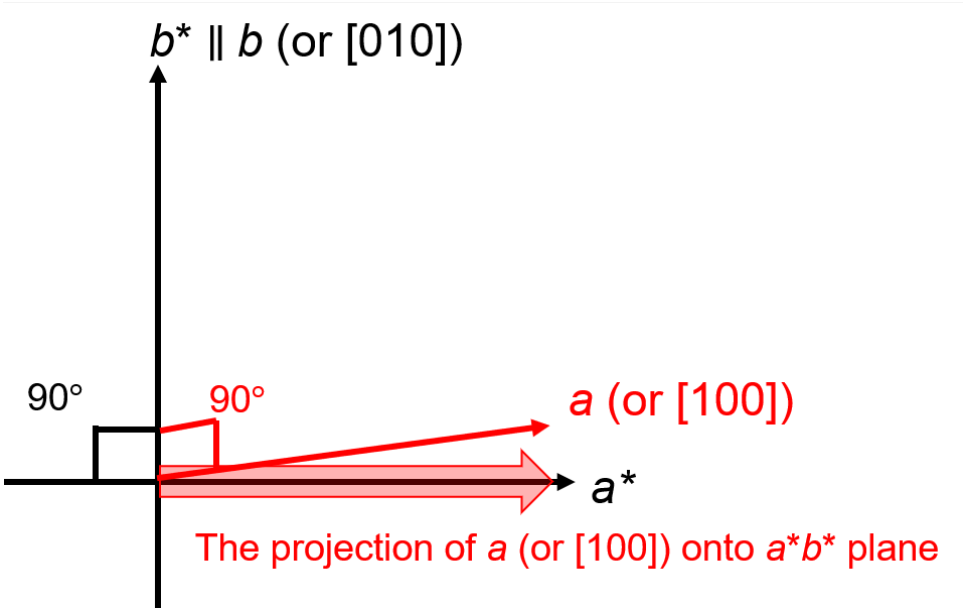

Figure 4.7 Schematic showing the relationship between crystal lattice vectors (a and b) and reciprocal lattice vectors (a* and b*) in AgEPh (E = S, Se, Te). b (or [010] is parallel to b*. The projection of a (or [100]) onto a*b* plane is parallel to a*. The angle between a and a* is 4.1° for AgSPh, 5.6° for AgSePh, and 2.9° for AgTePh.

The lines drawn from the origin towards (h00) and (0k0) diffraction spots in the ED patterns (Figure 4.5d-f) correspond to a^* and b^*, respectively. Because AgEPh belong to the monoclinic lattice system with $\alpha = \gamma = 90$ and $\beta > 90°$ ($\beta = 94.1°$ for AgSPh, 95.6° for AgSePh, and 92.9° for

AgTePh), *b* (or [010]) is parallel to *b**, but *a* (or [100]) is not actually parallel to *a**. The angle between *a* and *a** is 4.1° for AgSPh, 5.6° for AgSePh, and 2.9° for AgTePh. However, the projection of *a* (or [100]) onto the electron diffraction pattern plane (*a***b** plane) is parallel to *a** (Figure 4.7). Likewise, the projection of *a** onto the real space *ab* plane is parallel to *a*. Consequently, the crystallographic [100] and [010] axes can be depicted by drawing lines from the origin towards (*h*00) and (0*k*0) diffraction spots, respectively, and these axes can be superimposed onto the TEM images.

Notably, schematic illustration of crystals terminated with {110} planes closely resemble the actual macroscopic crystals in terms of their parallelogram shape, angles, and crystal orientation (Figure 4.5g-i). These findings facilitate to establish correlations between experimental observations on macroscopic crystals and their microscopic structure as well as theoretical calculations in future investigations.

4.3.3 Discrepancies in crystal structure descriptions of AgEPh (E = S, Se, Te)

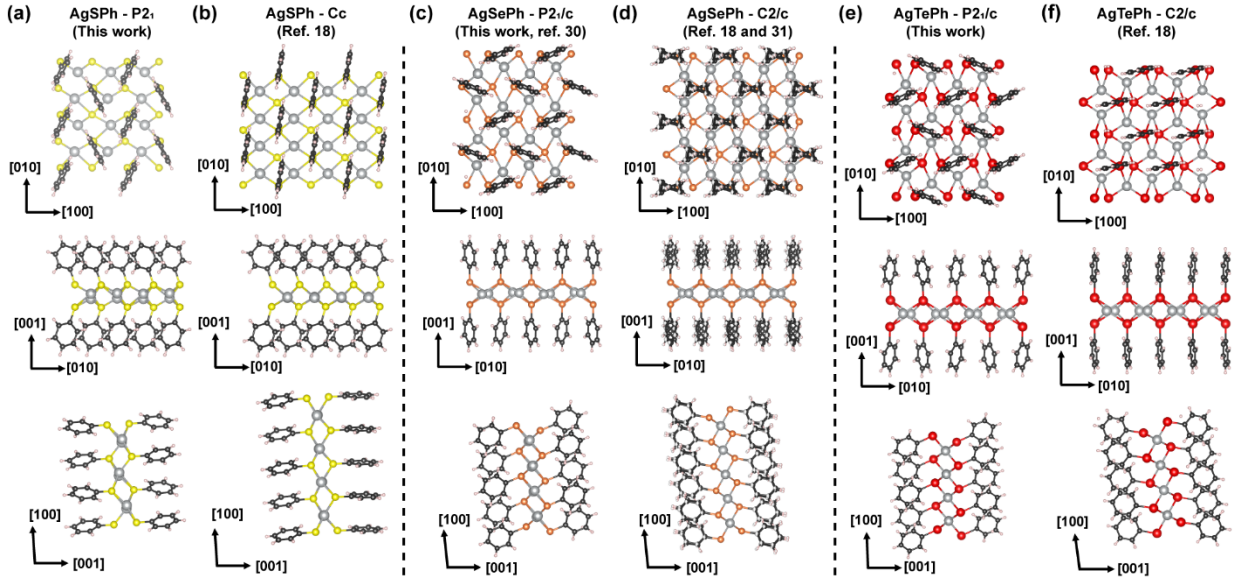

Figure 4.8 Crystal structures of AgSPh in (a) $P2_1$ and (b) Cc (Ref. [18]), AgSePh in (c) $P2_1/c$ (Ref. [30]) and (d) C2/c (Ref. [18] and [31]), and AgTePh in (e) $P2_1/c$ and (f) C2/c (Ref. [18]), depicted along crystallographic [001] (top), [100] (middle), and [010] (bottom) directions. In the [001] view, benzene rings at the bottom of AgE plane are omitted for clarity. Disordered atoms in AgSPh in $P2_1$ and AgSePh in C2/c are omitted for clarity.

Our space group assignments as well as crystal structures in terms of silver-chalcogen network and phenyl ligand array are different from the previous report of AgSPh in Cc,[18] AgSePh in C2/c,[18,31] and AgTePh in C2/c[18] at room temperature (Figure 4.8). For instance, whereas AgSPh in Cc exhibits nearly linear Ag-Ag chains along [010] direction, AgSPh in $P2_1$ shows distorted and zig-zag Ag-Ag chains. More strikingly, whereas AgEPh in C-centered structures exhibits linear arrangement of benzene rings (AgSPh and AgTePh) or disordered benzene rings (AgSePh), AgEPh in primitive structures exhibits herringbone arrangement of benzene rings. Considering the organic-inorganic hybrid nature of AgEPh in terms of both electronic band structures and vibrational modes,[21,32] the discrepancy in both inorganic structures and the arrangement of organic ligands between primitive structures and C-centered structures can be significant. In the previous report of C-centered lattices, colloidal AgEPh crystals were synthesized by the reaction between silver (I) oxide (or metallic silver) and benezeneselenol or benezenethiol (or diphenyl ditelluride) with isopropanol at 70-100 °C (Figure 4.10a).[18] The structures of these compounds were then

characterized by the serial femtosecond X-ray crystallography at room temperature. Thus, differences in the description of the crystal structures (Primitive *vs.* C-centered) could be due to a phase transformation occurring between 100 K and room temperature,[36] the existence of polymorphs at the same temperature arising from different synthesis conditions,[37] or differences in the crystal size and/or quality of identical materials.[38]

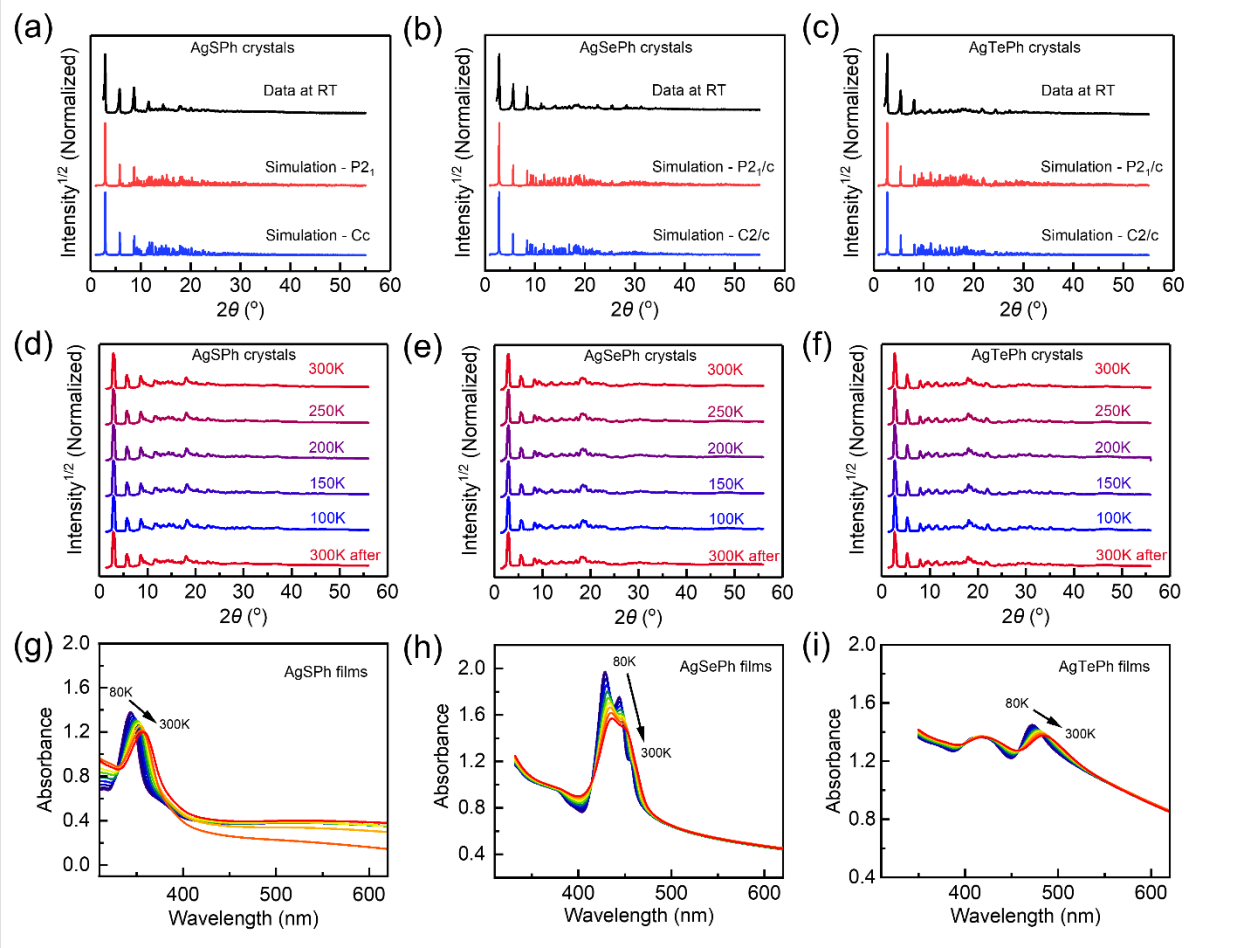

Figure 4.9 Powder X-ray diffraction (PXRD) (Mo K**α** radiation, **λ** = 0.71 Å) patterns of (a) AgSPh, (b) AgSePh, and (c) AgTePh crystals and the corresponding simulated patterns based on crystallographic information of primitive structures (red, this work and ref. [30]) and C-centered structures (blue, Ref. [18]). Temperature-dependent PXRD patterns of (d) AgSPh, (e) AgSePh, and (f) AgTePh crystals. Temperature-dependent absorption spectra of (g) AgSPh, (h) AgSePh, and (i) AgTePh thin films obtained by the tarnishing method.

To explore the possibility of a phase transition between 100 K and 300 K, we conducted temperature-dependent powder X-ray (Mo Kα radiation, λ = 0.71 Å) diffraction (PXRD) measurement of ground AgEPh crystals (Figure 4.9a-f). PXRD patterns were gradually shifted to smaller angles as decreasing temperatures due to unit cell contraction. However, the overall diffraction pattern and intensities were maintained without the disappearance of existing diffraction peaks or the emergence of new diffraction peaks, suggesting no phase transition. Given that the simulated PXRD patterns of primitive unit cells and C-center unit cells are very close to each other (Figure 4.9a-c), it is also possible that our instrument's resolution and sensitivity were not enough to detect a potential phase transition. To further evaluate the possibility of a phase transition, we performed temperature-dependent absorption measurement of AgEPh films since their electronic or optical properties may exhibit more dramatic change. AgEPh films were prepared by the tarnishing method where metallic silver films are reacted with vapor-transported diphenyl dichalcogenide at 100ºC in the presence of water vapor (Figure 4.10e-h).[21,24,29] However, the absorption spectral shapes of AgEPh films were gradually red-shifted as increasing temperatures without exhibiting any sudden changes, further supporting the absence of a phase transition.

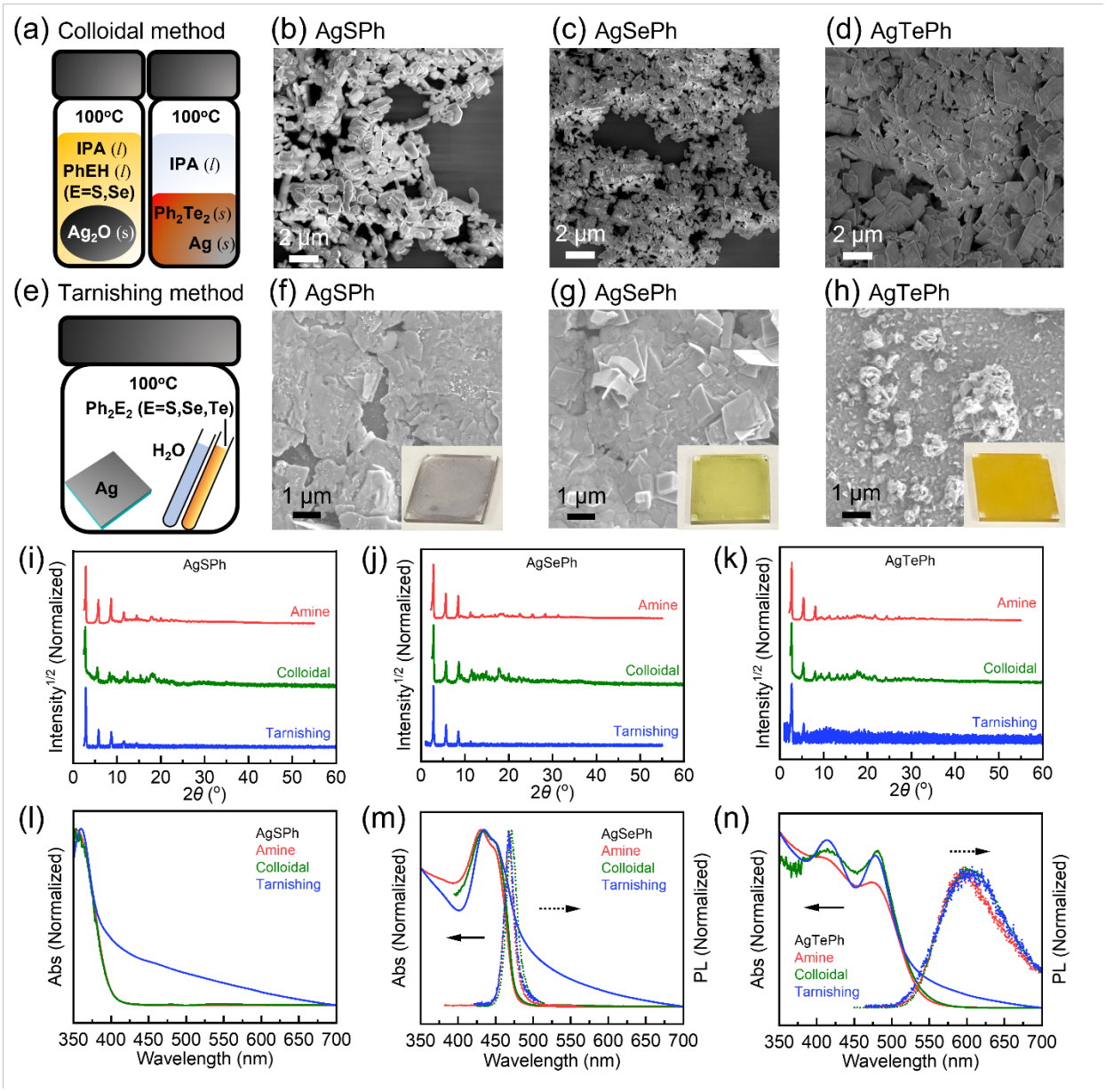

Figure 4.10 (a) Schematic illustration of the colloidal method used in Ref. [18]. Scanning electron microscopy (SEM) images of (b) AgSPh, (c) AgSePh, and (d) AgTePh nanocrystals obtained by the colloidal method used in Ref. [18]. (e) Schematic illustration of the tarnishing method. SEM images of (f) AgSPh, (g) AgSePh, and (h) AgTePh films obtained by the tarnishing. The insets show photographs of AgEPh films on a glass substrate with dimensions of 12.2 mm x 12.2 mm x 1.1 mm. Powder X-ray diffraction (PXRD) (Mo Kα radiation, λ = 0.71 Å) patterns of (i) AgSPh, (j) AgSePh, and (k) AgTePh crystals (red), nanocrystals (green), and films (blue), obtained by the amine-assisted method, colloidal method, and the tarnishing method, respectively. Diffuse reflectance UV-vis absorption and photoluminescence spectra of (l) AgSPh, (m) AgSePh, and (n) AgTePh crystals, obtained by the amine-assisted method, the colloidal method, and the tarnishing method, respectively.

Next, we evaluated the possibility of polymorphs existing at the same temperature. Polymorphs with distinct physical properties are commonly formed in metal organic chalcogenolates (MOCs) depending on the different synthesis conditions,[37] as we have already demonstrated the formation of 1D AgTePh and 2D AgTePh (Figure 4.3). Synthesis conditions for 2D AgEPh in amine-assisted method (Figure 4.1a), colloidal method [18] (Figure 4.10a), and the tarnishing method (Figure 4.10e) are all different in terms of precursors, solvents, and reaction temperatures. To assess whether 2D AgEPh obtained from different methods are identical materials or polymorphs, we compared their structural and optical properties (Figure 4.10i-n). The absorption and PL spectra as well as PXRD patterns of 2D AgEPh obtained from the amine-assisted method, colloidal method, the tarnishing method are nearly the same, suggesting that they are identical materials. (For AgEPh films from the tarnishing method, only the (00*h*) diffraction peaks were observed, indicating a preferential crystal orientation with the c-axis perpendicular to the substrate.)

Another possibility is the differences in crystal size and/or quality. Structures of AgEPh were previously assigned to C-centered lattices. However, for AgSPh, we found no indication of any lattice centering in our data (Table 4.5). In the cases of AgSePh and AgTePh, although C-lattice reflections are systematically weaker than average, they were still clearly observed (Tables 4.6 and 4.7). Nevertheless, we attempted to determine the structures of AgSePh and AgTePh in C-centered lattices, and reasonable models could be established in the C2/c space group for both (Figure 4.11). However, it should be noted that in this space group, we encountered over 10,000 systematic violations, and the phenyl ring is disordered over two positions with a 50:50 ratio. Although R-values are slightly lower in the C2/c model (as expected over 10,000 of the weakest reflections are excluded), we believe $P2_1/c$ description is superior to C2/c for AgSePh and AgTePh in our data because primitive structures make use of all collected data and contain all information. The AgEPh obtained by the colloidal method have lateral dimensions in the order of a few micrometers or smaller and a thickness in the sub-micrometer range (Figure 4.10b-d). These crystals might not have been large and high-quality enough to generate systematically weak X-ray reflections. In contrast, the size of AgSPh, AgSePh,[30] and AgTePh crystals used for SCXRD were 415 μm × 355 μm × 35 μm, 230 μm × 220 μm × 20 μm, 235 μm × 70 μm × 10 μm, respectively (Figure 4.12). Additionally, the suppression of defect-derived PL in AgSePh crystals obtained by the amine-assisted method, as previously reported, further supports the superior crystal quality.[30]

Table 4.5 Intensity statistics of SCXRD for AgSPh (Identification code: P23051). P, A, B, C, I, and F represent primitive, A-centered, B-centered, C-centered, body-centered, and face-centered lattices, respectively. N (total) indicates the number of reflections that should be absent among all collected reflections (61679) if the structure is described in X-lattices (X = A, B, C, I, or F). N (Int > 3σ) indicates the number of these reflections with intensities higher than three times the standard deviation (σ). Mean intensity represents the average intensity of these reflections, and Mean int/σ represents the average of intensity/σ for these reflections.

Lattice exceptions	P	A	B	C	I	F	All
N (total)	0	30269	30690	30963	30993	45961	61679
N (int>3sigma)	0	20936	21721	19771	23265	31214	43667
Mean intensity	0	14.7	19	16.4	20.2	16.7	24
Mean int/sigma	0	7.7	8.2	7.2	8.6	7.7	8.1

Table 4.6 Intensity statistics of SCXRD for AgSePh (Identification code: X21004).[30]

Lattice exceptions	P	A	B	C	I	F	All
N (total)	0	19560	19599	20097	19756	29628	39508
N (int>3sigma)	0	12960	13557	11769	14432	19143	27300
Mean intensity	0	15.7	15.8	1.9	13.4	11	15.9
Mean int/sigma	0	6.8	7.1	5	7.5	6.3	7.1

Table 4.7 Intensity statistics of SCXRD for AgTePh (Identification code: P23058).

Lattice exceptions	P	A	B	C	I	F	All
N (total)	0	36302	36259	36865	36325	54713	72691
N (int>3sigma)	0	17733	18350	9885	18268	22984	36957
Mean intensity	0	18	18.1	0.8	16.5	12.3	18.7
Mean int/sigma	0	6.8	6.9	2.3	6.9	5.3	7

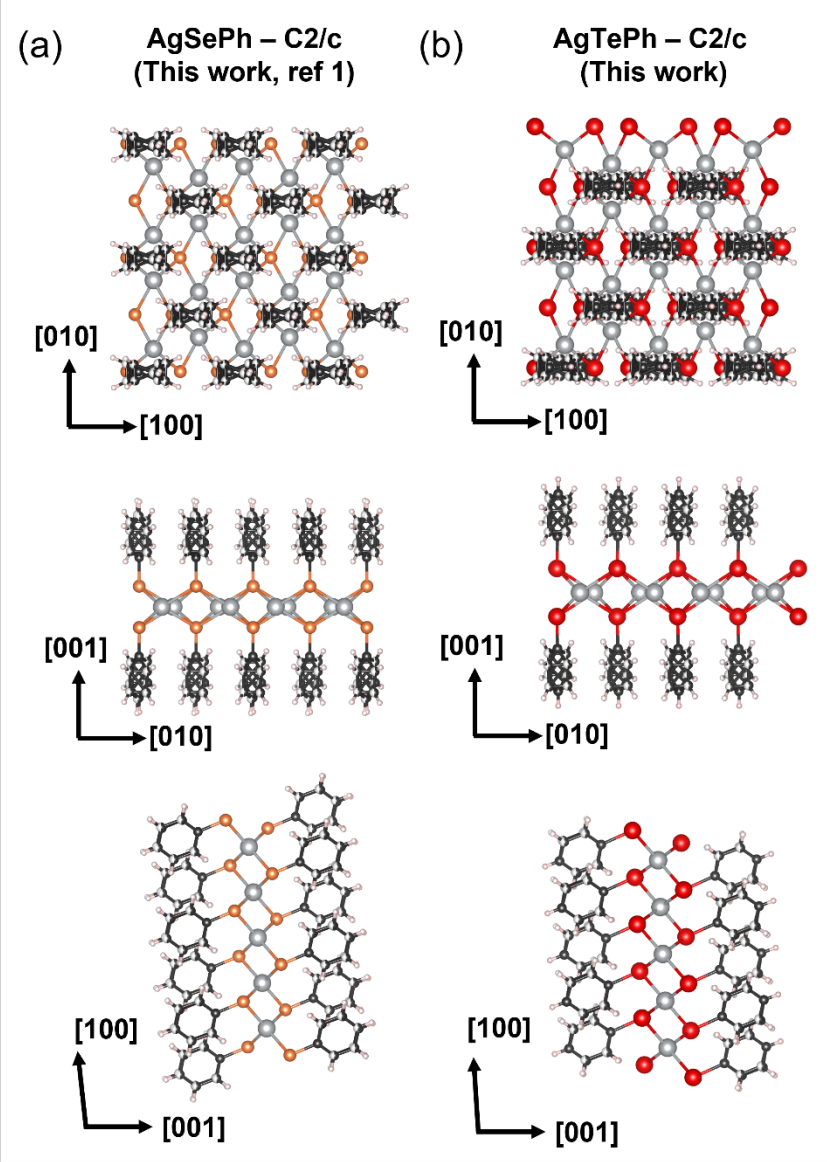

Figure 4.11 Crystal structures of AgSePh and AgTePh in C2/c obtained when they are forced into C-centered lattices by excluding >10,000 reflections from the collected data. In both cases, the phenyl ring is disordered over two positions with a 50:50 ratio.

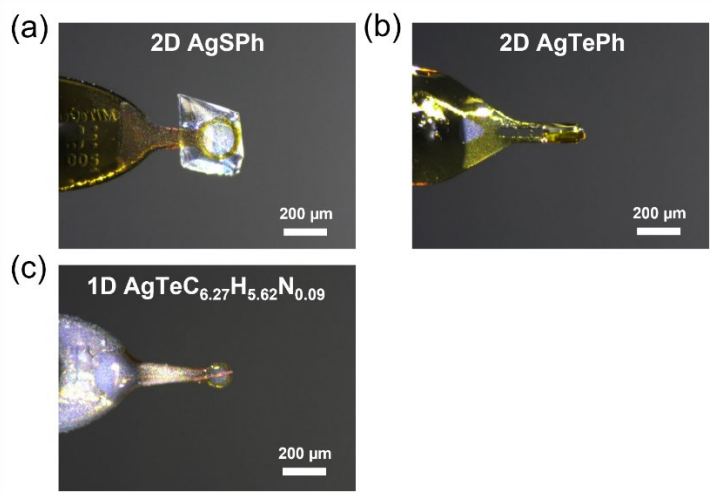

Figure 4.12 Images of AgSPh in $P2_1$, AgTePh in $P2_1/c$, and $AgTeC_{6.27}H_{5.62}N_{0.09}$ in P-1 used for single-crystal X-ray diffraction.

4.4 Conclusions

In conclusion, we have shown the growth of millimeter-sized single crystalline AgEPh (E = S, Se, Te) and revealed the relationship between their macroscopic morphologies and microscopic crystal structures. Furthermore, we have reported three new structures (2D AgSPh, 2D AgTePh, 1D AgTePh + $0.089C_3H_7N$), and we explored and discussed the discrepancies in crystal structure descriptions of 2D AgEPh (Primitive lattices vs C-centered lattices) in terms of phase transitions, polymorphism, and differences in crystal size and quality. Considering the growing interest on these emerging 2D hybrid materials, we believe that the synthesis of millimeter-sized single crystals, crystallographic information, and macroscopic-microscopic structural relationships provided in this work will serve as foundational knowledge for future experimental and theoretical investigations into their in-plane anisotropic electronic, optical, thermal properties arising from their low-symmetry structures.

4.5 Methods

Chemicals. Silver pellets (Ag, 99.99% pure) were purchased from Kurt J Lesker. Diphenyl disulfide (Ph_2S_2, 99.0+%), diphenyl diselenide (Ph_2Se_2, 97.0+%), and benzeneselenol (PhSeH, >95.0%) were purchased from TCI America. Diphenyl ditelluride (Ph_2Te_2, 98%), benzenethiol (≥99%), propylamine ($PrNH_2$, 98%), butylamine ($BuNH_2$, 99.5%), hexylamine ($HexNH_2$, 99%), toluene (>99.5%), isopropanol (IPA, ≥99.5%), potassium bromide (KBr, 99.0%) silver powders (Ag, ≥99.9%), silver nitrate ($AgNO_3$, ≥99.0%) and silver (I) oxide (Ag_2O, ≥99.99%) were purchased from Millipore Sigma.

Preparation of AgEPh (E = S, Se, Te) crystals by the amine-assisted method.[30] AgEPh crystals were synthesized by mixing a 20 mM solution of silver nitrate (AgNO3) in 1-butylamine ($BuNH_2$) and a 20 mM solution of diphenyl dichalcogenide (Ph2E2) in $BuNH_2$ in a sealed vial (Figure 1a). The vial was then stored under dark at room temperature for 2 weeks to obtain AgSPh crystals, 3 days for AgSePh crystals, and 2 months for AgTePh crystals. For AgSPh and AgSePh, no byproduct or intermediate phase was observed during the synthesis process, and similar results were obtained when propylamine ($PrNH_2$) and hexylamine ($HexNH_2$) were used instead of $BuNH_2$. However, intermediate phases or byproducts such as 1D fibers or 1D crystals (1D AgTePh + 0.089 C_3H_7N) were observed during the synthesis of 2D AgTePh.

Preparation of AgEPh (E = S, Se, Te) nanocrystals by the colloidal method.[18] For AgSPh and AgSePh nanocrystals, 100 mg of silver (I) oxide was placed in a 5 mL glass vial with 1 mL of isopropanol and 1 mL of benzenethiol (PhSH) or benzeneselenol (PhSeH). The vial is sealed and placed in a secondary container to avoid leakage of toxic and smelly PhSH or PhSeH. The container is heated in an oven at 100 °C for 1 day to obtain AgSPh or AgSePh crystals. For AgTePh crystals, 100 mg of metallic silver powders and 1.5 g of diphenyl ditelluride (Ph_2Te_2) were placed in a 5 mL glass vial with 1 mL of isopropanol. The vial is sealed and placed in a secondary container. The container is heated in an oven at 100 °C for 4 days to obtain AgTePh crystals. AgEPh crystals were retrieved after removing excess organic ligands by 3 cycles of centrifugation (6,000 rpm for 2 min) with toluene, isopropanol and ethanol, successively.

Preparation of AgEPh (E = S, Se, Te) films by the tarnishing method.[21,24,29] AgEPh thin films were prepared by a chemical transformation reaction between metallic silver and a vapor of

Ph_2E_2, known as the tarnishing method. Silver films with thickness of 15 nm were deposited on pre-cleaned glass substrates (12.2 x 12.2 x 1.1 mm^3, Luminescence Technology Corp.) by thermal evaporation with a deposition rate of ~1 Å/s. After that, the prepared silver films, Ph_2E_2 powder and 200 μL of deionized water in separate open culture tubes were sealed together inside a microwave reaction vial. After heating in an oven at 100 °C for 4~7 days, the silver films transformed into AgEPh films.

Polarized optical microscopy. The samples on transparent glass coverslips were mounted on an inverted microscope (Nikon, Ti-U Eclipse). Above and below the sample, a polarizer and an analyzer were placed, respectively, oriented orthogonally to each other. The sample was illuminated by an overhead light source (Nikon D-LH Halogen 12V 100W). The transmitted light through the sample was collected with an objective lens (Nikon, CFI S Plan Fluor ELWD, 40×, 0.6 NA) and then directed into a color CMOS camera (Thorlabs, DCC1645C-HQ). Polarized optical images were taken by rotating the sample stage.

Photoluminescence spectroscopy. PL spectra of AgSePh and AgTePh were measured with a home-built setup consisting of an inverted microscope (Nikon, Ti-U Eclipse) equipped with a 405 nm laser diode (Picoquant, LDHDC-405M, continuous wave mode) and a cooled charge-coupled detector (Princeton Instruments, PiMAX 4) on a spectrograph (Princeton Instruments, SP-2500). A Tecan Spark multimode plate reader with 355 nm excitation was used to measure PL of AgSPh, but no PL was detected.

UV-Vis spectroscopy and diffuse reflectance spectroscopy. Absorption spectra of AgEPh films prepared by the tarnishing method were obtained using Cary 5000 UV-Vis-NIR spectrometer. For temperature-dependent absorption spectra, samples were mounted inside a steady flow Janis ST-100 optical cryostat. The cryostat was then mounted in the Cary spectrometer, evacuated to below 3×10^{-5} Torr, and cooled with liquid nitrogen. The temperature was controlled with a model 335 Lakeshore temperature controller. Diffuse reflectance spectra of AgEPh crystals prepared by the amine-assisted method and AgEPh nanocrystals prepared by the methods in ref X were obtained using a Cary 5000 UV-Vis-NIR spectrometer equipped with a PIKE Technologies DiffuseIR accessory and Perkin Elmer 1050 UV-Vis-NIR spectrophotometer equipped with diffuse reflection accessory, respectively. For diffuse reflectance measurements, AgEPh crystals and nanocrystals were grinded with dry potassium bromide (KBr) to a ~0.3 wt% dilution and

diffuse reflectance spectra were normalized to a 100% KBr baseline. The obtained diffuse reflectance spectra were converted into absorption spectra by Kubelka-Munk transform:[39]

$$F(R) = \frac{(1-R)^2}{2R}$$

where F(R) is the Kubelka-Munk function with a value proportional to the sample's absorption coefficient, and R is the relative reflectance of the sample with the 100% KBr baseline.

Scanning electron microscopy (SEM). SEM images were collected using a Zeiss Merlin instrument operating at 1 kV and 100 pA.

Transmission electron microscopy (TEM) and electron diffraction (ED). TEM and ED were conducted using a FEI Tecnai G2 Spirit Twin instrument operating at 120 kV.

Room-temperature Powder X-ray diffraction (PXRD). Room temperature PXRD data were collected using a PANalytical Empyrean X-ray diffractometer (Mo Kα radiation, λ = 0.71 Å) equipped with Galipix 3D detector.

Single-Crystal X-ray Diffraction (SCXRD). SCXRD data at 100 K were collected on Bruker-AXS X8 Kappa Duo diffractometers with *IμS* micro-sources using Mo K_α radiation (λ = 0.71073 Å), coupled to a Photon 3 CPAD detector, performing φ and ω scans. All structures were solved by dual-space methods using SHELXT[40] and refined against F^2 on all data by full-matrix least squares with SHELXL-2017[41] following established refinement strategies.[42] All non-hydrogen atoms were refined anisotropically. All hydrogen atoms were included into the model at geometrically calculated positions and refined using a riding model. The isotropic displacement parameters of all hydrogen atoms were fixed to 1.2 times the *U*-value of the atoms they are linked to. Temperature-dependent transmission-mode PXRD data were collected using the SCXRD setup.

Temperature-dependent PXRD. Temperature-dependent transmission-mode PXRD data were collected using the SCXRD setup.

4.6 References

(1) Veselska, O.; Demessence, A. D10 Coinage Metal Organic Chalcogenolates: From Oligomers to Coordination Polymers. *Coord Chem Rev* **2018**, *355*, 240–270. https://doi.org/10.1016/j.ccr.2017.08.014.

(2) Wang, G.; Luo, S.; Di, T.; Fu, Z.; Xu, G. Layered Organic Metal Chalcogenides (OMCs): From Bulk to Two-Dimensional Materials. *Angewandte Chemie International Edition* **2022**, *61* (27). https://doi.org/10.1002/anie.202203151.

(3) Yan, H.; Hohman, J. N.; Li, F. H.; Jia, C.; Solis-Ibarra, D.; Wu, B.; Dahl, J. E. P.; Carlson, R. M. K.; Tkachenko, B. A.; Fokin, A. A.; Schreiner, P. R.; Vailionis, A.; Kim, T. R.; Devereaux, T. P.; Shen, Z.-X.; Melosh, N. A. Hybrid Metal–Organic Chalcogenide Nanowires with Electrically Conductive Inorganic Core through Diamondoid-Directed Assembly. *Nat Mater* **2017**, *16* (3), 349–355. https://doi.org/10.1038/nmat4823.

(4) Boles, M. A.; Ling, D.; Hyeon, T.; Talapin, D. V. The Surface Science of Nanocrystals. *Nat Mater* **2016**, *15* (2), 141–153. https://doi.org/10.1038/nmat4526.

(5) Dey, A.; Ye, J.; De, A.; Debroye, E.; Ha, S. K.; Bladt, E.; Kshirsagar, A. S.; Wang, Z.; Yin, J.; Wang, Y.; Quan, L. N.; Yan, F.; Gao, M.; Li, X.; Shamsi, J.; Debnath, T.; Cao, M.; Scheel, M. A.; Kumar, S.; Steele, J. A.; Gerhard, M.; Chouhan, L.; Xu, K.; Wu, X.; Li, Y.; Zhang, Y.; Dutta, A.; Han, C.; Vincon, I.; Rogach, A. L.; Nag, A.; Samanta, A.; Korgel, B. A.; Shih, C.-J.; Gamelin, D. R.; Son, D. H.; Zeng, H.; Zhong, H.; Sun, H.; Demir, H. V.; Scheblykin, I. G.; Mora-Seró, I.; Stolarczyk, J. K.; Zhang, J. Z.; Feldmann, J.; Hofkens, J.; Luther, J. M.; Pérez-Prieto, J.; Li, L.; Manna, L.; Bodnarchuk, M. I.; Kovalenko, M. V.; Roeffaers, M. B. J.; Pradhan, N.; Mohammed, O. F.; Bakr, O. M.; Yang, P.; Müller-Buschbaum, P.; Kamat, P. V.; Bao, Q.; Zhang, Q.; Krahne, R.; Galian, R. E.; Stranks, S. D.; Bals, S.; Biju, V.; Tisdale, W. A.; Yan, Y.; Hoye, R. L. Z.; Polavarapu, L. State of the Art and Prospects for Halide Perovskite Nanocrystals. *ACS Nano* **2021**, *15* (7), 10775–10981. https://doi.org/10.1021/acsnano.0c08903.

(6) Kotei, P. A.; Paley, D. W.; Oklejas, V.; Mittan-Moreau, D. W.; Schriber, E. A.; Aleksich, M.; Willson, M. C.; Inoue, I.; Owada, S.; Tono, K.; Sugahara, M.; Inaba-Inoue, S.; Aquila, A.; Poitevin, F.; Blaschke, J. P.; Lisova, S.; Hunter, M. S.; Sierra, R. G.; Gascón, J. A.; Sauter, N. K.; Brewster, A. S.; Hohman, J. N. Engineering Supramolecular Hybrid Architectures with Directional Organofluorine Bonds. *Small Science* **2024**, *4* (1). https://doi.org/10.1002/smsc.202300110.

(7) Aleksich, M.; Paley, D. W.; Schriber, E. A.; Linthicum, W.; Oklejas, V.; Mittan-Moreau, D. W.; Kelly, R. P.; Kotei, P. A.; Ghodsi, A.; Sierra, R. G.; Aquila, A.; Poitevin, F.; Blaschke, J. P.; Vakili, M.; Milne, C. J.; Dall'Antonia, F.; Khakhulin, D.; Ardana-Lamas, F.; Lima, F.; Valerio, J.; Han, H.; Gallo, T.; Yousef, H.; Turkot, O.; Bermudez Macias, I. J.; Kluyver, T.; Schmidt, P.; Gelisio, L.; Round, A. R.; Jiang, Y.; Vinci, D.; Uemura, Y.; Kloos, M.; Hunter, M.; Mancuso, A. P.; Huey, B. D.; Parent, L. R.; Sauter, N. K.; Brewster, A. S.; Hohman, J. N. XFEL Microcrystallography of Self-Assembling Silver *n* -Alkanethiolates. *J Am Chem Soc* **2023**, *145* (31), 17042–17055. https://doi.org/10.1021/jacs.3c02183.

(8) Hernandez Oendra, A. C.; Aspect, M. A.; Jaeggi, J. L.; Baumann, J.; Lightner, C. R.; Pun, A. B.; Norris, D. J. Tunable Synthesis of Metal–Organic Chalcogenide Semiconductor Nanocrystals. *Chemistry of Materials* **2023**, *35* (21), 9390–9398. https://doi.org/10.1021/acs.chemmater.3c02275.

(9) Yang, H.; Mandal, S.; Lee, Y. H.; Park, J. Y.; Zhao, H.; Yuan, C.; Huang, L.; Chen, M.; Dou, L. Dimensionality Engineering of Lead Organic Chalcogenide Semiconductors. *J Am Chem Soc* **2023**, *145* (44), 23963–23971. https://doi.org/10.1021/jacs.3c05745.

(10) Khamlue, R.; Sakurada, T.; Cho, Y.; Lee, W. S.; Leangtanom, P.; Taylor, M. G.; Naewthong, W.; Sripetch, P.; Na Ranong, B.; Autila, T.; Rungseesumran, T.; Kaewkhao, J.; Sudyoadsuk, T.; Kopwitthaya, A.; Müller, P.; Promarak, V.; Kulik, H. J.; Tisdale, W. A.; Paritmongkol, W. Heterocyclic Modification Leading to Luminescent 0D Metal Organochalcogenide with Stable X-Ray Scintillating Properties. *Chemistry of Materials* **2024**, *36* (10), 5238–5240. https://doi.org/10.1021/acs.chemmater.4c00653.

(11) Hawila, S.; Massuyeau, F.; Gautier, R.; Fateeva, A.; Lebègue, S.; Kim, W. J.; Ledoux, G.; Mesbah, A.; Demessence, A. Tuning the 1D–2D Dimensionality upon Ligand Exchange in Silver Thiolate Coordination Polymers with Photoemission Switching. *J Mater Chem B* **2023**, *11* (18), 3979–3984. https://doi.org/10.1039/D3TB00537B.

(12) Okhrimenko, L.; Cibaka Ndaya, C.; Fateeva, A.; Ledoux, G.; Demessence, A. Post-Synthetic Functionalization and Ligand Exchange Reactions in Gold(<scp>i</Scp>) Phenylthiolate-Based Coordination Polymers. *New Journal of Chemistry* **2020**, *44* (41), 17970–17975. https://doi.org/10.1039/D0NJ03833D.

(13) Sakurada, T.; Cho, Y.; Paritmongkol, W.; Lee, W. S.; Wan, R.; Su, A.; Shcherbakov-Wu, W.; Müller, P.; Kulik, H. J.; Tisdale, W. A. 1D Hybrid Semiconductor Silver 2,6-Difluorophenylselenolate. *J Am Chem Soc* **2023**, *145* (9), 5183–5190. https://doi.org/10.1021/jacs.2c11896.

(14) Li, Y.; Jiang, X.; Fu, Z.; Huang, Q.; Wang, G.-E.; Deng, W.-H.; Wang, C.; Li, Z.; Yin, W.; Chen, B.; Xu, G. Coordination Assembly of 2D Ordered Organic Metal Chalcogenides with Widely Tunable Electronic Band Gaps. *Nat Commun* **2020**, *11* (1), 261. https://doi.org/10.1038/s41467-019-14136-8.

(15) Veselska, O.; Dessal, C.; Melizi, S.; Guillou, N.; Podbevšek, D.; Ledoux, G.; Elkaim, E.; Fateeva, A.; Demessence, A. New Lamellar Silver Thiolate Coordination Polymers with Tunable Photoluminescence Energies by Metal Substitution. *Inorg Chem* **2019**, *58* (1), 99–105. https://doi.org/10.1021/acs.inorgchem.8b01257.

(16) Ke, F.; Zhou, C.; Zheng, M.; Li, H.; Bao, J.; Zhu, C.; Song, Y.; Xu, W. W.; Zhu, M. The Alloying-Induced Electrical Conductivity of Metal–Chalcogenolate Nanowires. *Chemical Communications* **2021**, *57* (70), 8774–8777. https://doi.org/10.1039/D1CC01849C.

(17) Nagaraju Myakala, S.; Rabl, H.; Schubert, J. S.; Batool, S.; Ayala, P.; Apaydin, D. H.; Cherevan, A.; Eder, D. MOCHAs: An Emerging Class of Materials for Photocatalytic H $_2$ Production. *Small* **2024**. https://doi.org/10.1002/smll.202400348.

(18) Schriber, E. A.; Paley, D. W.; Bolotovsky, R.; Rosenberg, D. J.; Sierra, R. G.; Aquila, A.; Mendez, D.; Poitevin, F.; Blaschke, J. P.; Bhowmick, A.; Kelly, R. P.; Hunter, M.; Hayes, B.; Popple, D. C.; Yeung, M.; Pareja-Rivera, C.; Lisova, S.; Tono, K.; Sugahara, M.; Owada, S.; Kuykendall, T.; Yao, K.; Schuck, P. J.; Solis-Ibarra, D.; Sauter, N. K.; Brewster, A. S.; Hohman, J. N. Chemical Crystallography by Serial Femtosecond X-Ray Diffraction. *Nature* **2022**, *601* (7893), 360–365. https://doi.org/10.1038/s41586-021-04218-3.

(19) Maserati, L.; Refaely-Abramson, S.; Kastl, C.; Chen, C. T.; Borys, N. J.; Eisler, C. N.; Collins, M. S.; Smidt, T. E.; Barnard, E. S.; Strasbourg, M.; Schriber, E. A.; Shevitski, B.; Yao, K.; Hohman, J. N.; Schuck, P. J.; Aloni, S.; Neaton, J. B.; Schwartzberg, A. M. Anisotropic 2D Excitons Unveiled in Organic–Inorganic Quantum Wells. *Mater Horiz* **2021**, *8* (1), 197–208. https://doi.org/10.1039/C9MH01917K.

(20) Rabl, H.; Myakala, S. N.; Rath, J.; Fickl, B.; Schubert, J. S.; Apaydin, D. H.; Eder, D. Microwave-Assisted Synthesis of Metal-Organic Chalcogenolate Assemblies as Electrocatalysts for Syngas Production. *Commun Chem* **2023**, *6* (1), 43. https://doi.org/10.1038/s42004-023-00843-3.

(21) Lee, W. S.; Cho, Y.; Powers, E. R.; Paritmongkol, W.; Sakurada, T.; Kulik, H. J.; Tisdale, W. A. Light Emission in 2D Silver Phenylchalcogenolates. *ACS Nano* **2022**, *16* (12), 20318–20328. https://doi.org/10.1021/acsnano.2c06204.

(22) Jiang, H.; Cao, L.; Li, Y.; Li, W.; Ye, X.; Deng, W.; Jiang, X.; Wang, G.; Xu, G. Organic "Receptor" Fully Covered Few-Layer Organic–Metal Chalcogenides for High-Performance Chemiresistive Gas Sensing at Room Temperature. *Chemical Communications* **2020**, *56* (40), 5366–5369. https://doi.org/10.1039/D0CC01092H.

(23) Maserati, L.; Prato, M.; Pecorario, S.; Passarella, B.; Perinot, A.; Thomas, A. A.; Melloni, F.; Natali, D.; Caironi, M. Photo-Electrical Properties of 2D Quantum Confined Metal–Organic Chalcogenide Nanocrystal Films. *Nanoscale* **2021**, *13* (1), 233–241. https://doi.org/10.1039/D0NR07409H.

(24) Paritmongkol, W.; Lee, W. S.; Shcherbakov-Wu, W.; Ha, S. K.; Sakurada, T.; Oh, S. J.; Tisdale, W. A. Morphological Control of 2D Hybrid Organic–Inorganic Semiconductor AgSePh. *ACS Nano* **2022**, *16* (2), 2054–2065. https://doi.org/10.1021/acsnano.1c07498.

(25) Ye, C.; Li, Z.; Chang, Z.; Wu, S.; Sun, Y.; Xu, W. Dual-Emission 2D Blue Luminescent Organic Silver Chalcogenide for Highly Selective Pb^{2+} Detection in an Aqueous Medium. *Inorg Chem* **2023**, *62* (5), 2334–2341. https://doi.org/10.1021/acs.inorgchem.2c04113.

(26) Schriber, E. A.; Popple, D. C.; Yeung, M.; Brady, M. A.; Corlett, S. A.; Hohman, J. N. Mithrene Is a Self-Assembling Robustly Blue Luminescent Metal–Organic Chalcogenolate Assembly for 2D Optoelectronic Applications. *ACS Appl Nano Mater* **2018**, *1* (7), 3498–3508. https://doi.org/10.1021/acsanm.8b00662.

(27) Low, K.-H.; Li, C.-H.; Roy, V. A. L.; Chui, S. S.-Y.; Chan, S. L.-F.; Che, C.-M. Homoleptic Copper(i) Phenylselenolate Polymer as a Single-Source Precursor for Cu2Se Nanocrystals. Structure, Photoluminescence and Application in Field-Effect Transistor. *Chem Sci* **2010**, *1* (4), 515. https://doi.org/10.1039/c0sc00212g.

(28) Das, A. K.; Biswas, S.; Kayal, A.; Reber, A. C.; Bhandary, S.; Chopra, D.; Mitra, J.; Khanna, S. N.; Mandal, S. Two-Dimensional Silver-Chalcogenolate-Based Cluster-Assembled Material: A *p* -Type Semiconductor. *Nano Lett* **2023**, *23* (19), 8923–8931. https://doi.org/10.1021/acs.nanolett.3c02269.

(29) Trang, B.; Yeung, M.; Popple, D. C.; Schriber, E. A.; Brady, M. A.; Kuykendall, T. R.; Hohman, J. N. Tarnishing Silver Metal into Mithrene. *J Am Chem Soc* **2018**, *140* (42), 13892–13903. https://doi.org/10.1021/jacs.8b08878.

(30) Paritmongkol, W.; Sakurada, T.; Lee, W. S.; Wan, R.; Müller, P.; Tisdale, W. A. Size and Quality Enhancement of 2D Semiconducting Metal–Organic Chalcogenolates by Amine Addition. *J Am Chem Soc* **2021**, *143* (48), 20256–20263. https://doi.org/10.1021/jacs.1c09106.

(31) Cuthbert, H. L.; Wallbank, A. I.; Taylor, N. J.; Corrigan, J. F. Synthesis and Structural Characterization of [Cu20Se4(M3-SePh)12(PPh3)6] and [Ag(SePh)]∞. *Z Anorg Allg Chem* **2002**, *628* (11), 2483–2488. https://doi.org/10.1002/1521-3749(200211)628:11<2483::AID-ZAAC2483>3.0.CO;2-U.

(32) Powers, E. R.; Paritmongkol, W.; Yost, D. C.; Lee, W. S.; Grossman, J. C.; Tisdale, W. A. Coherent Exciton-Lattice Dynamics in a 2D Metal Organochalcogenolate Semiconductor. *Matter* **2024**, *7* (4), 1612–1630. https://doi.org/10.1016/j.matt.2024.01.033.

(33) Kastl, C.; Schwartzberg, A. M.; Maserati, L. Picoseconds-Limited Exciton Recombination in Metal–Organic Chalcogenides Hybrid Quantum Wells. *ACS Nano* **2022**, *16* (3), 3715–3722. https://doi.org/10.1021/acsnano.1c07281.

(34) Kastl, C.; Bonfà, P.; Maserati, L. Anharmonic Exciton-Phonon Coupling in Metal-Organic Chalcogenides Hybrid Quantum Wells. *Adv Opt Mater* **2023**, *11* (7). https://doi.org/10.1002/adom.202202213.

(35) Yao, K.; Collins, M. S.; Nell, K. M.; Barnard, E. S.; Borys, N. J.; Kuykendall, T.; Hohman, J. N.; Schuck, P. J. Strongly Quantum-Confined Blue-Emitting Excitons in Chemically Configurable Multiquantum Wells. *ACS Nano* **2021**, *15* (3), 4085–4092. https://doi.org/10.1021/acsnano.0c08096.

(36) Paritmongkol, W.; Dahod, N. S.; Stollmann, A.; Mao, N.; Settens, C.; Zheng, S.-L.; Tisdale, W. A. Synthetic Variation and Structural Trends in Layered Two-Dimensional Alkylammonium Lead Halide Perovskites. *Chemistry of Materials* **2019**, *31* (15), 5592–5607. https://doi.org/10.1021/acs.chemmater.9b01318.

(37) Lavenn, C.; Okhrimenko, L.; Guillou, N.; Monge, M.; Ledoux, G.; Dujardin, C.; Chiriac, R.; Fateeva, A.; Demessence, A. A Luminescent Double Helical Gold(I)–Thiophenolate Coordination Polymer Obtained by Hydrothermal Synthesis or by Thermal Solid-State Amorphous-to-Crystalline Isomerization. *J Mater Chem C Mater* **2015**, *3* (16), 4115–4125. https://doi.org/10.1039/C5TC00119F.

(38) Marsh, R. E. Some Thoughts on Choosing the Correct Space Group. *Acta Crystallogr B* **1995**, *51* (6), 897–907. https://doi.org/10.1107/S0108768195008901.

(39) Kubelka, P.; Munk, F. An Article on Optics of Paint Layers. *Z. Tech. Phys* **1931**, *12*, 259–274.

(40) Sheldrick, G. M. SHELXT – Integrated Space-Group and Crystal-Structure Determination. *Acta Crystallogr A Found Adv* **2015**, *71* (1), 3–8. https://doi.org/10.1107/S2053273314026370.

(41) Sheldrick, G. M. Crystal Structure Refinement with SHELXL. *Acta Crystallogr C Struct Chem* **2015**, *71* (1), 3–8. https://doi.org/10.1107/S2053229614024218.

(42) Müller, P. Practical Suggestions for Better Crystal Structures. *Crystallogr Rev* **2009**, *15* (1), 57–83. https://doi.org/10.1080/08893110802547240.

Chapter 5

Light emission in 2D AgSePh and 2D AgTePh

The basis of this chapter has been published as:
Woo Seok Lee, Yeongsu Cho, Eric R. Powers, Watcharaphol Paritmongkol, Tomoaki Sakurada, Heather J. Kulik, William A. Tisdale. "Light Emission in 2D Silver Phenylchalcogenolates" *ACS Nano* **2022**, 16, 20318-20328.

5.1 Abstract

Silver phenylchalcogenolate (AgSePh – also known as "mithrene") and silver phenyltellurolate (AgTePh – also known as "tethrene") are two-dimensional (2D) van der Waals semiconductors belonging to an emerging class of hybrid organic-inorganic materials called metal-organic chalcogenolates. Despite having the same crystal structure, AgSePh and AgTePh exhibit strikingly different excitonic behavior. Whereas AgSePh exhibits narrow, fast luminescence with minimal Stokes shift, AgTePh exhibits comparatively slow luminescence that is significantly broadened and red-shifted from its absorption minimum. In this chapter, using time-resolved and temperature-dependent absorption and emission micro-spectroscopy, combined with sub-gap photoexcitation studies, we show that exciton dynamics in AgTePh films are dominated by intrinsic self-trapping behavior, whereas dynamics in AgSePh films are dominated by interaction of band-edge excitons with a finite number of extrinsic defect/trap states. Density functional theory calculations reveal that AgSePh has simple parabolic band edges with a direct gap at Γ whereas AgTePh has a saddle point at Γ with a horizontal splitting along Γ-N_1 direction. Correlation between the unique band structure of AgTePh and exciton self-trapping behavior is unclear, prompting further exploration of excitonic phenomena in this emerging class of hybrid 2D semiconductors.

5.2 Introduction

Two-dimensional (2D) semiconductors, including transition metal dichalcogenides (TMDs) and 2D halide perovskites, have attracted attention due to strong charge-charge and light-matter

interactions.[1–8] The atomically thin morphology leads to reduced dielectric screening and strong quantum confinement for charge carriers, resulting in the formation of excitons with binding energies up to hundreds of meV.[9–12] In 2D semiconductors, excitonic phenomena dominate the optical response at room temperature, leading to strong absorption, emission and nonlinear optical responses due to enhanced light-matter interaction.[13–17] Consequently, these materials have been envisioned for use in optoelectronic applications such as light-emitting diodes, lasers, solar cells and photo-detectors.[18–21]

2D metal organochalcogenolates (MOCs) – also referred to as metal-organic chalcogenides – are an emerging class of hybrid organic-inorganic 2D semiconductors.[22–28] Similar to TMDs and 2D perovskites, 2D MOCs crystallize in the form of three-dimensional solids consisting of 2D layers bound together by interlayer van der Waals forces (Figure 5.1a).[25] Each 2D layer consists of an inorganic sheet sandwiched by organic ligands, which are covalently bonded to the inorganic sheet. The presence of organic ligands, which decouple electronic interactions between inorganic layers, distinguish 2D MOCs from TMDs, which exhibit layer-dependent electronic properties.[7,29] Furthermore, 2D MOCs are distinguished from 2D perovskites by the covalent nature of bonding between organic and inorganic components, which allows chemical stability in air and solvents[30] and enables electronic bandgap tuning via organic ligand modification.[31]

Among the 2D MOCs reported so far, silver phenylchalcogenolate (AgSePh) – also known as "mithrene" – has attracted the most attention due to its natural blue (~467 nm) emission.[29,32–43] Recently, it was shown that silver phenyltellurolate (AgTePh) – known as "tethrene" – also crystallizes into a 2D structure at room temperature with the same monoclinic centrosymmetric space group $P2_1/c$ as AgSePh.[39] (Note that AgSePh and AgTePh have also been reported in the $C2/c$ structure,[32,36] which is very similar in structure to $P2_1/c$) However, AgTePh exhibits strikingly different optical behavior from AgSePh despite the structural and compositional similarity, implying a different physical mechanism underlying light emission in AgTePh.

Here, we investigate light emission in AgSePh and AgTePh thin films using time-resolved and temperature-dependent optical spectroscopy. AgTePh exhibited a single broad, Stokes-shifted emission feature as the sample was cooled from room temperature (300 K) to cryogenic conditions (5 K). As the AgTePh sample was cooled, the photoluminescence (PL) lifetime increased from ~1.5 ns at 300 K to >100 ns at 5 K, while the PL quantum yield (QY) increased from <1% at 300

K to ~100% at 5 K. In contrast, AgSePh exhibited a largely temperature-independent PL lifetime of ~70 ps and did not exhibit any broadband emission signatures until the sample was cooled below 200 K. These temperature-dependent observations, combined with sub-gap and power-dependent photoexcitation experiments, suggest that intrinsic exciton self-trapping dominates excitonic behavior in AgTePh, whereas exciton dynamics in AgSePh are dominated by interaction of free-excitons with extrinsic defects/trap states. Density functional theory (DFT) calculations revealed that AgSePh has a direct gap at Γ with simple parabolic band edges whereas AgTePh has a saddle point at Γ with a horizontal splitting along Γ-N_1 direction. Correlation between exciton self-trapping behavior and the unique band structures of AgTePh is unclear in that both valence band maximum (VBM) and conduction band minimum (CBM) in AgTePh are two-dimensionally dispersive [(m_h*, m_e*) = ($1.05m_o$, $1.08m_o$) along BM → Γ, ($1.24m_o$, $0.70m_o$) along BM → N_1, and ($0.52m_o$, $0.64m_o$) along BM → BM±k_y]. Overall, we discuss possible origins of these observations and highlight some of the fundamental questions in this emerging class of 2D semiconductors.

5.3 Results and Discussion

5.3.1 Structural and optical properties

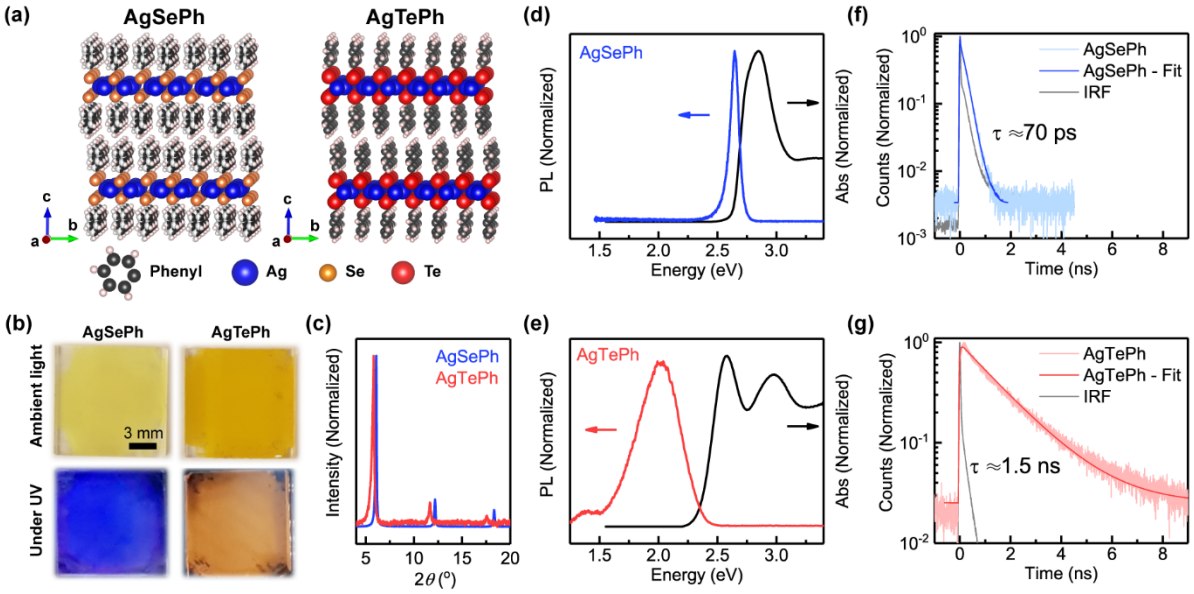

Figure 5.1 Structural and optical properties of AgSePh and AgTePh thin films. (a) Layered 2D structures of AgSePh and AgTePh. (b) Photographs of AgSePh and AgTePh films under ambient light (top) and 365 nm light-emitting diode excitation (bottom). The bottom images were taken through a 450 nm long-pass filter to remove scattering from the excitation light. (c) X-ray diffractograms of AgSePh and AgTePh films. (d, e) Absorption and emission spectra of AgSePh and AgTePh films at room temperature. (f, g) Time-resolved photoluminescence of AgSePh and AgTePh films. IRF denotes the instrument response function of the measurement instrument.

Silver phenylselenolate (AgSePh) and silver phenyltellurolate (AgTePh) films were prepared by a vapor-phase chemical transformation method.[34,35] Briefly, a 15 nm thick Ag film was deposited on a glass substrate by thermal evaporation, and then the silver-coated glass slide was placed inside a sealed pressure vessel containing deionized water and diphenyl diselenide (Ph_2Se_2) or diphenyl ditelluride (Ph_2Te_2) powder. After heating the vessel to 100°C for 3~4 days, the Ag film was transformed into a light yellow AgSePh film or a deep yellow AgTePh film (Figure 5.1b).

The structural and morphological properties of AgSePh and AgTePh films were investigated using powder X-ray diffraction (XRD) and scanning electron microscopy (SEM). Both AgSePh and AgTePh films showed evenly spaced (00*h*) XRD peaks below 20°

corresponding to the stacking periodicity of ~1.45 nm and ~1.52 nm, respectively (Figure 5.1c). SEM micrographs reveal a micro-crystalline morphology in both samples (Figure 5.2). AgSePh crystals are ~500 nm in size and aligned mostly parallel to the substrate, while AgTePh crystals are ~200 nm in size and randomly oriented.

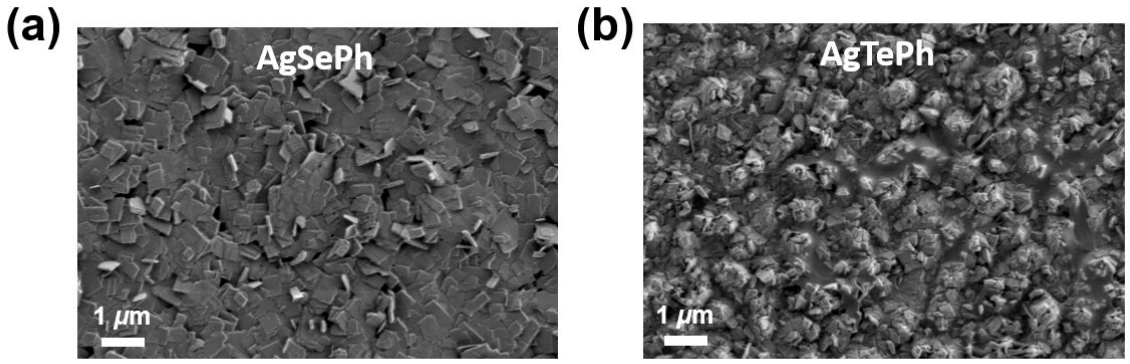

Figure 5.2 Scanning electron micrographs of (a) AgSePh and (b) AgTePh films.

Absorption spectra of AgSePh and AgTePh films at room temperature were collected using an integrating sphere accessory to suppress contributions from scattered light to the measured absorption spectrum (Figure 5.3). While this configuration improves the accuracy of the absorption measurement by collecting forward scattered light, it does not account for backscattered light – especially in microcrystalline films where the crystallite size is close to the wavelength of light.

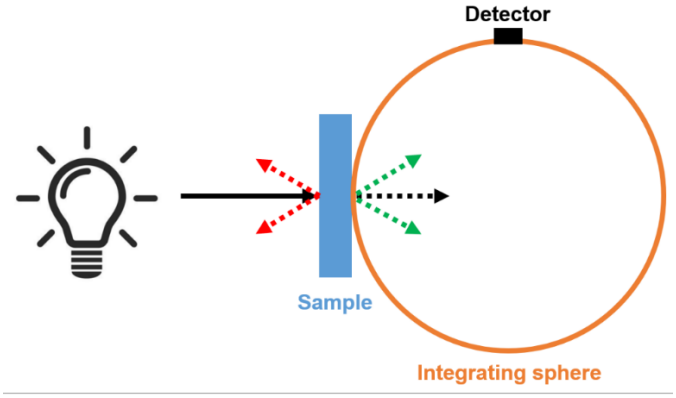

Figure 5.3 Schematic of room-temperature absorption measurement using the integrating sphere attachment (Agilent, Internal DRA 2500) for the Agilent Cary 5000 Spectrophotometer. Black

solid line, black dashed line, green dashed line, and red dashed line represent incident light, transmitted light, forward scattered light, and backscattered light, respectively.

Temperature-dependent absorption measurements can help distinguish true absorption signals from light scattering. Whereas actual electronic resonances in materials (including optical transitions at defects) will shift in wavelength, linewidth and intensity with changing temperature, light scattering due to sample morphology will be largely temperature-independent. In Figure 5.4, we show the temperature-dependent "apparent" absorption spectra of AgSePh and AgTePh films collected in transmission mode in an upright tower cryostat (Janis ST-100). The invariance of the long-wavelength scattering signal with temperature (beyond 510 nm in AgSePh and beyond 560 nm in AgTePh) confirms that this signal originates from scattering. Moreover, the sub-bandgap signal is heavily suppressed when the same measurement is performed with an integrating sphere (Figure 5.5).

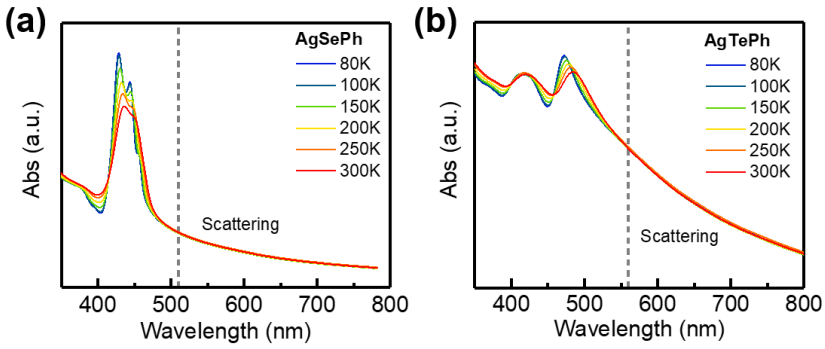

Figure 5.4 Temperature-dependent absorption spectra of (a) AgSePh and (b) AgTePh films collected in transmission mode in an upright tower cryostat (Janis ST-100).

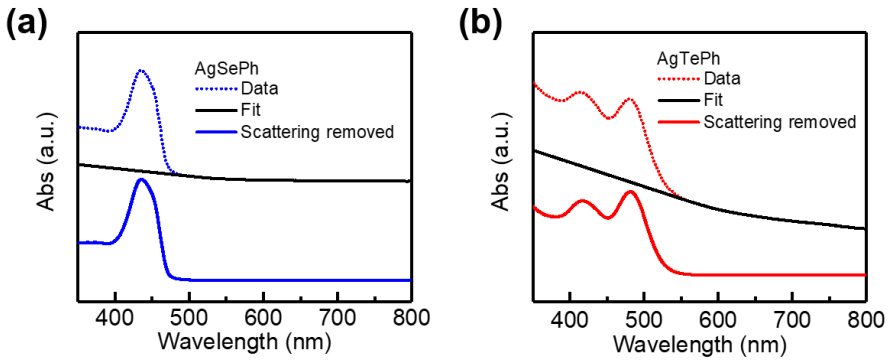

Figure 5.5 Scattering-suppressed absorption spectra measured at room temperature using an integrating sphere, and further removal of residual scattering contributions by extrapolating the sub-band gap signal.

We use a simple heuristic expression to account for scattering contributions to the measured raw absorption spectrum,

$$A = a \cdot \lambda + b, \tag{5.1}$$

where a and b are fitting constants. a and b were extracted from tangent lines at 510 nm for the AgSePh film and at 560 nm for the AgTePh film. Then, scattering removed absorption spectra in short wavelengths (below 510 nm for the AgSePh film and below 560 nm for the AgTePh film) were acquired by subtracting the linear fit from the raw data. For long wavelengths where the absorption did not show temperature-dependence, the intensity of scattering removed absorption was set to be zero.

Scattering-corrected absorption and photoluminescence spectra of AgSePh and AgTePh films are shown in Figure 5.1d and 5.1e. The room-temperature absorption spectrum of the AgSePh film shows two overlapping absorption peaks at 2.87 and 2.74 eV. When the temperature was reduced to 80 K, these two peaks blue-shifted to 2.91 (X_3) and 2.79 eV (X_2) and a new peak became resolvable at the lowest energy of 2.72 eV (X_1) (Figure 5.6a). These three optical transitions were previously assigned to three distinct excitonic states having an exciton binding energy of approximately 350 meV, with X_2 oriented perpendicular to X_1/X_3 within the 2D plane.[36]

The AgSePh film exhibited narrow photoluminescence (PL) centered around 2.65 eV with a full-width-at-half-maximum (FWHM) of ~10 meV at room temperature (Figure 5.1d). The PL

emission peak is close in energy to the X_1 absorption resonance, and the corresponding Stokes shift decreased from Δ_{SS} = 22.8 ± 5.7 meV at room temperature to Δ_{SS} = 1.9 ± 5.9 meV at 80 K (Figures 5.6c, 5.6e and 5.12). Because of the small Stokes shift and close tracking of the PL and absorption spectrum with temperature (Figures 5.6c and 5.8a), we assign light emission in AgSePh to band-edge "free" exciton emission. (Following convention, we described electron-hole pairs whose wavefunction is strongly delocalized over a few unit cells and which can move freely inside the crystal as "free-excitons" whereas excitons localized at defects or lattice sites as "bound excitons".) The PL decay of the AgSePh film at room temperature was well fit by a single exponential decay function convolved with the instrument response function (IRF), with an extracted PL lifetime of ~70 ps (Figure 5.1f).[44]

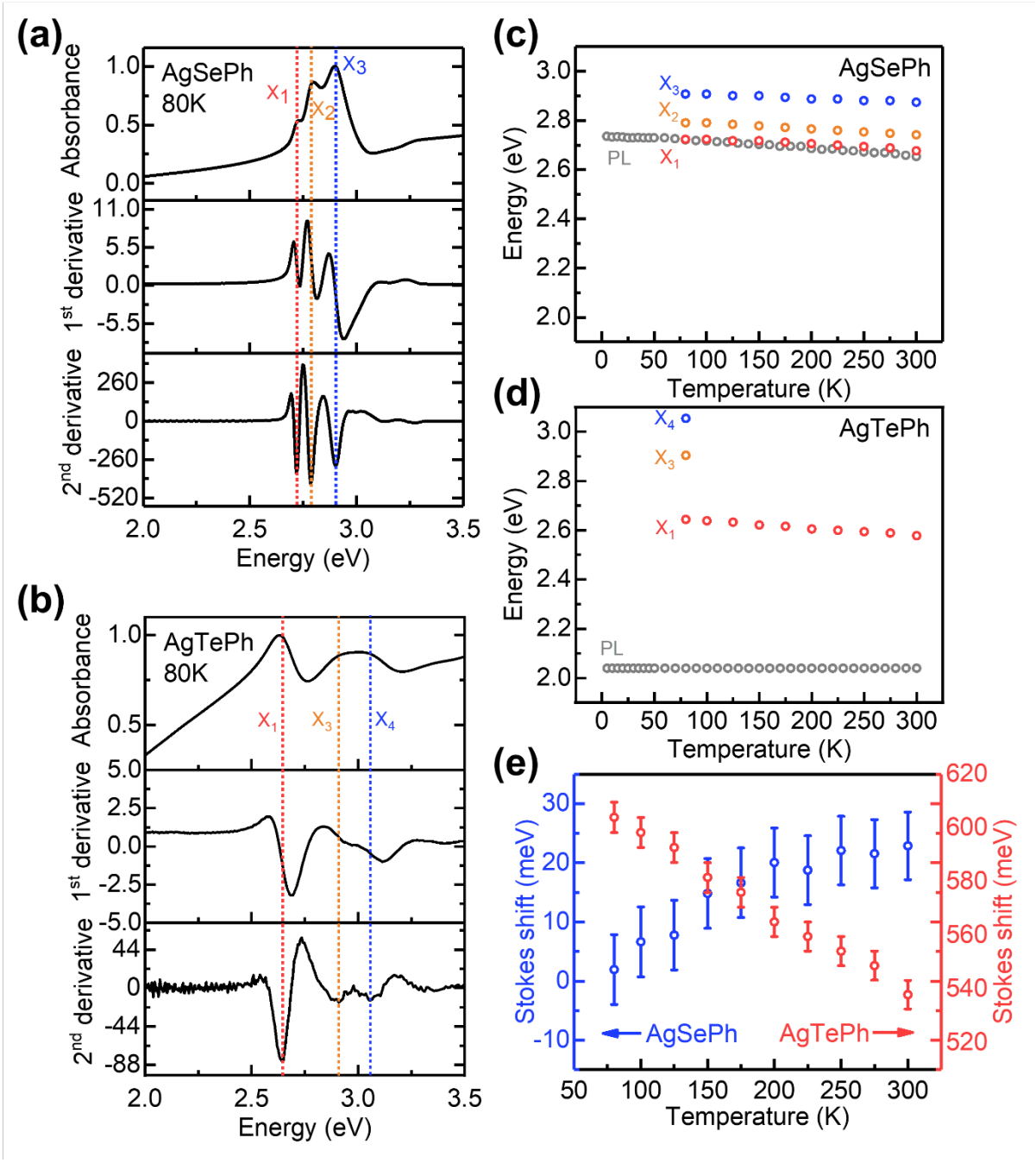

Figure 5.6 Absorption spectrum of (a) AgSePh and (b) AgTePh films at 80 K. Three absorption peaks are labeled X_1, X_2, and X_3 for AgSePh, and X_1, X_3, and X_4 for AgTePh. The reason why excitonic transitions in AgTePh are labelled as X_1, X_3, and X_4, instead of X_1, X_2, and X_3 will be explained in the Chapter 6. These spectra have not been corrected for light scattering. (c, d) X_n (n = 1,2,3, or 4) and PL peak positions as a function of temperature for (c) AgSePh and (d) AgTePh films. Note that X_3 and X_4 are strongly overlapping in the AgTePh spectrum and could not be distinguished above 100 K (Figures 5.4 and 5.7). (e) Temperature-dependent Stokes shift for AgSePh and AgTePh films. The error bars represent the uncertainty of wavelength calibration in the absorption and photoluminescence measurement (1.0 nm).

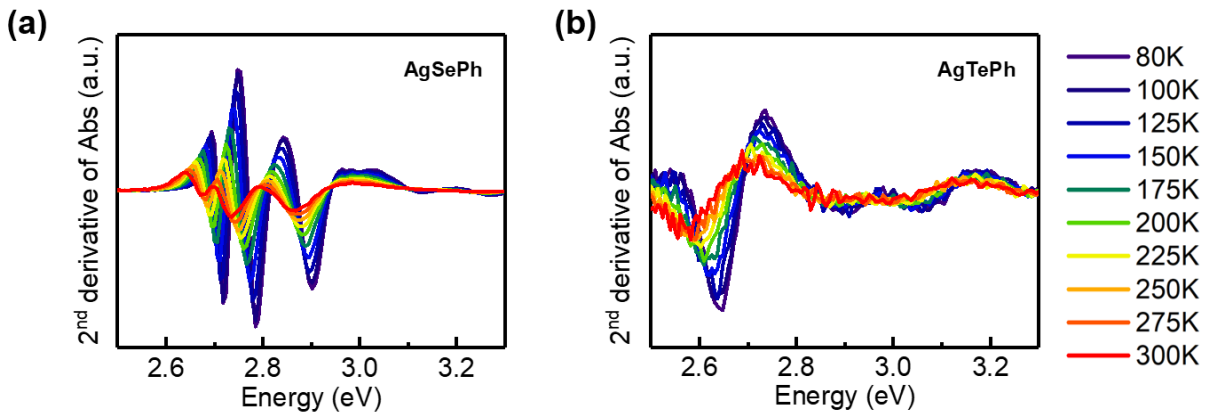

Figure 5.7 The second derivative of absorption spectrum of AgSePh and AgTePh films as a function of temperature.

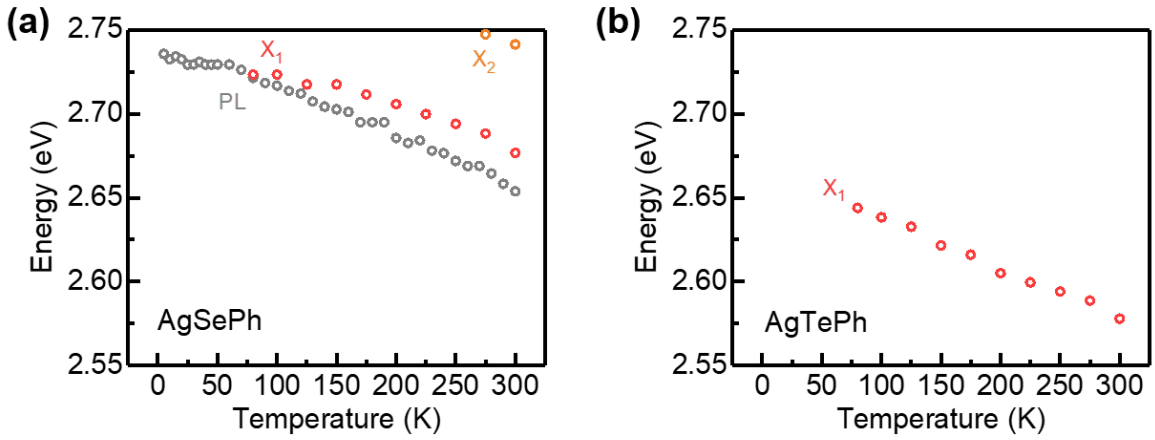

Figure 5.8 Excitonic absorption resonance peaks and photoluminescence peak positions as a function of temperature for (a) AgSePh and (b) AgTePh films. (Enlarged figures of Figure 5.6c and 5.6d)

The AgTePh film also showed two absorption peaks at room temperature, but with much larger energetic separation, positioned at 2.97 eV and 2.58 eV. When the temperature was reduced to 80 K, the AgTePh film also revealed three distinct absorption peaks positioned at 3.06 (X_4), 2.91 (X_3), and 2.65 eV (X_1) (Figure 2b). (The reason why excitonic transitions in AgTePh are labelled as X_1, X_3, and X_4, instead of X_1, X_2, and X_3 will be explained in the Chapter 6) As in AgSePh, the energies of these excitonic transitions blue-shifted with decreasing temperature

(Figure 5.6c,d). However, the AgTePh film exhibited significantly broader PL centered at 2.04 eV with a FWHM of ~420 meV. Moreover, the PL peak emission wavelength was invariant with temperature, leading to a Stokes shift that actually increased as the sample temperature decreased from $\Delta_{SS} \approx 540$ meV at room temperature to $\Delta_{SS} \approx 600$ meV at 80 K (Figures 5.6d, 5.6e and 5.12). The AgTePh PL decay at room temperature was also fit well by a single exponential decay function convolved with the IRF, but with an extracted PL lifetime of ~1.5 ns (Figure 5.1g).

Given the similarities in structure, composition, and absorption characteristics of AgSePh and AgTePh, the differences between their light emission characteristics is striking. Both materials crystallize in the same monoclinic $P2_1/c$[39] (or *C2/c* structure)[32] and form 2D layered van der Waals solids. In addition, both materials exhibit three distinct excitonic absorption resonances. However, whereas the three excitonic absorption resonances in the AgSePh film are close in energy, the AgTePh film exhibit much larger energetic separation between X_1 and X_3. More strikingly, whereas AgSePh exhibits narrow, fast luminescence with minimal Stokes shift, AgTePh exhibits comparatively slow luminescence that is significantly broadened and red-shifted from its absorption minimum, and which does not track the band gap energy with changing temperature.

5.3.2 Electronic band structure calculations

Electronic dispersion in AgSePh and AgTePh was calculated using approximate density functional theory (DFT) with the PBE functional and semi-empirical DFT-D2 correction to ensure van der Waals interactions were captured. Fully relativistic calculations were performed to incorporate the strong spin-orbit coupling of Te. These calculations used the reported monoclinic *C2/c* structures[32] of AgSePh and AgTePh (see Figure 5.10 for calculation in the $P2_1/c$ space group[39] and the Chapter 7). The calculated band structure with the projected density of states are shown in Figure 5.9a,d. The density of states results show that the bands of AgSePh and AgTePh have largely similar orbital contributions. The valence band is primarily comprised of chalcogen p orbitals and Ag d orbitals. The conduction band is dominated by C p orbitals, except near the conduction band minimum where the Ag s orbital, Ag p orbital, and chalcogen p orbital become more important. A distinct difference between AgSePh and AgTePh appears at the valence band maximum (VBM) and conduction band minimum (CBM). Whereas AgSePh has a simple parabola with a direct gap at Γ, AgTePh has a saddle point at Γ with a horizontal splitting in the x direction

(Γ-N_1 direction). The momentum of the VBM and CBM in AgTePh differ by only 0.04 $Å^{-1}$, and the indirect gap is only 11 meV smaller than the direct gap, leading to an *effectively* direct band gap (Figure 5.11). The difference in the band shape leads to a large 0.30 eV difference in the band gap, i.e., 1.33 eV for AgSePh and 1.63 eV for AgTePh, neglecting correlation effects. Electron and hole at the band edges of AgSePh and AgTePh have similar effective mass (Table 5.1).

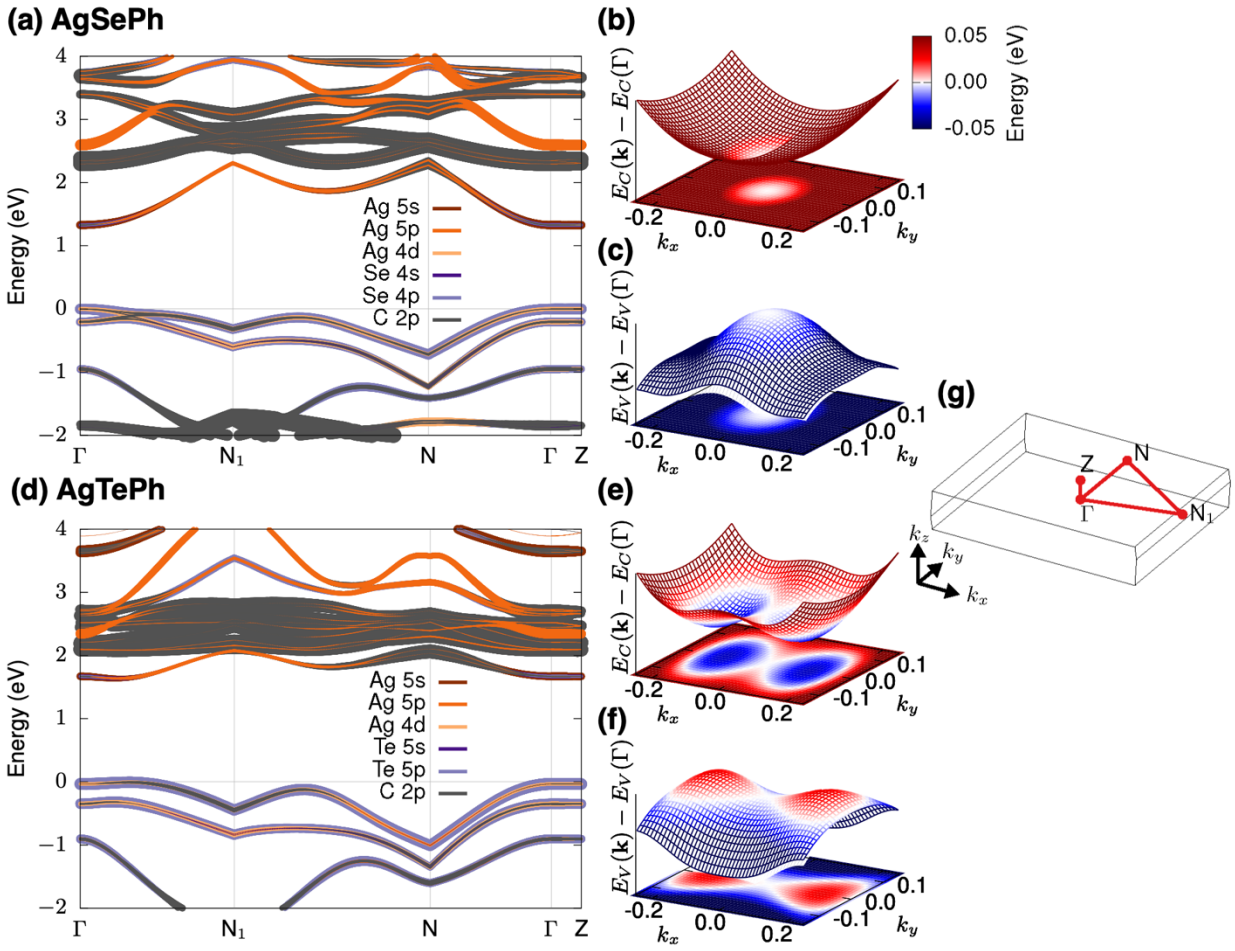

Figure 5.9 Density functional theory (DFT)-calculated band structure and density of states of (a) AgSePh and (d) AgTePh in *C2/c* space group. The color and width of the line indicates the type and contribution of each orbital to the band, respectively. Detailed shape of the conduction band minimum (b,e) and the valence band maximum (c,f) on Γ-N_1-N plane. The axes are fractions of the reciprocal lattice vector. Note that the high symmetry points are selected from the conventional lattice for the band structure instead of the primitive lattice. (g) Brillouin zone of the conventional lattice. Effective mass of hole and electron at the band edges of AgSePh and AgTePh are presented in Table 5.1.

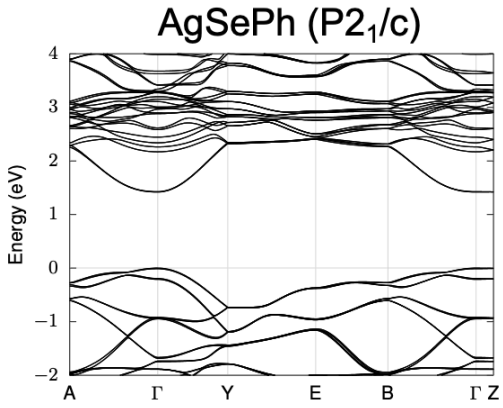

Figure 5.10 Band structure of AgSePh in $P2_1/c$ space group calculated with DFT using PBE functional and the DFT-D2 correction.

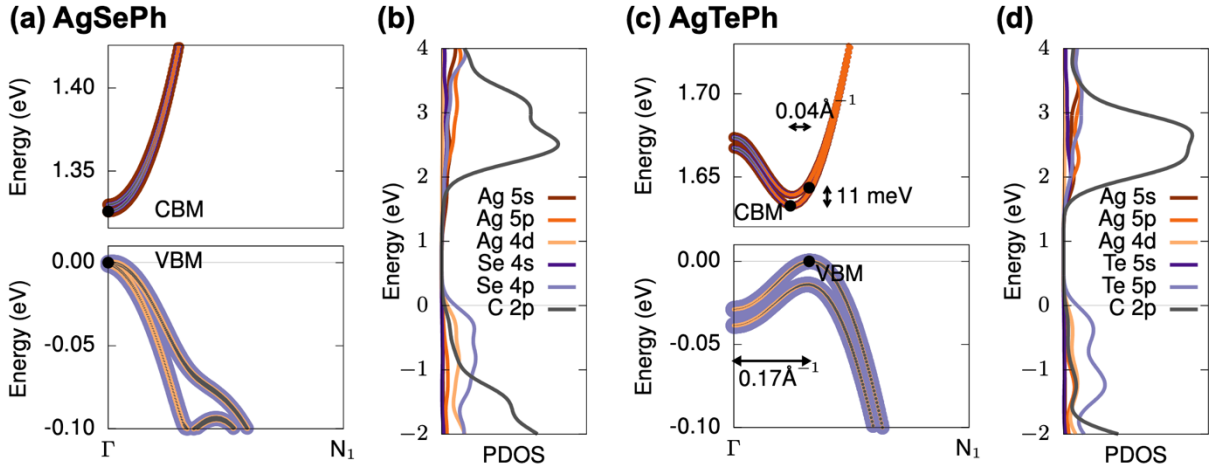

Figure 5.11 Enlarged conduction band minimum (CBM), valence band maximum (VBM), and projected density of states (PDOS) of (a,b) AgSePh and (c,d) AgTePh. The color and width of the line indicates the type and contribution of each orbital to the band, respectively.

Table 5.1 Effective mass of hole and electron at the band edges of AgSePh and AgTePh in the unit of the true electron mass. BM stands for the valence band maximum and conduction band minimum as specified in Figure 5.11.

AgSePh (*C2/c*)	Hole	Electron	AgTePh (*C2/c*)	Hole	Electron
$\Gamma \rightarrow N_1$	1.14	1.28	$BM \rightarrow N_1$	1.05	0.64
$\Gamma \rightarrow N$	0.77	0.42	$BM \rightarrow \Gamma$	1.24	0.70
AgSePh ($P2_1/c$)	Hole	Electron	$BM \rightarrow BM \pm k_y$	0.52	0.64
$\Gamma \rightarrow A$	0.69	1.00	$\Gamma \rightarrow N$	0.50	1.08
$\Gamma \rightarrow Y$	0.37	0.25			

5.3.3 Temperature-, location, and power-dependent photoluminescence micro-spectroscopy

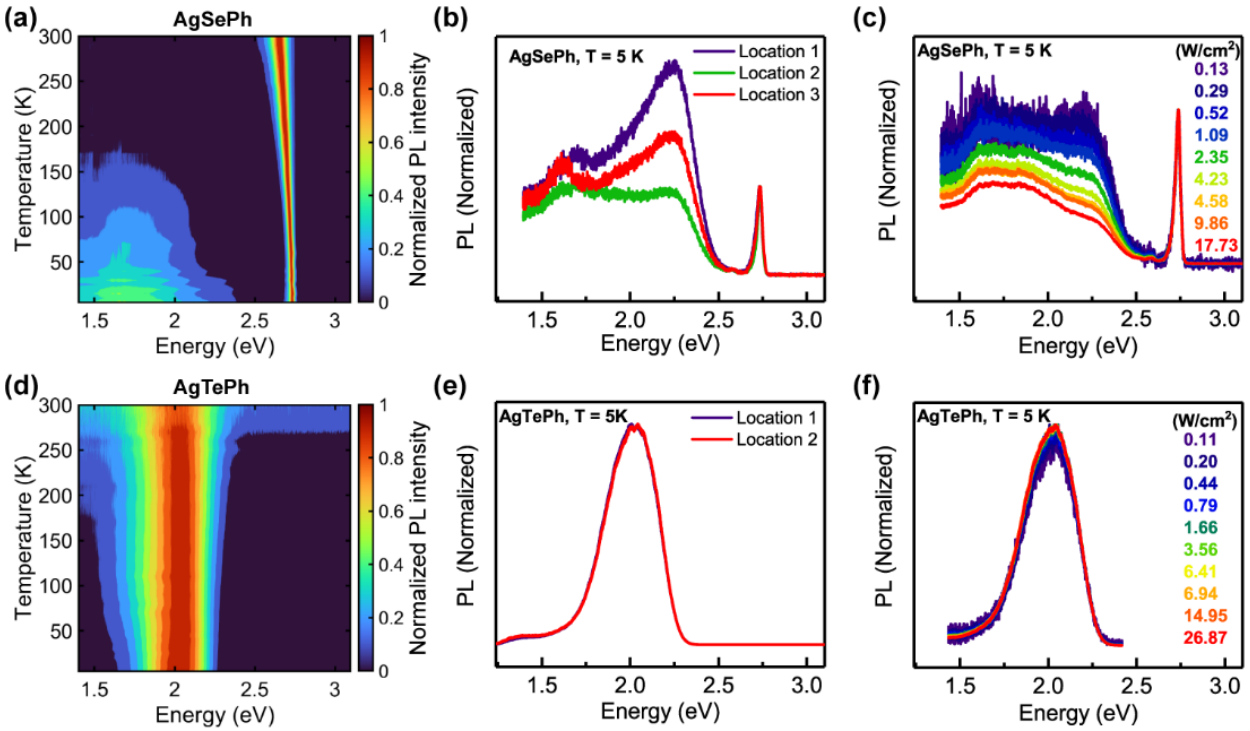

Figure 5.12 Temperature-, location-, power-dependent photoluminescence (PL) spectroscopy. (a, d) Temperature-dependent normalized PL spectra of AgSePh and AgTePh films. (b, e) Location-dependent PL spectra of AgSePh and AgTePh films at 5 K. (c, f) Power-dependent PL spectra of AgSePh and AgTePh films at 5 K.

To investigate light emission in AgSePh and AgTePh films, we measured the PL spectra of AgSePh and AgTePh films as a function of temperature from 5 K to 300 K as shown in Figure 5.12a,d. The samples were mounted under vacuum in a microscopy cryostat and excited by 405 nm light focused to ~1 μm spot on the sample surface, from either a variable repetition rate pulsed/CW laser diode or the second harmonic of a Ti:sapphire laser (see Methods). In the case of the AgSePh film, the free-exciton emission peak at ~2.6 eV gradually blue-shifted and narrowed with decreasing temperature, tracking the temperature-dependent shifting of the lowest-energy excitonic absorption resonance (Figure 5.6c). An additional broadband emission feature was also observed below 2.5 eV at low temperatures. In contrast to AgSePh, the AgTePh film exhibited a single broadband emission feature across all temperatures studied. The broad AgTePh emission

feature became slightly narrower at lower sample temperature, but its peak position remained constant.

Broad emission with a large Stokes shift in semiconductors has historically been assigned to defects,[45–48] self-trapped excitons (STEs),[40,49–51] or indirect bandgap recombination.[44,52] Charge-transfer excitons can also lead to broadband emission in hetero-structures with type II band alignment,[53–55] but we do not expect to observe this behavior in pure AgSePh and AgTePh. To clarify the origin of broadband emission in AgSePh and AgTePh films, we performed location- and power-dependent steady-state PL micro-spectroscopy.

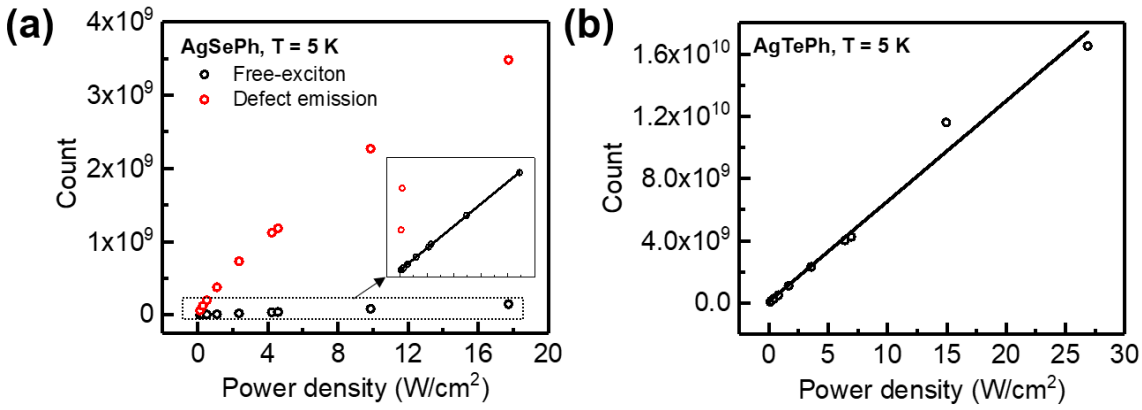

Figure 5.13 Power-dependent photoluminescence intensities of (a) AgSePh and (b) AgTePh films at 5 K. Free-exciton emission in the AgSePh film shows linear trend whereas the broad emission (defect emission) in the AgSePh film shows sublinear trend at high power densities. The broad emission in the AgTePh film shows linear trend.

Figure 5.12b,c shows the PL spectra of the AgSePh film at 5K (normalized to the intensity of the free-exciton emission feature) as a function of excitation spot location and excitation power, respectively. The spectral shape of the broad emission in AgSePh and its relative intensity to the free-exciton emission showed large location-to-location variation (Figure 5.12b). Moreover, the broad emission showed sub-linear scaling with excitation laser intensity (Figures 5.12c and 5.13a). This behavior is characteristic of extrinsic defect states, which are finite in number (*i.e.* saturable) and can exhibit spatial heterogeneity depending on local conditions during film growth.[45,48,51,56]

We note that another study recently reported a broad, low-energy spectral feature in transient absorption spectra of AgSePh films and assigned it to a self-trapped exciton (STE).[40] However, the reported photoinduced absorption feature was not observed in transient absorption measurements on our samples, and we cannot identify spectral emission from AgSePh that is characteristic of STEs. Moreover, sub-band-gap broad emission in AgSePh is suppressed in high-quality single crystals,[39] reinforcing our assignment of this feature to extrinsic defect states – rather than intrinsic behavior.

In contrast, the broad emission feature in AgTePh showed the same spectral shape regardless of location and excitation power (Figure 5.12e,f) and its intensity grew linearly with excitation laser power (Figure 5.13b). These observations indicate that the broad emission feature in AgTePh films arises from an intrinsic mechanism, such as STE or indirect recombination.[44,49]

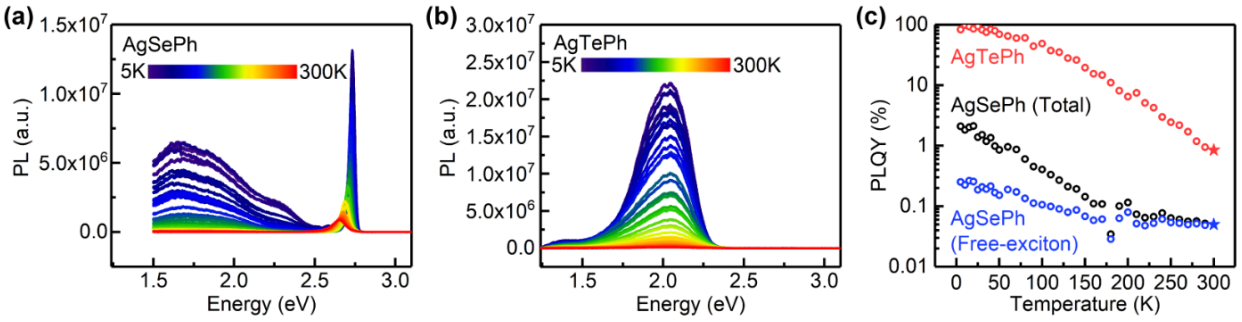

Figure 5.14 Temperature-dependent photoluminescence quantum yield (PLQY) of AgSePh and AgTePh films. (a, b) Temperature-dependent PL spectra of AgSePh and AgTePh films. (c) Temperature-dependent PLQY of free-exciton emission of the AgSePh film (blue) and overall spectrally integrated emission of AgSePh (black) and AgTePh films (red).

To further investigate the mechanisms of light emission, we measured the temperature-dependent PL quantum yield (PLQY) of AgSePh and AgTePh films (Figure 5.14). The PLQY of AgSePh and AgTePh films was first measured at room temperature using the absolute method in an integrating sphere.[57] Based on these measurements, the PLQY of AgSePh and AgTePh films at room temperature was calculated to be ~0.05% and ~0.85%, respectively (Figure 5.15). Then, the PLQY at lower sample temperatures was estimated by scaling the PLQY measured at room-

temperature by the temperature-dependent relative PL intensity, keeping all other experimental conditions constant (see Methods and Figure 5.14).

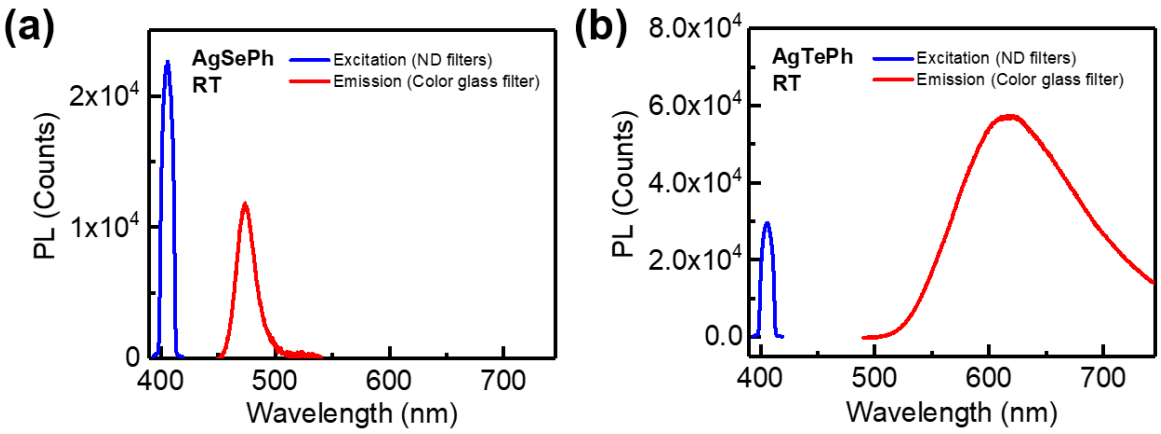

Figure 5.15 The differences of spectra in the excitation (blue) and the emission (red) regions of a photoluminescence quantum yield (PLQY) experiment on (a) AgSePh and (b) AgTePh films. The ratio of integrated emission and excitation signals after the correction from ND and color glass filters gives PLQY of ~0.05 % and ~0.85% for AgSePh and AgTePh films, respectively.

For the AgSePh films, since the free-exciton emission and defect emission are spectrally well-resolved, each feature could be separately integrated and quantified (Figure 5.14a). The free-exciton PLQY of the AgSePh film increased monotonically with decreasing temperature, approaching ~0.25 % at 5 K. The PLQY of the sub-gap defect-derived emission in AgSePh also increased monotonically with decreasing temperature, becoming the primary emission source at low temperature (based on spectral integration). The total PLQY, including free-exciton and sub-gap emission, of the AgSePh film was estimated to be ~2.1 % at 5K. These overall trends suggest the existence of thermally-activated nonradiative recombination channels that become partially suppressed at low temperatures.[43,58] Strikingly, however, there also remains a strong nonradiative recombination pathway in AgSePh even below 10 K.

In contrast, the PLQY of AgTePh films increased monotonically with decreasing temperature, approaching nearly unity at temperatures below 50 K. The observation of near-unity PLQY in AgTePh at cryogenic temperature strongly suggests that light emission in this material

does not originate from indirect bandgap recombination, which is also supported by the band structure calculation showing the *effectively* direct gap (Figures 5.9 and 5.11). Electron-hole recombination in indirect bandgap semiconductors is a phonon-assisted process, requiring the participation of phonons to conserve crystal momentum. Consequently, indirect bandgap recombination is strongly suppressed at lower sample temperature when the occupancy of phonon modes is reduced.[52] Consequently, the broad Stokes-shifted emission in AgTePh films most likely originates from an alternative mechanism, such as self-trapped exciton emission.

5.3.4 Sub-gap excitation photoluminescence spectroscopy

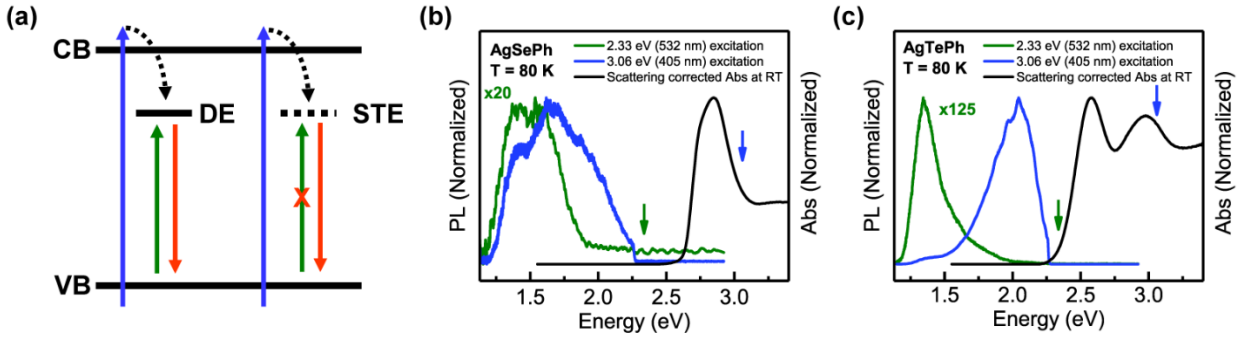

Figure 5.16 Sub-gap excitation. (a) Diagram showing the energy levels of conduction band (CB) and valence band (VB) edges, as well as hypothetical defect (DE) and self-trapped exciton (STE) states. Solid blue, green, red lines represent above-gap excitation, sub-gap excitation, and broad emission, respectively. (b,c) Photoluminescence spectra at 80 K of AgSePh and AgTePh films upon resonant (blue) and sub-gap (green) laser excitation. The absorption spectrum is included for reference.

To further distinguish between defect-derived mid-gap states and intrinsic self-trapped excitons (STEs), we performed sub-gap excitation PL spectroscopy (Figure 5.16). In these experiments, we compare the PL spectra under resonant (above-gap) photoexcitation to non-resonant (sub-gap) photoexcitation. Defect-derived mid-gap states are quasi-permanent electronic states that should be accessible upon direct photoexcitation from the ground state (albeit with possibly weak oscillator strength). In contrast, STEs are lattice deformations that are absent in the ground state configuration of the lattice; their formation is transiently induced by the presence of excited charge carriers.[59,60] Consequently, comparison of both the intensity and spectral shape of

PL under resonant and sub-gap excitation conditions can help differentiate STEs from defect-derived emission (Figure 5.16a).[45,51]

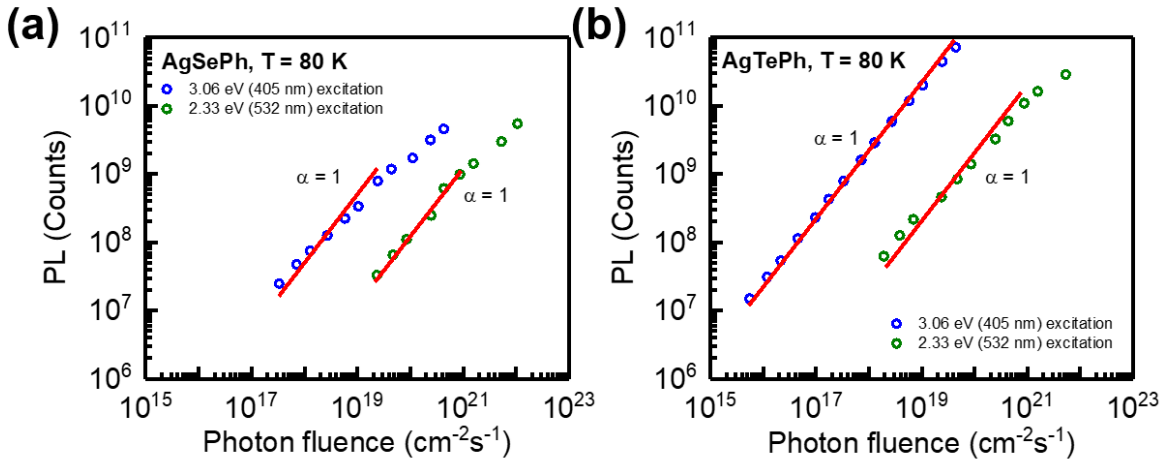

Figure 5.17 Power-dependent photoluminescence intensities of (a) AgSePh and (b) AgTePh films upon resonant excitation (3.06 eV, 405 nm) and subgap excitation (2.33eV, 532 nm) with fits to $I \propto P^{\alpha}$ where α = 1.

Figure 5.16b,c compares the PL spectrum under resonant (3.06 eV, 405 nm) and sub-gap (2.33 eV, 532 nm) laser excitation conditions in AgSePh and AgTePh films at T = 80 K. For AgSePh, a 550 nm long-pass filter was used to filter out the free-exciton emission near ~455 nm. All of the spectra shown in Figure 5.16 followed a linear power dependence, ruling out any contribution of two-photon absorption to the measured spectra (Figure 5.17). In the case of AgSePh, both above-gap and sub-gap excitation led to overlapping spectral emission (Figure 5.16b), supporting the assignment of broad emission in this sample to quasi-permanent defect states. The ~20x weaker emission under sub-gap excitation is explained by significantly reduced absorption at 532 nm compared to 405 nm (Figure 5.16b).

In contrast, the PL spectra of AgTePh under resonant and sub-gap photoexcitation were completely different (Figure 5.16c). Upon resonant (above-gap) excitation in AgTePh, the emission spectrum spanned from 1.6 eV to 2.2 eV (550-780 nm), while non-resonant (sub-gap) excitation produced emission below 1.6 eV (note that the shape of the sub-gap emission curve below ~1.4 eV is affected by reduced efficiency of a cooled charge-coupled device (CCD) camera

detector at longer wavelengths). Moreover, the PL peak intensity upon resonant excitation was ~10^2 times higher than that upon sub-gap excitation with the same incident laser intensity. These observations further support the conclusion that broad emission ranging from 1.6 eV to 2.2 eV in AgTePh does not arise from defects. On the other hand, we note that emission beyond ~800 nm (1.6 eV) in AgTePh films became stronger when the sample was intentionally degraded by long time photo-exposure (Figure 5.18), suggesting that PL in this spectral range is defect-derived.

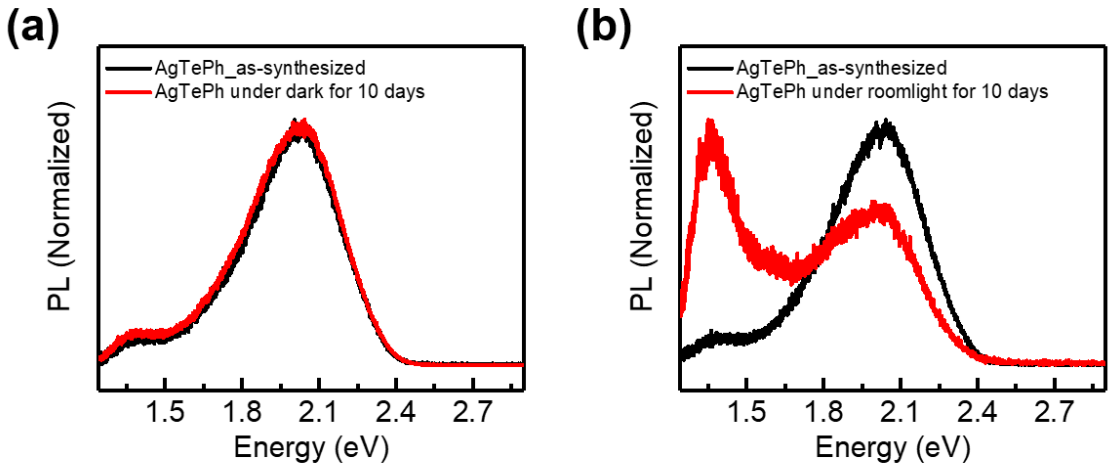

Figure 5.18 Comparison of photoluminescence spectra of AgTePh films stored for 10 days under dark and room-light. The emission spectra of AgTePh films did not change overtime when the sample was kept under dark. In contrast, emission beyond ~800 nm (1.6 eV) in AgTePh films became stronger when the sample was stored under room-light, suggesting sample degradation by photo-exposure.

5.3.5 Time-resolved spectroscopy

Temperature-dependent time-resolved photoluminescence (TRPL) spectroscopy data for AgTePh and AgSePh are shown in Figure 5.19a-f. Spectrally-resolved TRPL of the AgTePh film at 80 K is shown in Figure 5.19a. Similar PL decay dynamics at different wavelengths and a PL spectrum that is invariant with decay time was observed (Figures 5.19b and 5.20), further confirming that the broad emission in the AgTePh film arises from a homogeneous emission mechanism, such as an intrinsic STE.

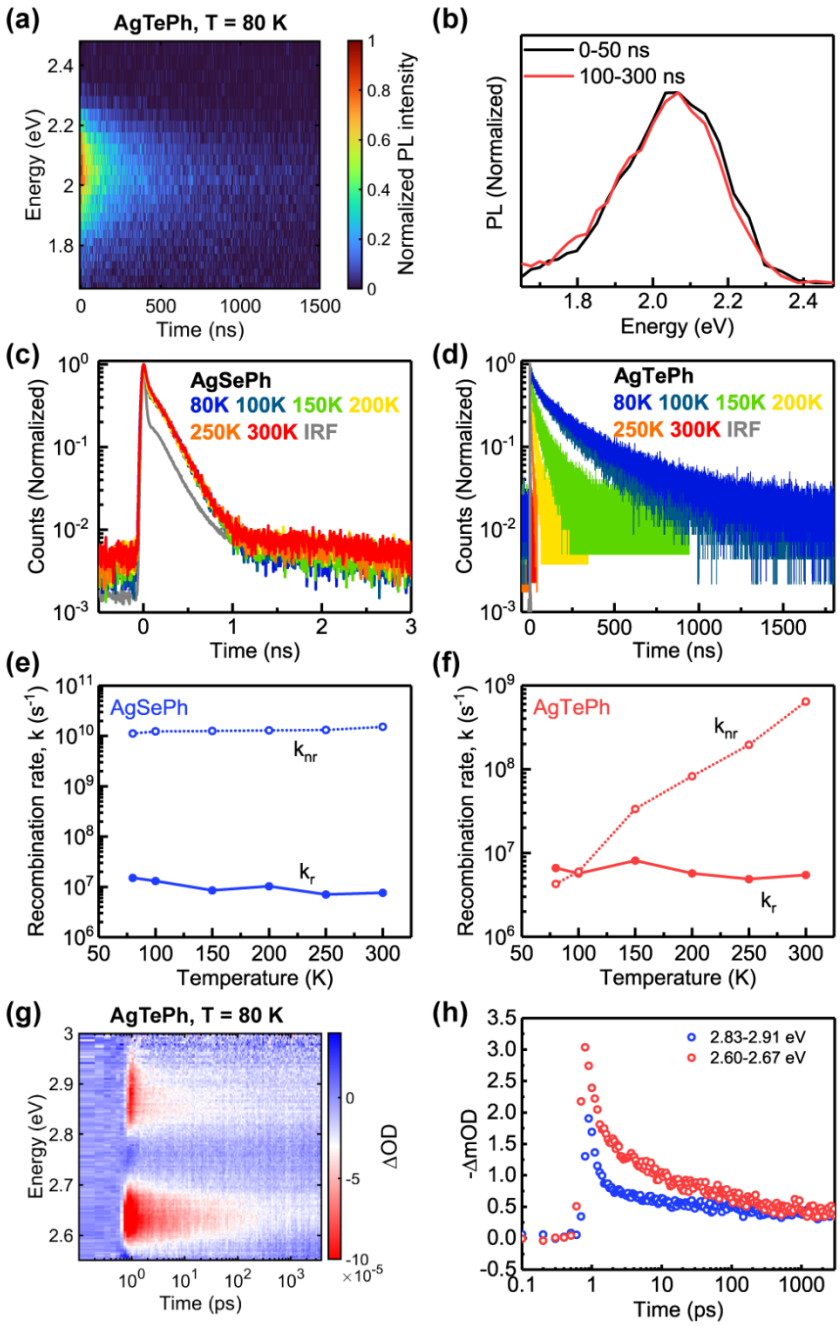

Figure 5.19 Time-resolved spectroscopy. (a) Spectrally-resolved time-resolved photoluminescence (TRPL) of the AgTePh film at 80 K. (b) Comparison of spectral slices corresponding to early time (0 – 50 ns, black) and late time (100 – 300 ns, red) emission in AgTePh at 80 K. (c, d) Temperature-dependent TRPL of AgSePh and AgTePh films. (e, f) Temperature-dependent radiative (k_r) and nonradiative (k_{nr}) recombination rates of AgSePh and AgTePh films determined from PL quantum yield and TRPL data. (g) 2D transient absorption color plot showing dynamics in the vicinity of the two ground-state excitonic absorption resonances in AgTePh at 300 K. (pump energy: 3.3 eV) (h) Ground-state bleach recovery of the two excitonic resonances in AgTePh at 300 K; spectral range 2.83 – 2.91 eV is shown in blue and 2.60 – 2.67 eV is shown in red.

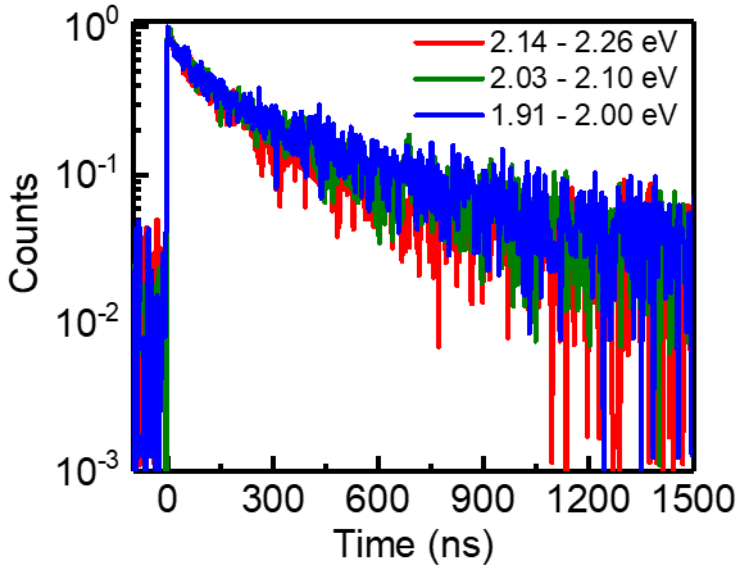

Figure 5.20 Normalized photoluminescence decay of the AgTePh film at different emission energies at 80 K.

Figures 5.19c,d shows temperature-dependent TRPL from 80 K to 300 K of AgSePh and AgTePh films, respectively. For AgTePh TRPL data, the entire broad emission spectrum was spectrally integrated. For AgSePh, a combination of shortpass and bandpass filters were used in the collection path to select only the free-exciton emission (Figure 5.21). In the case of the AgSePh film, PL decay traces were almost identical in the temperature range between 80 – 300 K. The PL lifetime was determined by fitting a single exponential decay model convolved with the IRF. For AgSePh, the fitted PL lifetime was temperature-independent (Figure 5.22). In contrast, PL from AgTePh films decayed more slowly with decreasing temperature. Because the PL decay of the AgTePh film could not be well-fitted with a single exponential function below 250 K, we extracted the time at which the PL count is reduced to 1/e (≈ 0.368) as the PL lifetime throughout the temperature range. The extracted PL lifetimes of the AgTePh film monotonically increased from 1.5 ns at 300 K to 92 ns at 80 K (Figure 5.22).

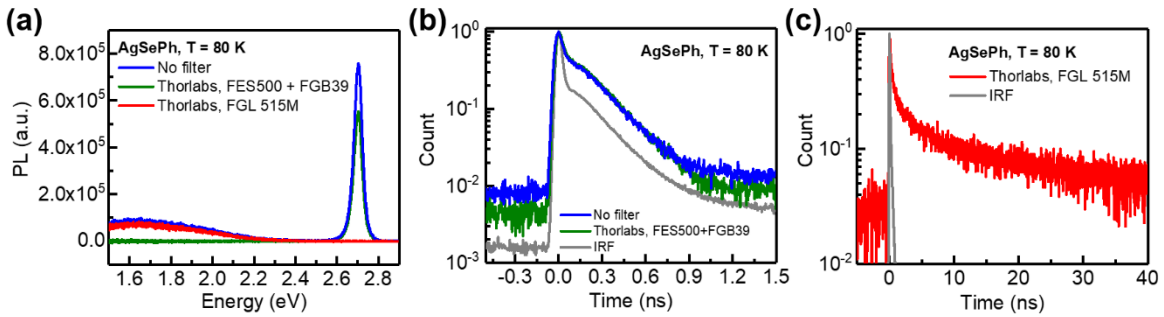

Figure 5.21 (a) Photoluminescence (PL) spectra and (b, c) time-resolved PL of the AgSePh film at 80 K with no filter (blue), shortpass and bandpass filters (green), and the longpass filter (red) in the collection path, respectively. Shortpass and bandpass filters were used to reject defect emissions and longpass filter was used to reject free-exciton emission. IRF denotes the instrument response function of the measurement.

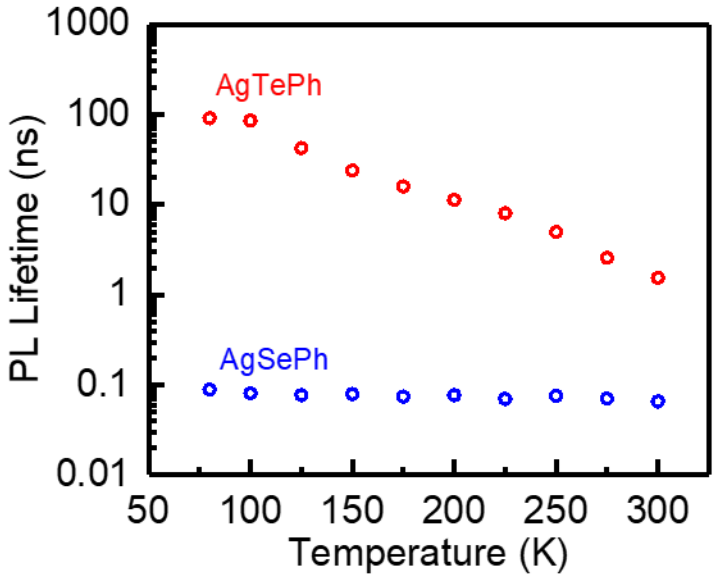

Figure 5.22 Temperature-dependent photoluminescence lifetime of AgSePh and AgTePh films.

The observed PL lifetime (τ_{TRPL}) has contributions from radiative (τ_r) and nonradiative (τ_{nr}) decay pathways, which are related through the relationship $\frac{1}{\tau_{TRPL}} = \frac{1}{\tau_r} + \frac{1}{\tau_{nr}}$. Additionally, the PLQY can be expressed by PLQY $= \frac{\tau_{TRPL}}{\tau_r}$.[44] Therefore, the radiative (k_r) and nonradiative (k_{nr})

recombination rates, which are the inverse values of their respective lifetimes, can be calculated from the separately measured τ_{TRPL} and PLQY data. Figure 5.19e,f shows the calculated k_r and k_{nr} of AgSePh and AgTePh films, respectively, as a function of temperature from 80 K to 300 K. In the case of the AgSePh film, trends of slightly increasing k_r and decreasing k_{nr} were observed as temperature was reduced, consistent with typical direct bandgap semiconductor behavior. In direct bandgap semiconductors, the momentum space thermally sampled by excitons within the direct transition valley decreases as temperature is reduced according to the Boltzmann distribution, increasing the rate of radiative recombination at lower temperature while suppressing other nonradiative recombination processes.[44]

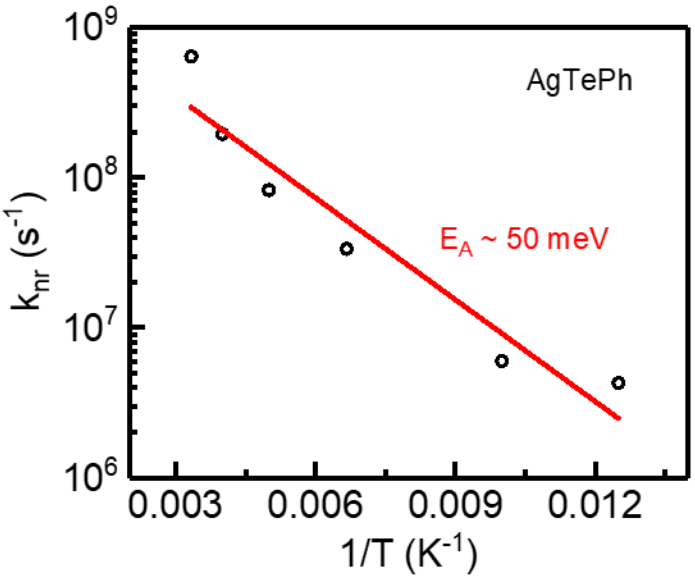

Figure 5.23 Nonradiative recombination rates of the AgTePh film as a function of temperature with a fit to the Arrhenius relation. The fitting gives a value of ~ 50 meV for an activation energy.

For the AgTePh film, a massive and monotonic decrease in k_{nr} was observed with decreasing temperature, while k_r was found to be mostly temperature-independent. Similar behavior has been observed in studies of STE luminescence from many conventional bulk and low dimensional materials.[58,59,61] STEs can decay radiatively or non-radiatively by emitting phonons,

forming defects, or hopping to quenching sites.[59] Nonradiative recombination channels are thermally activated in most cases, while the radiative recombination is generally independent of temperature. In many cases, one dominant nonradiative recombination channel is observed because it has the lowest activation energy, so the overall nonradiative recombination rate can be roughly approximated as $k_{nr} = k_0 \exp(-E_A/k_B T)$, where k_0 is the nonradiative recombination pre-exponential factor, E_A is the activation energy for the recombination process, and T is the temperature in Kelvin. An approximate $E_A \sim 50$ meV was found by fitting the temperature-dependent nonradiative transition rate in AgTePh (Figure 5.23).

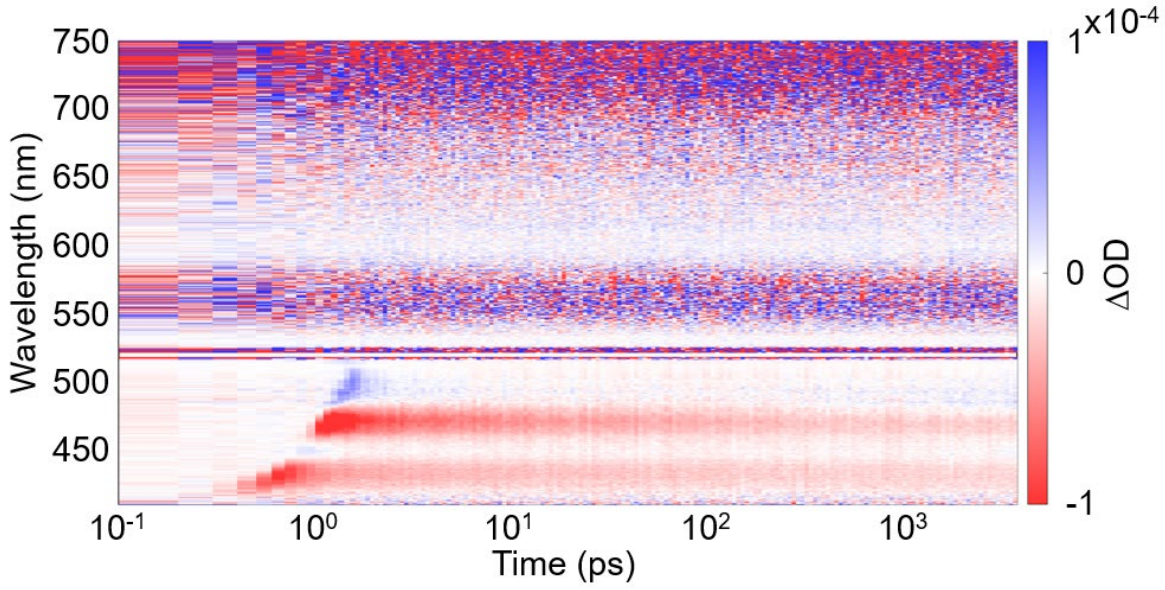

Figure 5.24 2D transient absorption color plot showing dynamics of the AgTePh film at 300 K.

Transient absorption (TA) spectroscopy was employed to probe the excited state dynamics in AgTePh films on even faster timescales (Figure 5.19g). The TA instrument has a time resolution of ~0.1 ps, whereas the TRPL instrument has a time resolution of ~50 ps (instrument response function). The TA spectrum reveals two strong excitonic resonances, consistent with the ground state absorption spectrum shown in Figure 5.1f. However, the TA peaks are centered at 2.85 eV (435 nm) and 2.63 eV (470 nm), while the absorption peaks are centered at 2.98 eV (416 nm) and 2.58 eV (480 nm). The differences arise from bandgap renormalization under higher excitation density and multiple competing contributions to the spectral shape of the TA signal (ground state

bleach, stimulated emission, excited state absorption). In addition to the ground state exciton resonances, the broadband TA probe pulse also spectrally covered the sub-bandgap region equivalent to the STE emission energy (Figure 5.24). However, no measurable TA signal from stimulated emission was observed in the region of the STE, likely due to the low oscillator strength of the STE and sensitivity limitations of our TA experimental setup.

Figure 5.19h shows the recovery dynamics of the two dominant TA bleach signals integrated over probe wavelength ranges of 2.83 – 2.91 eV and 2.60 – 2.67 eV. The fastest TA dynamics are completed within ~2 ps following photoexcitation, which could arise from both hot carrier cooling and STE formation.[40,62] Because there was no noticeable dynamics after ~ 2 ps, we assign it (or shorter) to the timescale of formation of STEs in AgTePh.

5.3.6 A complete description of exciton dynamics in AgTePh

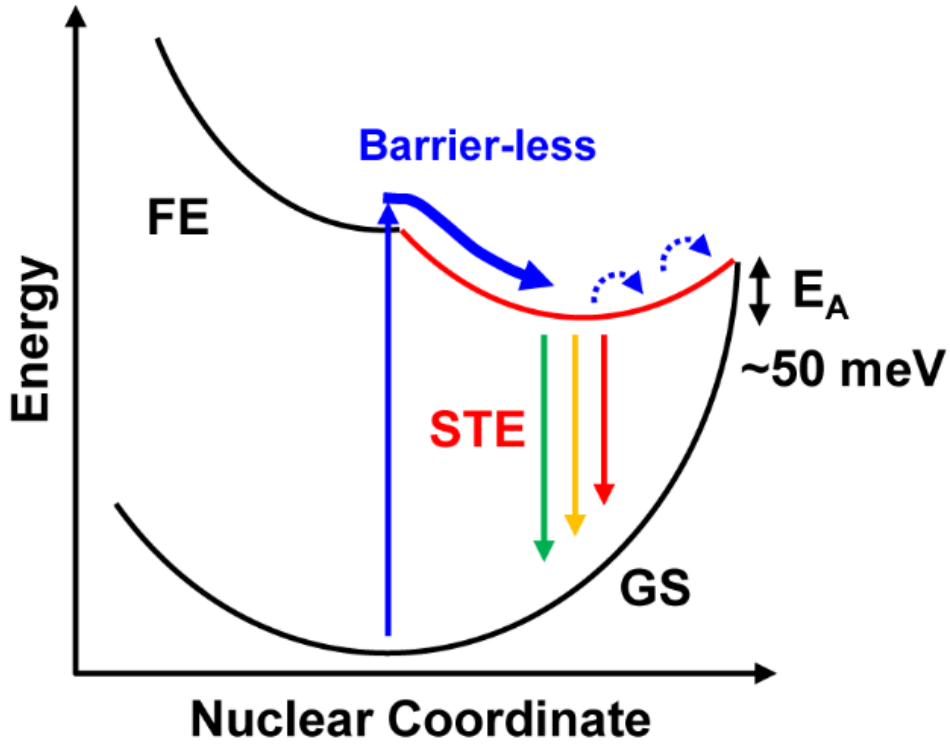

Figure 5.25 Schematic description of exciton dynamics in AgTePh. Potential energy surfaces corresponding to the free-exciton (FE), self-trapped exciton (STE), and electronic ground state (GS) are shown. STEs are readily formed through a nearly barrier-less transition from the initially excited FE species and then relax to the GS through radiative and nonradiative decay processes.

Based on all of the experimental observations reported here, we propose a schematic description of exciton dynamics in AgTePh (Figure 5.25). Free-excitons initially formed in AgTePh by optical excitation are quickly (<2 ps) self-trapped into a deep potential well induced by local lattice deformations. This self-trapping is not mediated by defects – as supported by location-, power-, and excitation wavelength-dependent steady-state PL and spectrally-resolved TRPL analysis – but is rather an intrinsic material response driven by strong electron-phonon interactions. The fast self-trapping time and absence of free-exciton emission down to 5 K imply a potential energy surface-crossing in configuration space that is nearly barrier-less. Finally, STEs relax back to the electronic ground state through a temperature-independent radiative recombination process or by thermally-activated non-radiative recombination.

5.4 Conclusions

Although our spectroscopic observation supports that the broadband emission in AgTePh arises from self-trapped excitons (STEs), the origin of differences between AgTePh and AgSePh is less clear. STE formation has been observed in materials featuring soft lattices and strong electron-phonon interactions, such as organic molecular crystals[63] and halide perovskites,[64] and are more likely to be observed when the materials dimensionality is reduced.[59,60] Given the hybrid organic-inorganic composition and 2D structure of AgTePh, it is unsurprising that STEs are observed. Moreover, the broadened excitonic transitions in AgTePh relative to AgSePh (Figure 5.6) and the greater shifting of the X_1 energy with temperature (66 meV for AgTePh *vs.* 47 meV for AgSePh from 300 K to 80 K – Figure 5.8) indicate stronger exciton-phonon coupling in AgTePh. However, how the unique electronic structure of AgTePh (Figure 5.9) contributes to self-trapping – if at all – is not obvious. Despite the saddle point at Γ, the conduction and valence band edges are two-dimensionally dispersive at their respective band extrema, meaning that charge carriers are delocalized in 2D real space in the absence of phonons. Moreover, effective masses of band edge carriers in AgSePh and AgTePh are comparable ($m_{eff} \approx 0.5\text{-}1.2m_0$). It is possible that the strong in-plane anisotropy of the AgTePh electronic structure acts to effectively reduce the electronic dimensionality, but higher-level calculations are needed to understand this behavior.

5.5 Methods

Chemicals. Silver pellets (Ag, 99.99% pure) were purchased from Kurt J Lesker. Diphenyl diselenide (Ph_2Se_2, 97.0+%) was purchased from TCI America. Diphenyl ditelluride (Ph_2Te_2, 98%) and Allura Red AC (98.0+%) were purchased from Millipore Sigma.

Preparation of AgSePh and AgTePh films. AgEPh (E = Se, Te) thin films were prepared by a chemical transformation reaction between metallic silver and Ph_2E_2 (E = Se, Te).[34,35] Silver films with thickness of 15 nm were deposited on glass substrates by thermal evaporation with a deposition rate of ~1 Å/s. After that, the prepared silver films, ~30 mg of Ph_2E_2 powder and 200 μL of deionized water in separate open culture tubes were sealed together inside a microwave reaction vial. After heating in an oven at 100 °C for 3 days, the silver films transformed into AgEPh (E = Se, Te) films.

Substrate preparation. Bare glass with dimensions of 12.2 x 12.2 x 1.1 mm was purchased from Luminescence Technology Corp. The glass substrates were cleaned by sonication for 3 min successively in acetone, isopropanol, and deionized water.

Steady-state PL micro-spectroscopy. Steady-state PL measurements were performed on an inverted microscope (Nikon, Ti-U Eclipse) with sample mounted either in air or under vacuum. The samples were excited by focusing the output of a 405 nm laser diode (Picoquant, LDHDC-405M, continuous wave mode) by an objective lens (Nikon, CFI S Plan Fluor ELWD, 40x, 0.6 NA) to ~1 μm spot. The excitation light polarization was controlled by a circular polarizer (Thorlabs, CP1R405). After excitation, the PL was collected in the epi configuration and passed through a dichroic mirror and a long-pass filter. It was then directed into a spectrograph (Princeton Instruments, SP-2500) mounted with a cooled charge-coupled device (CCD) camera detector (Princeton Instruments, Pixis). All spectra underwent Jacobian transformation from wavelength to photon energy,[65] but have *not* been corrected for wavelength-dependent efficiency of the spectrograph or CCD camera. Temperature-dependent PL spectroscopy was performed by mounting samples in a microscopy cryostat (Janis Research, ST-500) and flowing liquid helium through a cold finger attached to the base of the cryostat.

Sub-gap excitation PL micro-spectroscopy. PL spectra by sub-gap excitation was obtained by the same microscope and spectrograph as used for 405 nm excitation, but with a 532 nm

continuous wave laser (Coherent, Sapphire 532 LP). To filter out the free-exciton emission at ~455 nm in AgSePh, a 550 nm long-pass filter was used (Thorlabs FEL0550).

Time-resolved PL micro-spectroscopy. Time-resolved PL (TRPL) measurements were performed using the same microscope and cryostat setup as steady-state PL spectroscopy with some modifications. For the AgSePh film, the excitation light source was replaced by frequency-doubled light (405 nm) of the 810 nm output from a ~150 fs Ti:sapphire laser (Coherent Mira HP) operating at 76 MHz. For low-temperature measurements on AgTePh films, a variable repetition-rate 405 nm pulsed laser diode (Picoquant, LDHDC-405M) was used instead of the 76 MHz Ti:sapphire laser because of the long natural emission lifetime of AgTePh. For both samples, PL was detected by a Si avalanche photodiode (APD, Micro Photon Devices, PDM20) connected to a counting board for time-correlated single-photon counting (PicoQuant, PicoHarp 300). To account for the wavelength-dependent temporal response of the APD, different procedures were used to obtain the instrument response function (IRF). For AgSePh, the IRF was obtained by detecting Raman scattering from water at ~470 nm, which is close to the PL peak position of AgSePh. For AgTePh, the IRF was obtained by detecting the PL from Allura Red AC dye in water, which shows fast and broad emission centered near ~620 nm, similar to emission spectrum of AgTePh. For spectrally-resolved TRPL measurements, the emitted light was directed into a monochromator (Princeton Instruments, SP-2500) with a 300 gr/mm grating. The monochromator output was then focused into the Si avalanche photodiode.

Photoluminescence quantum yield. The measurement of PL quantum yield (QY) was performed at room temperature using the absolute quantum yield method in an integrating sphere.[34,57] The excitation light from a 405 nm laser diode (Picoquant, LDHDC-405M, continuous wave mode) was directed into an integrating sphere (Labsphere) containing the sample. The output signal was collected by an optical fiber mounted on an exit port of the integrating sphere and was directed into a spectrograph (Princeton Instruments, SP-2500) outfitted with the CCD camera (Princeton Instruments, Pixis 100B). Neutral density and color glass filters were inserted in front of the spectrograph to avoid oversaturation of the CCD and accounted for in all calculations. Absolute QY at lower sample temperature was estimated by scaling the QY measured at room-temperature by the temperature-dependent relative PL intensity.

Steady-state absorption spectroscopy. Optical absorption measurements were performed on films made from 15 nm thick silver films using a Cary 5000 UV-Vis-NIR spectrometer. Room temperature absorption spectra were collected in an integrating sphere geometry (Agilent, Internal DRA 2500), in air to minimize scattered light contributions to the signal. For temperature-dependent absorption spectra, samples were mounted inside a steady flow Janis ST-100 optical cryostat. The cryostat was then mounted in the Cary spectrometer, evacuated to below 3×10^{-5} Torr, and cooled with liquid nitrogen. The temperature was controlled with a model 335 Lakeshore temperature controller.

Transient absorption spectroscopy. The transient absorption (TA) spectroscopy experimental setup used has been described elsewhere,[51] with a few differences noted here. A non-collinear optical parametric amplifier (Spectra-Physics Spirit-NOPA) was used to generate the pump pulse centered at 375 nm. A pump fluence of 120 μW was selected to best balance TA signal intensity with photoinduced sample degradation. Broadband probe light was generated by first frequency doubling the 1040 nm fundamental laser to 520 nm in a β-barium borate crystal, then focusing the 520 nm light into a sapphire window to generate a supercontinuum. The pump and probe beams were overlapped to a spot diameter of ~120 μm using a 200 mm focal length concave mirror.

Density functional theory calculations. Density functional theory (DFT) calculations were performed with the PBE functional[66] and ultrasoft pseudopotential using Quantum-ESPRESSO.[67] DFT-D2[68] correction for the van der Waals interaction and fully relativistic scheme for the spin-orbit coupling were applied. The crystal structures reported in refs [32], [36], and [39] for AgTePh *C2/c*, AgSePh *C2/c* and AgSePh $P2_1/c$, respectively, were employed without further geometry optimization. We used a 6×6×2 Monkhorst-Pack k-mesh with a kinetic energy cutoff of 40 Ry.

Scanning electron microscopy (SEM). Scanning electron micrographs were collected using a Zeiss Merlin instrument operating at 1 kV and 100 pA.

Powder X-ray diffraction (PXRD). Powder X-ray diffraction data were collected using a PANalytical X'Pert Pro MPD X-ray diffractometer (Cu Kα radiation, λ = 1.54184 Å) with High-Speed Bragg-Brentano Optics. A 0.04 rad Soller slit, a 2° anti-scatter slit, a 10 mm mask, and a programmable divergence slit with an illuminated length of 6 mm were used in the incident beam

path. The diffracted beam optics included a 0.04 rad Soller slit, a Ni Filter, and an automatic receiving slit. The detector was an ultrafast X'Celerator RTMS detector.

5.6 References

(1) Novoselov, K. S.; Mishchenko, A.; Carvalho, A.; Castro Neto, A. H. 2D Materials and van Der Waals Heterostructures. *Science (1979)* **2016**, *353* (6298). https://doi.org/10.1126/science.aac9439.

(2) Ghimire, S.; Klinke, C. Two-Dimensional Halide Perovskites: Synthesis, Optoelectronic Properties, Stability, and Applications. *Nanoscale* **2021**, *13* (29), 12394–12422. https://doi.org/10.1039/D1NR02769G.

(3) Mauck, C. M.; Tisdale, W. A. Excitons in 2D Organic–Inorganic Halide Perovskites. *Trends Chem* **2019**, *1* (4), 380–393. https://doi.org/10.1016/j.trechm.2019.04.003.

(4) Tempelaar, R.; Berkelbach, T. C. Many-Body Simulation of Two-Dimensional Electronic Spectroscopy of Excitons and Trions in Monolayer Transition Metal Dichalcogenides. *Nat Commun* **2019**, *10* (1), 3419. https://doi.org/10.1038/s41467-019-11497-y.

(5) Tao, W.; Zhang, C.; Zhou, Q.; Zhao, Y.; Zhu, H. Momentarily Trapped Exciton Polaron in Two-Dimensional Lead Halide Perovskites. *Nat Commun* **2021**, *12* (1), 1400. https://doi.org/10.1038/s41467-021-21721-3.

(6) Yin, X.; Tang, C. S.; Zheng, Y.; Gao, J.; Wu, J.; Zhang, H.; Chhowalla, M.; Chen, W.; Wee, A. T. S. Recent Developments in 2D Transition Metal Dichalcogenides: Phase Transition and Applications of the (Quasi-)Metallic Phases. *Chem Soc Rev* **2021**, *50* (18), 10087–10115. https://doi.org/10.1039/D1CS00236H.

(7) Manzeli, S.; Ovchinnikov, D.; Pasquier, D.; Yazyev, O. V.; Kis, A. 2D Transition Metal Dichalcogenides. *Nat Rev Mater* **2017**, *2* (8), 17033. https://doi.org/10.1038/natrevmats.2017.33.

(8) Li, X.; Hoffman, J. M.; Kanatzidis, M. G. The 2D Halide Perovskite Rulebook: How the Spacer Influences Everything from the Structure to Optoelectronic Device Efficiency. *Chem Rev* **2021**, *121* (4), 2230–2291. https://doi.org/10.1021/acs.chemrev.0c01006.

(9) Chernikov, A.; Berkelbach, T. C.; Hill, H. M.; Rigosi, A.; Li, Y.; Aslan, B.; Reichman, D. R.; Hybertsen, M. S.; Heinz, T. F. Exciton Binding Energy and Nonhydrogenic Rydberg Series in Monolayer WS_2. *Phys Rev Lett* **2014**, *113* (7), 076802. https://doi.org/10.1103/PhysRevLett.113.076802.

(10) He, K.; Kumar, N.; Zhao, L.; Wang, Z.; Mak, K. F.; Zhao, H.; Shan, J. Tightly Bound Excitons in Monolayer WSe_2. *Phys Rev Lett* **2014**, *113* (2), 026803. https://doi.org/10.1103/PhysRevLett.113.026803.

(11) Passarelli, J. V.; Mauck, C. M.; Winslow, S. W.; Perkinson, C. F.; Bard, J. C.; Sai, H.; Williams, K. W.; Narayanan, A.; Fairfield, D. J.; Hendricks, M. P.; Tisdale, W. A.; Stupp, S. I. Tunable Exciton Binding Energy in 2D Hybrid Layered Perovskites through Donor–Acceptor Interactions

within the Organic Layer. *Nat Chem* **2020**, *12* (8), 672–682. https://doi.org/10.1038/s41557-020-0488-2.

(12) Blancon, J.-C.; Stier, A. V.; Tsai, H.; Nie, W.; Stoumpos, C. C.; Traoré, B.; Pedesseau, L.; Kepenekian, M.; Katsutani, F.; Noe, G. T.; Kono, J.; Tretiak, S.; Crooker, S. A.; Katan, C.; Kanatzidis, M. G.; Crochet, J. J.; Even, J.; Mohite, A. D. Scaling Law for Excitons in 2D Perovskite Quantum Wells. *Nat Commun* **2018**, *9* (1), 2254. https://doi.org/10.1038/s41467-018-04659-x.

(13) Saouma, F. O.; Stoumpos, C. C.; Wong, J.; Kanatzidis, M. G.; Jang, J. I. Selective Enhancement of Optical Nonlinearity in Two-Dimensional Organic-Inorganic Lead Iodide Perovskites. *Nat Commun* **2017**, *8* (1), 742. https://doi.org/10.1038/s41467-017-00788-x.

(14) Yao, K.; Yanev, E.; Chuang, H.-J.; Rosenberger, M. R.; Xu, X.; Darlington, T.; McCreary, K. M.; Hanbicki, A. T.; Watanabe, K.; Taniguchi, T.; Jonker, B. T.; Zhu, X.; Basov, D. N.; Hone, J. C.; Schuck, P. J. Continuous Wave Sum Frequency Generation and Imaging of Monolayer and Heterobilayer Two-Dimensional Semiconductors. *ACS Nano* **2020**, *14* (1), 708–714. https://doi.org/10.1021/acsnano.9b07555.

(15) Yin, X.; Ye, Z.; Chenet, D. A.; Ye, Y.; O'Brien, K.; Hone, J. C.; Zhang, X. Edge Nonlinear Optics on a MoS $_2$ Atomic Monolayer. *Science (1979)* **2014**, *344* (6183), 488–490. https://doi.org/10.1126/science.1250564.

(16) Scuri, G.; Zhou, Y.; High, A. A.; Wild, D. S.; Shu, C.; De Greve, K.; Jauregui, L. A.; Taniguchi, T.; Watanabe, K.; Kim, P.; Lukin, M. D.; Park, H. Large Excitonic Reflectivity of Monolayer $MoSe_2$ Encapsulated in Hexagonal Boron Nitride. *Phys Rev Lett* **2018**, *120* (3), 037402. https://doi.org/10.1103/PhysRevLett.120.037402.

(17) Borys, N. J.; Barnard, E. S.; Gao, S.; Yao, K.; Bao, W.; Buyanin, A.; Zhang, Y.; Tongay, S.; Ko, C.; Suh, J.; Weber-Bargioni, A.; Wu, J.; Yang, L.; Schuck, P. J. Anomalous Above-Gap Photoexcitations and Optical Signatures of Localized Charge Puddles in Monolayer Molybdenum Disulfide. *ACS Nano* **2017**, *11* (2), 2115–2123. https://doi.org/10.1021/acsnano.6b08278.

(18) Lv, R.; Robinson, J. A.; Schaak, R. E.; Sun, D.; Sun, Y.; Mallouk, T. E.; Terrones, M. Transition Metal Dichalcogenides and Beyond: Synthesis, Properties, and Applications of Single- and Few-Layer Nanosheets. *Acc Chem Res* **2015**, *48* (1), 56–64. https://doi.org/10.1021/ar5002846.

(19) Mueller, T.; Malic, E. Exciton Physics and Device Application of Two-Dimensional Transition Metal Dichalcogenide Semiconductors. *NPJ 2D Mater Appl* **2018**, *2* (1), 29. https://doi.org/10.1038/s41699-018-0074-2.

(20) Zhang, F.; Lu, H.; Tong, J.; Berry, J. J.; Beard, M. C.; Zhu, K. Advances in Two-Dimensional Organic–Inorganic Hybrid Perovskites. *Energy Environ Sci* **2020**, *13* (4), 1154–1186. https://doi.org/10.1039/C9EE03757H.

(21) Liang, C.; Gu, H.; Xia, Y.; Wang, Z.; Liu, X.; Xia, J.; Zuo, S.; Hu, Y.; Gao, X.; Hui, W.; Chao, L.; Niu, T.; Fang, M.; Lu, H.; Dong, H.; Yu, H.; Chen, S.; Ran, X.; Song, L.; Li, B.; Zhang, J.; Peng, Y.; Shao, G.; Wang, J.; Chen, Y.; Xing, G.; Huang, W. Two-Dimensional Ruddlesden–Popper Layered Perovskite Solar Cells Based on Phase-Pure Thin Films. *Nat Energy* **2020**, *6* (1), 38–45. https://doi.org/10.1038/s41560-020-00721-5.

(22) Veselska, O.; Podbevšek, D.; Ledoux, G.; Fateeva, A.; Demessence, A. Intrinsic Triple-Emitting 2D Copper Thiolate Coordination Polymer as a Ratiometric Thermometer Working over 400 K

Range. *Chemical Communications* **2017**, *53* (90), 12225–12228. https://doi.org/10.1039/C7CC06815H.

(23) Veselska, O.; Okhrimenko, L.; Guillou, N.; Podbevšek, D.; Ledoux, G.; Dujardin, C.; Monge, M.; Chevrier, D. M.; Yang, R.; Zhang, P.; Fateeva, A.; Demessence, A. An Intrinsic Dual-Emitting Gold Thiolate Coordination Polymer, $[Au(+I)(p\text{-}SPhCO_2H)]_n$, for Ratiometric Temperature Sensing. *J. Mater. Chem. C* **2017**, *5* (38), 9843–9848. https://doi.org/10.1039/C7TC03605A.

(24) Lavenn, C.; Guillou, N.; Monge, M.; Podbevšek, D.; Ledoux, G.; Fateeva, A.; Demessence, A. Shedding Light on an Ultra-Bright Photoluminescent Lamellar Gold Thiolate Coordination Polymer $[Au(p\text{-}SPhCO_2Me)]_n$. *Chemical Communications* **2016**, *52* (58), 9063–9066. https://doi.org/10.1039/C5CC10448C.

(25) Veselska, O.; Demessence, A. D10 Coinage Metal Organic Chalcogenolates: From Oligomers to Coordination Polymers. *Coord Chem Rev* **2018**, *355*, 240–270. https://doi.org/10.1016/j.ccr.2017.08.014.

(26) Hu, L.; de la Rama, L. P.; Efremov, M. Y.; Anahory, Y.; Schiettekatte, F.; Allen, L. H. Synthesis and Characterization of Single-Layer Silver−Decanethiolate Lamellar Crystals. *J Am Chem Soc* **2011**, *133* (12), 4367–4376. https://doi.org/10.1021/ja107817x.

(27) Veselska, O.; Cai, L.; Podbevšek, D.; Ledoux, G.; Guillou, N.; Pilet, G.; Fateeva, A.; Demessence, A. Structural Diversity of Coordination Polymers Based on a Heterotopic Ligand: Cu(II)-Carboxylate vs Cu(I)-Thiolate. *Inorg Chem* **2018**, *57* (5), 2736–2743. https://doi.org/10.1021/acs.inorgchem.7b03090.

(28) Low, K.-H.; Roy, V. A. L.; Chui, S. S.-Y.; Chan, S. L.-F.; Che, C.-M. Highly Conducting Two-Dimensional Copper(i) 4-Hydroxythiophenolate Network. *Chemical Communications* **2010**, *46* (39), 7328. https://doi.org/10.1039/c0cc02348e.

(29) Schriber, E. A.; Popple, D. C.; Yeung, M.; Brady, M. A.; Corlett, S. A.; Hohman, J. N. Mithrene Is a Self-Assembling Robustly Blue Luminescent Metal–Organic Chalcogenolate Assembly for 2D Optoelectronic Applications. *ACS Appl Nano Mater* **2018**, *1* (7), 3498–3508. https://doi.org/10.1021/acsanm.8b00662.

(30) Wang, Q.; Dong, S.-L.; Tao, D.-D.; Li, Z.; Jiang, Y.-B. Ag(I)-Thiolate Coordination Polymers: Synthesis, Structures and Applications as Emerging Sensory Ensembles. *Coord Chem Rev* **2021**, *432*, 213717. https://doi.org/10.1016/j.ccr.2020.213717.

(31) Li, Y.; Jiang, X.; Fu, Z.; Huang, Q.; Wang, G.-E.; Deng, W.-H.; Wang, C.; Li, Z.; Yin, W.; Chen, B.; Xu, G. Coordination Assembly of 2D Ordered Organic Metal Chalcogenides with Widely Tunable Electronic Band Gaps. *Nat Commun* **2020**, *11* (1), 261. https://doi.org/10.1038/s41467-019-14136-8.

(32) Schriber, E. A.; Paley, D. W.; Bolotovsky, R.; Rosenberg, D. J.; Sierra, R. G.; Aquila, A.; Mendez, D.; Poitevin, F.; Blaschke, J. P.; Bhowmick, A.; Kelly, R. P.; Hunter, M.; Hayes, B.; Popple, D. C.; Yeung, M.; Pareja-Rivera, C.; Lisova, S.; Tono, K.; Sugahara, M.; Owada, S.; Kuykendall, T.; Yao, K.; Schuck, P. J.; Solis-Ibarra, D.; Sauter, N. K.; Brewster, A. S.; Hohman, J. N. Chemical Crystallography by Serial Femtosecond X-Ray Diffraction. *Nature* **2022**, *601* (7893), 360–365. https://doi.org/10.1038/s41586-021-04218-3.

(33) Popple, D. C.; Schriber, E. A.; Yeung, M.; Hohman, J. N. Competing Roles of Crystallization and Degradation of a Metal–Organic Chalcogenolate Assembly under Biphasic Solvothermal Conditions. *Langmuir* **2018**, *34* (47), 14265–14273. https://doi.org/10.1021/acs.langmuir.8b03282.

(34) Paritmongkol, W.; Lee, W. S.; Shcherbakov-Wu, W.; Ha, S. K.; Sakurada, T.; Oh, S. J.; Tisdale, W. A. Morphological Control of 2D Hybrid Organic–Inorganic Semiconductor AgSePh. *ACS Nano* **2022**, *16* (2), 2054–2065. https://doi.org/10.1021/acsnano.1c07498.

(35) Trang, B.; Yeung, M.; Popple, D. C.; Schriber, E. A.; Brady, M. A.; Kuykendall, T. R.; Hohman, J. N. Tarnishing Silver Metal into Mithrene. *J Am Chem Soc* **2018**, *140* (42), 13892–13903. https://doi.org/10.1021/jacs.8b08878.

(36) Maserati, L.; Refaely-Abramson, S.; Kastl, C.; Chen, C. T.; Borys, N. J.; Eisler, C. N.; Collins, M. S.; Smidt, T. E.; Barnard, E. S.; Strasbourg, M.; Schriber, E. A.; Shevitski, B.; Yao, K.; Hohman, J. N.; Schuck, P. J.; Aloni, S.; Neaton, J. B.; Schwartzberg, A. M. Anisotropic 2D Excitons Unveiled in Organic–Inorganic Quantum Wells. *Mater Horiz* **2021**, *8* (1), 197–208. https://doi.org/10.1039/C9MH01917K.

(37) Schriber, E. A.; Rosenberg, D. J.; Kelly, R. P.; Ghodsi, A.; Hohman, J. N. Investigation of Nucleation and Growth at a Liquid–Liquid Interface by Solvent Exchange and Synchrotron Small-Angle X-Ray Scattering. *Front Chem* **2021**, *9*. https://doi.org/10.3389/fchem.2021.593637.

(38) Maserati, L.; Prato, M.; Pecorario, S.; Passarella, B.; Perinot, A.; Thomas, A. A.; Melloni, F.; Natali, D.; Caironi, M. Photo-Electrical Properties of 2D Quantum Confined Metal–Organic Chalcogenide Nanocrystal Films. *Nanoscale* **2021**, *13* (1), 233–241. https://doi.org/10.1039/D0NR07409H.

(39) Paritmongkol, W.; Sakurada, T.; Lee, W. S.; Wan, R.; Müller, P.; Tisdale, W. A. Size and Quality Enhancement of 2D Semiconducting Metal–Organic Chalcogenolates by Amine Addition. *J Am Chem Soc* **2021**, *143* (48), 20256–20263. https://doi.org/10.1021/jacs.1c09106.

(40) Kastl, C.; Schwartzberg, A. M.; Maserati, L. Picoseconds-Limited Exciton Recombination in Metal–Organic Chalcogenides Hybrid Quantum Wells. *ACS Nano* **2022**, *16* (3), 3715–3722. https://doi.org/10.1021/acsnano.1c07281.

(41) Maserati, L.; Pecorario, S.; Prato, M.; Caironi, M. Understanding the Synthetic Pathway to Large-Area, High-Quality [AgSePh] $_\infty$ Nanocrystal Films. *The Journal of Physical Chemistry C* **2020**, *124* (41), 22845–22852. https://doi.org/10.1021/acs.jpcc.0c07330.

(42) Huang, Q.-Q.; Li, Y.-Z.; Zheng, Z.; Jiang, X.-M.; Sun, S.-S.; Jiang, H.-J.; Deng, W.-H.; Wang, G.-E.; Zhai, T.-Y.; Li, M.-D.; Xu, G. Single-Component MLCT-Active Photodetecting Material Based on a Two-Dimensional Coordination Polymer. *CCS Chemistry* **2020**, *2* (1), 655–662. https://doi.org/10.31635/ccschem.019.201900045.

(43) Yao, K.; Collins, M. S.; Nell, K. M.; Barnard, E. S.; Borys, N. J.; Kuykendall, T.; Hohman, J. N.; Schuck, P. J. Strongly Quantum-Confined Blue-Emitting Excitons in Chemically Configurable Multiquantum Wells. *ACS Nano* **2021**, *15* (3), 4085–4092. https://doi.org/10.1021/acsnano.0c08096.

(44) Pelant, I.; Valenta, J. *Luminescence Spectroscopy of Semiconductors*; Oxford University Press, 2012. https://doi.org/10.1093/acprof:oso/9780199588336.001.0001.

(45) Kahmann, S.; Tekelenburg, E. K.; Duim, H.; Kamminga, M. E.; Loi, M. A. Extrinsic Nature of the Broad Photoluminescence in Lead Iodide-Based Ruddlesden–Popper Perovskites. *Nat Commun* **2020**, *11* (1), 2344. https://doi.org/10.1038/s41467-020-15970-x.

(46) Li, X.; Lian, X.; Pang, J.; Luo, B.; Xiao, Y.; Li, M.-D.; Huang, X.-C.; Zhang, J. Z. Defect-Related Broadband Emission in Two-Dimensional Lead Bromide Perovskite Microsheets. *J Phys Chem Lett* **2020**, *11* (19), 8157–8163. https://doi.org/10.1021/acs.jpclett.0c02355.

(47) Lee, W. S.; Kang, Y.; Sharma, M.; Lee, Y. M.; Jeon, S.; Sharma, A.; Demir, H. V.; Han, M. J.; Koh, W.; Oh, S. J. Ligand Exchange and Impurity Doping in 2D CdSe Nanoplatelet Thin Films and Their Applications. *Adv Electron Mater* **2022**, *8* (1). https://doi.org/10.1002/aelm.202100739.

(48) Ha, S. K.; Shcherbakov-Wu, W.; Powers, E. R.; Paritmongkol, W.; Tisdale, W. A. Power-Dependent Photoluminescence Efficiency in Manganese-Doped 2D Hybrid Perovskite Nanoplatelets. *ACS Nano* **2021**, *15* (12), 20527–20538. https://doi.org/10.1021/acsnano.1c09103.

(49) Zhou, L.; Liao, J.; Huang, Z.; Wei, J.; Wang, X.; Chen, H.; Kuang, D. Intrinsic Self-Trapped Emission in 0D Lead-Free ($C_4H_{14}N_2)_2In_2Br_{10}$ Single Crystal. *Angewandte Chemie* **2019**, *131* (43), 15581–15586. https://doi.org/10.1002/ange.201907503.

(50) Ma, W.; Song, X.; Yin, J.; Fei, H. Intrinsic Self-Trapped Broadband Emission from Zinc Halide-Based Metal–Organic Frameworks. *Chemical Communications* **2021**, *57* (11), 1396–1399. https://doi.org/10.1039/D0CC07320B.

(51) Paritmongkol, W.; Powers, E. R.; Dahod, N. S.; Tisdale, W. A. Two Origins of Broadband Emission in Multilayered 2D Lead Iodide Perovskites. *J Phys Chem Lett* **2020**, *11* (20), 8565–8572. https://doi.org/10.1021/acs.jpclett.0c02214.

(52) Zhong, X.; Lee, K.; Choi, B.; Meggiolaro, D.; Liu, F.; Nuckolls, C.; Pasupathy, A.; De Angelis, F.; Batail, P.; Roy, X.; Zhu, X. Superatomic Two-Dimensional Semiconductor. *Nano Lett* **2018**, *18* (2), 1483–1488. https://doi.org/10.1021/acs.nanolett.7b05278.

(53) Zhu, T.; Yuan, L.; Zhao, Y.; Zhou, M.; Wan, Y.; Mei, J.; Huang, L. Highly Mobile Charge-Transfer Excitons in Two-Dimensional WS_2 /Tetracene Heterostructures. *Sci Adv* **2018**, *4* (1). https://doi.org/10.1126/sciadv.aao3104.

(54) Zhang, J.; Zhu, X.; Wang, M.; Hu, B. Establishing Charge-Transfer Excitons in 2D Perovskite Heterostructures. *Nat Commun* **2020**, *11* (1), 2618. https://doi.org/10.1038/s41467-020-16415-1.

(55) Ceballos, F.; Bellus, M. Z.; Chiu, H.-Y.; Zhao, H. Ultrafast Charge Separation and Indirect Exciton Formation in a MoS_2 –$MoSe_2$ van Der Waals Heterostructure. *ACS Nano* **2014**, *8* (12), 12717–12724. https://doi.org/10.1021/nn505736z.

(56) Wu, X.; Trinh, M. T.; Niesner, D.; Zhu, H.; Norman, Z.; Owen, J. S.; Yaffe, O.; Kudisch, B. J.; Zhu, X.-Y. Trap States in Lead Iodide Perovskites. *J Am Chem Soc* **2015**, *137* (5), 2089–2096. https://doi.org/10.1021/ja512833n.

(57) Valenta, J. Determination of Absolute Quantum Yields of Luminescing Nanomaterials over a Broad Spectral Range: From the Integrating Sphere Theory to the Correct Methodology. *Nanoscience Methods* **2014**, *3* (1), 11–27. https://doi.org/10.1080/21642311.2014.884288.

(58) Thirumal, K.; Chong, W. K.; Xie, W.; Ganguly, R.; Muduli, S. K.; Sherburne, M.; Asta, M.; Mhaisalkar, S.; Sum, T. C.; Soo, H. Sen; Mathews, N. Morphology-Independent Stable White-Light Emission from Self-Assembled Two-Dimensional Perovskites Driven by Strong Exciton–Phonon Coupling to the Organic Framework. *Chemistry of Materials* **2017**, *29* (9), 3947–3953. https://doi.org/10.1021/acs.chemmater.7b00073.

(59) Song, K. S.; Williams, R. T. *Self-Trapped Excitons*; Springer Berlin Heidelberg: Berlin, Heidelberg, 1993; Vol. 105. https://doi.org/10.1007/978-3-642-97432-8.

(60) Emin, D. *Polarons*; Cambridge University Press, 2012. https://doi.org/10.1017/CBO9781139023436.

(61) Hu, T.; Smith, M. D.; Dohner, E. R.; Sher, M.-J.; Wu, X.; Trinh, M. T.; Fisher, A.; Corbett, J.; Zhu, X.-Y.; Karunadasa, H. I.; Lindenberg, A. M. Mechanism for Broadband White-Light Emission from Two-Dimensional (110) Hybrid Perovskites. *J Phys Chem Lett* **2016**, *7* (12), 2258–2263. https://doi.org/10.1021/acs.jpclett.6b00793.

(62) Cunningham, P. D.; Hanbicki, A. T.; McCreary, K. M.; Jonker, B. T. Photoinduced Bandgap Renormalization and Exciton Binding Energy Reduction in WS_2. *ACS Nano* **2017**, *11* (12), 12601–12608. https://doi.org/10.1021/acsnano.7b06885.

(63) Feng, S.; Yang, Y.; Gao, L.; Watanabe, K.; Taniguchi, T.; Hu, Z.; Lu, J.; Ni, Z. Tunable Self-Trapped Excitons in 2D Layered Rubrene. *Appl Phys Lett* **2021**, *118* (25). https://doi.org/10.1063/5.0049942.

(64) Li, S.; Luo, J.; Liu, J.; Tang, J. Self-Trapped Excitons in All-Inorganic Halide Perovskites: Fundamentals, Status, and Potential Applications. *J Phys Chem Lett* **2019**, *10* (8), 1999–2007. https://doi.org/10.1021/acs.jpclett.8b03604.

(65) Mooney, J.; Kambhampati, P. Get the Basics Right: Jacobian Conversion of Wavelength and Energy Scales for Quantitative Analysis of Emission Spectra. *J Phys Chem Lett* **2013**, *4* (19), 3316–3318. https://doi.org/10.1021/jz401508t.

(66) Perdew, J. P.; Burke, K.; Ernzerhof, M. Generalized Gradient Approximation Made Simple. *Phys Rev Lett* **1996**, *77* (18), 3865–3868. https://doi.org/10.1103/PhysRevLett.77.3865.

(67) Giannozzi, P.; Baroni, S.; Bonini, N.; Calandra, M.; Car, R.; Cavazzoni, C.; Ceresoli, D.; Chiarotti, G. L.; Cococcioni, M.; Dabo, I.; Dal Corso, A.; de Gironcoli, S.; Fabris, S.; Fratesi, G.; Gebauer, R.; Gerstmann, U.; Gougoussis, C.; Kokalj, A.; Lazzeri, M.; Martin-Samos, L.; Marzari, N.; Mauri, F.; Mazzarello, R.; Paolini, S.; Pasquarello, A.; Paulatto, L.; Sbraccia, C.; Scandolo, S.; Sclauzero, G.; Seitsonen, A. P.; Smogunov, A.; Umari, P.; Wentzcovitch, R. M. QUANTUM ESPRESSO: A Modular and Open-Source Software Project for Quantum Simulations of Materials. *Journal of Physics: Condensed Matter* **2009**, *21* (39), 395502. https://doi.org/10.1088/0953-8984/21/39/395502.

(68) Grimme, S. Semiempirical GGA-type Density Functional Constructed with a Long-range Dispersion Correction. *J Comput Chem* **2006**, *27* (15), 1787–1799. https://doi.org/10.1002/jcc.20495.

Chapter 6

Thermodynamic Stability and Excitonic Properties in 2D $AgX_{1-n}Y_nPh$ (X,Y = S, Se, Te) Alloys

The basis of this chapter has been adapted from:
Woo Seok Lee, Yeongsu Cho, Watcharaphol Paritmongkol, Tomoaki Sakurada, Seung Kyun Ha, Heater J. Kulik, William A. Tisdale. "Thermodynamic Stability and Excitonic Properties in 2D Silver Phenylchalcogenide Alloys" *In manuscript* (2024).

6.1 Abstract

Alloying is a powerful strategy for manipulating electronic band structures and optical properties of semiconductors. In this chapter, we investigate the thermodynamic stability and excitonic properties in alloys of two-dimensional (2D) hybrid organic-inorganic semiconductors known as silver phenylchalcogenides – AgEPh (E = S, Se, Te). Through systematic structural and optical characterizations, we demonstrate that the AgSePh-AgTePh system forms homogeneous alloys ($AgSe_{1-n}Te_nPh$, $0 \leq n \leq 1$) across all compositions, featuring tunable excitonic absorption resonances in the ultraviolet-visible range. Using temperature-dependent photoluminescence and sub-gap excitation spectroscopy, we reveal dual emissions spanning blue to near-infrared range, arising from band-edge free-exciton and self-trapped exciton states, which dynamically vary with composition and temperature. In contrast, we identify a miscibility gap in the AgSPh-AgSePh and AgSPh-AgTePh systems through composition-dependent X-ray diffraction, absorption and photoluminescence analysis. Density functional theory calculations of the free energy of mixing predict that the homogeneous alloy is favored over phase separation in the AgSePh-AgTePh system at room temperature, whereas phase separation is more favorable for both AgSPh-AgSePh and AgSPh-AgTePh systems than alloying. These experimental and theoretical results are explained by differences in the crystal structure of AgSPh and AgSePh/AgTePh.

6.2 Introduction

The bandgap that determines overall electronic and optical properties is one of the most important parameters in semiconductors for almost all applications including transistors, solar cells, light-emitting devices, photodetectors.[1] Many techniques have been developed to obtain a desirable bandgap for target applications by using strain effects[2,3] and/or quantum confinement effects.[4,5] Among them, alloying is a powerful technique for engineering electronic band structures and achieving application-specific properties.[6] By mixing two or several semiconductors at atomic scales, alloying allows to create all the bandgaps between those of the constituent semiconductors in principle and to obtain otherwise non-existent properties. This approach has been widely used from conventional bulk inorganic semiconductors[7–9] to low-dimensional hybrid organic-inorganic semiconductors[10–12] for wide applications in electronic and optic devices.

Silver phenylchalcogenides – AgEPh (E = S, Se, Te)[13–27] are two-dimensional (2D) semiconductors belonging to a broader class of hybrid organic-inorganic materials, metal organochalcogenides (MOCs).[28–37] These 2D semiconductors crystallize in the form of layered van der Waals solids consisting of inorganic AgE sheets covalently sandwiched by phenyl rings (Figure 6.1a). Despite having similar monoclinic structures and similar compositions,[13,23] each AgEPh exhibits unique excitonic properties. Whereas AgSePh and AgTePh show multiple excitonic absorption resonances in the visible ranges,[14,16,22] AgSPh exhibits a single absorption peak in the ultraviolet region at room temperature.[16] Furthermore, AgSPh exhibits no photoluminescence at room temperature while AgSePh and AgTePh exhibit narrow band-edge free-exciton emission and broad self-trapped exciton emission, respectively.[16,22] Strikingly different excitonic behaviors of AgEPh prompt exploration of excitonic phenomena in alloys of these emerging 2D semiconductors.

In this work, we explore the thermodynamic stability and excitonic properties of silver phenylchalcogenide alloys ($AgX_{1-n}Y_nPh$, $0 \leq n \leq 1$; X, Y = S, Se, Te). Systematic structural and optical characterizations show the formation of homogeneous $AgSe_{1-n}Te_nPh$ alloys at all compositions and, in contrast, a miscibility gap in the AgSPh-AgSePh and AgSPh-AgTePh systems. Composition- and temperature-dependent optical spectroscopic studies on $AgSe_{1-n}Te_nPh$ films reveal tunable excitonic absorption resonances in ultraviolet-visible range as well as dual emission from band-edge free-exciton and self-trapped exciton states in blue to near-infrared range.

Furthermore, we employ density functional theory calculations of the free energy of mixing to understand thermodynamic stability of $AgX_{1-n}Y_nPh$ alloys. Finally, we establish a correlation between the thermodynamic stability of $AgX_{1-n}Y_nPh$ alloys and the differences/similarities in the crystal structure of the parent materials.

6.3 Results and Discussion

6.3.1 Preparation and structural properties of $AgSe_{1-n}Te_nPh$ films

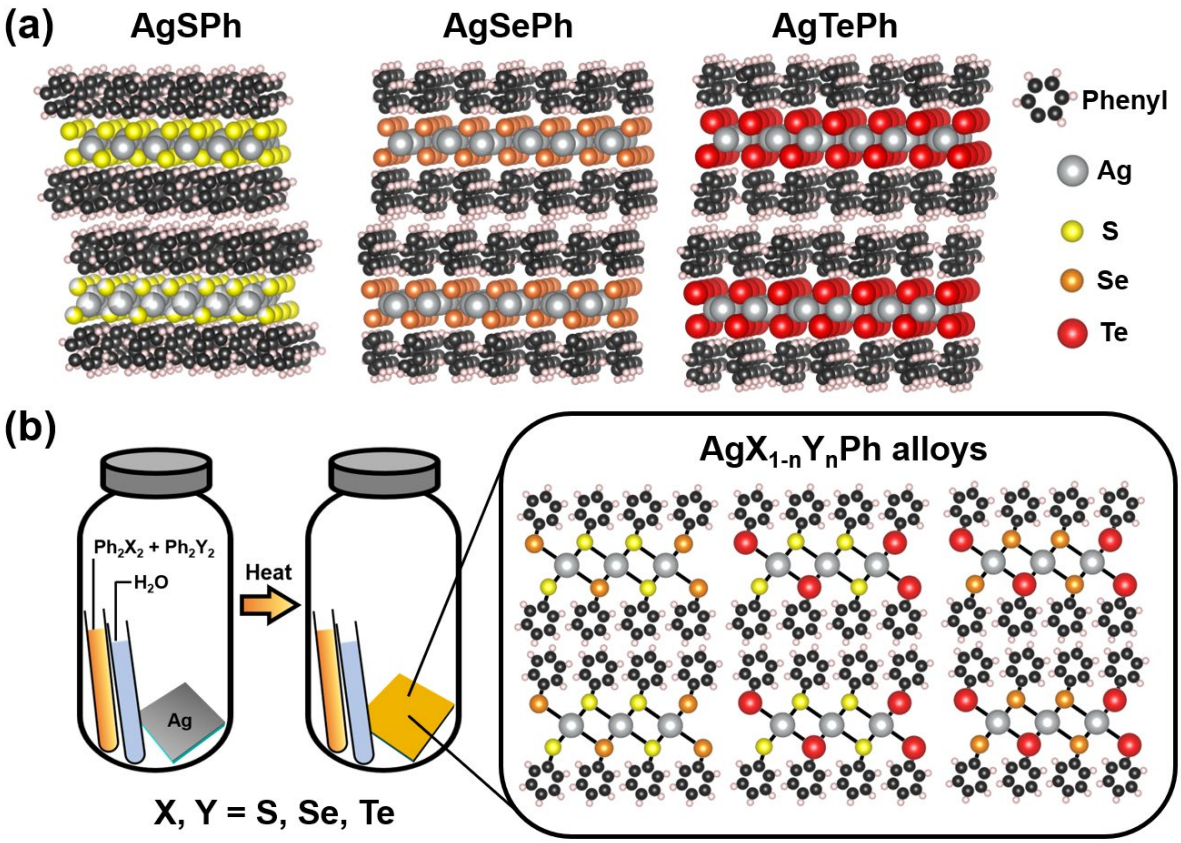

Figure 6.1 (a) Layered 2D structures of AgSPh, AgSePh and AgTePh. (b) Schematic of a chemical transformation reaction in a sealed container containing a Ag film, deionized water, and a mixture of diphenyl dichalcogenides (Ph_2X_2 + Ph_2Y_2) for creating $AgX_{1-n}Y_nPh$ alloy films (X, Y = S, Se, Te).

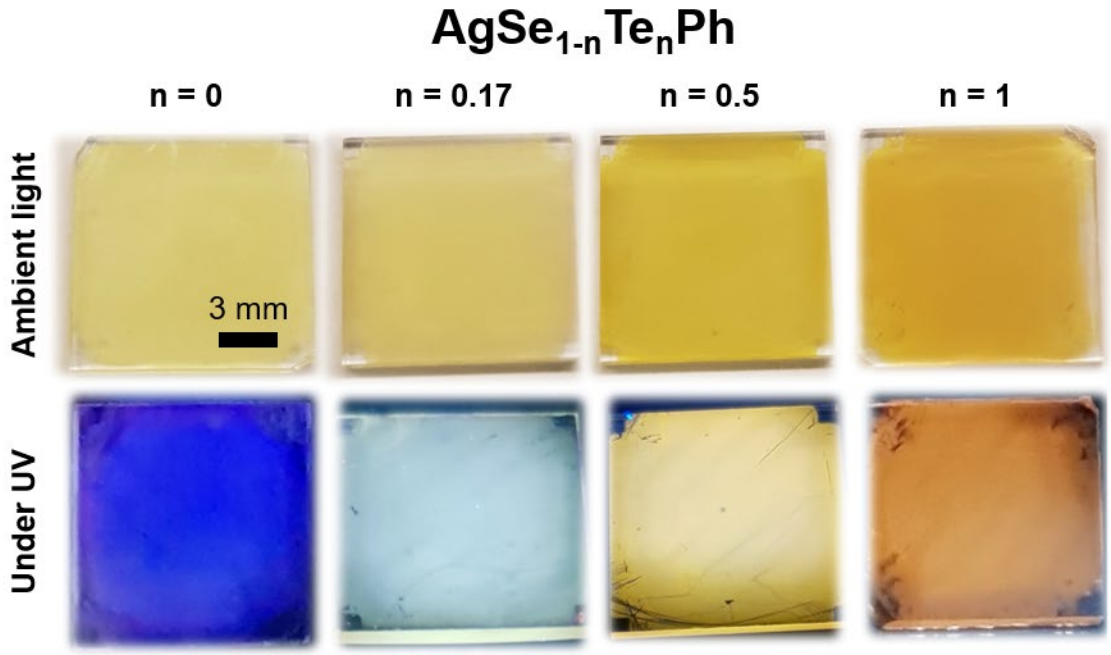

Figure 6.2 Photographs of $AgSe_{1-n}Te_nPh$ films under ambient light (top) and 365 nm light-emitting diode excitation (bottom). The bottom images were taken through a 450 nm long-pass filter to remove scattering from the excitation light.

Silver phenylselenide-telluride ($AgSe_{1-n}Te_nPh$) films were prepared by a vapor-phase chemical transformation method with some modifications (See Methods and Figure 6.1b).[17,22,26] Briefly, a 15 nm thick Ag film was deposited on a pre-cleaned glass substrate by a thermal evaporation. Then, the substrate was placed inside a sealed pressure vessel containing deionized water and a mixture of diphenyl diselenide (Ph_2Se_2) and diphenyl ditelluride (Ph_2Te_2) powder. After heating the vessel at 100 °C for 3-4 days, the Ag film was transformed into $AgSe_{1-n}Te_nPh$ films (Figure 6.2). The ratio of Ph_2Se_2 and Ph_2Te_2 in the precursor mixture was varied to control the actual Se and Te ratio in the resulting $AgSe_{1-n}Te_nPh$ films. Throughout the thesis, we refer to the mole fraction of Ph_2Te_2 in the precursor mixture ($Ph_2Te_2/(Ph_2Se_2 + Ph_2Te_2)$) as *n* in $AgSe_{1-n}Te_nPh$ films, rather than the actual mole fraction of Te in films (Te/(Se + Te)).

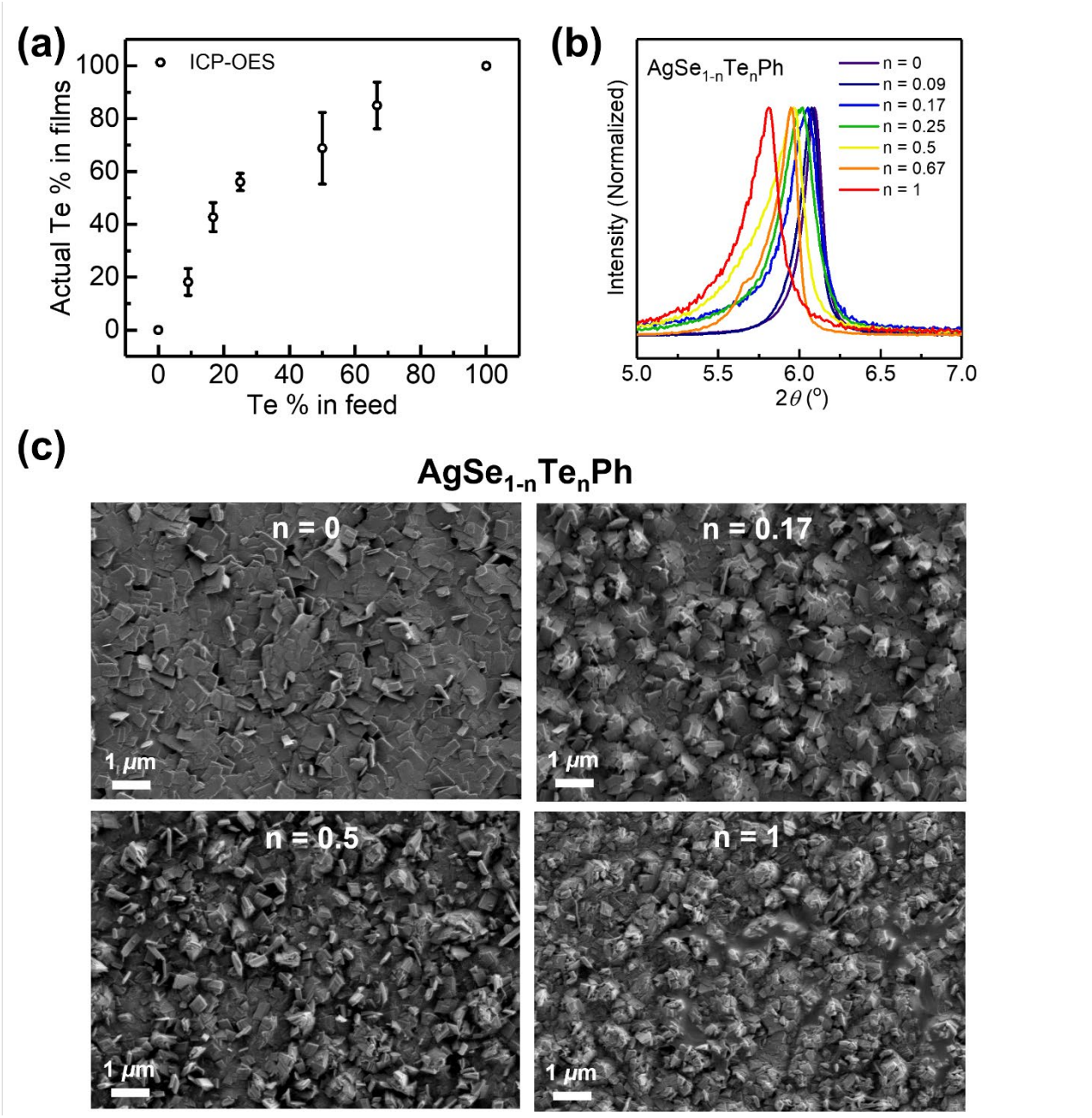

Figure 6.3 (a) Experimentally measured Te fraction in $AgSe_{1-n}Te_nPh$ films using ICP-OES vs. Te fraction in the precursor mixture. (b) Zoomed-in X-ray diffractograms showing (002) diffraction peaks of $AgSe_{1-n}Te_nPh$ films. (Cu K$\boldsymbol{\alpha}$ radiation, $\boldsymbol{\lambda}$ = 1.541 Å) (c) Scanning electron micrographs of $AgSe_{1-n}Te_nPh$ films.

The compositional and structural properties of $AgSe_{1-n}Te_nPh$ films were investigated using inductively coupled plasma optical emission spectroscopy (ICP-OES), powder X-ray diffraction (XRD) and scanning electron microscopy (SEM) (Figure 6.3). In Figure 6.3a, we compare the

experimentally measured Te fraction in $AgSe_{1-n}Te_nPh$ films with the Te fraction in the precursor (n). The actual Te fraction in $AgSe_{1-n}Te_nPh$ films monotonically increased with n. The actual Te fraction in $AgSe_{1-n}Te_nPh$ films was higher than Te fraction in feed materials. This may be due to the faster reaction kinetics between Ag and Ph_2Te_2 compared to Ag and Ph_2Se_2, as evidenced by the more rapid formation of AgTePh films compared to AgSePh films under the identical reaction condition. Figures 6.3b and 6.4 illustrates the XRD patterns of $AgSe_{1-n}Te_nPh$ films (Cu Kα radiation, λ = 1.541 Å). All $AgSe_{1-n}Te_nPh$ films showed evenly spaced (00h) diffraction peaks below 20°, corresponding to the stacking periodicity of the 2D structures. As n increased, the (00h) diffraction peaks of $AgSe_{1-n}Te_nPh$ films monotonically shifted to smaller diffraction angles without the emergence of new diffraction peaks, indicating the formation of homogeneous $AgSe_{1-n}Te_nPh$ alloys and lattice expansion. SEM micrographs revealed a sub-microcrystalline morphology in $AgSe_{1-n}Te_nPh$ films (Figures 6.3c and 6.5). In general, the lateral size of crystals decreased from ~500 nm (AgSePh) to ~200 nm (AgTePh) and the alignment of crystals changed from mostly parallel to the substrate (AgSePh) to relatively random (AgTePh) with increasing Te fraction.

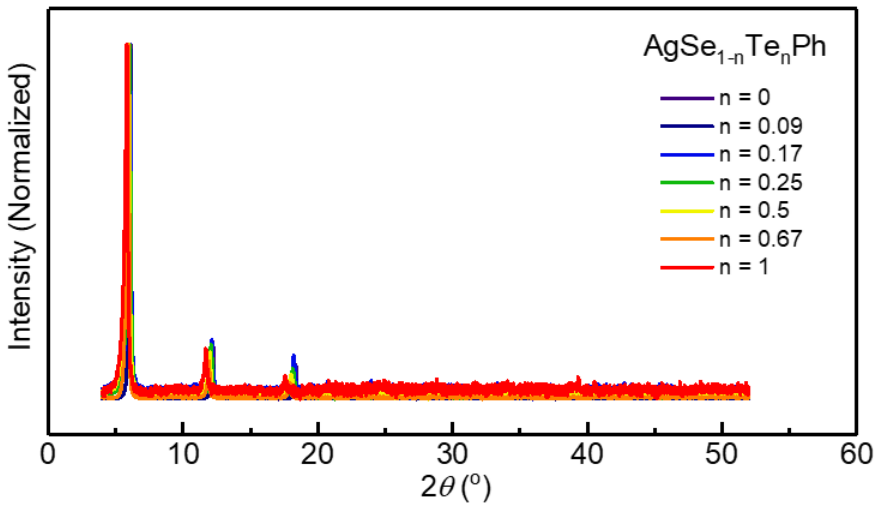

Figure 6.4 X-ray diffractograms of $AgSe_{1-n}Te_nPh$ films. (Cu Kα radiation, λ = 1.541 Å)

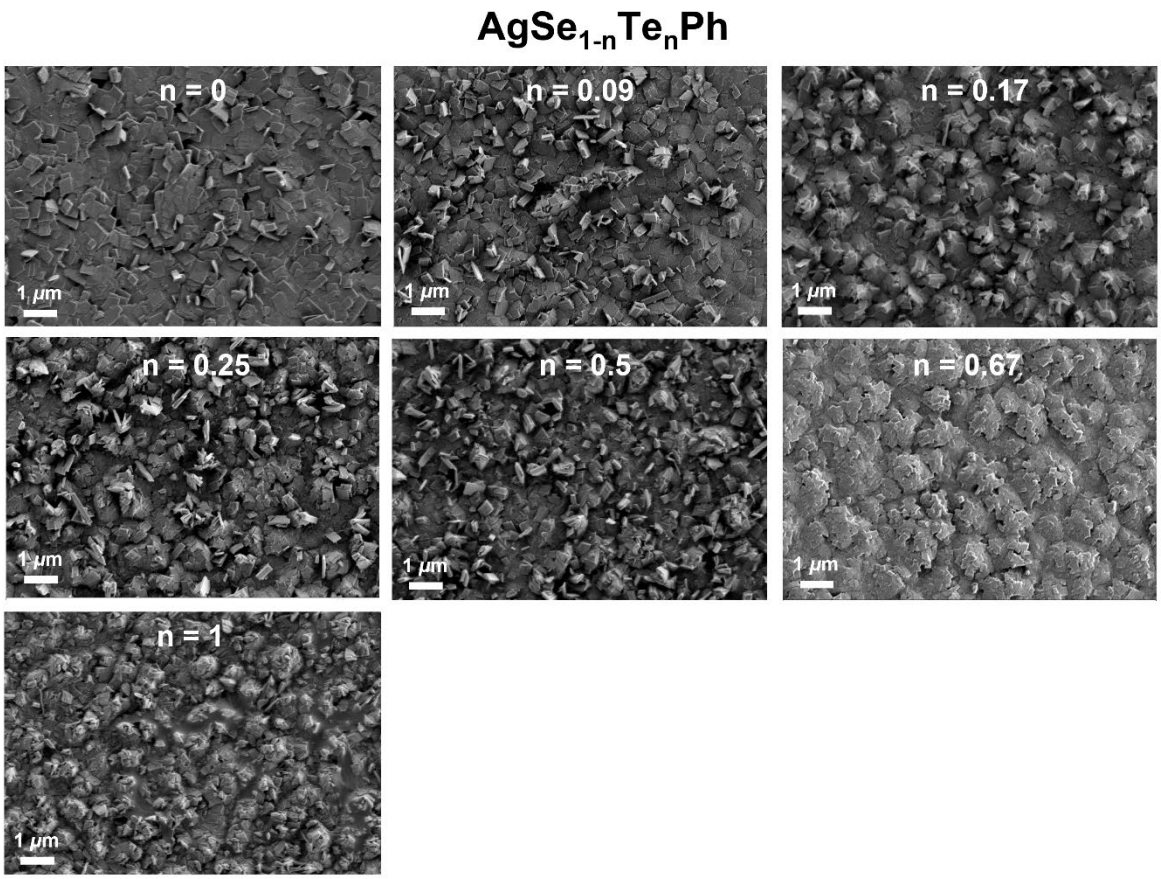

Figure 6.5 Scanning electron micrographs of $AgSe_{1-n}Te_nPh$ films.

6.3.2 Optical properties of $AgSe_{1-n}Te_nPh$ films

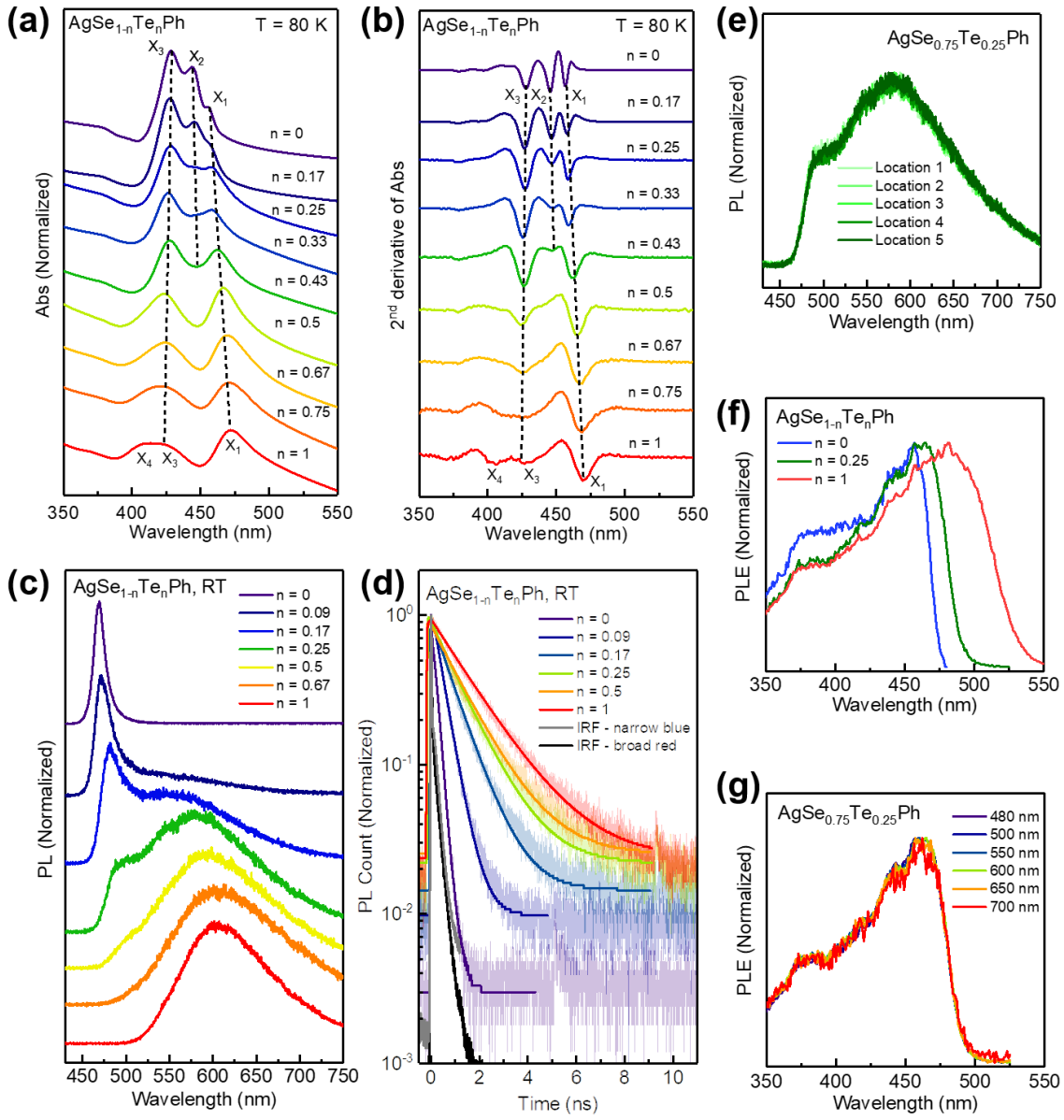

Figure 6.6 (a) Absorption spectra and (b) their second derivatives of $AgSe_{1-n}Te_nPh$ films at 80 K. (c) Photoluminescence spectra and (d) time-resolved photoluminescence traces of $AgSe_{1-n}Te_nPh$ films at room temperature. (e) Location-dependent photoluminescence spectra of the $AgSe_{0.75}Te_{0.25}Ph$ film at room temperature. (f) Photoluminescence excitation spectra of AgSePh (emission wavelength: 500 nm), $AgSe_{0.75}Te_{0.25}Ph$ (emission wavelength: 600 nm) and AgTePh (emission wavelength: 650 nm) films at room temperature. (g) Photoluminescence excitation spectra of the $AgSe_{0.75}Te_{0.25}Ph$ film as a function of emission wavelength at room temperature.

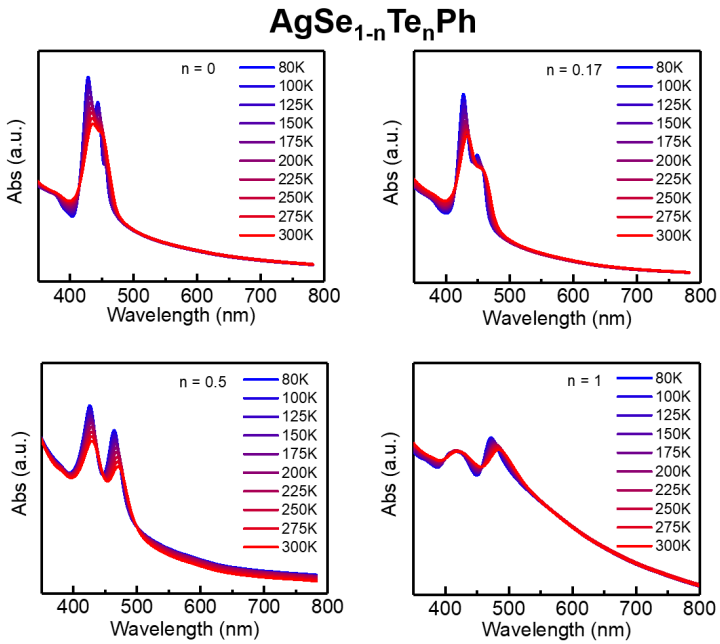

Figure 6.7 Temperature-dependent absorption spectra of $AgSe_{1-n}Te_nPh$ films.

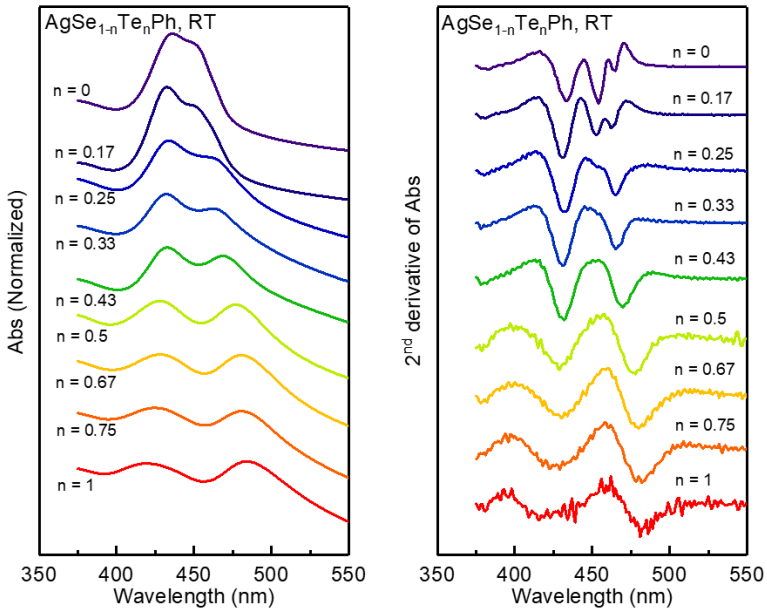

Figure 6.8 Absorption spectra and their second derivatives of $AgSe_{1-n}Te_nPh$ films at room temperature.

Absorption spectra and their second derivatives of $AgSe_{1-n}Te_nPh$ films at 80 K are shown in Figure 6.6a,b. The AgSePh film exhibited three distinct excitonic absorption peaks at 457 nm (2.71 eV, X_1), 446 nm (2.78 eV, X_2), and 428 nm (2.90 eV, X_3), consistent with previous reports.[14,16,17,22] As the Te fraction increased in $AgSe_{1-n}Te_nPh$ films, the X_1 peak monotonically red-shifted from 457 nm (2.71 eV) in AgSePh to 469 nm (2.64 eV) in AgTePh, whereas the X_3 peak monotonically blue-shifted from 428 nm (2.90 eV) in AgSePh to 424 nm (2.92 eV) in AgTePh. In contrast, the position of the X_2 peak remained relatively unchanged as the Te fraction increased. More strikingly, its absorption intensity was reduced with increasing Te fraction, becoming unresolvable when the Te fraction exceeded 50 %. This reduction in intensity suggests a significant decrease in the oscillator strength of the X_2 exciton as the Te fraction increased. Interestingly, another excitonic absorption peak emerged at 406 nm (3.05 eV, X_4) in AgTePh. As the temperature increases to room temperature, all the X_n excitonic peaks in $AgSe_{1-n}Te_nPh$ films red-shifted and broadened (Figures 6.7 and 6.8).

The room temperature photoluminescence (PL) spectra and time-resolved PL traces of $AgSe_{1-n}Te_nPh$ films are shown in Figure 6.6c,d. The AgSePh film exhibited narrow blue emission centered at 467 nm, previously assigned to the band-edge free-exciton emission.[16,21,22] As the Te fraction increased, this narrow free-exciton emission peak gradually red-shifted (Figure 6.9). Additionally, a broad emission centered around 550 nm emerged, which also gradually red-shifted with increasing Te fraction, dominating over the narrow free-exciton emission. Eventually, the AgTePh film exhibited a single broadband emission, previously assigned to the self-trapped exciton emission.[22] The PL decay of $AgSe_{1-n}Te_nPh$ films at room temperature was well fit by a mono-exponential function convolved with the instrument response function (Figure 6.6d). The extracted lifetime increased monotonically from ~100 ps in AgSePh to ~1.6 ns in AgTePh as the Te fraction increased (Figure 6.10). The spectral shape of PL emission and PL decay traces of $AgSe_{1-n}Te_nPh$ films were almost invariant to the excitation spot location (Figures 6.6e, 6.10 and 6.11), supporting the homogeneity of alloy films. Moreover, spatially homogeneous PL suggests that the red-shifted broad emission feature in $AgSe_{1-n}Te_nPh$ films arise from an intrinsic mechanism such as self-trapped exciton emission in AgTePh.

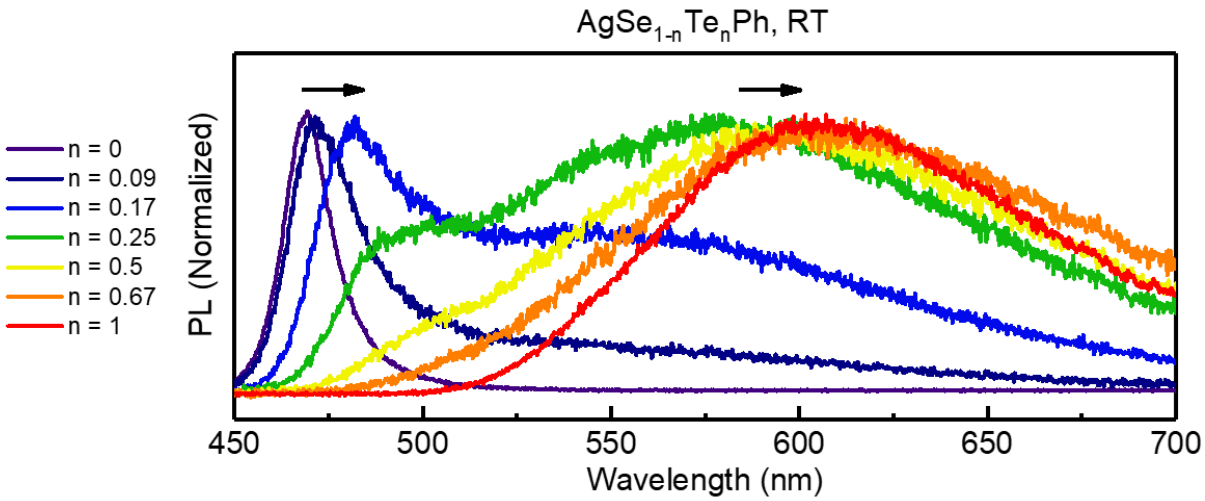

Figure 6.9 Photoluminescence spectra of $AgSe_{1-n}Te_nPh$ films at room temperature. Arrows indicate that narrow emission at ~ 470 nm and broadband emission at ~ 550 nm are both red-shifted as Te fraction increases.

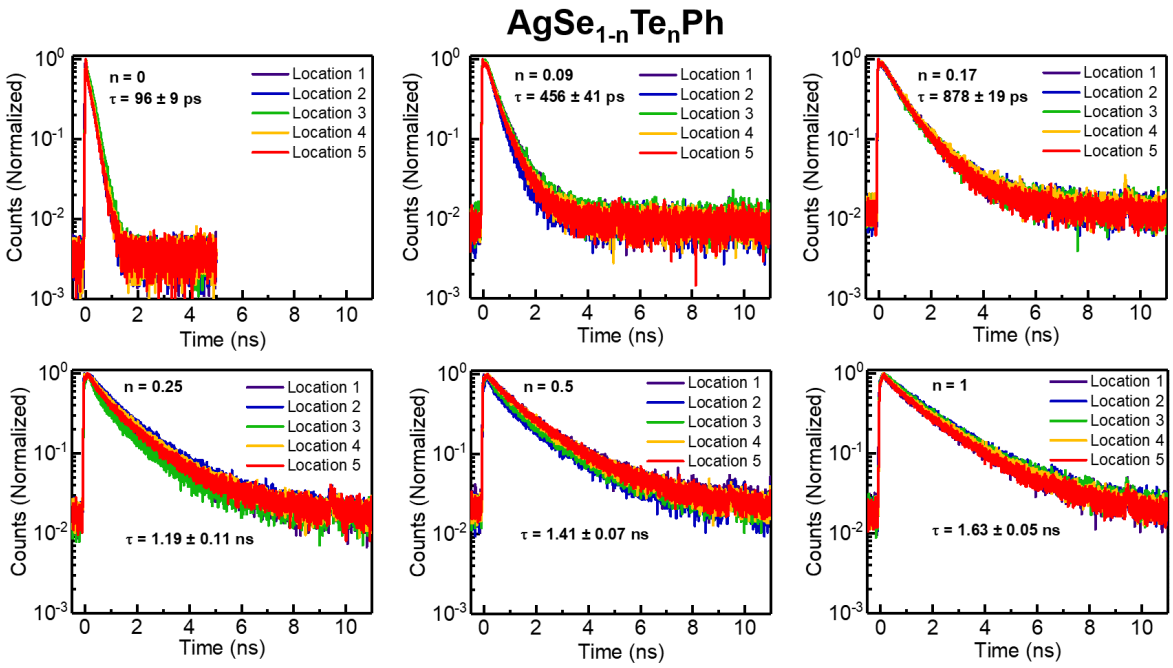

Figure 6.10 Location-dependent time-resolved photoluminescence traces of $AgSe_{1-n}Te_nPh$ films at room temperature.

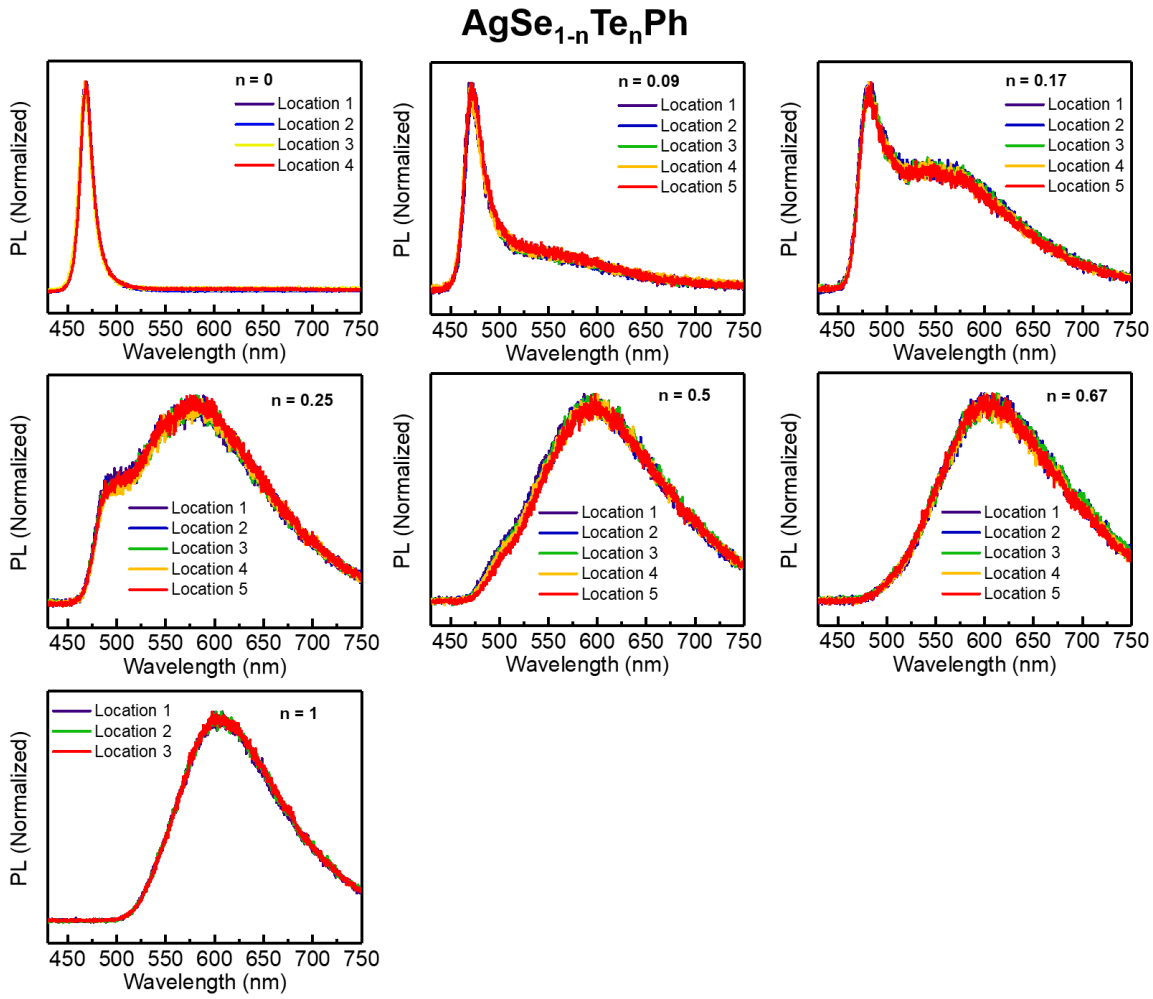

Figure 6.11 Location-dependent photoluminescence spectra of $AgSe_{1-n}Te_nPh$ films at room temperature.

To further assess the degree of homogeneity in $AgSe_{1-n}Te_nPh$ films, we measured PL excitation (PLE) spectra of AgSePh and AgTePh films, and a $AgSe_{0.75}Te_{0.25}Ph$ film as a representative of alloy films (Figures 6.6f,g and 6.12). The PLE spectra of $AgSe_{1-n}Te_nPh$ films exhibited a red-shift as the Te fraction increased, consistent with the red-shift of the X_1 exciton in absorption spectra. Importantly, the PLE spectra of the $AgSe_{0.75}Te_{0.25}Ph$ film showed no dependence on emission wavelength covering a range from 480 nm to 700 nm. This indicates that both the narrow blue emission and the red-shifted broad emission arise from a single, identical optical transition.

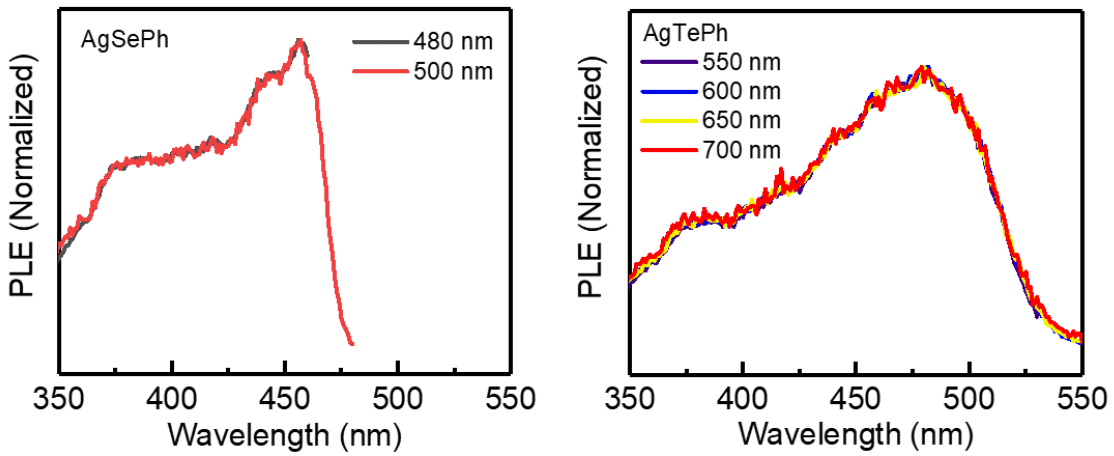

Figure 6.12 Photoluminescence excitation spectra of AgSePh and AgTePh films as a function of emission wavelength at room temperature.

6.3.3 Temperature-dependent photoluminescence of $AgSe_{1-n}Te_nPh$ films

To investigate the mechanisms of light emission in $AgSe_{1-n}Te_nPh$ films, we performed temperature-dependent PL micro-spectroscopy from 5 K to 300 K on the $AgSe_{0.83}Te_{0.17}Ph$ film as a representative case (Figure 6.13). The free-exciton emission peak at ~480 nm (2.58 eV) gradually blue-shifted with decreasing temperature, while the broadband emission maintained its peak position with a narrowing PL line width at lower temperatures (Figure 6.13a). Additionally, as the temperature decreased, the broadband emission became more dominant than the free-exciton emission which became undetectable below 125 K. The broadband emission feature exhibited the spectral shape invariant to location and excitation power, and its intensity scaled linearly with excitation laser power, suggesting its intrinsic mechanism such as self-trapped exciton emission in AgTePh (Figure 6.14). Moreover, the broadband emission spanning between 550-750 nm was not observed upon subgap (532 nm, 2.33 eV) laser excitation, but only observed upon resonant (405 nm, 3.06 eV) laser excitation, further ruling out extrinsic defect-derived midgap states as its origin (Figure 6.15).

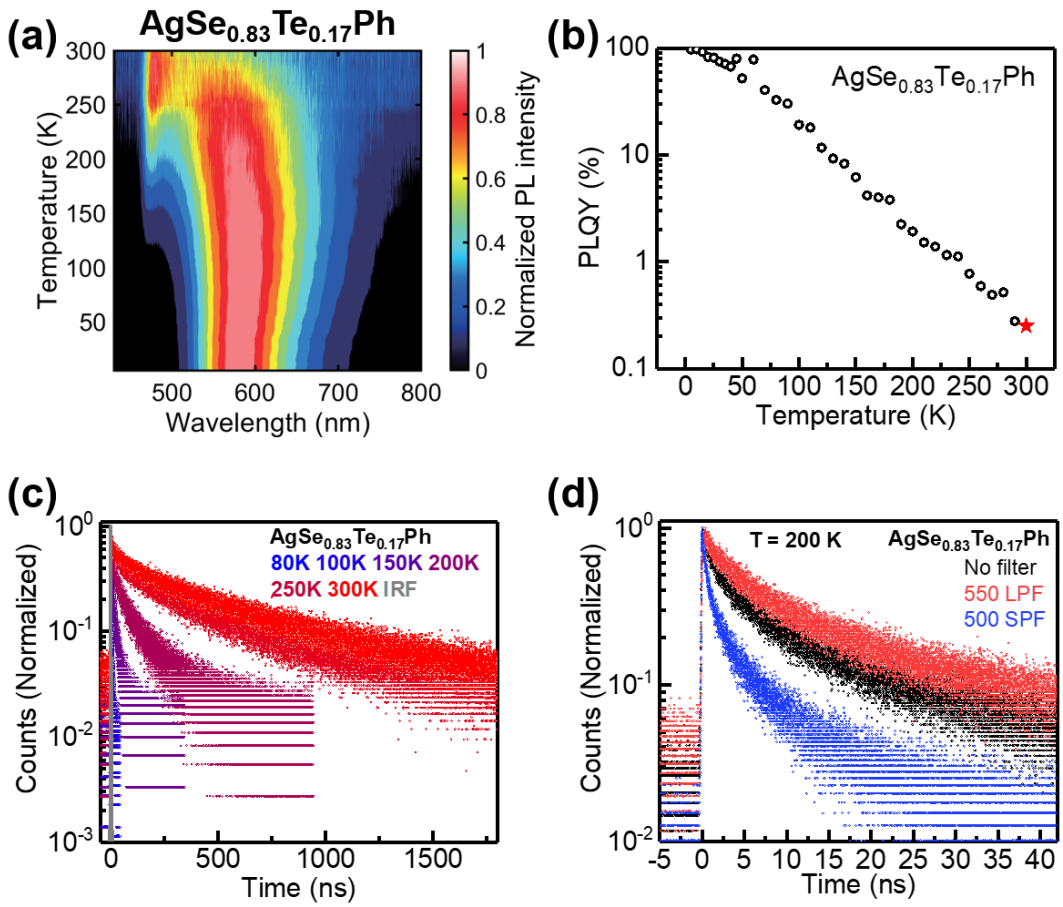

Figure 6.13 (a) Temperature-dependent normalized photoluminescence (PL) spectra of the $AgSe_{0.83}Te_{0.17}Ph$ film. Temperature-dependent (b) PL quantum yield and (c) time-resolved PL (TRPL) of the $AgSe_{0.83}Te_{0.17}Ph$ film, integrated over the entire emission. IRF denotes the instrument response function of the measurement. (d) TRPL of the $AgSe_{0.83}Te_{0.17}Ph$ film at 200 K with no filter (black), 500 nm shortpass filter (blue), and 550 nm longpass filter (red) in the collection path, respectively.

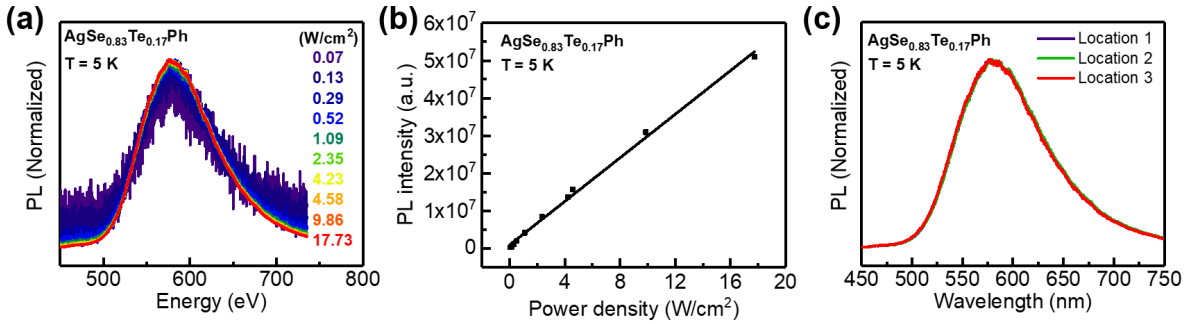

Figure 6.14 Power-dependent (a) normalized photoluminescence spectra and (b) photoluminescence intensities of the $AgSe_{0.83}Te_{0.17}Ph$ film at 5 K. (c) Location-dependent normalized photoluminescence spectra of the $AgSe_{0.83}Te_{0.17}Ph$ film at 5 K.

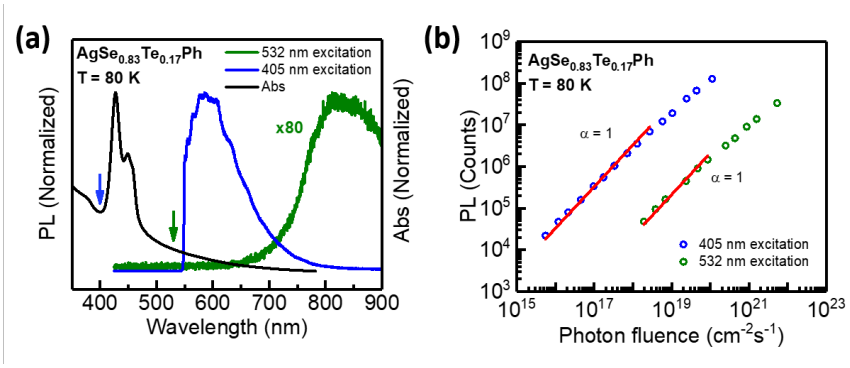

Figure 6.15 (a) Photoluminescence spectra of the $AgSe_{0.83}Te_{0.17}Ph$ film at 80 K upon resonant (blue) and subgap (green) laser excitation. (b) Power-dependent photoluminescence intensities of the $AgSe_{0.83}Te_{0.17}Ph$ film at 80 K upon resonant excitation and subgap exctiation with fits to $I \propto P^{\alpha}$ where $\alpha = 1$. Linear power dependence rules out any contribution of two-photon absorption to the measured spectra in (a).

The temperature-dependent PL quantum yield (PLQY) of the overall spectrally integrated emission of the $AgSe_{0.83}Te_{0.17}Ph$ film is shown in Figure 6.13b. The overall PLQY of the $AgSe_{0.83}Te_{0.17}Ph$ film increased monotonically with decreasing temperature from ~0.27% at room temperature to near unity at 5 K (Figures 6.13b and 6.16). Figure 6.13c shows temperature-dependent spectrally integrated PL decay from 80 K to 300 K of the $AgSe_{0.83}Te_{0.17}Ph$ film. Because the overall PL decay was not well described by a mono-exponential function below 250 K, the PL lifetime was extracted by the time at which the PL count is reduced to 1/e (≈ 0.368) throughout the temperature range. The extracted PL lifetimes of the $AgSe_{0.83}Te_{0.17}Ph$ film monotonically increased from 0.9 ns at 300 K to 140 ns at 80 K (Figure 6.17).

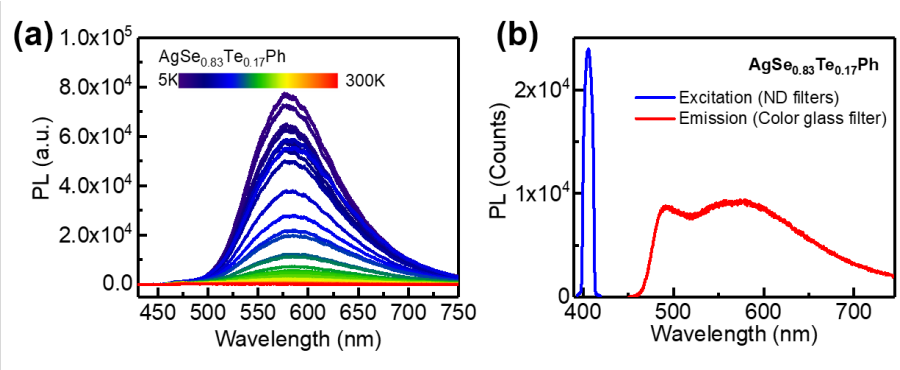

Figure 6.16 (a) Temperature-dependent PL spectra of the $AgSe_{0.83}Te_{0.17}Ph$ film. (b) The differences of spectra in the excitation (blue) and the emission (red) regions of a photoluminescence quantum yield (PLQY) measurement on the $AgSe_{0.83}Te_{0.17}Ph$ film. The ratio of integrated emission and excitation signals after the correction from neutral density (ND) filters gives PLQY of ~0.27% for the $AgSe_{0.83}Te_{0.17}Ph$ film.

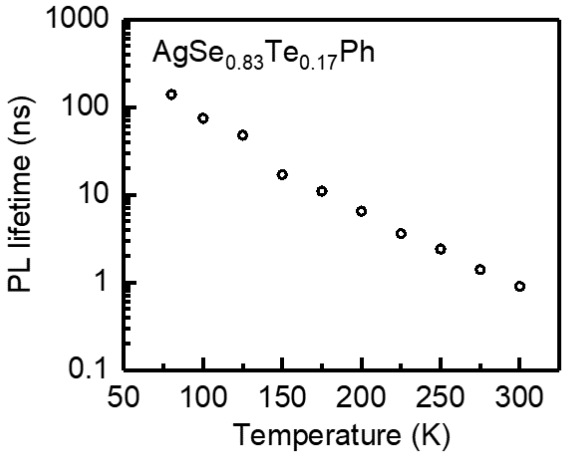

Figure 6.17 Temperature-dependent photoluminescence lifetimes of the $AgSe_{0.83}Te_{0.17}Ph$ film.

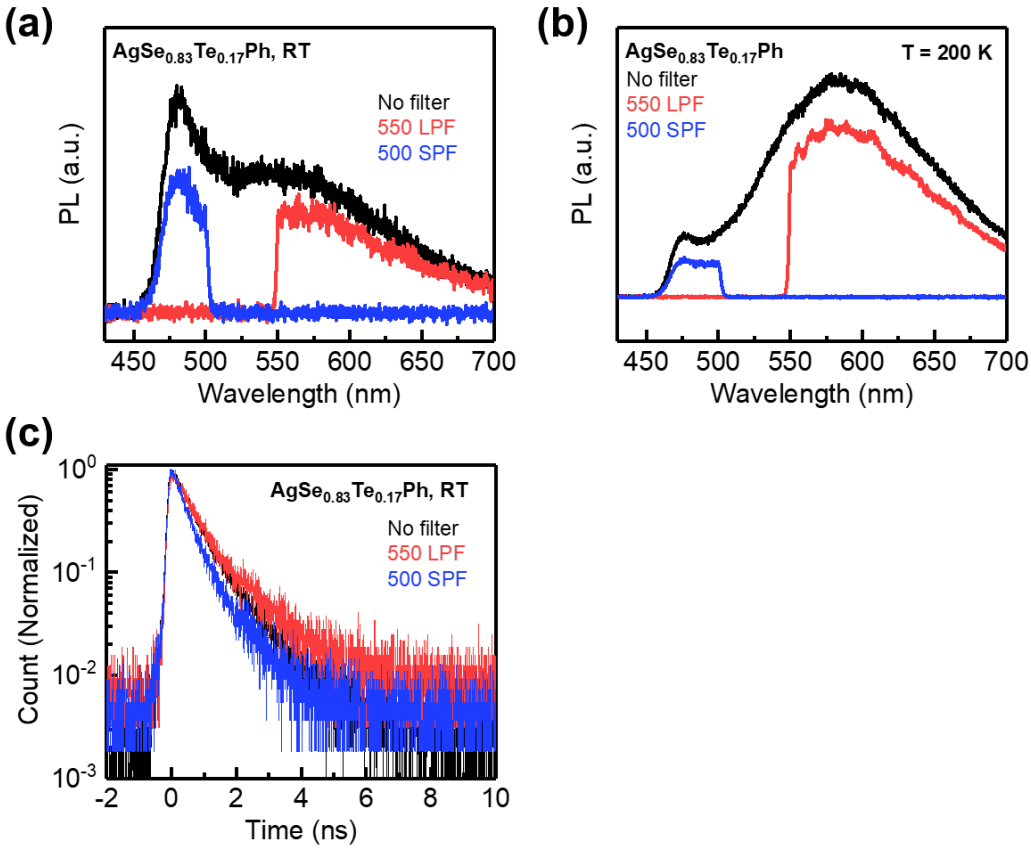

Figure 6.18 Photoluminescence spectra of the $AgSe_{0.83}Te_{0.17}Ph$ film (a) at room temperature and (b) at 200 K with no filter (black), 500 nm shortpass filter (blue), and 550 nm longpass filter (red) in the collection path, respectively. (c) Time-resolved photoluminescence traces of the $AgSe_{0.83}Te_{0.17}Ph$ film at 200 K with no filter (black), 500 nm shortpass filter (blue), and 550 nm longpass filter (red) in the collection path, respectively.

To investigate emission wavelength-dependent PL decay dynamics in the $AgSe_{0.83}Te_{0.17}Ph$ film, we selectively collected emissions with wavelength shorter than 500 nm and longer than 550 nm using short-pass and long-pass filters, respectively (Figure 6.13d). At room temperature, the $AgSe_{0.83}Te_{0.17}Ph$ film exhibited relatively similar PL decay dynamics (~ 0.9 ns) for both short-wavelength emission (<500 nm) and long-wavelength emission (>550 nm) (Figure 6.18). However, when the sample was cooled to 200 K, the long-wavelength PL decayed much slower (~7.4 ns) compared to room temperature, while the short-wavelength PL still exhibited fast decay dynamics (~ 1 ns). As the broadband emission with long wavelengths became more dominant over short-wavelength free-exciton emission with decreasing temperature, the trends of monotonically increasing PLQY and PL lifetimes of the $AgSe_{0.83}Te_{0.17}Ph$ film at lower temperatures are primarily contributed by the broadband emission. These trends in the temperature-dependent PLQY and PL lifetimes of broadband emission in the $AgSe_{0.83}Te_{0.17}Ph$ film are consistent with the temperature-dependent behavior of self-trapped exciton emission in AgTePh.[22] Similar trends were also observed in the $AgSe_{0.5}Te_{0.5}Ph$ film (Figure 6.19).

Based on all of the experimental observations reported above, we conclude that AgSePh and AgTePh systems form complete solid solutions ($AgSe_{1-n}Te_nPh$, $0 \leq n \leq 1$) at all compositions, as supported by XRD, absorption, steady-state PL, time-resolved PL, and PLE analysis. Notably, $AgSe_{1-n}Te_nPh$ exhibits dual emission of narrow free-exciton emission and red-shifted broad self-trapped exciton emission. The self-trapped exciton emission becomes gradually dominant over free-exciton emission as the Te fraction increases, suggesting a strengthening of exciton-phonon coupling with increasing Te fraction.

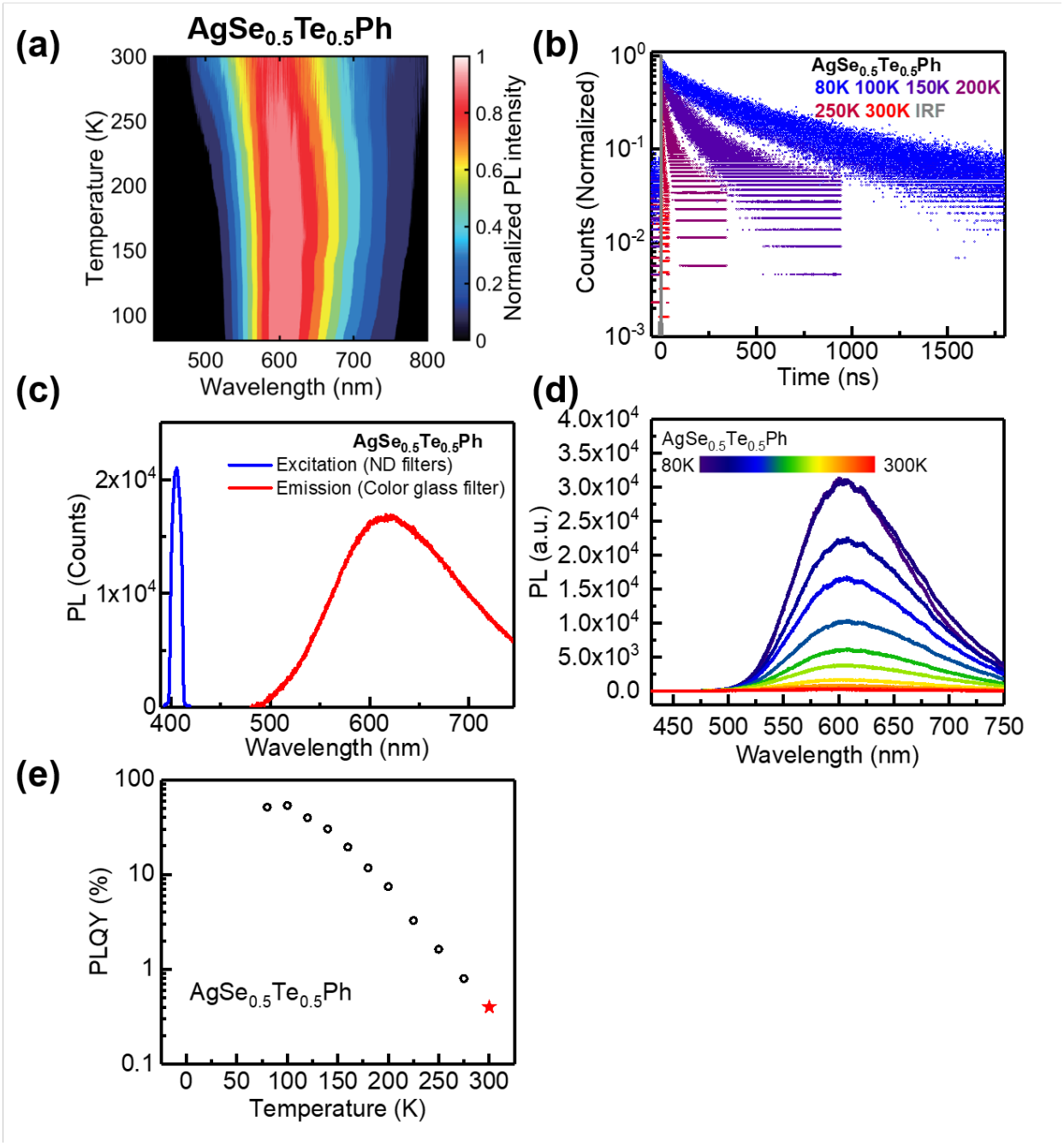

Figure 6.19 (a) Temperature-dependent normalized photoluminescence (PL) spectra of the $AgSe_{0.5}Te_{0.5}Ph$ film. (b) Temperature-dependent time-resolved photoluminescence of overall spectrally integrated emission of the $AgSe_{0.5}Te_{0.5}Ph$ film. (c) The differences of spectra in the excitation (blue) and the emission (red) regions of a photoluminescence quantum yield (PLQY) measurement on the $AgSe_{0.5}Te_{0.5}Ph$ film. The ratio of integrated emission and excitation signals after the correction from neutral density (ND) filters gives PLQY of ~0.40% for the $AgSe_{0.5}Te_{0.5}Ph$ film. (d) Temperature-dependent PL spectra of the $AgSe_{0.5}Te_{0.5}Ph$ film. (e) Temperature-dependent photoluminescence quantum yield of overall spectrally integrated emission of the $AgSe_{0.5}Te_{0.5}Ph$ film.

6.3.4 Analysis of $AgS_{1-n}Se_nPh$ and $AgS_{1-n}Te_nPh$ films

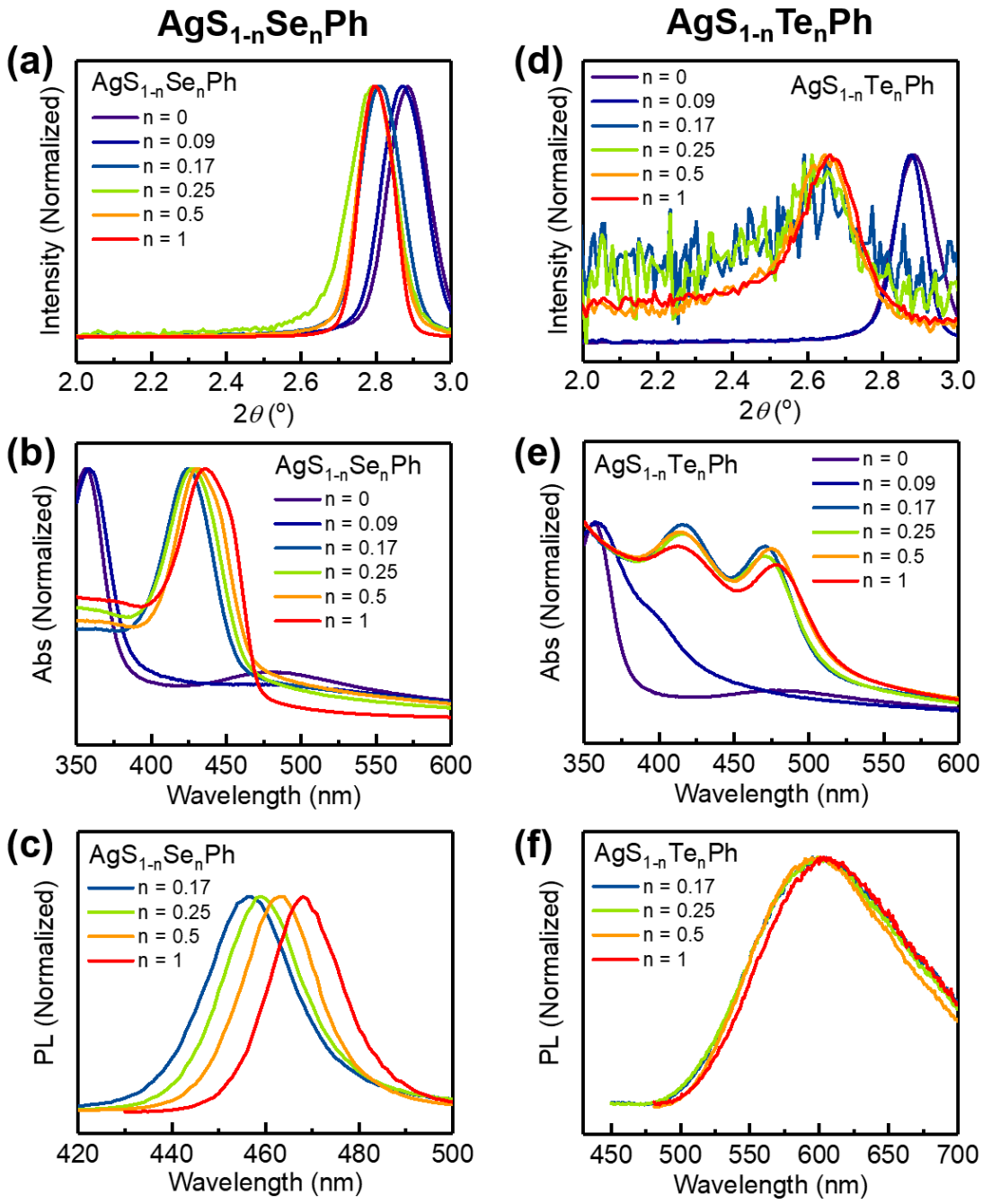

Figure 6.20 (a) Zoomed-in X-ray diffractograms showing (002) diffraction peaks (Mo K**α** radiation, **λ** = 0.71 Å), (b) absorption spectra and (c) photoluminescence spectra of $AgS_{1-n}Se_nPh$ films at room temperature. (d) Zoomed-in X-ray diffractograms showing (002) diffraction peaks (Mo K**α** radiation, **λ** = 0.71 Å), (e) absorption spectra and (f) photoluminescence spectra of $AgS_{1-n}Te_nPh$ films at room temperature.

We also investigated the potential formation of silver phenylsulfide-selenide ($AgS_{1-n}Se_nPh$) and silver phenylsulfide-telluride ($AgS_{1-n}Te_nPh$) alloys (Figure 6.20). $AgS_{1-n}Se_nPh$ and $AgS_{1-n}Te_nPh$ films were prepared using a similar method employed for $AgSe_{1-n}Te_nPh$ films by substituting organic ligand precursors. Specifically, a mixture of diphenyl disulfide (Ph_2S_2) and Ph_2Se_2 powders was used to prepare $AgS_{1-n}Se_nPh$ films and a mixture of Ph_2S_2 and Ph_2Te_2 powders was used for $AgS_{1-n}Te_nPh$ films. As in the case of $AgSe_{1-n}Te_nPh$ films, we refer to the Ph_2Se_2 fraction (Ph_2Te_2 fraction) in the precursor mixture as *n* in $AgS_{1-n}Se_nPh$ films ($AgS_{1-n}Te_nPh$ films).

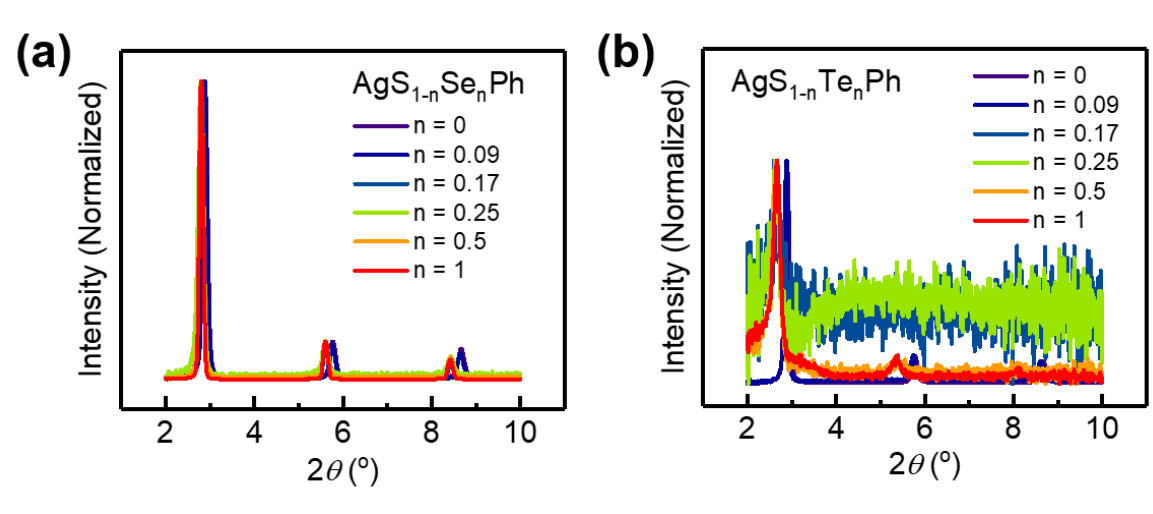

Figure 6.21 X-ray diffractograms of (a) $AgS_{1-n}Se_nPh$ and (b) $AgS_{1-n}Te_nPh$ films. (Mo Kα radiation, λ = 0.71 Å)

Figures 6.20a and 6.21a illustrate the XRD patterns of $AgS_{1-n}Se_nPh$ films (Mo Kα radiation, λ = 0.71 Å). All $AgS_{1-n}Se_nPh$ films showed evenly spaced (00*h*) diffraction peaks below 10°, corresponding to the stacking periodicity of the layered 2D structures. In contrast to $AgSe_{1-n}Te_nPh$ films, the (002) peak of $AgS_{1-n}Se_nPh$ films did not exhibit a gradual shift with increasing *n*. The (002) peak of AgSPh and $AgS_{0.91}Se_{0.09}Ph$ films was positioned at ~2.88°, whereas the (002) peak of $AgS_{1-n}Se_nPh$ films with $n \geq 0.17$ was positioned at ~2.80°, suggesting a miscibility gap between AgSPh and AgSePh. The miscibility gap was also observed in the absorption and PL spectra of $AgS_{1-n}Se_nPh$ films (Figure 6.20b,c). The AgSPh film exhibited an excitonic absorption centered at ~ 356 nm, slightly shifting to ~ 358 nm in $AgS_{0.91}Se_{0.09}Ph$ film. In contrast, the $AgS_{0.83}Se_{0.17}Ph$ film exhibited an absorption spectrum centered around 425nm that resembles the absorption

spectral shape of the AgSePh film. As the Se fraction increased further, the overall absorption spectrum gradually red-shifted. Similarly, whereas AgSPh and $AgS_{0.91}Se_{0.09}Ph$ films did not exhibit any emission upon 365 nm photoexcitation, $AgS_{1-n}Se_nPh$ films with $n \geq 0.17$ exhibit narrow PL with a peak monotonically shifting from ~457 nm in the $AgS_{0.83}Se_{0.17}Ph$ film to ~468 nm in the AgSePh film as the Se fraction increased.

Figures 6.20d-f and 6.21b illustrates the XRD patterns (Mo Kα radiation, λ = 0.71 Å), absorption spectra and PL spectra of $AgS_{1-n}Te_nPh$ films. Similar to $AgS_{1-n}Se_nPh$ films, a miscibility gap was clearly observed in $AgS_{1-n}Te_nPh$ films. Whereas the XRD patterns, absorption spectra and PL spectra of the $AgS_{0.91}Te_{0.09}Ph$ film are similar to those of the AgSPh film, $AgS_{1-n}Te_nPh$ films with $n \geq 0.17$ exhibited XRD patterns, absorption spectra and PL spectra that resemble those of the AgTePh film. Taken together, these observations suggest a miscibility gap in both the AgSPh-AgSePh system and the AgSPh-AgTePh system, while the AgSePh-AgTePh system forms complete solid solutions at all compositions.

6.3.5 Calculations of the thermodynamic stability of $AgX_{1-n}Y_nPh$ alloys (X, Y = S, Se, Te)

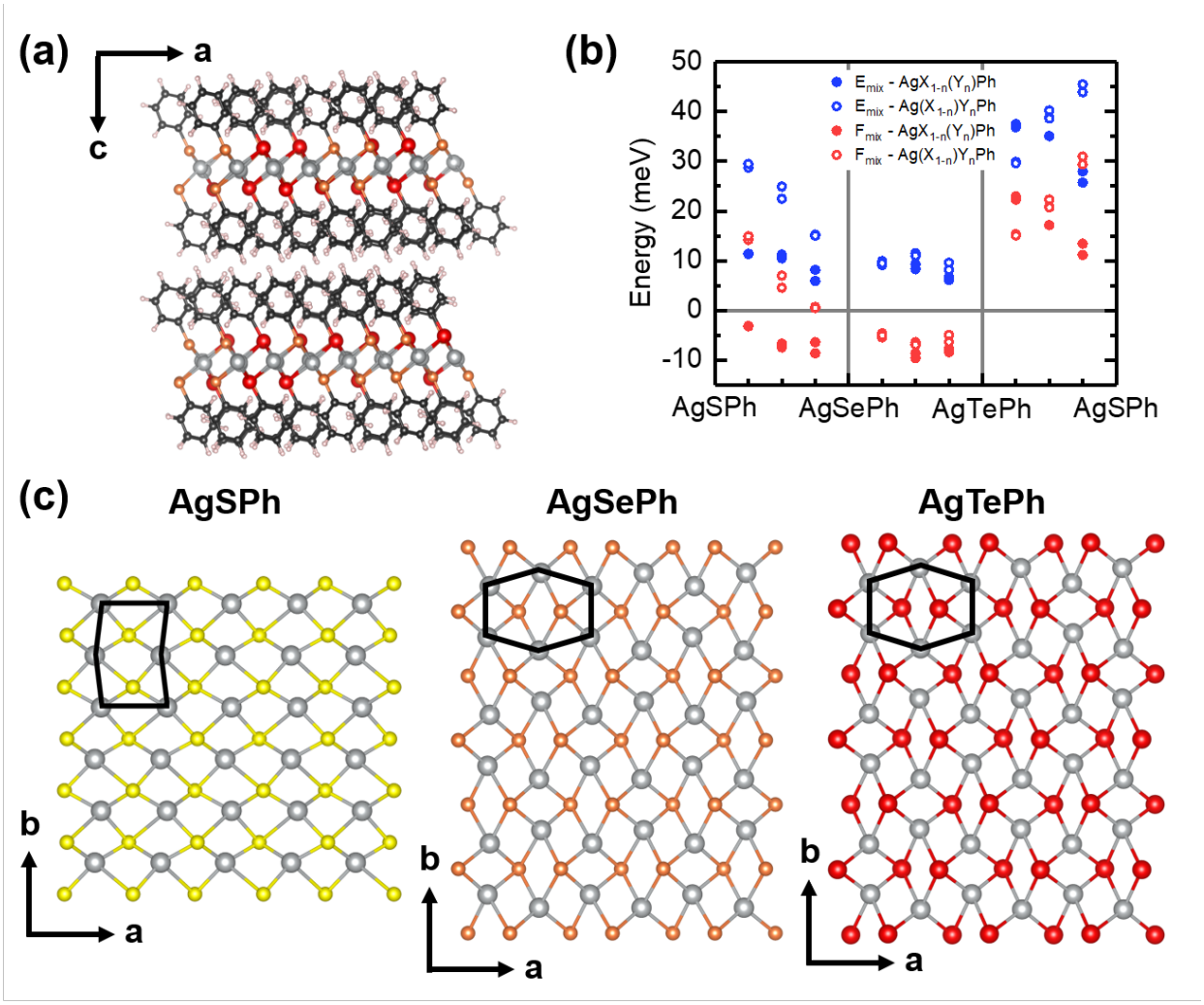

Figure 6.22 (a) 3 x 3 x 1 supercell of $AgX_{1-n}Y_nPh$ (X, Y = S, Se, Te) for density functional theory calculations. $AgSe_{0.5}Te_{0.5}Ph$ is shown as an example. (b) Internal (E_{mix}) and free energies (F_{mix}) of mixing per formula unit for $AgX_{1-n}Y_nPh$. (c) Top views of crystal structures of AgSPh ($P2_1$ space group[38]), AgSePh ($P2_1/c$ space group[23]), and AgTePh ($P2_1/c$ space group[38]) with phenyl rings omitted.

To understand the degree of miscibility in $AgX_{1-n}Y_nPh$ alloys (X, Y = S, Se, Te), we calculated the free energies of mixing of $AgS_{1-n}Se_nPh$, $AgSe_{1-n}Te_nPh$, and $AgS_{1-n}Te_nPh$, respectively, using the density functional theory (DFT) with the semi-local PBE functional (see Methods for details). The alloys were modeled by 3 x 3 x 1 supercells as shown in Figure 6.22a,

based on the monoclinic $P2_1$ structure of AgSPh[38] and the monoclinic $P2_1/c$ structures of AgSePh[23] and AgTePh[38]. For each $AgX_{1-n}Y_nPh$ alloy system, we considered three different chalcogen ratios: $X_{0.25}Y_{0.75}$, $X_{0.5}Y_{0.5}$, and $X_{0.75}Y_{0.25}$. For each chalcogen ratio, we considered 4 different configurations to collect reasonable statistics as follows: 2 configurations were generated by randomly replacing X atoms in AgXPh with Y atoms, which is referred to as $AgX_{1-n}(Y_n)Ph$. The other 2 configurations were generated randomly replacing Y atoms in AgYPh with X atoms, which is referred to as $Ag(X_{1-n})Y_nPh$. The atomic positions and the cell dimension were fully optimized for both pure AgXPh and alloy at the Γ point.

We define the free energy of mixing per formula unit ($AgX_nY_{1-n}Ph$) as

$$F_{mix}(n) = E_{mix}(n) + k_BT[nlog(n) + (1-n)log(1-n)] \quad (6.1)$$

where T is assumed to be 300 K and $E_{mix}(n)$ is the internal energy of mixing:

$$E_{mix}(n) = E_{AgX_{1-n}Y_{1-n}Ph} - [nE_{AgXPh} + (1-n)E_{AgYPh}] \quad (6.2)$$

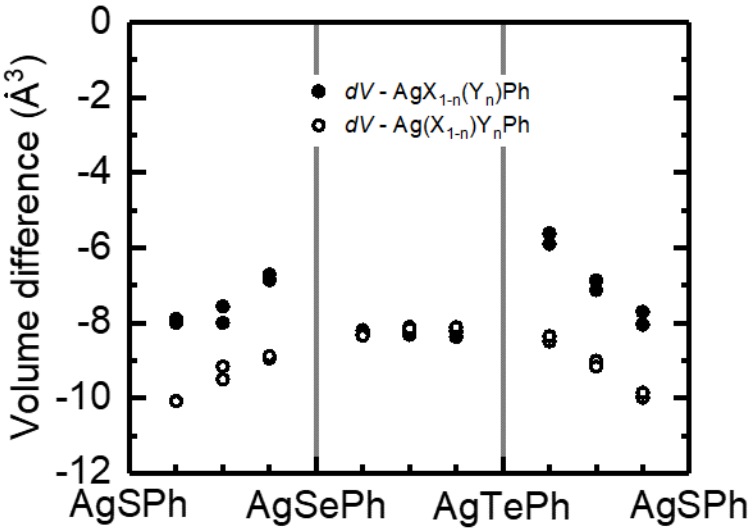

Figure 6.23 The calculated volume difference between host materials and alloys per formula unit in Å^3 ($AgX_nY_{1-n}Ph$; X, Y = S, Se, Te): $dV = V_{AgX_{1-n}Y_{1-n}Ph} - \{(nV_{AgXPh} + (1-n)V_{AgYPh}\}$

Figure 6.22b shows the mixing energies of $AgX_{1-n}Y_nPh$ systems per formula unit (cell volume per formula unit is shown in Figure 6.23). The internal energies of mixing (E_{mix}) were

positive for all $AgX_{1-n}Y_nPh$ systems at all compositions and configurations, indicating that the homogenous alloy is not energetically favored over segregated phases. However, the free energies of mixing (F_{mix}) of the $AgSe_{1-n}Te_nPh$ system at 300 K were negative for all compositions and configurations, predicting that the homogeneous mixing is more favorable than phase separation due to the entropic contributions. In contrast, F_{mix} of the $AgS_{1-n}Te_nPh$ system at 300 K were still positive for all compositions and configurations, predicting a miscibility gap in the AgSPh-AgTePh system. Interestingly, the sign of F_{mix} of the AgSPh-AgSePh system depended on the host material. F_{mix} of $AgS_{1-n}(Se_n)Ph$ were negative for all compositions and configurations whereas F_{mix} of $Ag(S_{1-n})Se_nPh$ were positive for all compositions and configurations. Overall, the calculated thermodynamic stability of $AgX_{1-n}Y_nPh$ systems is largely consistent with our experimental observations.

Crystal structures of AgSPh, AgSePh and AgTePh shown in Figure 6.22c help explain the thermodynamic stability of their alloys. Complete substitutional solid solution is predicted under following conditions according to Hume-Rothery rules:[39,40] 1) Solute and solvent must have the same crystal structure. Solute and solvent atoms must have 2) similar size, 3) equal valence and 4) similar electronegativity. Both AgSePh and AgTePh crystallize in the monoclinic $P2_1/c$ space group with Ag-Ag honeycomb networks whereas AgSPh crystallizes in the monoclininc $P2_1$ space group with Ag-Ag concave hexagon networks. Therefore, AgSePh and AgTePh can be completely soluble in one another at all compositions, whereas the different crystal structures of AgSPh compared to AgSePh/AgTePh cannot support complete solution between AgSPh and AgSePh/AgTePh.

6.4 Conclusions

In conclusion, our joint experimental-theoretical study demonstrated that the AgSePh-AgTePh system forms homogeneous complete solid solution ($AgSe_{1-n}Te_nPh$) at all compositions whereas both the AgSPh-AgSePh system and AgSPh-AgTePh system exhibit a miscibility gap. These observations were correlated with the differences in crystal structures of AgSePh compared to AgSePh/AgTePh. Moreover, through temperature- and composition-dependent optical spectroscopy, we showed tunable excitonic absorption resonances in ultraviolet-visible range,

alongside dual emission from band-edge free-exciton and self-trapped exciton states in blue to near-infrared range in $AgSe_{1-n}Te_nPh$ films. This work not only highlights tunable excitonic properties and exciton-phonon coupling strength via alloying but also offers insights into structure-composition-exciton property relationship in these emerging hybrid semiconductors.

6.5 Methods

Chemicals. Silver pellets (Ag, 99.99% pure) were purchased from Kurt J Lesker. Diphenyl disulfide (Ph_2S_2, 99.0+%) and diphenyl diselenide (Ph_2Se_2, 97.0+%) were purchased from TCI America. Diphenyl ditelluride (Ph_2Te_2, 98%), Allura Red AC (98.0+%), nitric acid (HNO_3, 70%) were purchased from Millipore Sigma.

Substrate preparation. Bare glass with dimensions of 12.2 x 12.2 x 1.1 mm was purchased from Luminescence Technology Corp. The glass substrates were cleaned by sonication for 3 min successively in acetone, isopropanol, and deionized water.

Preparation of $AgX_{1-n}Y_nPh$ films. $AgX_nY_{1-n}Ph$ (X, Y = S, Se, Te) thin films were prepared by a chemical transformation reaction between metallic silver and a vapor of Ph_2X_2 and Ph_2Y_2 (X, Y = S, Se, Te).[17,22,26] Silver films with thickness of 15 nm were deposited on glass substrates by thermal evaporation with a deposition rate of ~1 Å/s. After that, the prepared silver films, a mixture of Ph_2X_2 and Ph_2Y_2 powder and 200 µL of deionized water in separate open culture tubes were sealed together inside a microwave reaction vial. After heating in an oven at 100 °C for 4~7 days, the silver films transformed into $AgX_nY_{1-n}Ph$ films. The ratio of Ph_2X_2 and Ph_2Y_2 powders in the precursor was varied to control the actual ratio of X and Y in $AgX_{1-n}Y_nPh$ films

Steady-state PL micro-spectroscopy. Steady-state PL measurements of $AgX_{1-n}Y_nPh$ films were performed on an inverted microscope (Nikon, Ti-U Eclipse) with sample mounted either in air or under vacuum. The samples were excited by focusing the output of a 405 nm laser diode (Picoquant, LDHDC-405M, continuous wave mode) by an objective lens (Nikon, CFI S Plan Fluor ELWD, 40x, 0.6 NA) to ~1 µm spot. The excitation light polarization was controlled by a circular polarizer (Thorlabs, CP1R405). After excitation, the PL was collected in the epi configuration and passed through a dichroic mirror and a long-pass filter. It was then directed into a spectrograph (Princeton Instruments, SP-2500) mounted with a cooled charge-coupled device (CCD) camera

detector (Princeton Instruments, Pixis). All spectra underwent Jacobian transformation from wavelength to photon energy,[41] but have not been corrected for wavelength-dependent efficiency of the spectrograph or CCD camera. Temperature-dependent PL spectroscopy was performed by mounting samples in a microscopy cryostat (Janis Research, ST-500) and flowing liquid helium through a cold finger attached to the base of the cryostat.

Sub-gap excitation PL micro-spectroscopy. PL spectra by sub-gap excitation was obtained by the same microscope and spectrograph as used for 405 nm excitation, but with a 532 nm continuous wave laser (Coherent, Sapphire 532 LP). To filter out the free exciton emission at ~470 nm in $AgSe_{0.83}Te_{0.17}Ph$, a 550 nm long-pass filter was used (Thorlabs FEL0550).

Time-resolved PL micro-spectroscopy. Time-resolved PL (TRPL) measurements were performed using the same microscope and cryostat setup as steady-state PL spectroscopy with some modifications. For room temperature measurement of $AgSe_{1-n}Te_nPh$ films ($0 \leq n \leq 1$), the excitation light source was replaced by frequency-doubled light (405 nm) of the 810 nm output from a ~150 fs Ti:sapphire laser (Coherent Mira HP) operating at 76 MHz. For low temperature measurement of $AgSe_{0.83}Te_{0.17}Ph$ and $AgSe_{0.5}Te_{0.5}Ph$ films, a variable repetition-rate 405 nm pulsed laser diode (Picoquant, LDHDC-405M) was used instead of the 76 MHz Ti:sapphire laser because of the long natural emission lifetime. For all cases, PL was detected by a Si avalanche photodiode (Micro Photon Devices, PDM20) connected to a counting board for time-correlated single-photon counting (APD, PicoQuant, PicoHarp 300). To account for the wavelength-dependent temporal response of the APD, different procedures were used to obtain the instrument response function (IRF). For AgSePh and $AgSe_{0.17}Te_{0.09}Ph$ films, the IRF was obtained by detecting Raman scattering from water at ~470 nm, which is close to the peak position of narrow blue emission of AgSePh and $AgSe_{0.17}Te_{0.09}Ph$ films. For other $AgSe_{1-n}Te_nPh$ films ($0.17 \leq n \leq 1$), the IRF was obtained by detecting the PL from Allura Red AC dye in water, which shows fast and broad emission centered near ~620 nm, similar to broad emission spectrum of $AgSe_{1-n}Te_nPh$ films ($0.17 \leq n \leq 1$).

Photoluminescence quantum yield. The measurement of PL quantum yield (QY) was performed at room temperature using the absolute quantum yield method in an integrating sphere.[17,22,42] The excitation light from a 405 nm laser diode (Picoquant, LDHDC-405M, continuous wave mode) was directed into an integrating sphere (Labsphere) containing the sample.

The output signal was collected by an optical fiber mounted on an exit port of the integrating sphere and was directed into a spectrograph (Princeton Instruments, SP-2500) outfitted with the CCD camera (Princeton Instruments, Pixis 100B). Neutral density and color glass filters were inserted in front of the spectrograph to avoid oversaturation of the CCD and accounted for in all calculations. Absolute QY at lower sample temperature was estimated by scaling the QY measured at room-temperature by the temperature-dependent relative PL intensity.

Steady-state absorption spectroscopy. Optical absorption measurements were performed on films made from 15 nm thick silver films using a Cary 5000 UV-Vis-NIR spectrometer. Room temperature absorption spectra were collected in an integrating sphere geometry (Agilent, Internal DRA 2500), in air to minimize scattered light contributions to the signal. For temperature-dependent absorption spectra, samples were mounted inside a steady flow Janis ST-100 optical cryostat. The cryostat was then mounted in the Cary spectrometer, evacuated to below 3×10^{-5} Torr, and cooled with liquid nitrogen. The temperature was controlled with a model 335 Lakeshore temperature controller.

Photoluminescence excitation spectra (PLE). PLE spectra were recorded with a Tecan Spark multimode plate reader using the excitation scan mode with an emission band of 5 nm.

PL spectra of $AgS_nSe_{1-n}Ph$ and $AgS_nTe_{1-n}Ph$ films. PL spectra of $AgS_nSe_{1-n}Ph$ and $AgS_nTe_{1-n}Ph$ films were recorded with a Tecan Spark multimode plate reader using a monochromator upon 365 nm excitation.

Density functional theory calculations. The internal energy of mixing was calculated using Vienna Ab initio Simulation Package version 6.3.1.[43–46] The density functional theory calculations were performed at the Γ point, employing the PBE functional[47] and projector augmented wave pseudopotentials[48] with a kinetic energy cutoff of 500 eV. DFT-D3[49] with Becke-Johnson damping[50] was applied as a dispersion correction. The geometry, including the cell dimension, was optimized until the total energy difference between steps was below 1 meV. Multiple geometry optimizations were carried out, in all cases fully relaxing both the atomic positions and the cell dimensions. The final energy was recalculated after the geometry was fully optimized to minimize the effect of Pulay stress.

Inductively coupled plasma optical emission spectrsocopy (ICP-OES). ICP-OES was performed using Agilent 5100 ICP-OES. Calibration was done using ICP standards from Millipore Sigma. ICP-OES samples were prepared by dissolving $AgX_nY_{1-n}Ph$ films in 5 mL of 3% HNO_3 solution.

Scanning electron microscopy (SEM). Scanning electron micrographs were collected using a Zeiss Merlin instrument operating at 1 kV and 100 pA.

Powder X-ray diffraction (PXRD). Powder X-ray diffraction data of $AgSe_nTe_{1-n}Ph$ films were collected using a PANalytical X'Pert Pro MPD X-ray diffractometer (Cu Kα radiation, λ = 1.54184 Å) with High-Speed Bragg-Brentano Optics. A 0.04 rad Soller slit, a 2° anti-scatter slit, a 10 mm mask, and a programmable divergence slit with an illuminated length of 6 mm were used in the incident beam path. The diffracted beam optics included a 0.04 rad Soller slit, a Ni Filter, and an automatic receiving slit. The detector was an ultrafast X'Celerator RTMS detector. Powder X-ray diffraction data of $AgS_nSe_{1-n}Ph$ and $AgS_nTe_{1-n}Ph$ films were collected using a PANalytical Empyrean X-ray diffractometer (Mo Kα radiation, λ = 0.71 Å) and Galipix 3D detector.

6.6 References

(1) Neamen, D. *Semiconductor Physics And Devices*; 2012.

(2) Peng, Z.; Chen, X.; Fan, Y.; Srolovitz, D. J.; Lei, D. Strain Engineering of 2D Semiconductors and Graphene: From Strain Fields to Band-Structure Tuning and Photonic Applications. *Light Sci Appl* **2020**, *9* (1), 190. https://doi.org/10.1038/s41377-020-00421-5.

(3) Francaviglia, L.; Giunto, A.; Kim, W.; Romero-Gomez, P.; Vukajlovic-Plestina, J.; Friedl, M.; Potts, H.; Güniat, L.; Tütüncüoglu, G.; Fontcuberta i Morral, A. Anisotropic-Strain-Induced Band Gap Engineering in Nanowire-Based Quantum Dots. *Nano Lett* **2018**, *18* (4), 2393–2401. https://doi.org/10.1021/acs.nanolett.7b05402.

(4) Alivisatos, A. P. Semiconductor Clusters, Nanocrystals, and Quantum Dots. *Science (1979)* **1996**, *271* (5251), 933–937. https://doi.org/10.1126/science.271.5251.933.

(5) García de Arquer, F. P.; Talapin, D. V.; Klimov, V. I.; Arakawa, Y.; Bayer, M.; Sargent, E. H. Semiconductor Quantum Dots: Technological Progress and Future Challenges. *Science (1979)* **2021**, *373* (6555). https://doi.org/10.1126/science.aaz8541.

(6) Ning, C.-Z.; Dou, L.; Yang, P. Bandgap Engineering in Semiconductor Alloy Nanomaterials with Widely Tunable Compositions. *Nat Rev Mater* **2017**, *2* (12), 17070. https://doi.org/10.1038/natrevmats.2017.70.

(7) Vurgaftman, I.; Meyer, J. R.; Ram-Mohan, L. R. Band Parameters for III–V Compound Semiconductors and Their Alloys. *J Appl Phys* **2001**, *89* (11), 5815–5875. https://doi.org/10.1063/1.1368156.

(8) Kudrawiec, R.; Hommel, D. Bandgap Engineering in III-Nitrides with Boron and Group V Elements: Toward Applications in Ultraviolet Emitters. *Appl Phys Rev* **2020**, *7* (4). https://doi.org/10.1063/5.0025371.

(9) Basu, R. A Review on Single Crystal and Thin Film Si–Ge Alloy: Growth and Applications. *Mater Adv* **2022**, *3* (11), 4489–4513. https://doi.org/10.1039/D2MA00104G.

(10) Zhu, T.; Gong, X. Low-dimensional Perovskite Materials and Their Optoelectronics. *InfoMat* **2021**, *3* (10), 1039–1069. https://doi.org/10.1002/inf2.12211.

(11) Dou, L.; Wong, A. B.; Yu, Y.; Lai, M.; Kornienko, N.; Eaton, S. W.; Fu, A.; Bischak, C. G.; Ma, J.; Ding, T.; Ginsberg, N. S.; Wang, L.-W.; Alivisatos, A. P.; Yang, P. Atomically Thin Two-Dimensional Organic-Inorganic Hybrid Perovskites. *Science (1979)* **2015**, *349* (6255), 1518–1521. https://doi.org/10.1126/science.aac7660.

(12) Weidman, M. C.; Seitz, M.; Stranks, S. D.; Tisdale, W. A. Highly Tunable Colloidal Perovskite Nanoplatelets through Variable Cation, Metal, and Halide Composition. *ACS Nano* **2016**, *10* (8), 7830–7839. https://doi.org/10.1021/acsnano.6b03496.

(13) Schriber, E. A.; Paley, D. W.; Bolotovsky, R.; Rosenberg, D. J.; Sierra, R. G.; Aquila, A.; Mendez, D.; Poitevin, F.; Blaschke, J. P.; Bhowmick, A.; Kelly, R. P.; Hunter, M.; Hayes, B.; Popple, D. C.; Yeung, M.; Pareja-Rivera, C.; Lisova, S.; Tono, K.; Sugahara, M.; Owada, S.; Kuykendall, T.; Yao, K.; Schuck, P. J.; Solis-Ibarra, D.; Sauter, N. K.; Brewster, A. S.; Hohman, J. N. Chemical Crystallography by Serial Femtosecond X-Ray Diffraction. *Nature* **2022**, *601* (7893), 360–365. https://doi.org/10.1038/s41586-021-04218-3.

(14) Kastl, C.; Schwartzberg, A. M.; Maserati, L. Picoseconds-Limited Exciton Recombination in Metal–Organic Chalcogenides Hybrid Quantum Wells. *ACS Nano* **2022**, *16* (3), 3715–3722. https://doi.org/10.1021/acsnano.1c07281.

(15) Maserati, L.; Prato, M.; Pecorario, S.; Passarella, B.; Perinot, A.; Thomas, A. A.; Melloni, F.; Natali, D.; Caironi, M. Photo-Electrical Properties of 2D Quantum Confined Metal–Organic Chalcogenide Nanocrystal Films. *Nanoscale* **2021**, *13* (1), 233–241. https://doi.org/10.1039/D0NR07409H.

(16) Maserati, L.; Refaely-Abramson, S.; Kastl, C.; Chen, C. T.; Borys, N. J.; Eisler, C. N.; Collins, M. S.; Smidt, T. E.; Barnard, E. S.; Strasbourg, M.; Schriber, E. A.; Shevitski, B.; Yao, K.; Hohman, J. N.; Schuck, P. J.; Aloni, S.; Neaton, J. B.; Schwartzberg, A. M. Anisotropic 2D Excitons Unveiled in Organic–Inorganic Quantum Wells. *Mater Horiz* **2021**, *8* (1), 197–208. https://doi.org/10.1039/C9MH01917K.

(17) Paritmongkol, W.; Lee, W. S.; Shcherbakov-Wu, W.; Ha, S. K.; Sakurada, T.; Oh, S. J.; Tisdale, W. A. Morphological Control of 2D Hybrid Organic–Inorganic Semiconductor AgSePh. *ACS Nano* **2022**, *16* (2), 2054–2065. https://doi.org/10.1021/acsnano.1c07498.

(18) Schriber, E. A.; Rosenberg, D. J.; Kelly, R. P.; Ghodsi, A.; Hohman, J. N. Investigation of Nucleation and Growth at a Liquid–Liquid Interface by Solvent Exchange and Synchrotron Small-Angle X-Ray Scattering. *Front Chem* **2021**, *9*. https://doi.org/10.3389/fchem.2021.593637.

(19) Kastl, C.; Bonfà, P.; Maserati, L. Anharmonic Exciton-Phonon Coupling in Metal-Organic Chalcogenides Hybrid Quantum Wells. *Adv Opt Mater* **2023**, *11* (7). https://doi.org/10.1002/adom.202202213.

(20) Rabl, H.; Myakala, S. N.; Rath, J.; Fickl, B.; Schubert, J. S.; Apaydin, D. H.; Eder, D. Microwave-Assisted Synthesis of Metal-Organic Chalcogenolate Assemblies as Electrocatalysts for Syngas Production. *Commun Chem* **2023**, *6* (1), 43. https://doi.org/10.1038/s42004-023-00843-3.

(21) Yao, K.; Collins, M. S.; Nell, K. M.; Barnard, E. S.; Borys, N. J.; Kuykendall, T.; Hohman, J. N.; Schuck, P. J. Strongly Quantum-Confined Blue-Emitting Excitons in Chemically Configurable Multiquantum Wells. *ACS Nano* **2021**, *15* (3), 4085–4092. https://doi.org/10.1021/acsnano.0c08096.

(22) Lee, W. S.; Cho, Y.; Powers, E. R.; Paritmongkol, W.; Sakurada, T.; Kulik, H. J.; Tisdale, W. A. Light Emission in 2D Silver Phenylchalcogenolates. *ACS Nano* **2022**, *16* (12), 20318–20328. https://doi.org/10.1021/acsnano.2c06204.

(23) Paritmongkol, W.; Sakurada, T.; Lee, W. S.; Wan, R.; Müller, P.; Tisdale, W. A. Size and Quality Enhancement of 2D Semiconducting Metal–Organic Chalcogenolates by Amine Addition. *J Am Chem Soc* **2021**, *143* (48), 20256–20263. https://doi.org/10.1021/jacs.1c09106.

(24) Maserati, L.; Pecorario, S.; Prato, M.; Caironi, M. Understanding the Synthetic Pathway to Large-Area, High-Quality [AgSePh] $_\infty$ Nanocrystal Films. *The Journal of Physical Chemistry C* **2020**, *124* (41), 22845–22852. https://doi.org/10.1021/acs.jpcc.0c07330.

(25) Popple, D. C.; Schriber, E. A.; Yeung, M.; Hohman, J. N. Competing Roles of Crystallization and Degradation of a Metal–Organic Chalcogenolate Assembly under Biphasic Solvothermal Conditions. *Langmuir* **2018**, *34* (47), 14265–14273. https://doi.org/10.1021/acs.langmuir.8b03282.

(26) Trang, B.; Yeung, M.; Popple, D. C.; Schriber, E. A.; Brady, M. A.; Kuykendall, T. R.; Hohman, J. N. Tarnishing Silver Metal into Mithrene. *J Am Chem Soc* **2018**, *140* (42), 13892–13903. https://doi.org/10.1021/jacs.8b08878.

(27) Schriber, E. A.; Popple, D. C.; Yeung, M.; Brady, M. A.; Corlett, S. A.; Hohman, J. N. Mithrene Is a Self-Assembling Robustly Blue Luminescent Metal–Organic Chalcogenolate Assembly for 2D Optoelectronic Applications. *ACS Appl Nano Mater* **2018**, *1* (7), 3498–3508. https://doi.org/10.1021/acsanm.8b00662.

(28) Yan, H.; Hohman, J. N.; Li, F. H.; Jia, C.; Solis-Ibarra, D.; Wu, B.; Dahl, J. E. P.; Carlson, R. M. K.; Tkachenko, B. A.; Fokin, A. A.; Schreiner, P. R.; Vailionis, A.; Kim, T. R.; Devereaux, T. P.; Shen, Z.-X.; Melosh, N. A. Hybrid Metal–Organic Chalcogenide Nanowires with Electrically Conductive Inorganic Core through Diamondoid-Directed Assembly. *Nat Mater* **2017**, *16* (3), 349–355. https://doi.org/10.1038/nmat4823.

(29) Hawila, S.; Massuyeau, F.; Gautier, R.; Fateeva, A.; Lebègue, S.; Kim, W. J.; Ledoux, G.; Mesbah, A.; Demessence, A. Tuning the 1D–2D Dimensionality upon Ligand Exchange in Silver Thiolate Coordination Polymers with Photoemission Switching. *J Mater Chem B* **2023**, *11* (18), 3979–3984. https://doi.org/10.1039/D3TB00537B.

(30) Wang, G.; Luo, S.; Di, T.; Fu, Z.; Xu, G. Layered Organic Metal Chalcogenides (OMCs): From Bulk to Two-Dimensional Materials. *Angewandte Chemie International Edition* **2022**, *61* (27). https://doi.org/10.1002/anie.202203151.

(31) Okhrimenko, L.; Cibaka Ndaya, C.; Fateeva, A.; Ledoux, G.; Demessence, A. Post-Synthetic Functionalization and Ligand Exchange Reactions in Gold(I) Phenylthiolate-Based Coordination Polymers. *New Journal of Chemistry* **2020**, *44* (41), 17970–17975. https://doi.org/10.1039/D0NJ03833D.

(32) Sakurada, T.; Cho, Y.; Paritmongkol, W.; Lee, W. S.; Wan, R.; Su, A.; Shcherbakov-Wu, W.; Müller, P.; Kulik, H. J.; Tisdale, W. A. 1D Hybrid Semiconductor Silver 2,6-Difluorophenylselenolate. *J Am Chem Soc* **2023**, *145* (9), 5183–5190. https://doi.org/10.1021/jacs.2c11896.

(33) Veselska, O.; Demessence, A. D10 Coinage Metal Organic Chalcogenolates: From Oligomers to Coordination Polymers. *Coord Chem Rev* **2018**, *355*, 240–270. https://doi.org/10.1016/j.ccr.2017.08.014.

(34) Khamlue, R.; Sakurada, T.; Cho, Y.; Lee, W. S.; Leangtanom, P.; Taylor, M. G.; Naewthong, W.; Sripetch, P.; Na Ranong, B.; Autila, T.; Rungseesumran, T.; Kaewkhao, J.; Sudyoadsuk, T.; Kopwitthaya, A.; Müller, P.; Promarak, V.; Kulik, H. J.; Tisdale, W. A.; Paritmongkol, W. Heterocyclic Modification Leading to Luminescent 0D Metal Organochalcogenide with Stable X-Ray Scintillating Properties. *Chemistry of Materials* **2024**, *36* (10), 5238–5240. https://doi.org/10.1021/acs.chemmater.4c00653.

(35) Powers, E. R.; Paritmongkol, W.; Yost, D. C.; Lee, W. S.; Grossman, J. C.; Tisdale, W. A. Coherent Exciton-Lattice Dynamics in a 2D Metal Organochalcogenolate Semiconductor. *Matter* **2024**, *7* (4), 1612–1630. https://doi.org/10.1016/j.matt.2024.01.033.

(36) Hernandez Oendra, A. C.; Aspect, M. A.; Jaeggi, J. L.; Baumann, J.; Lightner, C. R.; Pun, A. B.; Norris, D. J. Tunable Synthesis of Metal–Organic Chalcogenide Semiconductor Nanocrystals. *Chemistry of Materials* **2023**, *35* (21), 9390–9398. https://doi.org/10.1021/acs.chemmater.3c02275.

(37) Yang, H.; Mandal, S.; Lee, Y. H.; Park, J. Y.; Zhao, H.; Yuan, C.; Huang, L.; Chen, M.; Dou, L. Dimensionality Engineering of Lead Organic Chalcogenide Semiconductors. *J Am Chem Soc* **2023**, *145* (44), 23963–23971. https://doi.org/10.1021/jacs.3c05745.

(38) Synthesis and Structural Anisotropy of Single Crystalline 2D AgEPh (E = S, Se, Te) in Manuscript.

(39) Callister, W. D. *Wiley: Materials Science and Engineering: An Introduction, 8th Edition - William D. Callister, David G. Rethwisch*; 2010.

(40) Rohrman, F. A. The Theory of the Properties of Metals and Alloys (Mott, N. F.; Jones, H.). *J Chem Educ* **1937**, *14* (2), 99. https://doi.org/10.1021/ed014p99.

(41) Mooney, J.; Kambhampati, P. Get the Basics Right: Jacobian Conversion of Wavelength and Energy Scales for Quantitative Analysis of Emission Spectra. *J Phys Chem Lett* **2013**, *4* (19), 3316–3318. https://doi.org/10.1021/jz401508t.

(42) Valenta, J. Determination of Absolute Quantum Yields of Luminescing Nanomaterials over a Broad Spectral Range: From the Integrating Sphere Theory to the Correct Methodology. *Nanoscience Methods* **2014**, *3* (1), 11–27. https://doi.org/10.1080/21642311.2014.884288.

(43) Kresse, G.; Hafner, J. *Ab Initio* Molecular Dynamics for Liquid Metals. *Phys Rev B* **1993**, *47* (1), 558–561. https://doi.org/10.1103/PhysRevB.47.558.

(44) Kresse, G.; Furthmüller, J. Efficient Iterative Schemes for *Ab Initio* Total-Energy Calculations Using a Plane-Wave Basis Set. *Phys Rev B* **1996**, *54* (16), 11169–11186. https://doi.org/10.1103/PhysRevB.54.11169.

(45) Kresse, G.; Furthmüller, J. Efficiency of Ab-Initio Total Energy Calculations for Metals and Semiconductors Using a Plane-Wave Basis Set. *Comput Mater Sci* **1996**, *6* (1), 15–50. https://doi.org/10.1016/0927-0256(96)00008-0.

(46) Kresse, G.; Joubert, D. From Ultrasoft Pseudopotentials to the Projector Augmented-Wave Method. *Phys Rev B* **1999**, *59* (3), 1758–1775. https://doi.org/10.1103/PhysRevB.59.1758.

(47) Perdew, J. P.; Burke, K.; Ernzerhof, M. Generalized Gradient Approximation Made Simple. *Phys Rev Lett* **1996**, *77* (18), 3865–3868. https://doi.org/10.1103/PhysRevLett.77.3865.

(48) Blöchl, P. E. Projector Augmented-Wave Method. *Phys Rev B* **1994**, *50* (24), 17953–17979. https://doi.org/10.1103/PhysRevB.50.17953.

(49) Grimme, S.; Antony, J.; Ehrlich, S.; Krieg, H. A Consistent and Accurate *Ab Initio* Parametrization of Density Functional Dispersion Correction (DFT-D) for the 94 Elements H-Pu. *J Chem Phys* **2010**, *132* (15). https://doi.org/10.1063/1.3382344.

(50) Grimme, S.; Ehrlich, S.; Goerigk, L. Effect of the Damping Function in Dispersion Corrected Density Functional Theory. *J Comput Chem* **2011**, *32* (7), 1456–1465. https://doi.org/10.1002/jcc.21759.

Chapter 7

Excitonic Anisotropy in Single Crystalline 2D AgEPh (E = S, Se, Te)

The basis of this chapter has been adapted from:
Woo Seok Lee, Yeongsu Cho, Katarzyna Posmyk, Paulina Peksa, Mateusz Dyksik, Nicholas Samulewicz, Paulina Płochocka, Michał Baranowski, Heather J. Kulik, William A. Tisdale "Excitonic Anisotropy in Single Crystalline 2D AgEPh (E = S, Se, Te)" *In manuscript* (2024).

7.1 Abstract

The discovery of low-dimensional semiconductors has opened up avenues for exploring many-body interactions among quasiparticles (such as excitons, phonons, and photons) that lie at the heart of condensed matter physics and materials science. Two-dimensional (2D) hybrid organic-inorganic silver phenylchalcogenides (AgEPh; E = S, Se, Te) can provide an excellent platform for such studies due to large exciton binding energy, strong exciton-lattice interactions, and natural photonic cavity structure. In this chapter, using the combination of multiple polarization-resolved optical spectroscopy and *ab initio* calculations, we reveal strikingly distinct excitonic structure and anisotropy in these emerging materials. We show that multiple excitonic transitions with giant in-plane anisotropy dominate absorption in AgSePh and AgTePh, whereas absorption in AgSPh is in-plane isotropic. Anisotropy of low-lying free-excitons in AgSePh and self-trapped exciton in AgTePh is further identified in their photoluminescence. Density functional theory and GW with the Bethe-Salpeter equation (GW-BSE) calculations predict multiple 2D excitonic transitions with in-plane anisotropy in these materials. Unexpectedly, we observe that the lowest excitonic transition in AgSePh is resolved as two orthogonal transitions at 4 K that are consistent with two lowest-lying and brightest s-like intralayer excitons predicted in GW-BSE calculations in terms of their energy order, oscillator strengths, and polarization. These findings lay the foundation for a comprehensive understanding of excitonic structures and behaviors in AgEPh, which will serve as a knowledge base for further investigation into many-body physics in these emerging materials.

7.2 Introduction

Excitons, electron-hole pairs bound by Coulomb interaction, represent the lowest electronic excitation in a semiconductor.[1–3] The properties of excitons strongly depend on the crystal structure and dimension of the host materials.[4–8] In two-dimensional (2D) semiconductors, the combined effects of quantum confinement and reduced dielectric screening leads to tightly bound excitons with binding energies up to hundreds of meV, dominating optical response of materials.[9–14] Additionally, these spatial and dielectric confinement effects result in anisotropic excitons with transition dipole moment lying in the 2D plane,[5,15,16] enabling the enhanced optical coupling efficiency along the out-of-plane direction. If the 2D materials have in-plane anisotropy in structure, these 2D excitons may have additional in-plane anisotropy, providing more degree of freedom to control light-matter coupling efficiency.

While robust excitons within visible spectrum and strong in-plane anisotropy are essential for the development of advanced optoelectronic and photonic applications with polarization-selectivity and directional energy transport, 2D semiconductors discovered so far possess one of these properties, but rarely both. For example, transition metal dichalcogenides (MoS_2 and WS_2)[5,17–19] and 2D perovskites[15,20,21] possess robust excitons within visible range, but their excitonic phenomena tend to be in-plane isotropic due to their high-symmetry in-plane structure. Conversely, while many in-plane anisotropic 2D materials, such as black phosphorous,[22,23] SnSe,[24] GaTe,[25] $ReSe_2$,[26] and $PdSe_2$,[27] have been recently discovered, their bandgap is in the infrared range even in their monolayer limit.

Silver phenylchalcogenides (AgEPh; E = S, Se, Te) are covalently-bonded 2D hybrid organic-inorganic van der Waals semiconductors belonging to a broader family of metal organochalcogenolates.[28–51] AgEPh feature tunable excitonic phenomena in ultraviolet-visible range via alloying,[31,49] optical anisotropy,[40] air stability, and heavy-metal free composition, exhibiting potential uses in optoelectronics,[39,41] photonics,[51] catalysis,[29,43] and sensing.[50] Importantly, recent progress in synthesis enabled the synthesis of single crystals with sufficient size and quality for singe-crystal X-ray diffraction,[30,46] revealing their highly anisotropic and low-symmetry crystal structure both in-plane and out-of-plane directions. Here, we unveil strikingly distinct excitonic structure and anisotropy in these emerging materials, arising from their low-

symmetry crystal structure, using multiple polarization-resolved optical spectroscopy, combined with density functional theory and GW with the Bethe-Salpeter equation calculations.

7.3 Results and Discussion

7.3.1 Polarization-resolved absorption and photoluminescence of AgEPh (E = S, Se, Te) at room temperature

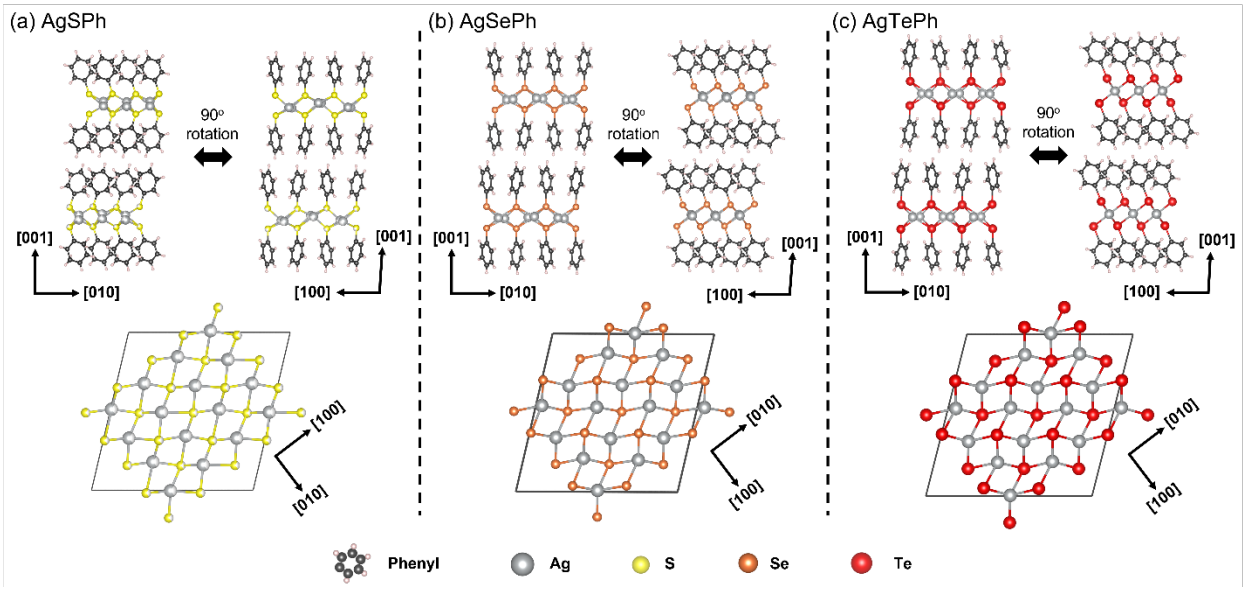

Figure 7.1 Crystal structures of (a) AgSPh in $P2_1$, (b) AgSePh in $P2_1/c$, and (c) AgTePh in $P2_1/c$. Disordered atoms in AgSPh are omitted for clarity. Phenyl rings are omitted for clarity in [001] view. The parallelograms outlined with a black solid line in [001] view represent virtual crystals terminated by {110} planes.

Two-dimensional (2D) silver phenylchalcogenides (AgEPh; E = S, Se, Te) exhibits structural anisotropy along both in-plane and out-of-plane directions,[30] suggesting the presence of anisotropic excitons (Figure 7.1). The layered structure with inorganic sheets sandwiched between organic ligands suggests the strong spatial and dielectric confinement of excitons within in-plane. Additionally, in-plane anisotropic crystal structure implies the presence of 2D excitons with in-plane anisotropy.

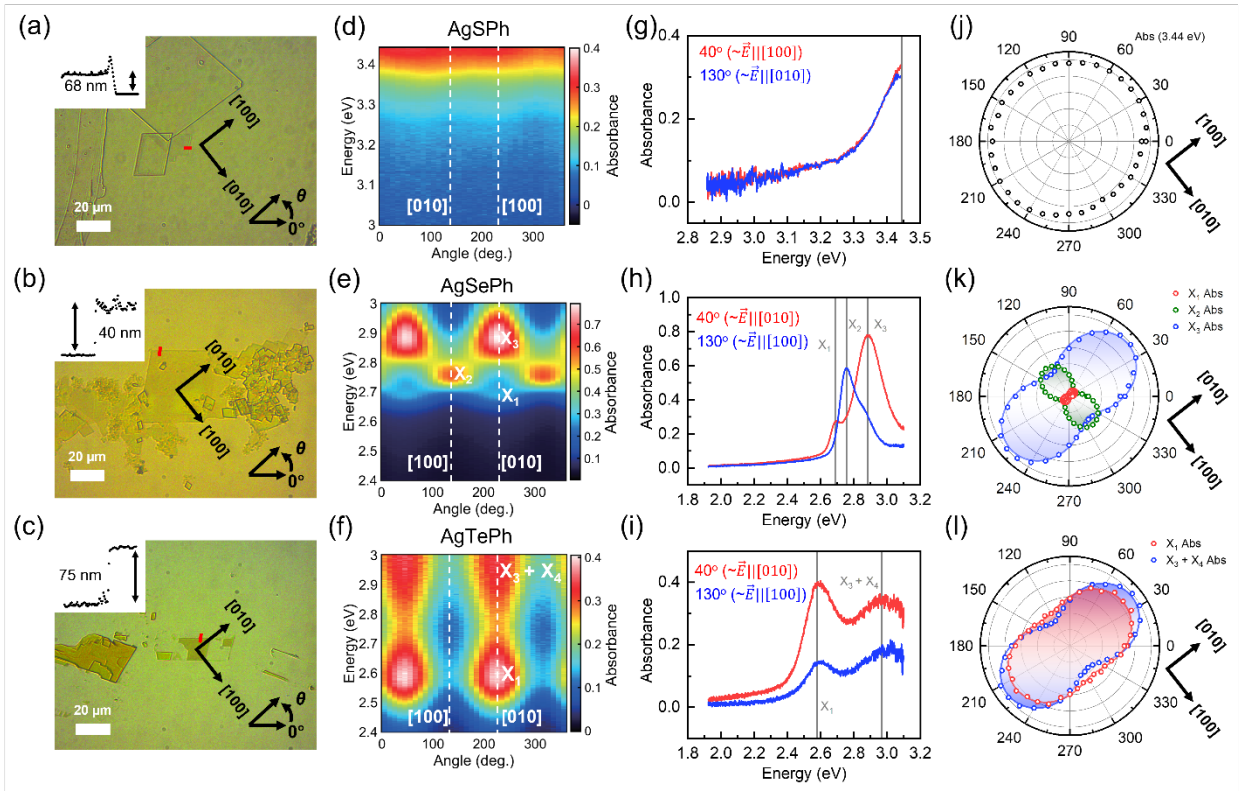

Figure 7.2 Optical micrographs of the (a) 68-nm thick AgSPh, (b) 40 nm-thick AgSePh and (c) 75 nm-thick AgTePh single crystal. Insets: surface profiles along the red solid line, measured using atomic force microscopy. 2D color plots showing absorption spectra of thin (d) AgSPh, (e) AgSePh and (f) AgTePh single crystal as a function of polarization angle of incident light. Vertical dashed lines are references for the crystallographic [100] and [010]. Polarization-resolved absorption spectra of thin (g) AgSPh, (h) AgSePh and (i) AgTePh single crystal when a linear polarizer was rotated to angles of 40° (red) and 130° (blue). Polar plot showing intensities of the absorption peaks of thin (j) AgSPh, (k) AgSePh and (l) AgTePh single crystal as a function of polarization of incident light. Solid line: sinusoidal fit applied to the experimental data. See Figures 7.4-7.6 for details.

To investigate the in-plane exciton anisotropy of AgEPh, we performed polarization-resolved micro-absorption spectroscopy (Figures 7.2-7.6). Briefly, AgEPh single crystal with a parallelogram shape, synthesized by the amine-assisted method, was mounted on an inverted microscope (Figures 7.2a-c). In particular, crystals thinner than 80 nm were prepared through careful searching or mechanical exfoliation to eliminate potential photonic effects (we will address photonic effects in the later section). The sample was illuminated with a broadband light from an overhead source, with a linear polarizer placed between the sample and the light source. The transmitted light through the sample was spatially filtered through a pinhole (spatial resolution:

~15 μm, see Figure 7.4b,c) to select a region of interest. The spatially filtered light was then directed into a spectrograph equipped with a cooled charge-coupled device (CCD) detector. The absorbance [$A = -log_{10}(I/I_0)$] of the sample was calculated by comparing the spectrum of the transmitted light through the crystal (I) with the spectrum of the transmitted light through the bare substrate (I_0) under the same experimental condition, which ensures the cancellation of polarization effects from the optics in the data. Polarization-resolved micro-absorption spectra of the AgEPh single crystal was measured by rotating the linear polarizer from 0° (corresponding to the selected polarization of the incident light being parallel to the bottom edge of the crystal in Figures 7.2a-c) to 360° at a step size of 10° (Figures 7.2d-f and 7.4-7.6).

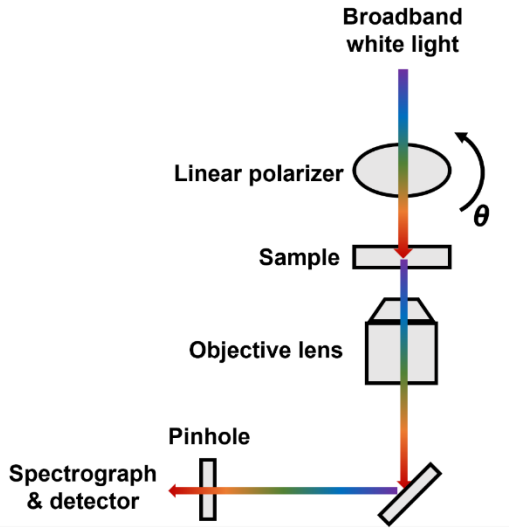

Figure 7.3 Schematic showing the experimental setup for the polarization-resolved micro-absorption spectroscopy.

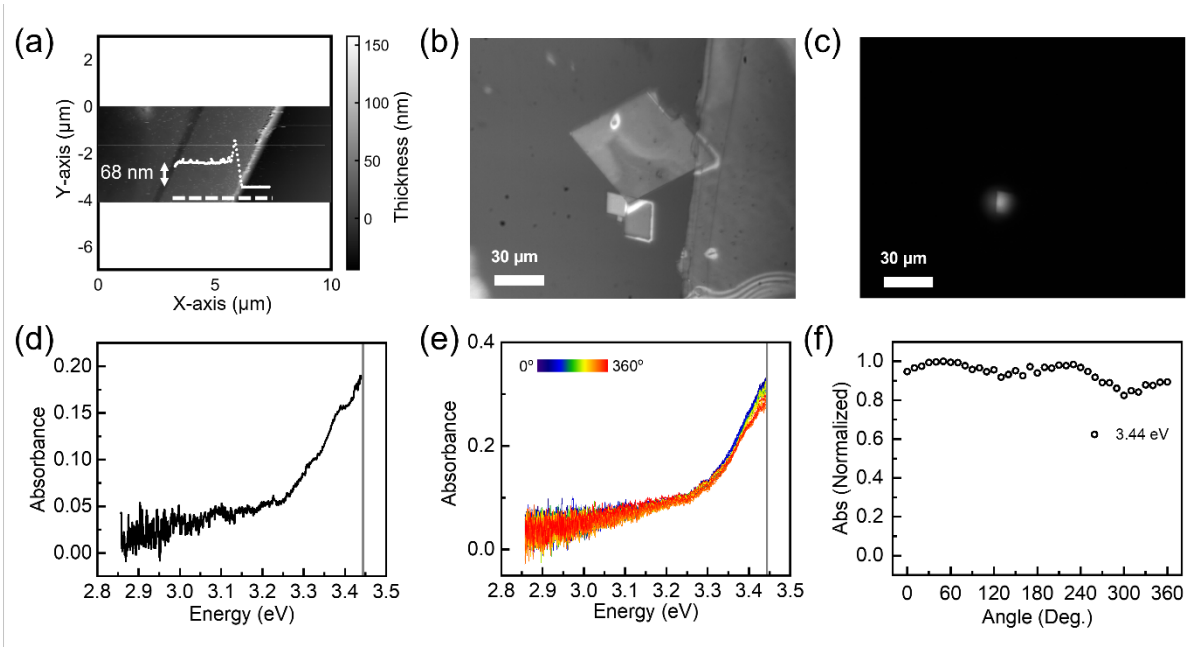

Figure 7.4 (a) Atomic force microscopy image of 68 nm-thick AgSPh crystal. Images of the 68 nm-thick AgSPh crystal captured in the collection path (b) without a pinhole and (c) with a pinhole. (d) Absorption spectra of the 68 nm-thick AgSPh crystal without a linear polarizer. (e) Absorption spectra of the 68 nm-thick AgSPh crystal as a function of polarization angle of incident light. (f) Polarization-dependent intensities of absorption at 3.44 eV.

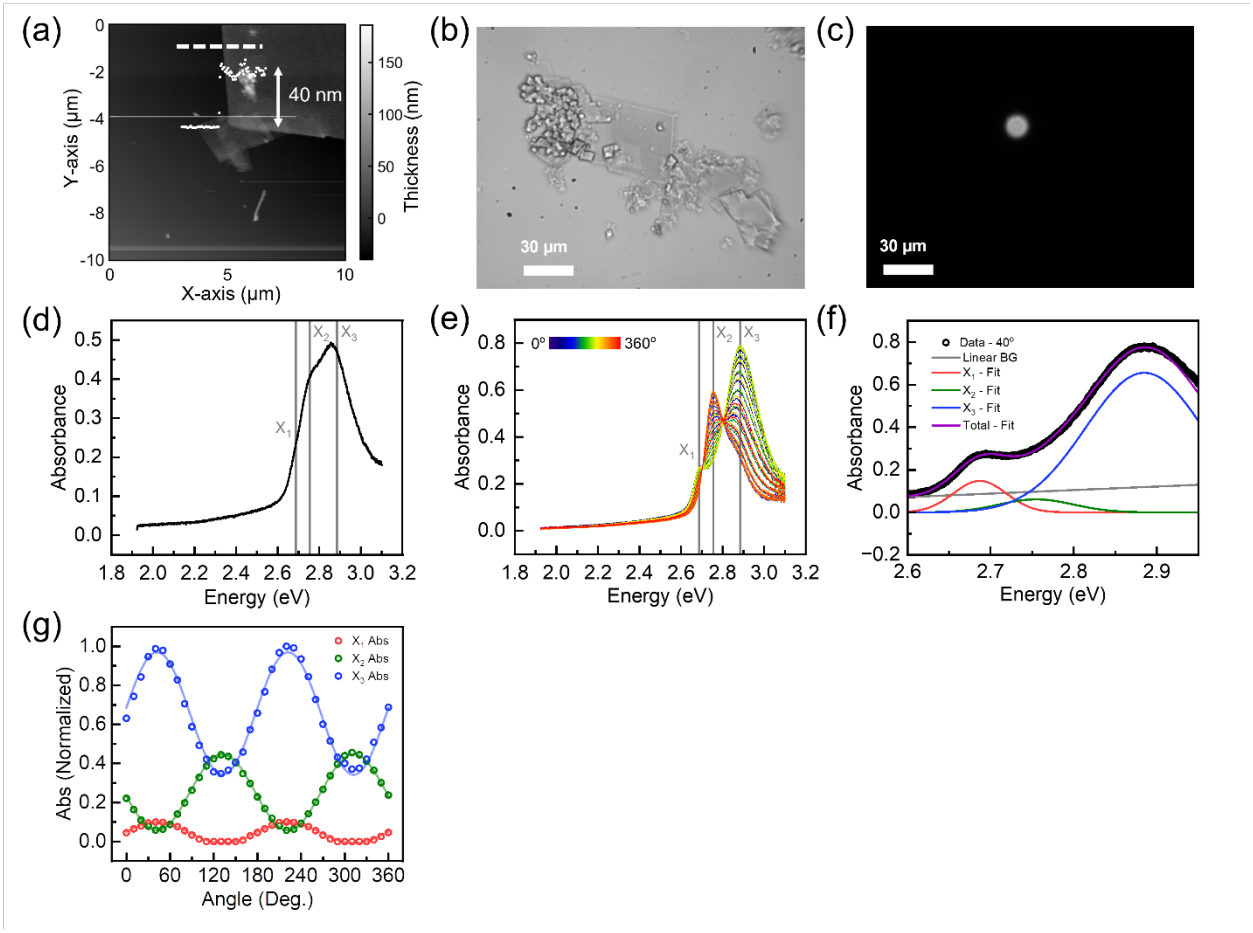

Figure 7.5 (a) Atomic force microscopy image of 40 nm-thick AgSePh crystal. Images of the 40 nm-thick AgSePh crystal captured in the collection path (b) without a pinhole and (c) with a pinhole. (d) Absorption spectra of the 40 nm-thick AgSePh crystal without a linear polarizer. (e) Absorption spectra of the 40 nm-thick AgSePh crystal as a function of polarization angle of incident light. (f) Three Gaussian fit with a peak position of 2.687 eV (X_1, red), 2.755 eV (X_2, green), and 2.885 (X_3, blue) on top of a linear background, applied to the absorption spectra for the linear polarizer angle of 40°. (g) Polarization-dependent absorption intensities of X_1, X_2 and X_3 excitons, obtained by integrating the Gaussian fits. Solid lines represent sinusoidal fit ($a + b \cdot \sin^2(\theta - c)$) applied to the experimental data.

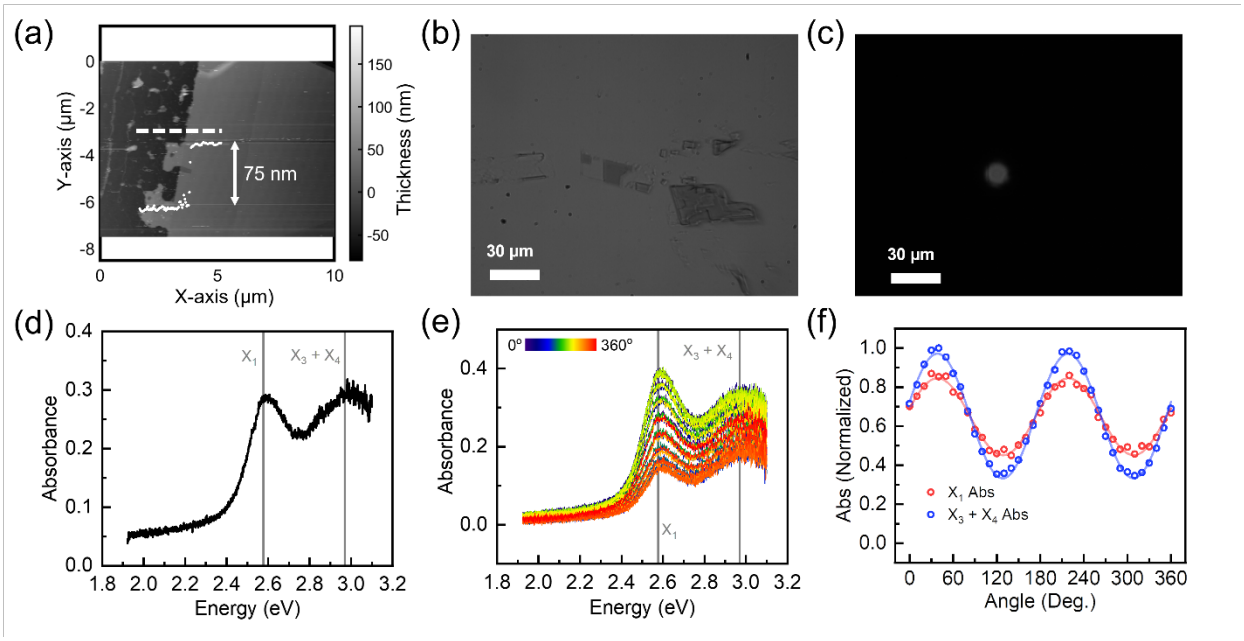

Figure 7.6 (a) Atomic force microscopy image of 75 nm-thick AgTePh crystal. Images of the 75 nm-thick AgTePh crystal captured in the collection path (b) without a pinhole and (c) with a pinhole. (d) Absorption spectra of the 75 nm-thick AgTePh crystal without a linear polarizer. (e) Absorption spectra of the 75 nm-thick AgTePh crystal as a function of polarization angle of incident light. (f) Polarization-dependent intensities of absorption at 2.577 eV (X_1, red) and 2.969 (X_3 + X_4, blue). Solid lines represent sinusoidal fit ($a + b \cdot \sin^2(\theta - c)$) applied to the experimental data.

In the case of the AgSPh, the absorption spectra with a peak at ~3.44 eV remained nearly identical regardless of the polarization state (Figures 7.2d,g,j and 7.4), suggesting in-plane isotropic imaginary part of refractive index. In contrast, the AgSePh exhibited a strong polarization dependence of absorption (Figure 7.2e). When the polarization of incident light was parallel to the crystallographic [010] orientation, excitonic resonances at ~2.687 eV (X_1) and ~2.885 eV (X_3) became clearly resolvable and exhibited the highest intensity (Figure 7.2h). Conversely, when the light polarization was aligned with the [100] orientation, an excitonic resonance at ~2.755 eV (X_2) became predominant, while the absorption intensity of X_1 and X_3 excitons was significantly suppressed. To assess the extent of absorption anisotropy, the polarization-resolved absorption spectra were fit with three Gaussian functions corresponding to X_1, X_2, and X_3 excitons (Figure 7.5f). The absorption intensities of these excitons were determined by integrating the Gaussian fit as a function of polarization. The integrated intensities are plotted in polar coordinates alongside

crystal orientation information (Figures 7.2k and 7.5g). The polar plot clearly exhibits that X_1 and X_3 excitons are polarized along [010] orientation whereas X_2 exciton is polarized along [100] orientation, consistent with the previous report.[40] The AgTePh also exhibited strong absorption anisotropy (Figures 7.2f and 7.6). Both absorption peaks at ~2.577 eV (X_1) and ~2.969 eV (X_3 + X_4) exhibited their maximum intensity when the incident light was polarized along the [010] orientation (Figure 7.2j). The absorption around ~2.969 eV at room temperature consists of two excitonic resonances that become resolvable at ~2.91 eV (X_3) and ~3.05 eV (X_4) at 80 K, as shown in our previous reports.[45,49] Because of the unclarity of energies of X_3 and X_4 excitons at room temperature arising from their significant broadening and overlapping, we extracted the absolute absorption intensity at ~2.577 eV (X_1) and at ~2.969 eV (X_3 + X_4) instead of Gaussian fitting, as a function of polarization angle. The polar plot clearly exhibits that both X_1 and X_3 + X_4 excitons are polarized along [010] orientation (Figure 7.2l).

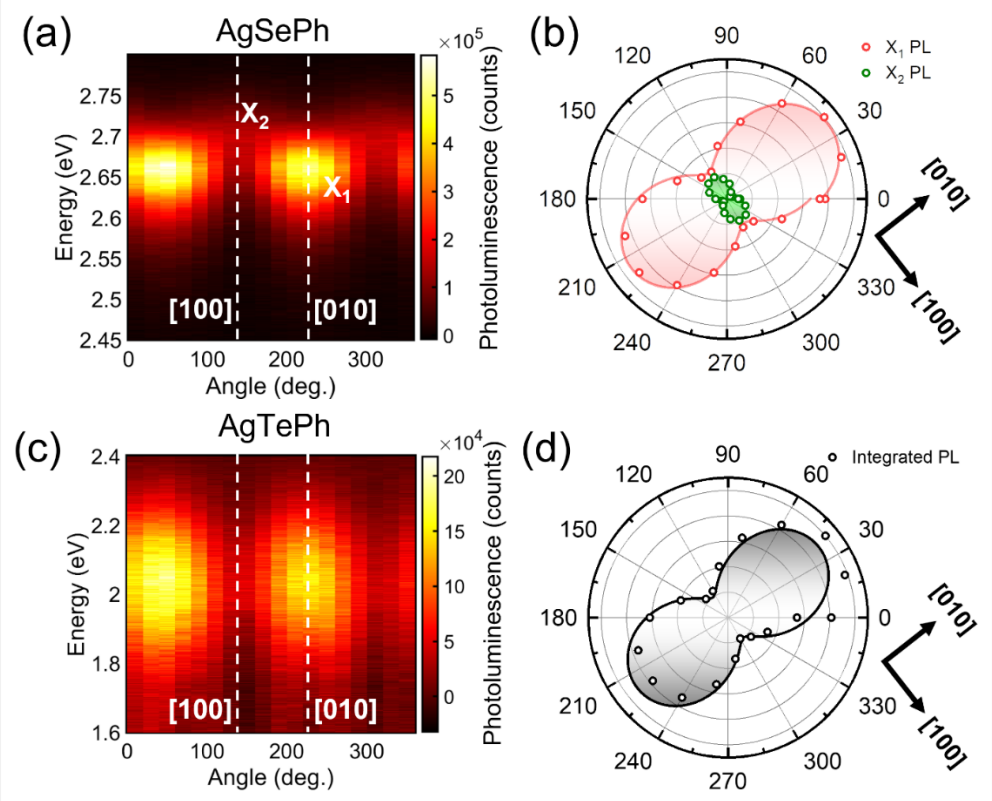

Figure 7.7 2D color plots showing photoluminescence spectra of (a) 40 nm-thick AgSePh and (c) 75 nm-thick AgTePh single crystal as a function of polarization angle of the emitted light. Polar plots showing photoluminescence intensities of (b) 40 nm-thick AgSePh and (d) 75 nm-thick AgTePh single crystal as a function of polarization angle of the emitted light. Solid line: sinusoidal fit applied to the experimental data. See Figures 7.10-7.11 for details.

Strong absorption anisotropy in AgSePh and AgTePh suggests the presence of anisotropy in photoluminescence (PL). (Note that AgSPh did not show any PL) To investigate the PL anisotropy in AgSePh and AgTePh, we performed polarization-resolved micro-PL spectroscopy on the identical single crystal used for polarization-resolved absorption measurement (Figures 7.7-7.11). Briefly, the single crystal, mounted on an inverted microscope, was excited by a 405 nm CW laser diode focused to a spot of ~1 μm in diameter. A circular polarizer was placed between the sample and the light source to eliminate the impact of excitation light's polarization on the PL anisotropy. After excitation, the PL was collected in the epi-configuration and guided into a spectrograph with a CCD detector. A linear polarizer was placed in the PL collection path and rotated from 0° to 360° at a step size of 20, to collect polarization-resolved PL spectra. We confirmed that the polarization response from the optical components in the PL collection path is negligible by conducting measurements using unpolarized broadband light placed on the sample stage (Figure 7.9).

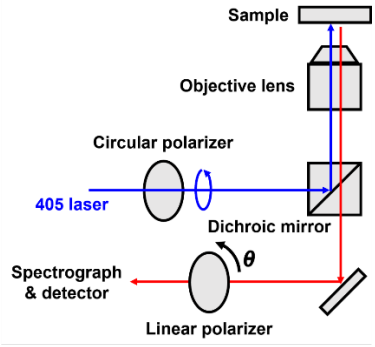

Figure 7.8 Schematic showing the experimental setup for the polarization-resolved micro-PL spectroscopy.

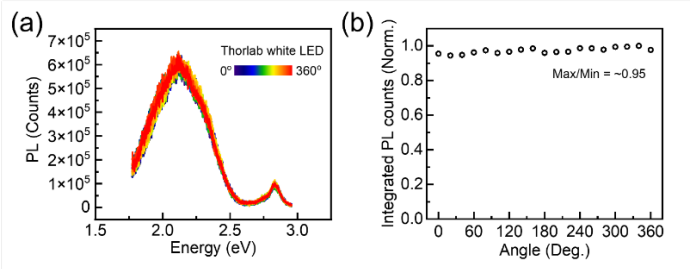

Figure 7.9 (a) PL spectra of the unpolarized white LED (Thorlab MCWHL2-C3) mounted on the sample stage, as a function of the rotation angle of the linear polarizer shown in Figure 7.8. (b) Normalized integrated PL in (a), as a function of the rotation angle of the linear polarizer. The ration between the maximum and minimum values is ~0.95, indicating that the experimental setup has a negligible impact on the polarization-dependent signals.

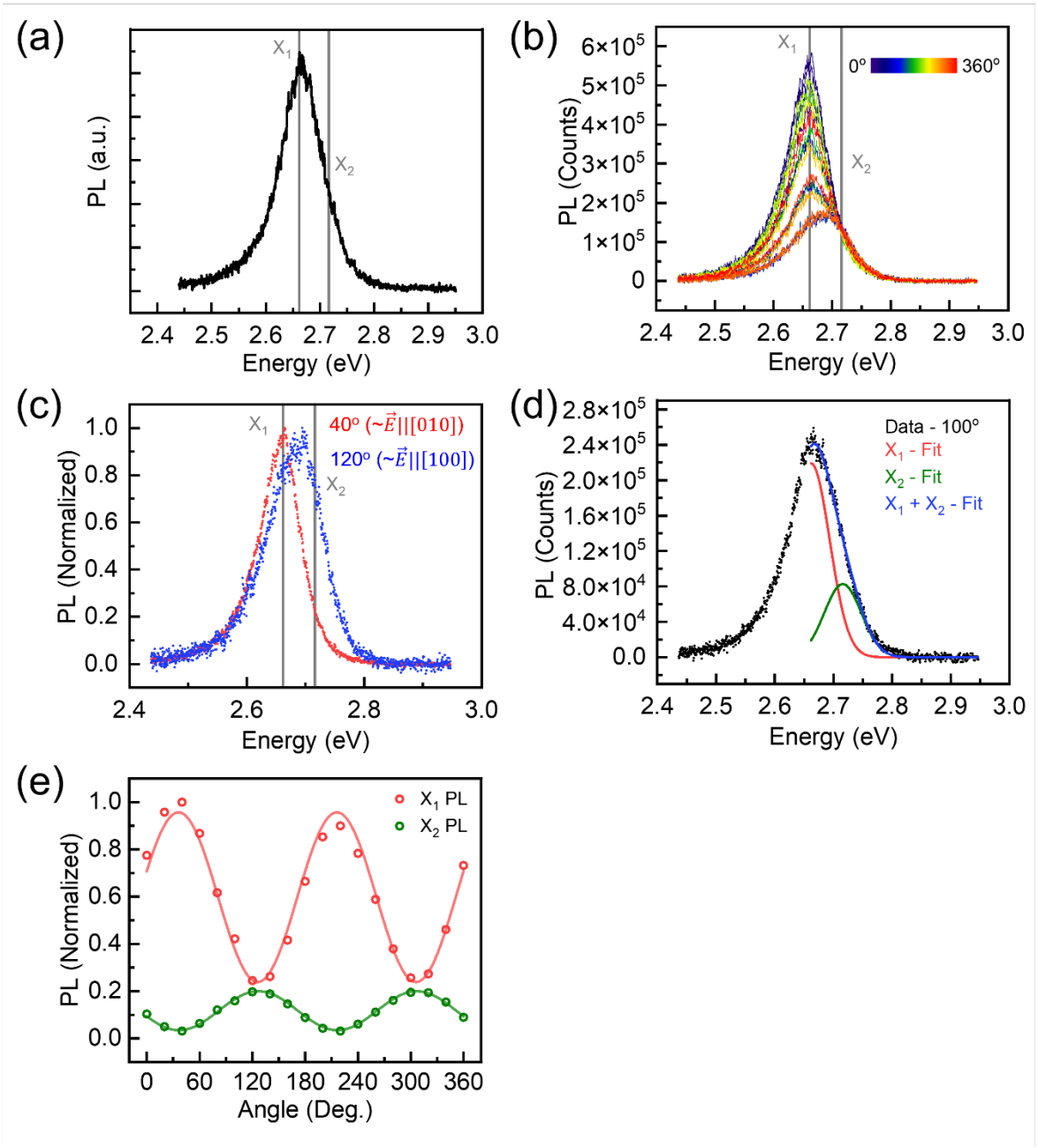

Figure 7.10 (a) PL spectrum of the 40 nm-thick AgSePh crystal (Figure 7.7b) without a linear polarizer. (b) PL spectra of the 40 nm-thick AgSePh crystal as a function of polarization of emitted light. (c) Polarization-resolved PL spectra of the 40 nm-thick AgSePh crystal for the linear polarizer angles of 40° ($\sim\vec{E}$||[100], red) and 120° ($\sim\vec{E}$||[010], blue). (d) Two Gaussian fit with a peak position of 2.662 eV (X_1, red) and 2.716 eV (X_2, blue) applied to the PL spectra for the linear polarizer angles of 100°. Only the high-energy side of the PL spectra was used for the Gaussian fit due to the asymmetry of the spectra, which is likely caused by defect-derived emission or phonon-mediated emission on the low-energy side. (e) The polarization-dependent PL intensities of the X_1 and the X_2 excitons, obtained by integrating the Gaussian fit. Solid line represents a sinusoidal fit $[a + b\cdot\sin^2(\theta\text{-}c)]$ applied to the experimental data.

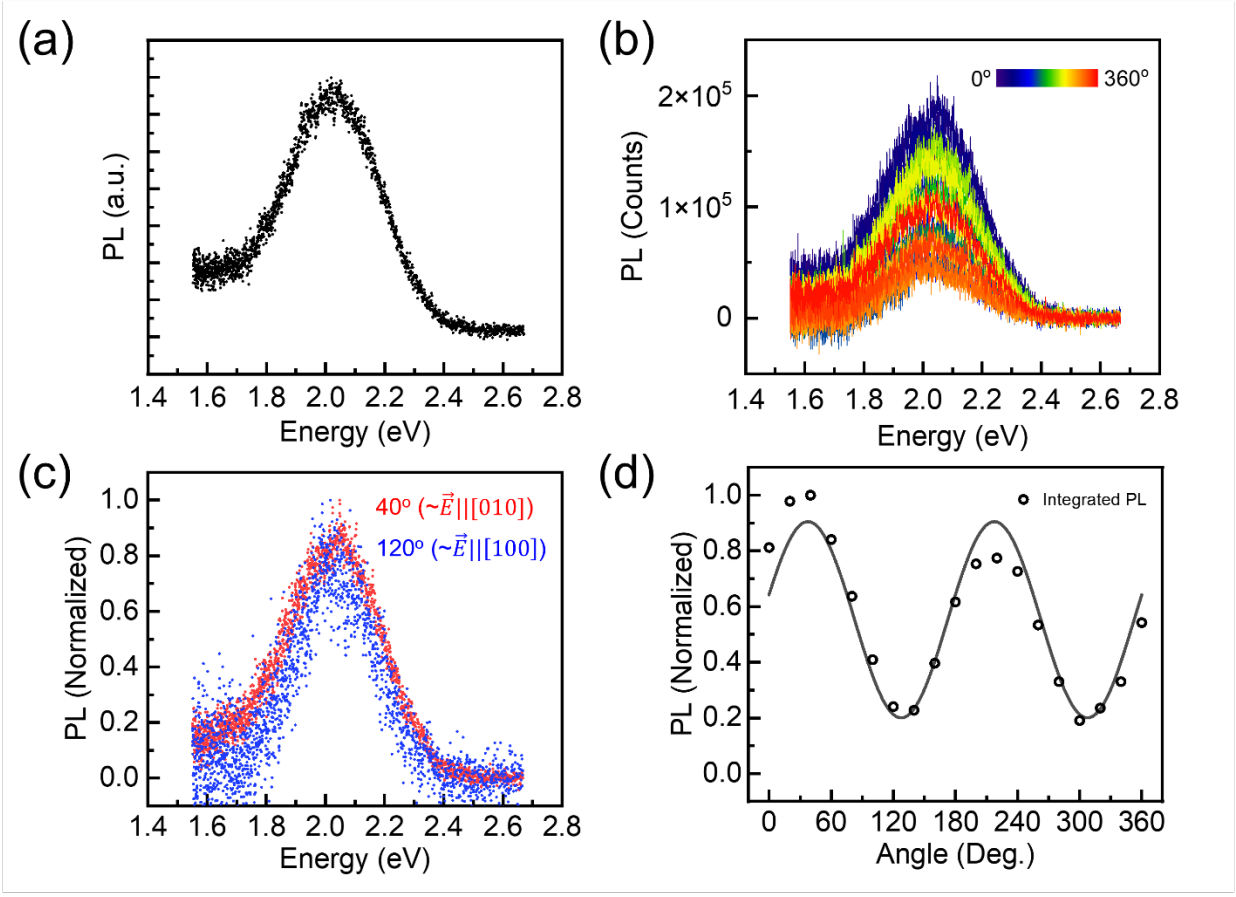

Figure 7.11 (a) PL spectrum of the 75 nm-thick AgTePh crystal (Figure 7.7c) without a linear polarizer. (b) PL spectra of the 75 nm-thick AgTePh crystal as a function of polarization angle of emitted light. (c) Polarization-resolved PL spectra of the 75 nm-thick AgTePh crystal for the linear polarizer angles of 40° (~$\vec{E}$||[010], red) and 120° (~$\vec{E}$||[100], blue). (d) The integrated intensities for the entire PL spectrum as a function of polarization of the emitted light. Solid line represents a sinusoidal fit [a + b·sin^2(θ-c)] applied to the experimental data.

Figure 7.7a displays polarization-resolved PL spectra of the 40 nm-thick AgSePh single crystal. The dataset could be well fit by two Gaussian functions with a peak at 2.662 eV and 2.716 eV, respectively (Figure 7.10). These energies correspond to energies of X_1 and X_2 excitons, considering a slight red-shift from their absorption energies. The PL intensities of X_1 and X_2 excitons as a function of polarization were determined by integrating the Gaussian fit and these PL intensities were polar-plotted (Figure 7.7b). The polar plot reveals that PL of the X_1 exciton is polarized along the [010] direction whereas the PL of the X_2 exciton is polarized along the [100] direction, consistent with their absorption anisotropy. Figure 7.7c shows polarization-resolved PL

spectra of the 75 nm-thick AgTePh single crystal. The normalized PL spectra remained nearly identical regardless of the polarization state (Figure 7.11). Thus, the entire PL spectra were integrated to assess the PL anisotropy. Figure 7.7d displays the integrated PL intensities on a polar plot, revealing that the PL in AgTePh is polarized along with the [010] direction. Interestingly, the polarization of the PL is identical to the polarization of X_1 exciton observed in the absorption measurement, despite the significant red-shift from the absorption of the X_1 exciton. The significantly red-shifted and broad PL in AgTePh was previously assigned to the self-trapped exciton emission.[45] This self-trapping phenomenon occurs when free-excitons are trapped into a deep potential well induced by their strong interaction with phonons.[52,53] The conservation of their polarization states during the self-trapping process highlights the robustness of their polarization states and potentially suggests the anisotropic exciton-phonon interaction.[27,42]

7.3.2 Density functional theory and GW with the Bethe-Salpeter equation calculations

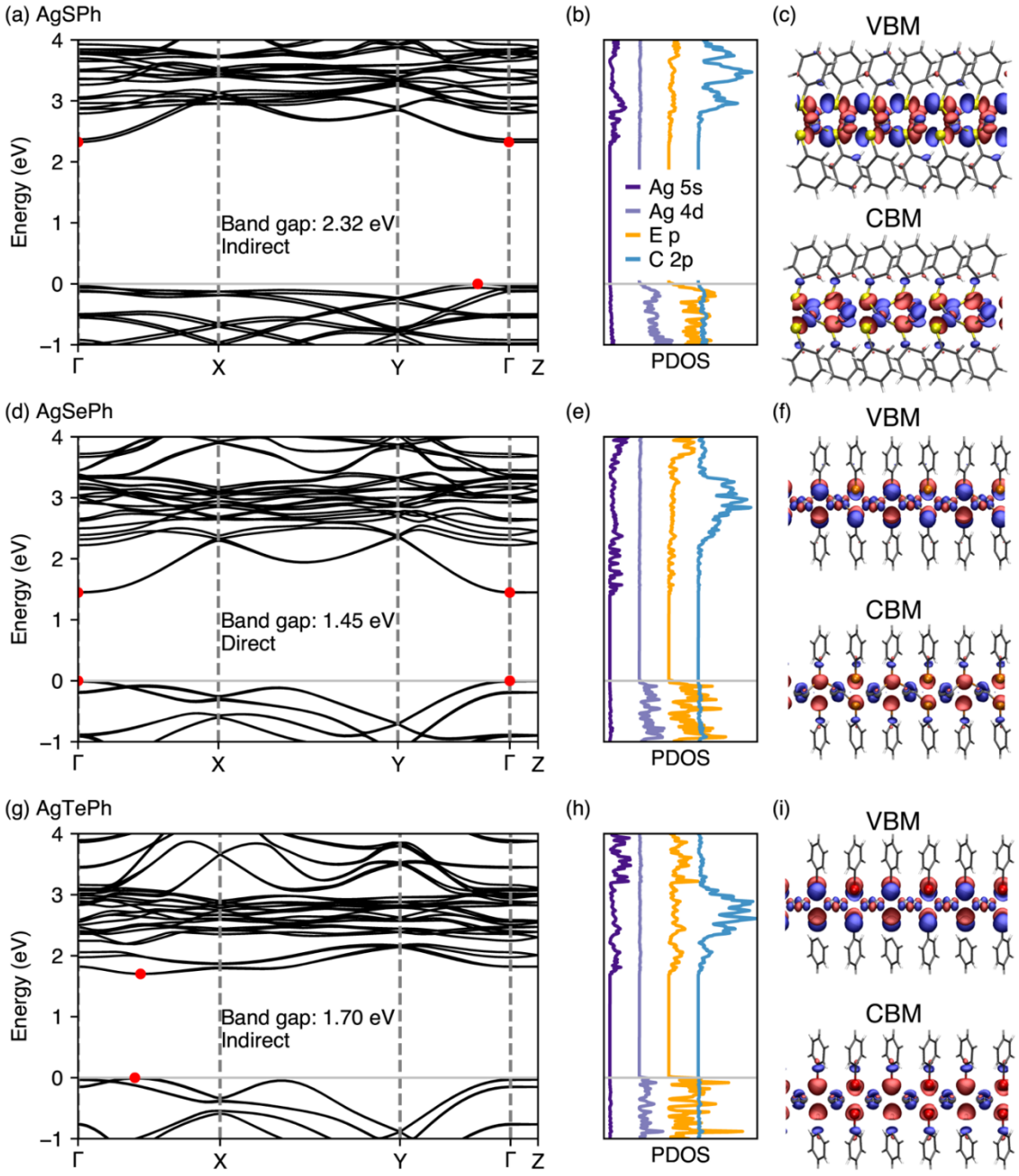

Figure 7.12 Density functional theory (DFT)-calculated electronic band structures of (a) AgSPh in $P2_1$, (d) AgSePh in $P2_1/c$, and (g) AgTePh in $P2_1/c$. The valence band maximum (VBM) and the conduction band minimum (CBM) are marked with red circles. Orbital projected density of states of (b) AgSPh, (e) AgSePh, and (h) AgTePh. Wavefunctions of the VBM and the CBM of (c) AgSPh, (f) AgSePh, and (i) AgTePh. Blue and red surfaces represent the positive and negative phases of the wavefunction, respectively, with an isosurface level set at $8 \times 10^{-4}\ e/bohr^{-3}$. Atoms are colored as follows: Ag: gray, S: yellow, Se: orange, Te: red, C: black, H: white.

Electronic band structures of AgEPh were investigated using density functional theory (DFT) calculations (Figure 7.12). These calculations used the reported structures of AgSPh in monoclinic $P2_1$,[30] AgSePh in monoclinic $P2_1/c$,[46] and AgTePh in monoclinic $P2_1/c$.[30] The calculated band structure of AgSPh reveals an indirect gap of 2.32 eV with a direct gap of 2.38 eV at Γ. Notably, due to the lack of inversion symmetry in AgSPh, unlike AgSePh and AgTePh (Figure 7.1a), AgSPh exhibits a slight splitting in its band structure corresponding to the two symmetrically inequivalent layers within the unit cell (Figure 7.12a). AgSePh features a direct gap of 1.45 eV at Γ and AgTePh has an indirect gap of 1.701 eV with a nearly equivalent direct gap of 1.702 eV (Figure 7.12d,g). For all AgEPh, the bands exhibit negligible dispersion along the out-of-plane direction (band extrema or $\Gamma \rightarrow Z$) but exhibit strong dispersion along the other two in-plane directions (band extrema or $\Gamma \rightarrow X$ and Y), indicating confinement of electrons and holes within the 2D plane while being delocalized within the plane.

The projected density of states show that the bands of AgEPh have largely similar orbital contributions (Figure 7.12b,e,h). The valence band maximum (VBM) is primarily composed of Ag 4d orbitals and chalcogen p orbitals, while the conduction band minimum (CBM) is dominated by Ag 5s orbital and chalcogen p orbitals. Conduction bands above CBM are dominated by C 2p orbitals. Furthermore, the wavefunctions of the VBM and CBM for all AgEPh are predominantly located at the Ag-chalcogen sheet, further suggesting that charge carriers are confined within the inorganic sheet (Figure 7.12c,f,i).

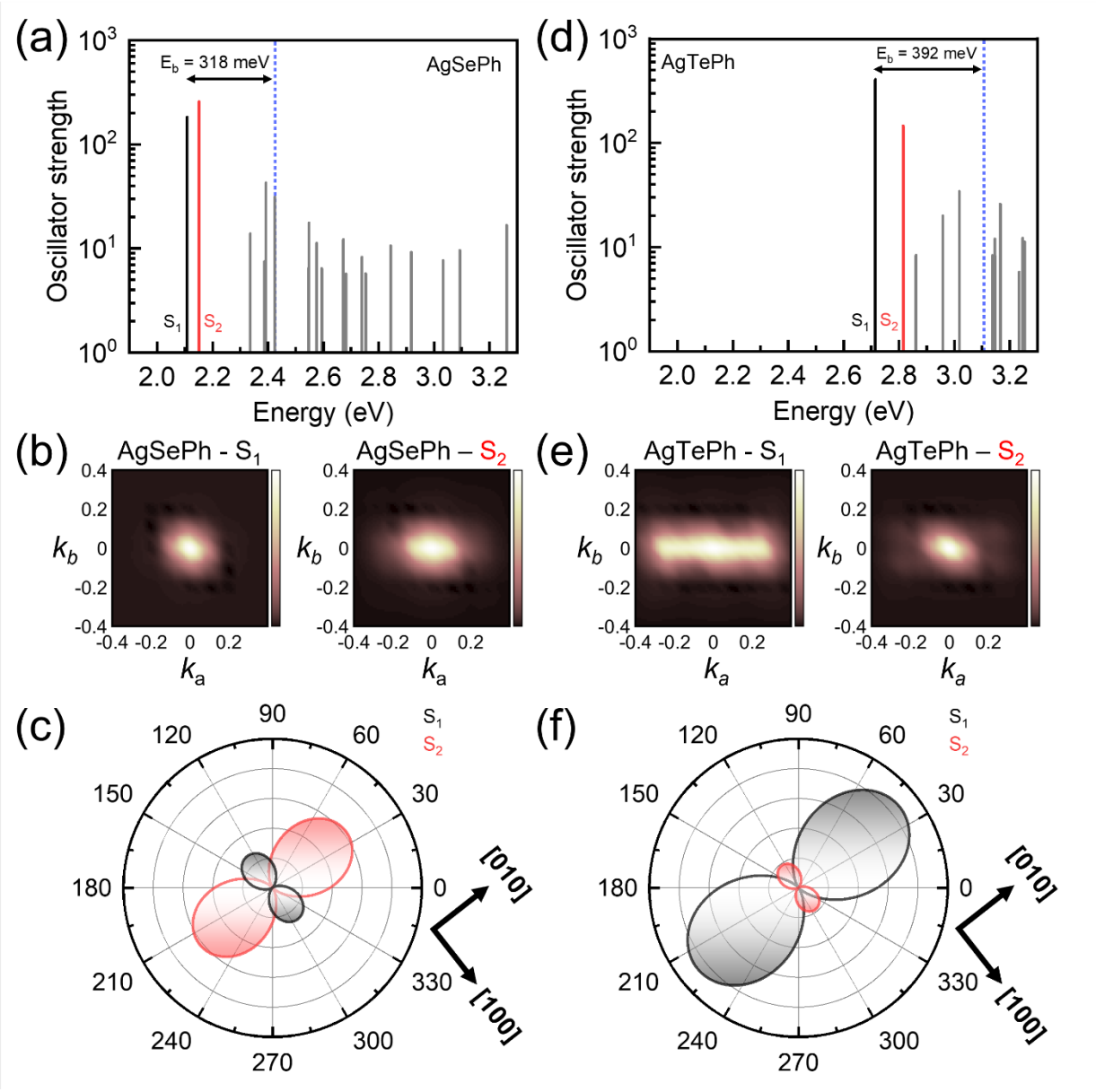

Figure 7.13 Excitation spectra of (a) AgSePh in $P2_1/c$ and (d) AgTePh in $P2_1/c$, calculated using GW-BSE. The GW band gap is indicated by a blue vertical dotted line. Vertical bars represent excitations with oscillator strengths greater than 5 a.u.. Black and red bars represent the lowest (S_1) and the second lowest (S_2) excitations in energy among those excitations. S_1 (left) and S_2 (right) exciton wavefunctions of (b) AgSePh and (e) AgTePh shown in a([100])b([010]-plane in k-space. Absorption intensities of S_1 and S_2 excitons of (c) AgSePh and (f) AgTePh, projected on ab-plane in real space.

Table 7.1 Excitation energy, oscillator strength, identification of whether the state is s-like or p-like, identification of whether the state is intralayer or interlayer, and polarization of excitations of AgSePh in $P2_1/c$ and AgTePh in $P2_1/c$, calculated using GW-BSE. Only excitations with energy below GW band gap and with oscillator strength greater than 5 a.u. are included. See Tables 7.2 and 7.3 for all excitations below GW bandgap of AgSePh in $P2_1/c$ and AgTePh in $P2_1/c$, respectively.

AgSePh in $P2_1/c$ (GW bandgap: 2.426 eV)					AgTePh in $P2_1/c$ (GW bandgap: 3.107 eV)				
Energy (eV)	Oscillator strength (a.u.)	s-like vs. p-like	Intra vs. Inter	Polarization	Energy (eV)	Oscillator strength (a.u.)	Intra vs. Inter	s-like vs. p-like	Polarization
2.108 (S_1)	182.9	s	Intra	[100]	2.715 (S_1)	407.9	Intra	s	[010]
2.151 (S_2)	258.4	s	Intra	[010]	2.815 (S_2)	146.3	Intra	s	[100]
2.336	13.9	s	Intra	[100]	2.861	8.4	Intra	s	[010]
2.386	7.5	s	Inter	[010]	2.958	20	Intra	s	[100]
2.393	42.7	s	Intra	[010]	3.018	34.3	Intra	p	[010]
2.425	31.3	p	Intra	[100]					

We performed GW with the Bethe-Salpeter equation (GW-BSE) calculations of AgSePh in $P2_1/c$[46] and AgTePh in $P2_1/c$[30] to understand their observed optical anisotropy (Figure 7.13 and Table 7.1). The GW renormalizes the direct gap to 2.43 eV for AgSePh and 3.11 eV for AgTePh. Calculated absorption spectra of AgSePh and AgTePh are shown in Figures 7.13a and 7.13d, respectively, revealing multiple exciton states below the computed GW band gap (See Tables 7.2 and 7.3 for all excitations below GW gap of AgSePh and AgTePh, respectively). Notably, the lowest-energy exciton (S_1) exhibits a significant exciton binding energy of 318 meV for AgSePh and 392 meV for AgTePh. For both AgSePh and AgTePh, the lowest (S_1) and the second lowest (S_2) excitons in energy exhibit much stronger oscillator strength than other low-energy excitons. These S_1 and S_2 excitons in AgSePh and AgTePh are both s-like intralayer excitons that are delocalized in the 2D plane (Figures 7.13b,e, 7.14 and 7.15). Figure 7.13b,d displays the *ab*-plane ([100]-[010]-plane in real space) projected absorption intensities of these two brightest excitons in AgSePh and AgTePh, respectively. It was revealed that the S_1 and S_2 excitons in AgSePh are polarized along [100] and [010], respectively, whereas S_1 and S_2 excitons in AgTePh are polarized along [010] and [100], respectively. Other low-energy excitons below the GW gap in AgSePh and AgTePh also exhibit polarization along either [100] or [010] as summarized in the Table 7.1.

Table 7.2 Energy and oscillator strength of excitations below GW gap (2.426 eV) of AgSePh in $P2_1/c$, calculated using GW-BSE.

AgSePh in $P2_1/c$		
State	Energy (eV)	Oscillator strength
1 (S_1)	2.10799	1.829E+02
2	2.11498	1.502E-04
3	2.15096	1.214E-03
4 (S_6)	2.15135	2.584E+02
5	2.27773	3.542E-04
6	2.27782	9.347E-01
7	2.32416	1.049E-02
8	2.32847	5.306E-04
9	2.33592	1.389E+01
10	2.33837	3.027E-04
11	2.34269	3.840E-03
12	2.34362	3.888E-03
13	2.34434	1.004E-02
14	2.34850	1.116E-02
15	2.36463	8.931E-05
16	2.36617	3.224E+00
17	2.37663	3.691E-05
18	2.38170	6.127E-03
19	2.38487	1.610E-04
20	2.38620	7.497E+00
21	2.38996	1.942E-03
22	2.39267	4.274E+01
23	2.39329	3.917E-02
24	2.39455	3.033E+00
25	2.39515	1.911E-02
26	2.39876	1.953E-04
27	2.40851	2.322E-04
28	2.41164	3.057E-03
29	2.41283	3.715E+00
30	2.41319	5.749E-04
31	2.41491	1.303E-01
32	2.41557	2.893E-01
33	2.42460	3.130E+01

Table 7.3 Energy and oscillator strength of excitations below GW gap (3.107 eV) of AgTePh in $P2_1/c$, calculated using GW-BSE.

AgTePh in $P2_1/c$								
State	Energy (eV)	Oscillator strength	State	Energy (eV)	Oscillator strength	State	Energy (eV)	Oscillator strength
1	2.71458	4.000E-04	31	2.99059	7.336E-04	61	3.07532	4.110E-02
2 (S_1)	2.71465	4.079E+02	32	2.99373	1.568E-05	62	3.07679	1.497E+00
3	2.77376	2.155E-01	33	2.99514	2.967E-02	63	3.07717	3.746E-01
4	2.77411	4.806E-03	34	2.99528	1.750E-06	64	3.07835	3.101E+00
5 (S_2)	2.81501	1.463E+02	35	3.00506	5.402E-02	65	3.08145	3.994E+00
6	2.81738	2.316E-03	36	3.00549	2.872E-05	66	3.08176	1.031E-02
7	2.86095	3.070E-04	37	3.01512	1.443E-01	67	3.08191	8.830E-01
8	2.86126	8.395E+00	38	3.01603	2.253E+00	68	3.08204	9.710E-04
9	2.92766	1.109E-02	39	3.01699	2.161E-02	69	3.08316	4.716E-02
10	2.92774	6.483E-01	40	3.01786	3.426E+01	70	3.08372	1.248E-01
11	2.93027	4.309E-01	41	3.02512	2.164E-02	71	3.08613	1.624E-03
12	2.93052	5.335E-04	42	3.02952	1.236E-03	72	3.08765	4.231E-03
13	2.93290	3.407E-03	43	3.03334	4.676E-04	73	3.09094	5.331E-02
14	2.93344	3.926E-03	44	3.03375	1.185E-04	74	3.09181	2.598E-02
15	2.95009	8.346E-04	45	3.03527	1.157E+00	75	3.09553	9.890E-01
16	2.95034	1.069E-01	46	3.03751	4.788E-02	76	3.09611	1.408E-02
17	2.95818	1.995E+01	47	3.03962	2.062E-01	77	3.09643	1.818E+00
18	2.95849	7.910E-02	48	3.04031	1.006E-05	78	3.09749	6.181E-02
19	2.95873	9.387E-02	49	3.04357	7.122E-02	79	3.09762	4.919E-02
20	2.95878	8.864E-03	50	3.04428	1.315E-03	80	3.09837	1.699E-01
21	2.96654	1.838E-01	51	3.05207	1.464E-01	81	3.09925	8.307E-03
22	2.96779	3.177E-03	52	3.05241	9.916E-02	82	3.10063	2.527E-02
23	2.97124	3.410E-06	53	3.05262	2.368E-01	83	3.10197	1.844E+00
24	2.97155	3.561E-01	54	3.05297	3.730E-03	84	3.10301	1.883E+00
25	2.97796	9.745E-04	55	3.05415	1.342E-03	85	3.10355	5.891E-01
26	2.98142	3.542E-03	56	3.05465	1.075E-01	86	3.10385	5.972E-02
27	2.98292	3.850E-04	57	3.06629	1.816E+00	87	3.10524	1.029E-02
28	2.98300	3.919E-02	58	3.06692	5.230E-01	88	3.10538	3.462E-03
29	2.98311	1.120E-07	59	3.07293	1.878E-01			
30	2.98343	1.323E-01	60	3.07392	2.549E-02			

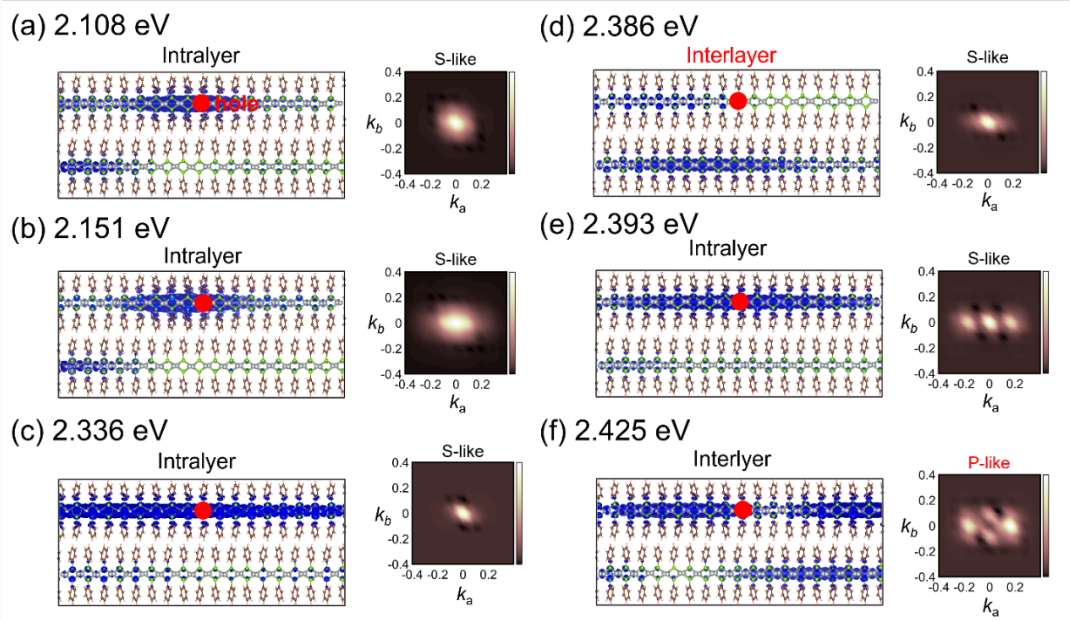

Figure 7.14 The wavefunctions of excitons with oscillator strength greater than 5, shown in real-space (left) and k-space (right), respectively, for AgSePh in $P2_1/c$. For real-space, the wavefunction of electron is shown with the position of the hole fixed (red circle). For the k-space visualization, the exciton wavefunctions are shown in a([100])b([010])-plane.

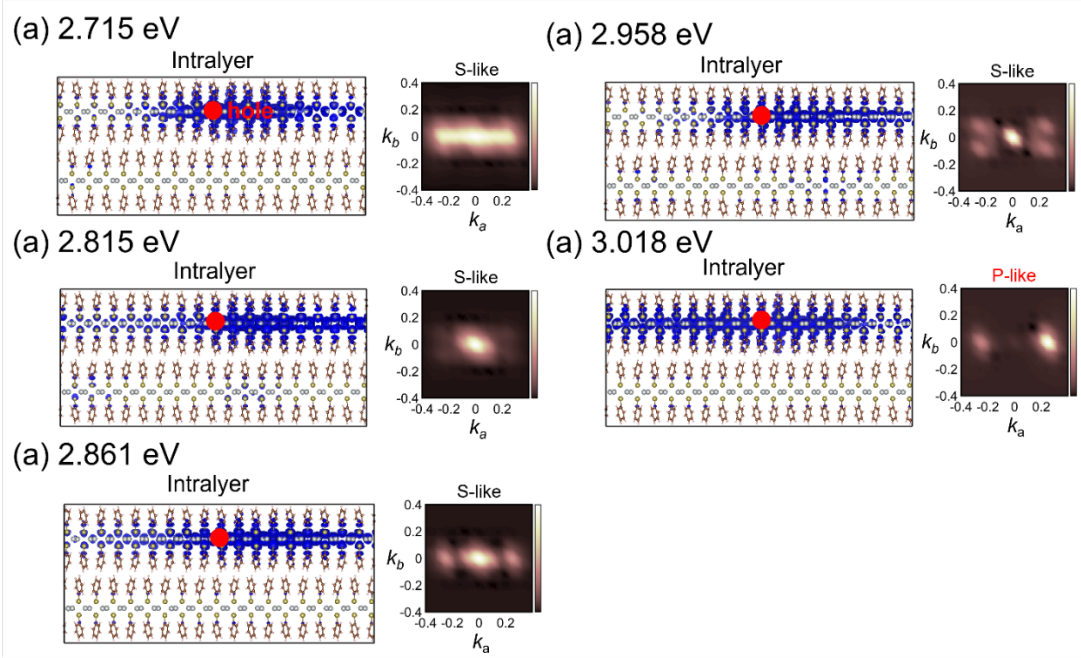

Figure 7.15 The wavefunctions of excitons with oscillator strength greater than 5, shown in real-space (left) and k-space (right), respectively, for AgTePh in $P2_1/c$. For real-space, the wavefunction of electron is shown with the position of the hole fixed (red circle). For the k-space visualization, the exciton wavefunctions are shown in a([100])b([010])-plane.

While GW-BSE calculations revealed multiple excitons with in-plane anisotropy below the bandgap, the characteristics of these excitons, such as energy, oscillator strength, and polarization, are different from experimental observations at room temperature. For example, in the room temperature experiment, we observed that the lowest-energy X_1 exciton and the second lowest-energy X_2 exciton in AgSePh are polarized along [010] and [100], respectively, which is opposite to the results of GW-BSE calculations (S_1 || [100] and S_2 || [010]). Additionally, GW-BSE predicts a greater number of excitons below bandgap than the number of excitons that we experimentally resolved at room temperature. These discrepancies may arise from limitations of our calculations which did not include any nuclear motions or lattice vibrations as well as limitations in experiments that could not resolve dim excitons with weak oscillator strengths that were buried under or overlapping with other bright excitons. Subsequently, we investigated the optical properties at cryogenic temperature to facilitate a direct comparison with results from GW-BSE calculations.

7.3.3 Polarization-resolved reflectance of AgSePh at 4 K

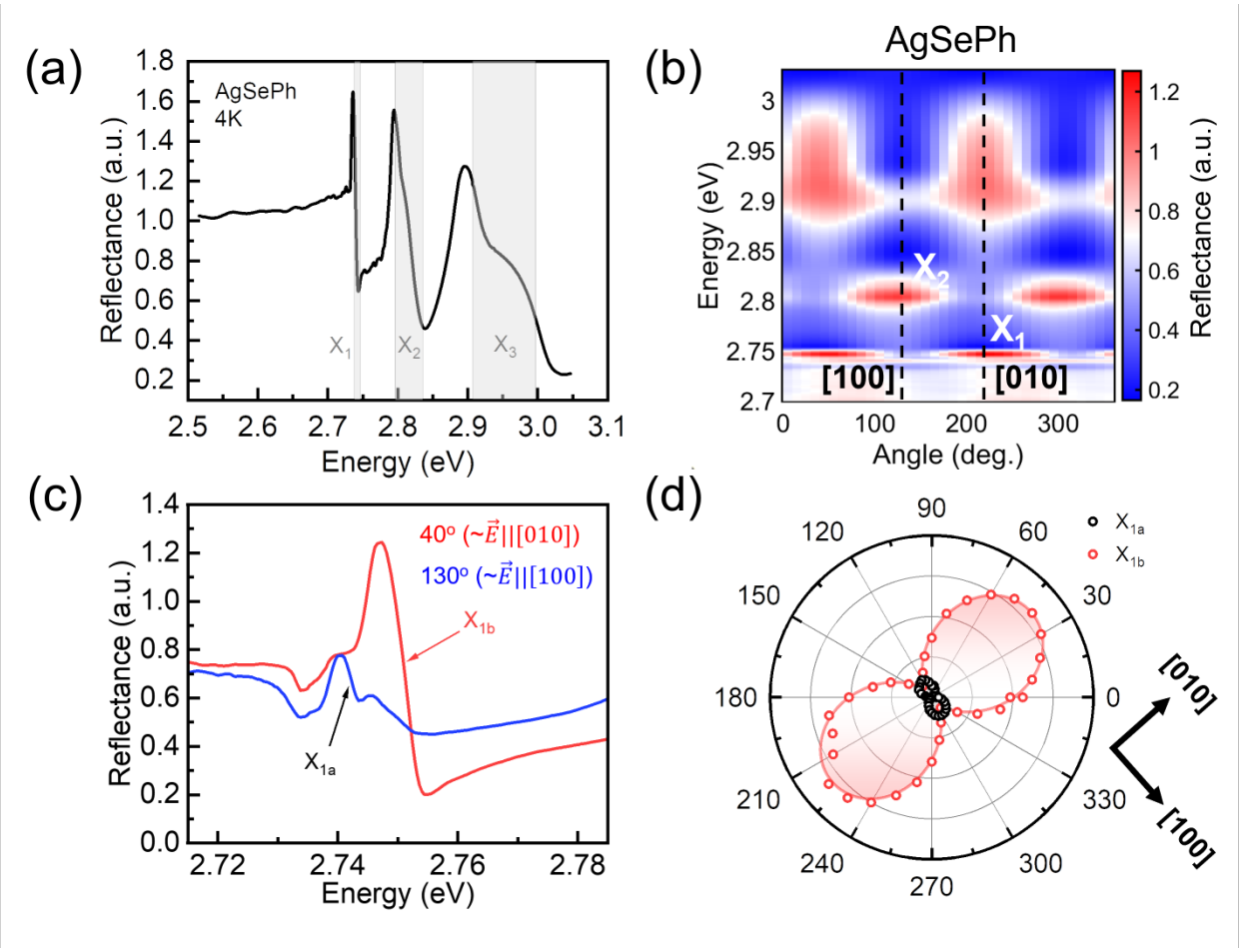

Figure 7.16 (a) The reflectance spectrum of AgSePh crystal, measured with unpolarized incident light at 4 K. (b) The 2D color plot showing reflectance spectra of AgSePh crystal as a function of the linear polarization analyzer angle in the detection path. (c) Polarization-resolved reflectance spectra of AgSePh crystal when the light polarization axis is along crystallographic [100] (red) and [010] (blue). (d) The polar plot showing the amplitudes of X_{1a} (~2.739 eV) and X_{1b} (~2.748 eV) excitonic resonances, extracted by fitting the reflectance spectra with the sum of two Lorentz resonances. Solid line: sinusoidal fit applied to the amplitudes of X_{1a} and X_{1b} resonances.

To further investigate exciton anisotropy of AgSePh with reduced nuclei motions and thermal lattice vibrations, we performed polarization-resolved micro-reflectance measurement at 4 K. Briefly, the sample was mounted on the cold finger of a liquid Helium flow cryostat. The sample was illuminated with a broadband unpolarized white light through a 50x magnification microscope objective. The reflected light was collected in the epi-configuration and guided into a

spectrograph with a CCD detector. Figure 7.16a exhibits the reflectance spectra of AgSePh measured with the unpolarized incident light, revealing a sharp transition at ~2.74 eV (X_1) and broad transitions at ~2.81 eV (X_2) and at ~2.95 eV (X_3) in a good agreement with transitions at room temperature considering thermal red-shift. Next, a linear polarizer and a half-wave plate were inserted in the detection path to probe the intensity of reflected light with a given polarization orientation. The polarization-resolved micro-reflectance spectra were collected by rotating the half-wave plate (Figure 7.16b). The 2D color plot of polarization-resolved reflectance spectra clearly reveals anisotropy in these transitions where X_1 (||[010]) and X_2 (||[100]) transitions are orthogonally polarized (Figure 7.16b), consistent with the polarization-resolved absorption data at room temperature (Figure 7.2e). Interestingly, we found that the excitonic transition near ~2.74 eV can be resolved as two distinct transitions at ~2.739 eV (X_{1a}) and at ~2.749 eV (X_{1b}) as shown in Figure 7.16c.

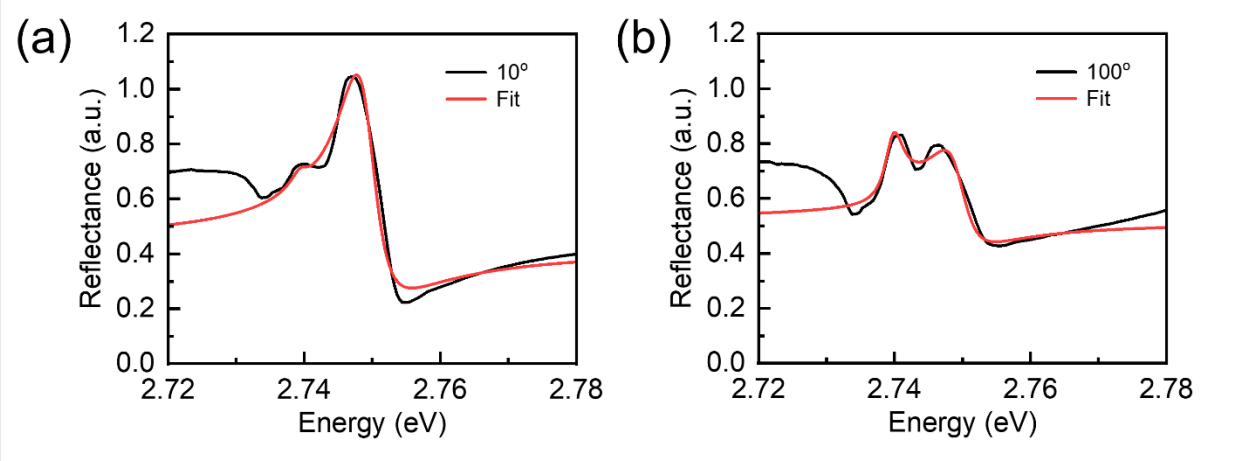

Figure 7.17 Examples of the two Lorentz resonances fitting for the half-wave plate angles of 10° and 100°, respectively. The amplitude of each resonance, C_{1a} and C_{1b}, as a function of polarization is polar-plotted in Figure 7.16d.

To assess the amplitude and anisotropy of these two transitions, we fit the polarization-resolved reflectance spectra near ~2.74 eV with the sum of two Lorentz resonances corresponding to X_{1a} and X_{1b} transitions (Figure 7.17) using following equation:

$$r(E) = r_0 + Re[C_{1a} \cdot e^{i\varphi_{1a}} \cdot (E - E_{1a} + i\Gamma_{1a})^{-1} + C_{1b} \cdot e^{i\varphi_{1b}} \cdot (E - E_{1b} + i\Gamma_{1b})^{-1}] \qquad (7.1)$$

where C_i, φ_i, E_i, and Γ_i are the amplitude, phase, energy, and broadening parameter of each resonance (i = 1a or 1b).

Figure 7.16d exhibits the transition amplitude of X_{1a} and X_{1b} as a function of polarization in a polar plot, revealing X_{1a} is polarized along [100] orientation whereas X_{1b} is polarized along [010] orientation. Surprisingly, the order in energy, transition intensity, and polarization of X_{1a} and X_{1b} transitions nicely match with S_1 and S_2 excitons in GW-BSE calculations. This suggests that S_1 and S_2 excitons in GW-BSE calculations may correspond to X_{1a} and X_{1b} excitons, rather than X_1 and X_2 excitons, in our experimental observations. Furthermore, given that GW-BSE calculations predict the greater number of excitons with sufficient oscillator strengths and polarization along either [100] or [010] below GW bandgap than our experimental observations, this implies that the potential presence of other dim excitons in AgSePh and AgTePh that could be further resolved in future investigations.

7.3.4 Photonic effects on optical properties of AgEPh (E = S, Se, Te)

2D AgEPh (E = S, Se, Te) crystals naturally have an Fabry-Perot cavity structure[54] due to their high refractive index compared to air and glass substrate which causes the top and bottom facets to act as mirrors[40,51]. Thus, photonic effects such as interference[54] or even exciton-polariton interactions[55] can occur when their thickness is in the range of wavelength of our interest. The minimum thickness (t) to see these effects is $t = \lambda/4n$ where λ is wavelength of our interest and n is the real part of the refractive index. To explore potential photonic effects on absorption and photoluminescence spectra of AgEPh crystals, we prepared 500 nm-thick AgSPh, 420 nm-thick AgSePh, and 280 nm-thick AgTePh crystals (Figures 7.18-7.22).

The absorption peak of the 500 nm-thick AgSPh was slightly red-shifted compared to the 68-nm thick AgSPh, likely due to interference effect (Figures 7.4 and 7.18). More importantly, the 500 nm-thick AgSPh exhibited polarization-dependent absorption spectra while the 68-nm thick AgSPh did not), suggesting the anisotropic real part of refractive index (as also confirmed by polarized-light microscopic images in Figure 7.18b,c) and isotropic imaginary part of refractive index within in-plane. The 420 nm-thick AgSePh exhibited much more dramatic photonic effects (Figures 7.5 and 7.19). It showed a fringe pattern below the absorption onset likely due to interference. More strikingly, it exhibited significant polarization-dependent signals above absorption onset that is completely different from the 40 nm-thick AgSePh. This may be due to combination of interference and exciton-polariton interactions arising from strong oscillator

strength, high exciton binding energy, negligible Stokes shift, and natural optical cavity structure of AgSePh. The 280 nm-thick AgTePh crystal exhibited comparatively similar polarization-resolved absorption spectra to the 75 nm-thick AgTePh crystal (Figures 7.6 and 7.19). Overall, these observations suggest that 2D AgEPh, especially AgSePh, can provide a platform to study and exploit exciton-photonics in the absence of artificial cavity.

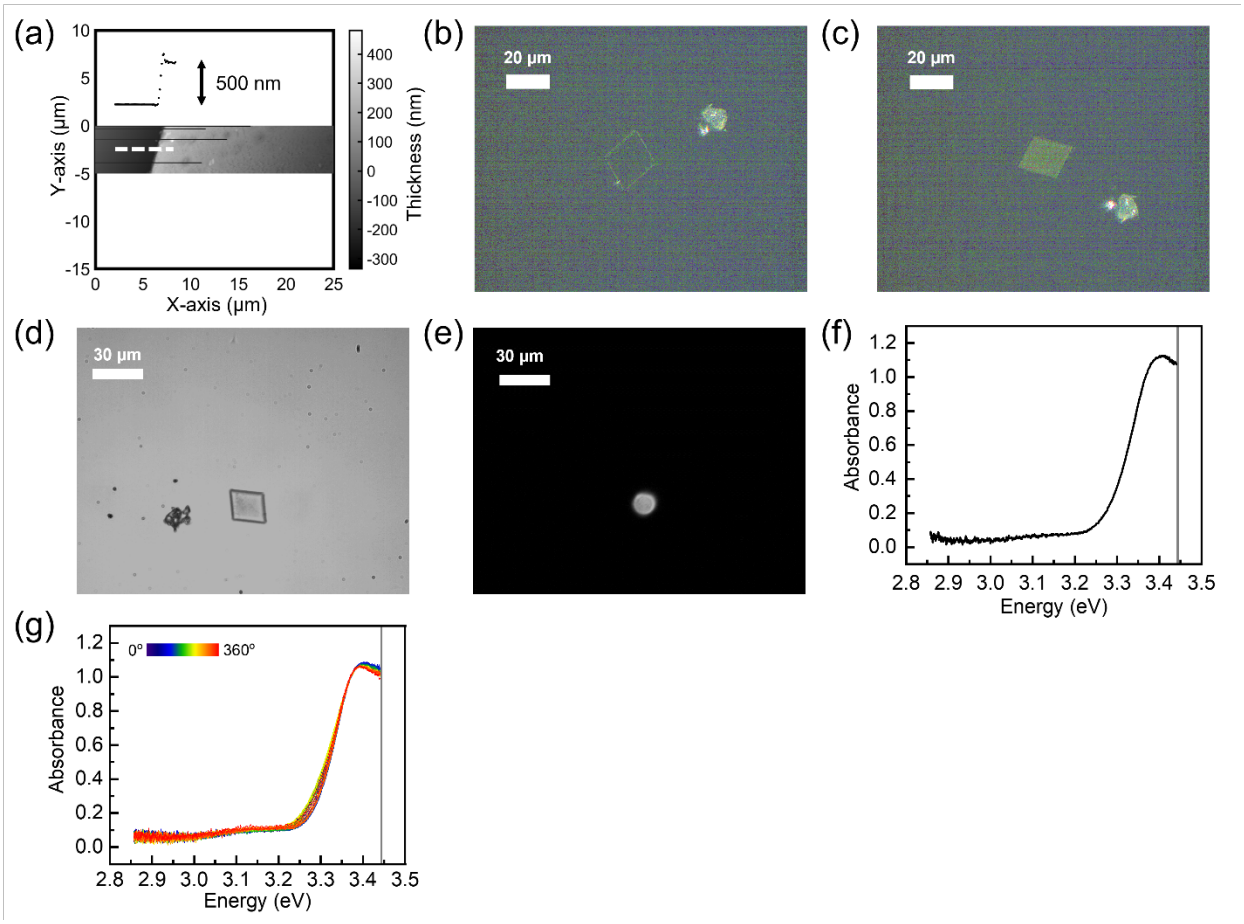

Figure 7.18 (a) Atomic force microscopy image of 500 nm-thick AgSPh crystal. (b,c) Polarized optical micrographs of the 500 nm-thick AgSPh crystal. The change in brightness across the crystal from (b) complete darkness to (c) brightness as the crystal was rotated indicates that the crystal is single. Images of the 500 nm-thick AgSPh crystal captured in the collection path (d) without a pinhole and (e) with a pinhole. (f) Absorption spectra of the 500 nm-thick AgSPh crystal without a linear polarizer. (g) Absorption spectra of the 500 nm-thick AgSPh crystal as a function of polarization angle of incident light.

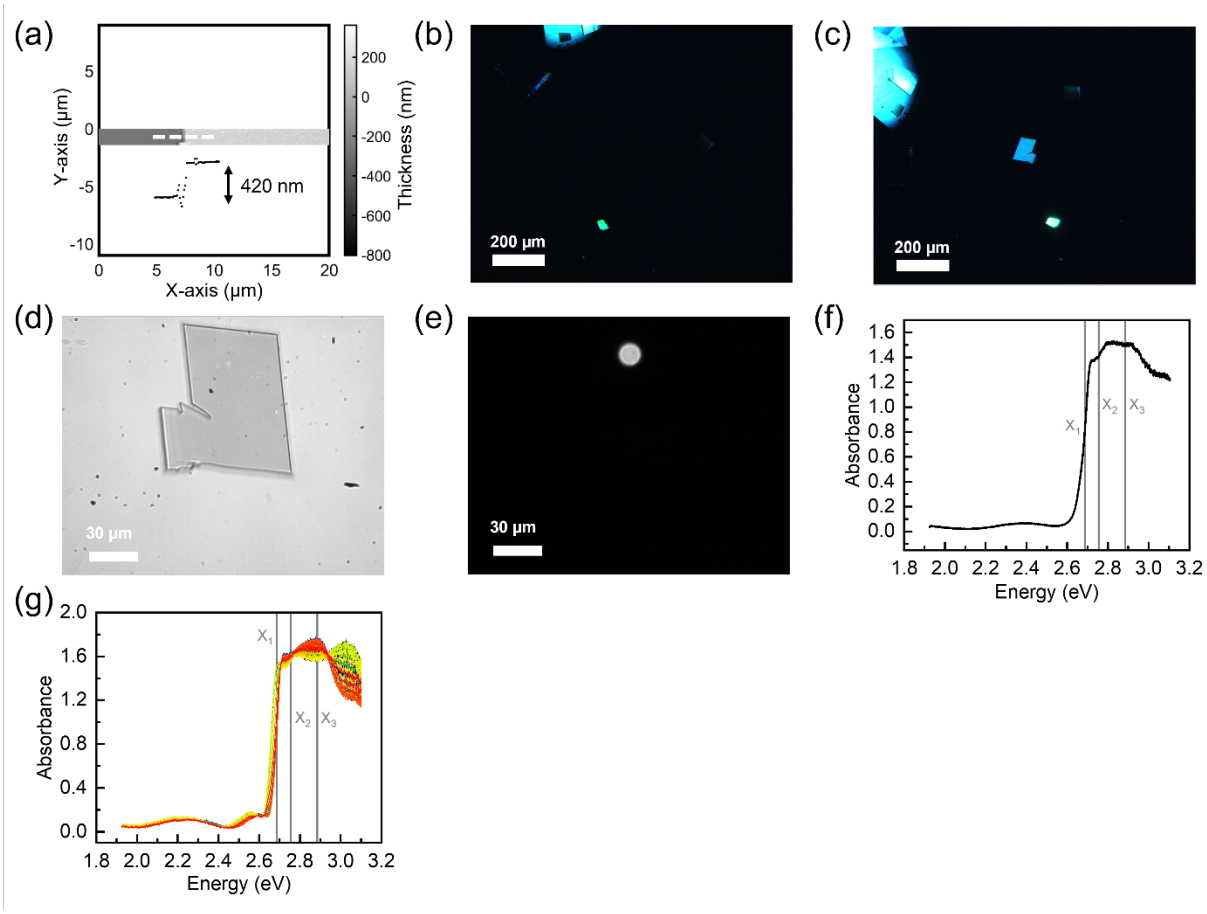

Figure 7.19 (a) Atomic force microscopy image of 420 nm-thick AgSePh crystal. (b,c) Polarized optical micrographs of the 420 nm-thick AgSePh crystal. The change in brightness across the crystal from (b) complete darkness to (c) brightness as the crystal was rotated indicates that the crystal is single. Images of the 420 nm-thick AgSePh crystal captured in the collection path (d) without a pinhole and (e) with a pinhole. (f) Absorption spectra of the 420 nm-thick AgSePh crystal without a linear polarizer. (g) Absorption spectra of the 420 nm-thick AgSePh crystal as a function of polarization angle of incident light.

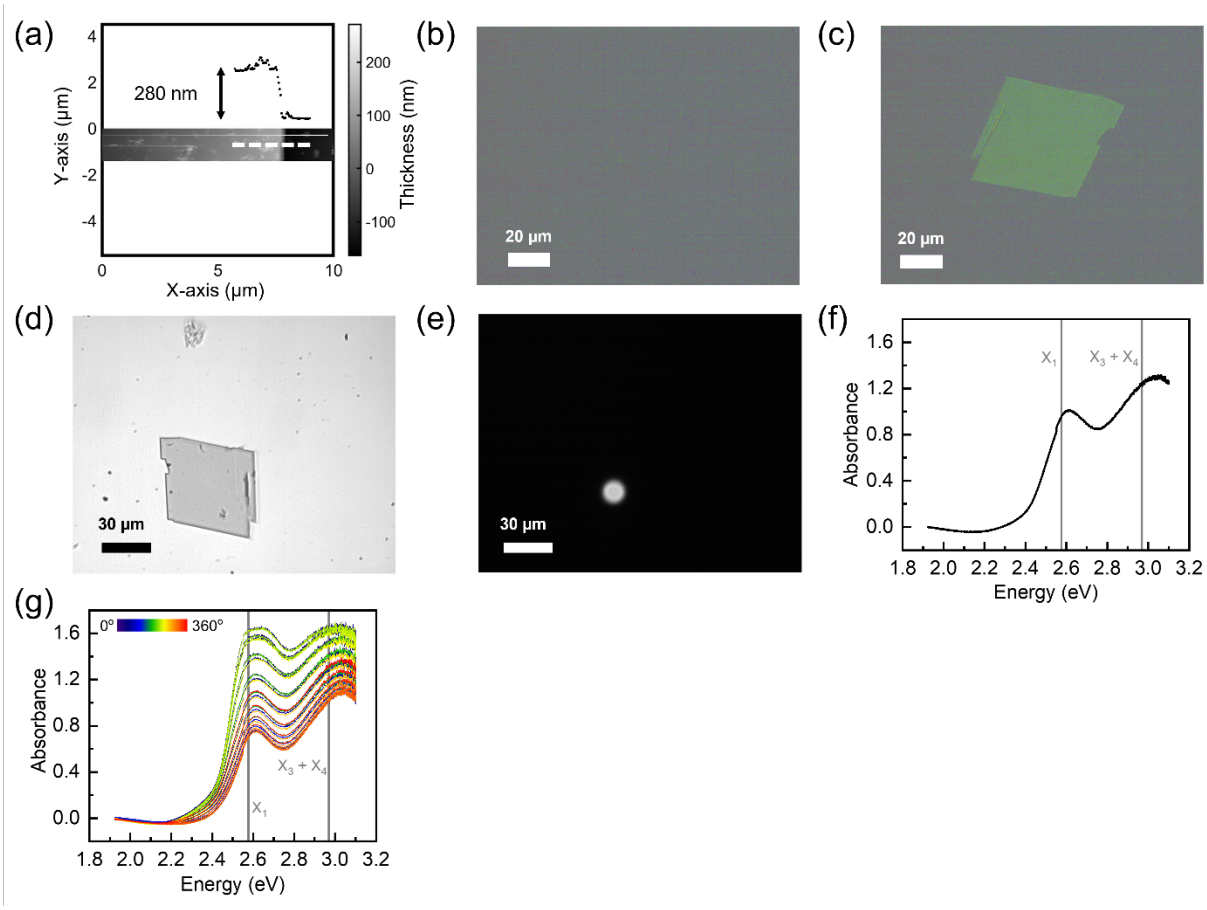

Figure 7.20 (a) Atomic force microscopy image of 280 nm-thick AgTePh crystal. (b,c) Polarized optical micrographs of the 280 nm-thick AgTePh crystal. The change in brightness across the crystal from (b) complete darkness to (c) brightness as the crystal was rotated indicates that the crystal is single. Images of the 280 nm-thick AgTePh crystal captured in the collection path (d) without a pinhole and (e) with a pinhole. (f) Absorption spectra of the 280 nm-thick AgTePh crystal without a linear polarizer. (g) Absorption spectra of the 280 nm-thick AgTePh crystal as a function of polarization angle of incident light.

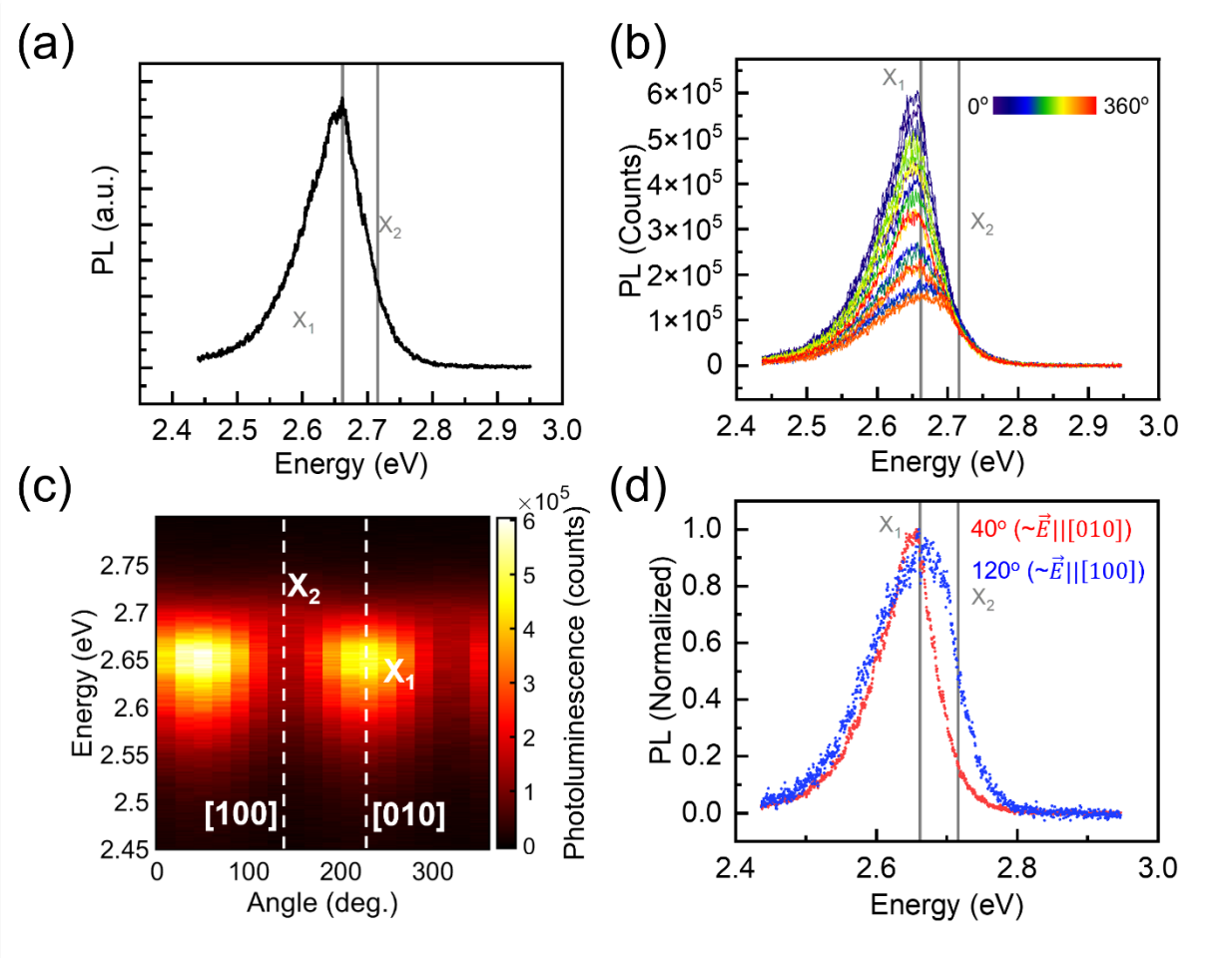

Figure 7.21 (a) PL spectrum of the 420 nm-thick AgSePh crystal (Figure 7.19) without a linear polarizer. (b) PL spectra of the 420 nm-thick AgSePh crystal as a function of polarization of emitted light. (c) 2D color plot showing PL spectra of the 420 nm-thick AgSePh crystal. (d) Polarization-resolved PL spectra of the 420 nm-thick AgSePh crystal for the linear polarizer angles of 40° ($\sim\vec{E}$||[100], red) and 120° ($\sim\vec{E}$||[010], blue). The results are largely the same as those observed in thinner crystals (Figure 7.5).

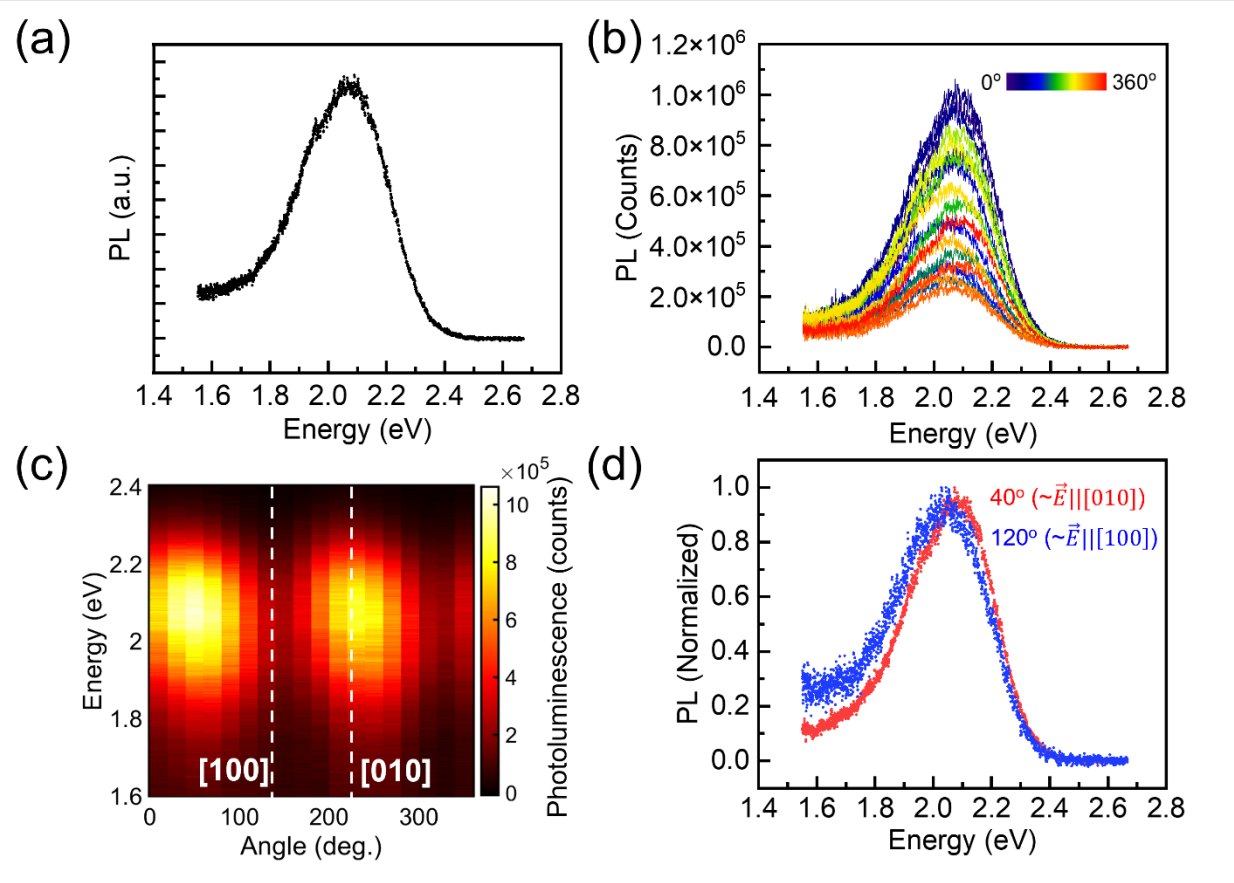

Figure 7.22 (a) PL spectrum of the 280 nm-thick AgTePh crystal (Figure 7.20) without a linear polarizer. (b) PL spectra of the 280 nm-thick AgTePh crystal as a function of polarization of emitted light. (c) 2D color plot showing PL spectra of the 280 nm-thick AgTePh crystal. (d) Polarization-resolved PL spectra of the 280 nm-thick AgTePh crystal for the linear polarizer angles of 40° (~$\vec{E}$||[100], red) and 120° (~$\vec{E}$||[010], blue). A slight difference between two spectra is likely due to the interference effect. The results are largely the same as those observed in thinner crystals (Figure 7.6).

7.4 Conclusions

In conclusion, our spectroscopic measurements combined with *ab initio* calculations reveal the anisotropy of multiple robust excitons in in-plane anisotropic 2D AgEPh, which dominate their optical responses in the ultraviolet-visible range. Our findings highlight the richness and complexity of excitons within the visible range in these emerging 2D semiconductors, likely arising from their low-symmetry crystal structures. GW-BSE calculation offer an atomistic and electronic perspective on the origins of excitonic peaks and their anisotropy, further elucidating the relationship between the crystal structure and the optical properties. These excitons have been reported to strongly couple with lattices or phonons in these hybrid 2D materials, leading to coherent excited state oscillation in AgSePh[33,42] and self-trapped excitons in AgTePh.[45] Furthermore, due to their natural photonic cavity structure, these excitons can couple with photons to form exciton-polaritons at a certain range of thickness.[51] Taken all together, we propose these in-plane anisotropic 2D hybrid semiconductors as an ideal platform for the investigation of excitonic physics and many-body interactions among quasiparticles including electrons, excitons, phonons, and photons.

7.5 Methods

Chemicals. Diphenyl disulfide (Ph_2S_2, 99.0+%) and diphenyl diselenide (Ph_2Se_2, 97.0+%) were purchased from TCI America. Diphenyl ditelluride (Ph_2Te_2, 98%), propylamine ($PrNH_2$, 98%), butylamine ($BuNH_2$, 99.5%), toluene (>99.5%), ammonium hydroxide solution (NH_3/H_2O; ACS reagent, 28.0-30.0% NH_3 basis), silver nitrate ($AgNO_3$, ≥99.0%) were purchased from Millipore Sigma.

Preparation of AgEPh (E = S, Se, Te) crystals.[30,46] AgEPh crystals were synthesized by mixing a 20 mM solution of silver nitrate ($AgNO_3$) in 1-butylamine ($BuNH_2$) and a 20 mM solution of diphenyl dichalcogenide (Ph_2E_2) in $BuNH_2$ in a sealed vial. The vial was then stored under dark at room temperature for 2 weeks to obtain AgSPh crystals, 3 days for AgSePh crystals, and 2 months for AgTePh crystals. The synthesized AgEPh crystals are typically much thicker than 1 μm. Thus, 68 nm-thick AgSPh and 75 nm-thick AgTePh were prepared through mechanical exfoliation, and 500 nm-thick AgSPh, 420 nm-thick AgSePh, and 280 nm-thick AgTePh were

prepared through careful search. Thin (< 100 nm) AgSePh can also be obtained by mechanical exfoliation, but 40 nm-thick AgSePh that we discussed in this manuscript was prepared by a biphasic hydrothermal method. For the biphasic method, a mixture of toluene containing Ph_2Se_2 (3mM) and aqueous ammonia (NH_3/H_2O) containing $AgNO_3$ (3mM) was heated at 180 ºC for 1 hour. Thickness of crystals were measured using atomic force microscope (BRUKER, Dimension XR).

Polarized optical microscopy. The samples on transparent glass coverslips were mounted on an inverted microscope (Nikon, Ti-U Eclipse). Above and below the sample, a polarizer and an analyzer were placed, respectively, oriented orthogonally to each other. The sample was illuminated by an overhead light source (Nikon D-LH Halogen 12V 100W). The transmitted light through the sample was collected with an objective lens (Nikon, CFI S Plan Fluor ELWD, 40×, 0.6 NA) and then directed into a color CMOS camera (Thorlabs, DCC1645C-HQ). Polarized optical images were taken by rotating the sample stage.

Micro-absorption spectroscopy. The samples on transparent glass coverslips were mounted on the inverted microscope. The sample was illuminated by an overhead light source (Thorlabs M365L2-C5 for AgSPh / Nikon D-LH Halogen 12V 100W for AgSePh and AgTePh). The transmitted light through the sample was collected with the 40× objective lens and then spatially filtered through a 600 μm in diameter pinhole (spatial resolution: ~15 μm, see figures S2b,c) to select a region of interest. The spatially filtered light was then directed into a spectrograph (Princeton Instruments, SP-2500) equipped with a cooled charge-coupled device (CCD) detector (Princeton Instruments, PIMAX 4: 1024 EMB). The absorbance $[A = -log_{10}(I/I_0)]$ of the sample was calculated by comparing the spectrum of the transmitted light through the crystal (I) with the spectrum of the transmitted light through the bare substrate (I_0) under the same experimental condition, which ensures the cancellation of polarization effects from the optics in the data. For polarization-resolved micro-absorption measurement, a linear polarizer (Thorlabs, LPUV050 for AgSPh /Thorlabs, LPVISE100-A for AgSePh and AgTePh) was inserted between the sample and the light source, and then rotated from 0° to 360° at a step size of 10°.

Micro-photoluminescence spectroscopy. The samples on transparent glass coverslips were mounted on the inverted microscope and excited by focusing a 405 nm light (Picoquant, LDHDC-405M, continuous wave mode) through the 40× objective lens to ~1 μm spot. The polarization

state of the excitation light was controlled by a circular polarizer (Thorlabs, CP1R405). After excitation, the PL was collected in the epi-configuration and passed through a dichroic mirror and a long-pass filter. It was then directed into the spectrograph with the CCD detector. For polarization-resolved PL measurement, a linear polarizer (Thorlabs, LPVISE100-A) was placed in the PL collection path and rotated from 0° to 360° at a step size of 20°. All spectra underwent Jacobian transformation from wavelength to photon energy,[56] but have not been corrected for wavelength-dependent efficiency of the spectrograph or CCD camera. We confirmed that the polarization response from the optical components in the PL collection path is negligible by conducting measurements using unpolarized broadband light (Thorlabs, MCWHL2-C3) placed on the sample stage (Figure S9).

Micro-reflectance spectroscopy. The samples were mounted on the cold finger of a liquid Helium flow cryostat. The sample was illuminated with a broadband unpolarized white light, provided by a Tungsten halogen light source, through a 50× magnification microscope objective with numerical aperture NA = 0.55. The reflected light was collected in the epi-configuration and guided into a 500 mm long monochromator equipped with a grating of 1200 grooves/mm and with a liquid nitrogen-cooled CCD detector. For polarization-resolved reflectance measurement, a linear polarizer and a half-wave plate were inserted in the detection path to probe the intensity of reflected light with a given polarization orientation. Polarization-resolved reflectance spectra were collected by rotating the half-wave plate at a step size of 10°.

Computational methods. Density functional theory (DFT) calculations of AgEPh were carried out using Quantum-ESPRESSO version 6.7.[57] The kinetic energy cutoff was set at 90 Ry. For the charge density calculations, an 8x8x2 k-point mesh was used. We employed norm-conserving pseudopotentials[58] and the Perdew Burke Ernzerhof (PBE) exchange correlation functional.[59] The crystal structure was determined through single-crystal X-ray diffraction, as reported in references [30] and [46], and was used directly without further geometry optimization. A one-shot G_0W_0 calculation was performed using the generalized plasmon-pole model as implemented in BerkeleyGW version 3.0.[60–62] Quasiparticle energies were computed using the Kohn-Sham wavefunctions and energies calculated with PBE functional on a 4x4x1 k-mesh. The dielectric screening cutoff energy was set at 10 Ry, and a total of 2000 bands were included. The absorption spectra were computed by solving the Bethe-Salpeter equation with the electron-hole

interaction kernel on a 4x4x1 k-mesh, which was then interpolated to a 12x12x1 k-mesh. The kernel included 6 occupied and 18 empty bands.

7.6 References

(1) Fox, M. *Optical Properties of Solids*, Second.; Oxford University Press, 2010.

(2) Pelant, I.; Valenta, J. *Luminescence Spectroscopy of Semiconductors*; Oxford University Press, 2012. https://doi.org/10.1093/acprof:oso/9780199588336.001.0001.

(3) Koch, S. W.; Kira, M.; Khitrova, G.; Gibbs, H. M. Semiconductor Excitons in New Light. *Nat Mater* **2006**, *5* (7), 523–531. https://doi.org/10.1038/nmat1658.

(4) Wang, F.; Dukovic, G.; Brus, L. E.; Heinz, T. F. The Optical Resonances in Carbon Nanotubes Arise from Excitons. *Science (1979)* **2005**, *308* (5723), 838–841. https://doi.org/10.1126/science.1110265.

(5) Schuller, J. A.; Karaveli, S.; Schiros, T.; He, K.; Yang, S.; Kymissis, I.; Shan, J.; Zia, R. Orientation of Luminescent Excitons in Layered Nanomaterials. *Nat Nanotechnol* **2013**, *8* (4), 271–276. https://doi.org/10.1038/nnano.2013.20.

(6) Huang, D.; Choi, J.; Shih, C.-K.; Li, X. Excitons in Semiconductor Moiré Superlattices. *Nat Nanotechnol* **2022**, *17* (3), 227–238. https://doi.org/10.1038/s41565-021-01068-y.

(7) Tran, K.; Moody, G.; Wu, F.; Lu, X.; Choi, J.; Kim, K.; Rai, A.; Sanchez, D. A.; Quan, J.; Singh, A.; Embley, J.; Zepeda, A.; Campbell, M.; Autry, T.; Taniguchi, T.; Watanabe, K.; Lu, N.; Banerjee, S. K.; Silverman, K. L.; Kim, S.; Tutuc, E.; Yang, L.; MacDonald, A. H.; Li, X. Evidence for Moiré Excitons in van Der Waals Heterostructures. *Nature* **2019**, *567* (7746), 71–75. https://doi.org/10.1038/s41586-019-0975-z.

(8) Scholes, G. D.; Rumbles, G. Excitons in Nanoscale Systems. *Nat Mater* **2006**, *5* (9), 683–696. https://doi.org/10.1038/nmat1710.

(9) Passarelli, J. V.; Mauck, C. M.; Winslow, S. W.; Perkinson, C. F.; Bard, J. C.; Sai, H.; Williams, K. W.; Narayanan, A.; Fairfield, D. J.; Hendricks, M. P.; Tisdale, W. A.; Stupp, S. I. Tunable Exciton Binding Energy in 2D Hybrid Layered Perovskites through Donor–Acceptor Interactions within the Organic Layer. *Nat Chem* **2020**, *12* (8), 672–682. https://doi.org/10.1038/s41557-020-0488-2.

(10) Dou, L.; Wong, A. B.; Yu, Y.; Lai, M.; Kornienko, N.; Eaton, S. W.; Fu, A.; Bischak, C. G.; Ma, J.; Ding, T.; Ginsberg, N. S.; Wang, L.-W.; Alivisatos, A. P.; Yang, P. Atomically Thin Two-Dimensional Organic-Inorganic Hybrid Perovskites. *Science (1979)* **2015**, *349* (6255), 1518–1521. https://doi.org/10.1126/science.aac7660.

(11) Mao, L.; Stoumpos, C. C.; Kanatzidis, M. G. Two-Dimensional Hybrid Halide Perovskites: Principles and Promises. *J Am Chem Soc* **2019**, *141* (3), 1171–1190. https://doi.org/10.1021/jacs.8b10851.

(12) He, K.; Kumar, N.; Zhao, L.; Wang, Z.; Mak, K. F.; Zhao, H.; Shan, J. Tightly Bound Excitons in Monolayer WSe_2. *Phys Rev Lett* **2014**, *113* (2), 026803. https://doi.org/10.1103/PhysRevLett.113.026803.

(13) Mak, K. F.; Lee, C.; Hone, J.; Shan, J.; Heinz, T. F. Atomically Thin MoS_2 : A New Direct-Gap Semiconductor. *Phys Rev Lett* **2010**, *105* (13), 136805. https://doi.org/10.1103/PhysRevLett.105.136805.

(14) Weidman, M. C.; Seitz, M.; Stranks, S. D.; Tisdale, W. A. Highly Tunable Colloidal Perovskite Nanoplatelets through Variable Cation, Metal, and Halide Composition. *ACS Nano* **2016**, *10* (8), 7830–7839. https://doi.org/10.1021/acsnano.6b03496.

(15) Li, J.; Ma, J.; Cheng, X.; Liu, Z.; Chen, Y.; Li, D. Anisotropy of Excitons in Two-Dimensional Perovskite Crystals. *ACS Nano* **2020**, *14* (2), 2156–2161. https://doi.org/10.1021/acsnano.9b08975.

(16) Gao, Y.; Weidman, M. C.; Tisdale, W. A. CdSe Nanoplatelet Films with Controlled Orientation of Their Transition Dipole Moment. *Nano Lett* **2017**, *17* (6), 3837–3843. https://doi.org/10.1021/acs.nanolett.7b01237.

(17) Rasmussen, F. A.; Thygesen, K. S. Computational 2D Materials Database: Electronic Structure of Transition-Metal Dichalcogenides and Oxides. *The Journal of Physical Chemistry C* **2015**, *119* (23), 13169–13183. https://doi.org/10.1021/acs.jpcc.5b02950.

(18) Wang, G.; Chernikov, A.; Glazov, M. M.; Heinz, T. F.; Marie, X.; Amand, T.; Urbaszek, B. Colloquium: Excitons in Atomically Thin Transition Metal Dichalcogenides. *Rev Mod Phys* **2018**, *90* (2), 021001. https://doi.org/10.1103/RevModPhys.90.021001.

(19) Munkhbat, B.; Wróbel, P.; Antosiewicz, T. J.; Shegai, T. O. Optical Constants of Several Multilayer Transition Metal Dichalcogenides Measured by Spectroscopic Ellipsometry in the 300–1700 Nm Range: High Index, Anisotropy, and Hyperbolicity. *ACS Photonics* **2022**, *9* (7), 2398–2407. https://doi.org/10.1021/acsphotonics.2c00433.

(20) Li, M.; Han, S.; Teng, B.; Li, Y.; Liu, Y.; Liu, X.; Luo, J.; Hong, M.; Sun, Z. Minute-Scale Rapid Crystallization of a Highly Dichroic 2D Hybrid Perovskite Crystal toward Efficient Polarization-Sensitive Photodetector. *Adv Opt Mater* **2020**, *8* (9). https://doi.org/10.1002/adom.202000149.

(21) Steger, M.; Janke, S. M.; Sercel, P. C.; Larson, B. W.; Lu, H.; Qin, X.; Yu, V. W.; Blum, V.; Blackburn, J. L. On the Optical Anisotropy in 2D Metal-Halide Perovskites. *Nanoscale* **2022**, *14* (3), 752–765. https://doi.org/10.1039/D1NR06899G.

(22) Zhou, Y.; Zhang, M.; Guo, Z.; Miao, L.; Han, S.-T.; Wang, Z.; Zhang, X.; Zhang, H.; Peng, Z. Recent Advances in Black Phosphorus-Based Photonics, Electronics, Sensors and Energy Devices. *Mater Horiz* **2017**, *4* (6), 997–1019. https://doi.org/10.1039/C7MH00543A.

(23) Wang, X.; Jones, A. M.; Seyler, K. L.; Tran, V.; Jia, Y.; Zhao, H.; Wang, H.; Yang, L.; Xu, X.; Xia, F. Highly Anisotropic and Robust Excitons in Monolayer Black Phosphorus. *Nat Nanotechnol* **2015**, *10* (6), 517–521. https://doi.org/10.1038/nnano.2015.71.

(24) Jo, S. S.; Wu, C.; Zhu, L.; Yang, L.; Li, M.; Jaramillo, R. Photonic Platforms Using In-Plane Optical Anisotropy of Tin (II) Selenide and Black Phosphorus. *Adv Photonics Res* **2021**, *2* (12). https://doi.org/10.1002/adpr.202100176.

(25) Wang, H.; Chen, M.-L.; Zhu, M.; Wang, Y.; Dong, B.; Sun, X.; Zhang, X.; Cao, S.; Li, X.; Huang, J.; Zhang, L.; Liu, W.; Sun, D.; Ye, Y.; Song, K.; Wang, J.; Han, Y.; Yang, T.; Guo, H.; Qin, C.; Xiao, L.; Zhang, J.; Chen, J.; Han, Z.; Zhang, Z. Gate Tunable Giant Anisotropic Resistance in Ultra-Thin GaTe. *Nat Commun* **2019**, *10* (1), 2302. https://doi.org/10.1038/s41467-019-10256-3.

(26) Zhang, E.; Wang, P.; Li, Z.; Wang, H.; Song, C.; Huang, C.; Chen, Z.-G.; Yang, L.; Zhang, K.; Lu, S.; Wang, W.; Liu, S.; Fang, H.; Zhou, X.; Yan, H.; Zou, J.; Wan, X.; Zhou, P.; Hu, W.; Xiu, F. Tunable Ambipolar Polarization-Sensitive Photodetectors Based on High-Anisotropy ReSe2 Nanosheets. *ACS Nano* **2016**, *10* (8), 8067–8077. https://doi.org/10.1021/acsnano.6b04165.

(27) Pi, L.; Hu, C.; Shen, W.; Li, L.; Luo, P.; Hu, X.; Chen, P.; Li, D.; Li, Z.; Zhou, X.; Zhai, T. Highly In-Plane Anisotropic 2D PdSe2 for Polarized Photodetection with Orientation Selectivity. *Adv Funct Mater* **2021**, *31* (3). https://doi.org/10.1002/adfm.202006774.

(28) Cuthbert, H. L.; Wallbank, A. I.; Taylor, N. J.; Corrigan, J. F. Synthesis and Structural Characterization of [Cu20Se4(M3-SePh)12(PPh3)6] and [Ag(SePh)]∞. *Z Anorg Allg Chem* **2002**, *628* (11), 2483–2488. https://doi.org/10.1002/1521-3749(200211)628:11<2483::AID-ZAAC2483>3.0.CO;2-U.

(29) Nagaraju Myakala, S.; Rabl, H.; Schubert, J. S.; Batool, S.; Ayala, P.; Apaydin, D. H.; Cherevan, A.; Eder, D. MOCHAs: An Emerging Class of Materials for Photocatalytic H_2 Production. *Small* **2024**. https://doi.org/10.1002/smll.202400348.

(30) Synthesis and Structural Anisotropy of Single Crystalline 2D AgEPh (E = S, Se, Te) in Manuscript.

(31) Hernandez Oendra, A. C.; Aspect, M. A.; Jaeggi, J. L.; Baumann, J.; Lightner, C. R.; Pun, A. B.; Norris, D. J. Tunable Synthesis of Metal–Organic Chalcogenide Semiconductor Nanocrystals. *Chemistry of Materials* **2023**, *35* (21), 9390–9398. https://doi.org/10.1021/acs.chemmater.3c02275.

(32) Khamlue, R.; Sakurada, T.; Cho, Y.; Lee, W. S.; Leangtanom, P.; Taylor, M. G.; Naewthong, W.; Sripetch, P.; Na Ranong, B.; Autila, T.; Rungseesumran, T.; Kaewkhao, J.; Sudyoadsuk, T.; Kopwitthaya, A.; Müller, P.; Promarak, V.; Kulik, H. J.; Tisdale, W. A.; Paritmongkol, W. Heterocyclic Modification Leading to Luminescent 0D Metal Organochalcogenide with Stable X-Ray Scintillating Properties. *Chemistry of Materials* **2024**, *36* (10), 5238–5240. https://doi.org/10.1021/acs.chemmater.4c00653.

(33) Powers, E. R.; Paritmongkol, W.; Yost, D. C.; Lee, W. S.; Grossman, J. C.; Tisdale, W. A. Coherent Exciton-Lattice Dynamics in a 2D Metal Organochalcogenolate Semiconductor. *Matter* **2024**, *7* (4), 1612–1630. https://doi.org/10.1016/j.matt.2024.01.033.

(34) Wang, G.; Luo, S.; Di, T.; Fu, Z.; Xu, G. Layered Organic Metal Chalcogenides (OMCs): From Bulk to Two-Dimensional Materials. *Angewandte Chemie International Edition* **2022**, *61* (27). https://doi.org/10.1002/anie.202203151.

(35) Sakurada, T.; Cho, Y.; Paritmongkol, W.; Lee, W. S.; Wan, R.; Su, A.; Shcherbakov-Wu, W.; Müller, P.; Kulik, H. J.; Tisdale, W. A. 1D Hybrid Semiconductor Silver 2,6-Difluorophenylselenolate. *J Am Chem Soc* **2023**, *145* (9), 5183–5190. https://doi.org/10.1021/jacs.2c11896.

(36) Veselska, O.; Demessence, A. D10 Coinage Metal Organic Chalcogenolates: From Oligomers to Coordination Polymers. *Coord Chem Rev* **2018**, *355*, 240–270. https://doi.org/10.1016/j.ccr.2017.08.014.

(37) Schriber, E. A.; Paley, D. W.; Bolotovsky, R.; Rosenberg, D. J.; Sierra, R. G.; Aquila, A.; Mendez, D.; Poitevin, F.; Blaschke, J. P.; Bhowmick, A.; Kelly, R. P.; Hunter, M.; Hayes, B.; Popple, D. C.; Yeung, M.; Pareja-Rivera, C.; Lisova, S.; Tono, K.; Sugahara, M.; Owada, S.; Kuykendall, T.; Yao, K.; Schuck, P. J.; Solis-Ibarra, D.; Sauter, N. K.; Brewster, A. S.; Hohman, J. N. Chemical Crystallography by Serial Femtosecond X-Ray Diffraction. *Nature* **2022**, *601* (7893), 360–365. https://doi.org/10.1038/s41586-021-04218-3.

(38) Kastl, C.; Schwartzberg, A. M.; Maserati, L. Picoseconds-Limited Exciton Recombination in Metal–Organic Chalcogenides Hybrid Quantum Wells. *ACS Nano* **2022**, *16* (3), 3715–3722. https://doi.org/10.1021/acsnano.1c07281.

(39) Maserati, L.; Prato, M.; Pecorario, S.; Passarella, B.; Perinot, A.; Thomas, A. A.; Melloni, F.; Natali, D.; Caironi, M. Photo-Electrical Properties of 2D Quantum Confined Metal–Organic Chalcogenide Nanocrystal Films. *Nanoscale* **2021**, *13* (1), 233–241. https://doi.org/10.1039/D0NR07409H.

(40) Maserati, L.; Refaely-Abramson, S.; Kastl, C.; Chen, C. T.; Borys, N. J.; Eisler, C. N.; Collins, M. S.; Smidt, T. E.; Barnard, E. S.; Strasbourg, M.; Schriber, E. A.; Shevitski, B.; Yao, K.; Hohman, J. N.; Schuck, P. J.; Aloni, S.; Neaton, J. B.; Schwartzberg, A. M. Anisotropic 2D Excitons Unveiled in Organic–Inorganic Quantum Wells. *Mater Horiz* **2021**, *8* (1), 197–208. https://doi.org/10.1039/C9MH01917K.

(41) Paritmongkol, W.; Lee, W. S.; Shcherbakov-Wu, W.; Ha, S. K.; Sakurada, T.; Oh, S. J.; Tisdale, W. A. Morphological Control of 2D Hybrid Organic–Inorganic Semiconductor AgSePh. *ACS Nano* **2022**, *16* (2), 2054–2065. https://doi.org/10.1021/acsnano.1c07498.

(42) Kastl, C.; Bonfà, P.; Maserati, L. Anharmonic Exciton-Phonon Coupling in Metal-Organic Chalcogenides Hybrid Quantum Wells. *Adv Opt Mater* **2023**, *11* (7). https://doi.org/10.1002/adom.202202213.

(43) Rabl, H.; Myakala, S. N.; Rath, J.; Fickl, B.; Schubert, J. S.; Apaydin, D. H.; Eder, D. Microwave-Assisted Synthesis of Metal-Organic Chalcogenolate Assemblies as Electrocatalysts for Syngas Production. *Commun Chem* **2023**, *6* (1), 43. https://doi.org/10.1038/s42004-023-00843-3.

(44) Yao, K.; Collins, M. S.; Nell, K. M.; Barnard, E. S.; Borys, N. J.; Kuykendall, T.; Hohman, J. N.; Schuck, P. J. Strongly Quantum-Confined Blue-Emitting Excitons in Chemically Configurable Multiquantum Wells. *ACS Nano* **2021**, *15* (3), 4085–4092. https://doi.org/10.1021/acsnano.0c08096.

(45) Lee, W. S.; Cho, Y.; Powers, E. R.; Paritmongkol, W.; Sakurada, T.; Kulik, H. J.; Tisdale, W. A. Light Emission in 2D Silver Phenylchalcogenolates. *ACS Nano* **2022**, *16* (12), 20318–20328. https://doi.org/10.1021/acsnano.2c06204.

(46) Paritmongkol, W.; Sakurada, T.; Lee, W. S.; Wan, R.; Müller, P.; Tisdale, W. A. Size and Quality Enhancement of 2D Semiconducting Metal–Organic Chalcogenolates by Amine Addition. *J Am Chem Soc* **2021**, *143* (48), 20256–20263. https://doi.org/10.1021/jacs.1c09106.

(47) Trang, B.; Yeung, M.; Popple, D. C.; Schriber, E. A.; Brady, M. A.; Kuykendall, T. R.; Hohman, J. N. Tarnishing Silver Metal into Mithrene. *J Am Chem Soc* **2018**, *140* (42), 13892–13903. https://doi.org/10.1021/jacs.8b08878.

(48) Schriber, E. A.; Popple, D. C.; Yeung, M.; Brady, M. A.; Corlett, S. A.; Hohman, J. N. Mithrene Is a Self-Assembling Robustly Blue Luminescent Metal–Organic Chalcogenolate Assembly for 2D

Optoelectronic Applications. *ACS Appl Nano Mater* **2018**, *1* (7), 3498–3508. https://doi.org/10.1021/acsanm.8b00662.

(49) Thermodynamic Stability and Excitonic Properties in 2D Silver Phenylchalcogenide Alloys in Manuscript.

(50) Fratelli, I.; Maserati, L.; Basiricò, L.; Galeazzi, A.; Passarella, B.; Ciavatti, A.; Caironi, M.; Fraboni, B. Layered Metal-Organic Chalcogenide Thin Films for Flexible and Large-Area X-Ray Direct Detection. *Front Phys* **2023**, *11*. https://doi.org/10.3389/fphy.2023.1325164.

(51) Anantharaman, S. B.; Lynch, J.; Aleksich, M.; Stevens, C. E.; Munley, C.; Choi, B.; Shenoy, S.; Darlington, T.; Majumdar, A.; Shuck, P. J.; Hendrickson, J.; Hohman, J. N.; Jariwala, D. Ultrastrong Light-Matter Coupling in 2D Metal-Chalcogenates. **2023**.

(52) Song, K. S.; Williams, R. T. *Self-Trapped Excitons*; Springer Berlin Heidelberg: Berlin, Heidelberg, 1993; Vol. 105. https://doi.org/10.1007/978-3-642-97432-8.

(53) Emin, D. *Polarons*; Cambridge University Press, 2012. https://doi.org/10.1017/CBO9781139023436.

(54) Pedrotti, F. L.; Pedrotti, L. M.; Pedrotti, L. S. *Introduction to Optics*; Cambridge University Press, 2017. https://doi.org/10.1017/9781108552493.

(55) Kang, H.; Ma, J.; Li, J.; Zhang, X.; Liu, X. Exciton Polaritons in Emergent Two-Dimensional Semiconductors. *ACS Nano* **2023**, *17* (24), 24449–24467. https://doi.org/10.1021/acsnano.3c07993.

(56) Mooney, J.; Kambhampati, P. Get the Basics Right: Jacobian Conversion of Wavelength and Energy Scales for Quantitative Analysis of Emission Spectra. *J Phys Chem Lett* **2013**, *4* (19), 3316–3318. https://doi.org/10.1021/jz401508t.

(57) Giannozzi, P.; Baroni, S.; Bonini, N.; Calandra, M.; Car, R.; Cavazzoni, C.; Ceresoli, D.; Chiarotti, G. L.; Cococcioni, M.; Dabo, I.; Dal Corso, A.; de Gironcoli, S.; Fabris, S.; Fratesi, G.; Gebauer, R.; Gerstmann, U.; Gougoussis, C.; Kokalj, A.; Lazzeri, M.; Martin-Samos, L.; Marzari, N.; Mauri, F.; Mazzarello, R.; Paolini, S.; Pasquarello, A.; Paulatto, L.; Sbraccia, C.; Scandolo, S.; Sclauzero, G.; Seitsonen, A. P.; Smogunov, A.; Umari, P.; Wentzcovitch, R. M. QUANTUM ESPRESSO: A Modular and Open-Source Software Project for Quantum Simulations of Materials. *Journal of Physics: Condensed Matter* **2009**, *21* (39), 395502. https://doi.org/10.1088/0953-8984/21/39/395502.

(58) Hamann, D. R. Optimized Norm-Conserving Vanderbilt Pseudopotentials. *Phys Rev B* **2013**, *88* (8), 085117. https://doi.org/10.1103/PhysRevB.88.085117.

(59) Perdew, J. P.; Burke, K.; Ernzerhof, M. Generalized Gradient Approximation Made Simple. *Phys Rev Lett* **1996**, *77* (18), 3865–3868. https://doi.org/10.1103/PhysRevLett.77.3865.

(60) Deslippe, J.; Samsonidze, G.; Strubbe, D. A.; Jain, M.; Cohen, M. L.; Louie, S. G. BerkeleyGW: A Massively Parallel Computer Package for the Calculation of the Quasiparticle and Optical Properties of Materials and Nanostructures. *Comput Phys Commun* **2012**, *183* (6), 1269–1289. https://doi.org/10.1016/j.cpc.2011.12.006.

(61) Rohlfing, M.; Louie, S. G. Electron-Hole Excitations and Optical Spectra from First Principles. *Phys Rev B* **2000**, *62* (8), 4927–4944. https://doi.org/10.1103/PhysRevB.62.4927.

(62) Hybertsen, M. S.; Louie, S. G. Electron Correlation in Semiconductors and Insulators: Band Gaps and Quasiparticle Energies. *Phys Rev B* **1986**, *34* (8), 5390–5413. https://doi.org/10.1103/PhysRevB.34.5390.

Chapter 8

Giant excitonic anisotropy in 2D Silver Organochalcogenolates with semi-1D Ag-Ag chains

8.1 Abstract

In this chapter, we reveal the significant electronic and excitonic anisotropy of AgSePh-F_2(2,3) compared to AgSePh using polarization-resolved optical spectroscopy and density functional theory calculations. We provide a concrete structural explanation for these observations: AgSePh features a 2D hexagonal Ag-Ag network with uniform Ag-Ag bond lengths, whereas AgSePh-F_2(2,3) exhibits a significantly distorted Ag-Ag hexagon where one Ag-Ag bond length is much longer than the others, resulting in semi-1D Ag-Ag chains. This semi-1D-like inorganic structure in AgSePh-F_2(2,3) may cause the valence electron density to distribute primarily along this 1D direction, leading to its anisotropic electronic band structure, different absorption spectrum, and giant excitonic anisotropy compared to AgSePh. This relationship between Ag-Ag bond parameters and the absorption spectrum is generalizable to other 2D blue-emitting AgSePh-R compounds, resolving the puzzle of the divergence between the AgSePh-like absorption spectrum and the AgSePh-F_2(2,3)-like absorption spectrum.

8.2 Introduction

Silver phenylselenolate (AgSePh),[1,2] also known as "mithrene",[3,4] is an emerging two-dimensional (2D) hybrid organic-inorganic semiconductors that belongs to the broader class of metal organochalcogenolates (MOCs).[5] Attracting significant attention due to its narrow blue emission (~467 nm), this material has been extensively studied over the past seven years, exhibiting many promising properties such as strong exciton binding energy and in-plane optical anisotropy.[6,7]

Another crucial feature of AgSePh is the covalent bonding between organic and inorganic components, which allows for the tunability of its dimension, structure, and electronic bandgap through organic functionalization. This tunability is exemplified in materials like zero-dimensional (0D) silver pyridinylselenolate (AgSePy),[8] one-dimensional (1D) silver 2,6-difluorophenylseleonlate [AgSePh-F_2(2,6)],[9] and various other 2D silver organoselenolates (2D AgSePh-R)[2] including 2D silver 2,3-difluorophenylseleonlate [AgSePh-F_2(2,3)].

Interestingly, among 12 blue-emitting 2D AgSePh-R compounds discovered so far (Figure 3.11), only two types of absorption spectra were observed: excitonic absorption peaks crowded near 450 nm, as in AgSePh, or excitonic absorption peaks separated by a large energetic gap, as in AgSePh-F_2(2,3). However, the origin of the divergence in absorption spectra among blue-emitting 2D AgSePh-R remains unknown.

Using polarization-resolved optical micro-spectroscopy and density functional theory calculations, we reveal anisotropic electronic band structure and giant excitonic anisotropy in AgSePh-F_2(2,3) compared to AgSePh. We offer a detailed structural explanation for these findings: AgSePh possesses a 2D hexagonal Ag-Ag network with uniform bond lengths, whereas AgSePh-F_2(2,3) shows a notably distorted Ag-Ag hexagon with one bond length significantly longer than the others, resulting in semi-1D Ag-Ag chains. This semi-1D inorganic structure in AgSePh-F_2(2,3) likely causes the valence electron density to concentrate along the 1D direction, leading to its anisotropic electronic band structure, distinct absorption spectrum, and significant excitonic anisotropy compared to AgSePh. This correlation between Ag-Ag bond parameters and the absorption spectrum can be extended to other 2D blue-emitting AgSePh-R compounds, resolving the divergence between the AgSePh-like and AgSePh-F_2(2,3)-like absorption spectra.

8.3 Results and Discussion

8.3.1 Synthesis and crystal structure of 2D AgSePh-R

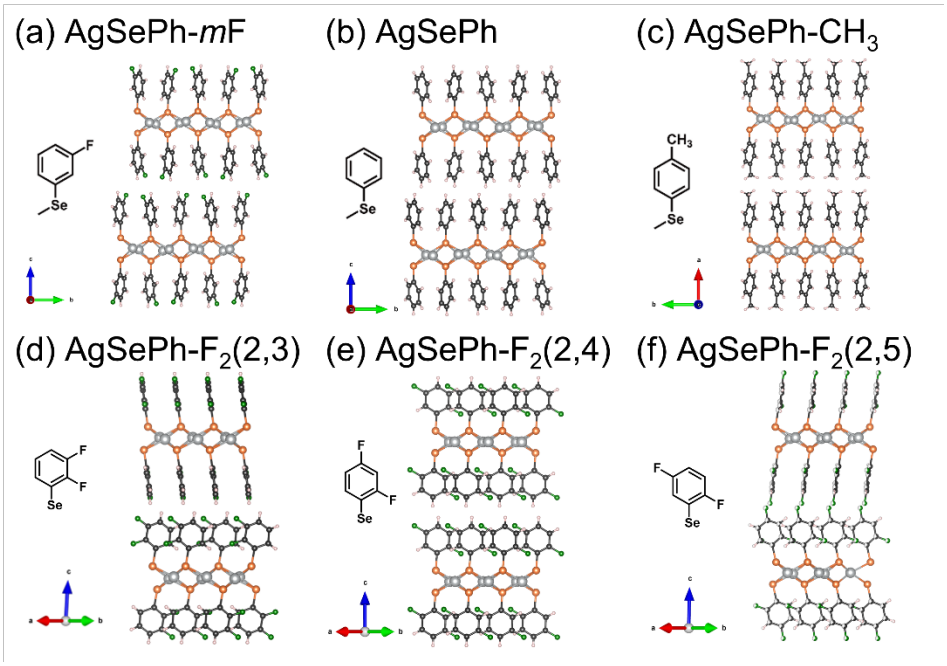

Figure 8.1 2D layered structures of (a) AgSePh-*m*F in $P2_12_12_1$, (b) AgSePh in $P2_1/c$, (c) AgSePh-CH_3 in $P2_1/c$, (d) AgSePh-F_2(2,3) in $P2_1/n$, (e) AgSePh-F_2(2,4) in P-1, and (f) AgSePh-F_2(2,5) in P-1.

To prepare silver organochalcogenides [AgSePh-R; R = *meta*-F (*m*F), H, CH_3, F_2(2,3), F_2(2,4), F_2(2,5)], diorganic diselenide ligands were first synthesized via Grignard reactions,[9] except for diphenyl diselenide which is commercially available. The AgSePh-R crystals were then synthesized using the amine-assisted method.[2] Briefly, a solution of silver nitrate ($AgNO_3$) in 1-butylmaine ($BuNH_2$) and a solution of diorganic diselenide in $BuNH_2$ were mixed in a sealed vial. The vial was stored under dark at room temperature for a few days to weeks to obtain AgSePh-R crystals. Single-crystal X-ray diffraction (SCXRD) revealed their anisotropic 2D layered structures consisting of inorganic AgSe layers sandwiched between organic ligands (Figure 8.1). Detailed crystallographic information of these crystals will be discussed in two forthcoming publications authored by Tomoaki Sakurada (a former Tisdale group member) and other co-workers including myself.

8.3.2 Two different types of absorption spectra among 2D AgSePh-R

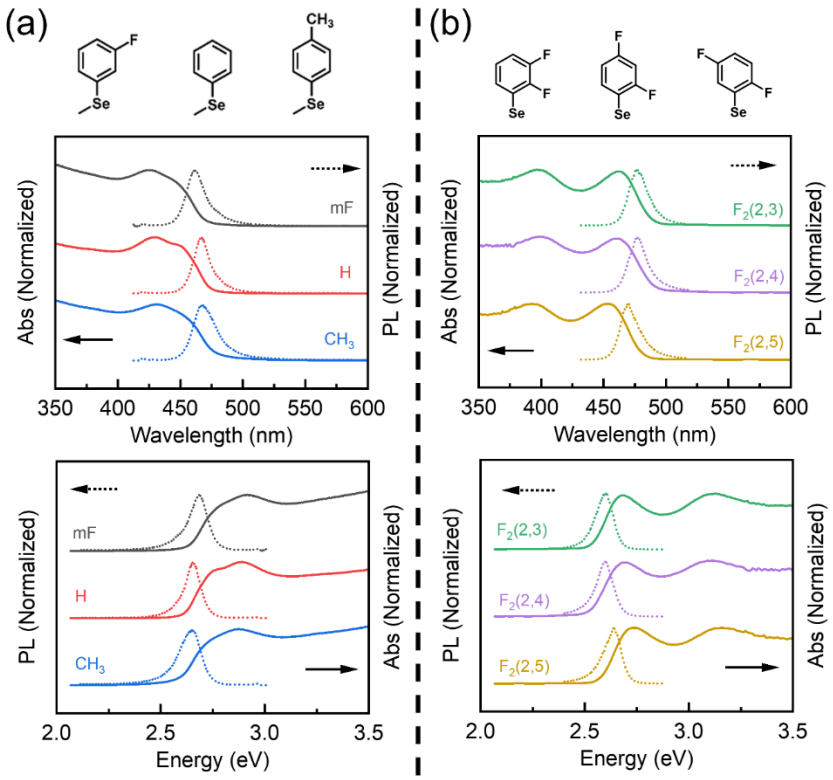

Figure 8.2 Absorption and photoluminescence spectra of 2D AgSePh-R where (a) R = *m*F, H, CH3, and (b) R = F_2(2,3), F_2(2,4), F_2(2,5).

Diffuse reflectance UV-vis absorption and photoluminescence (PL) spectra of 2D AgSePh-R crystals at room temperature are shown in Figure 8.2. Interestingly, two types of absorption spectra were observed. In the case of AgSePh (AgSePh-H), AgSePh-*m*F, and AgSePh-CH_3, two overlapping excitonic absorption resonances were observed in the range of 430-460 nm (2.69~2.88 eV). In contrast, AgSePh-F_2(2,3), AgSePh-F_2(2,4), and AgSePh-F_2(2,5) exhibited two excitonic absorption peaks, with large energetic separation, centered at ~400 nm (~3.10 eV) and ~460 nm (~2.69 eV). When excited by 405 nm light, all crystals exhibited narrow blue emission centered at 462-477 nm (2.60~2.68 eV).

8.3.3 Polarization-resolved optical spectroscopy on 2D AgSePh-F_2(2,3)

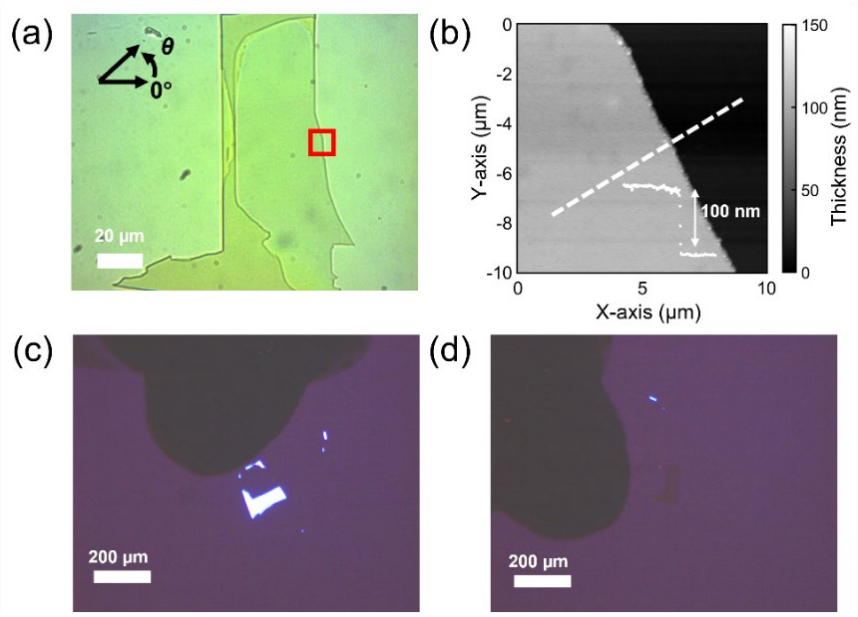

Figure 8.3 (a) Optical micrograph of the exfoliated AgSePh-F_2(2,3) crystal. (b) Atomic force microscopy image for the red boxed region in (a), confirming a thickness of 100 nm. (c,d) Polarized optical micrographs of the AgSePh-F_2(2,3) crystal. The change in brightness across the crystal from (c) complete brightness to (d) darkness as the crystal was rotated indicates that the crystal is single.

To investigate the origin of divergent absorption spectra of AgSePh-F_2(2,3), AgSePh-F_2(2,4), and AgSePh-F_2(2,5) compared to those of AgSePh (a prototypical material and the most studied in this family) and the others, we performed polarization-resolved micro-absorption and micro-PL spectroscopy on AgSePh-F_2(2,3) as a representative.

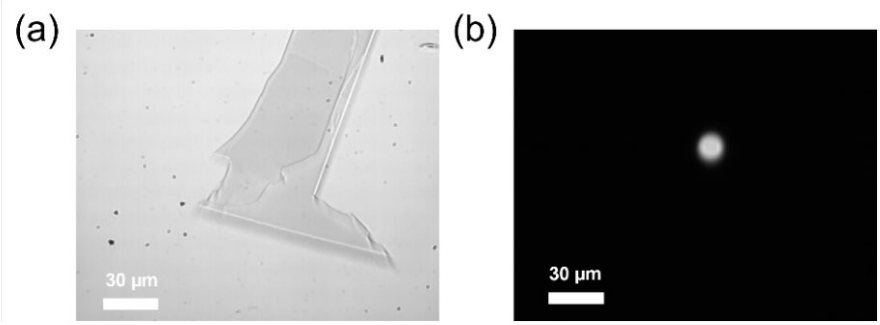

Figure 8.4 Images of the 100 nm-thick AgSePh-F_2(2,3) crystal captured in the collection path (a) without a pinhole and (b) with a pinhole for micro-absorption measurement.

For these studies, 100 nm-thick AgSePh-F_2(2,3) single crystal was prepared through mechanical exfoliation to avoid potential photonic effects (Figure 8.3). The polarization-resolved absorption and PL of the crystal was measured using the same micro-optical spectroscopy setup as described in detail in Chapter 7, with a spatial resolution of ~15 μm in diameter for micro-absorption (Figure 8.4) and an excitation spot size of <1 μm in diameter for micro-PL measurement. For both measurements, the linear polarizer was rotated from 0° (corresponding to the selected polarization of the light being parallel to the bottom edge of the crystal in Figure 8.3a) to 360°. The step size was 10° for absorption and 20° for PL measurements.

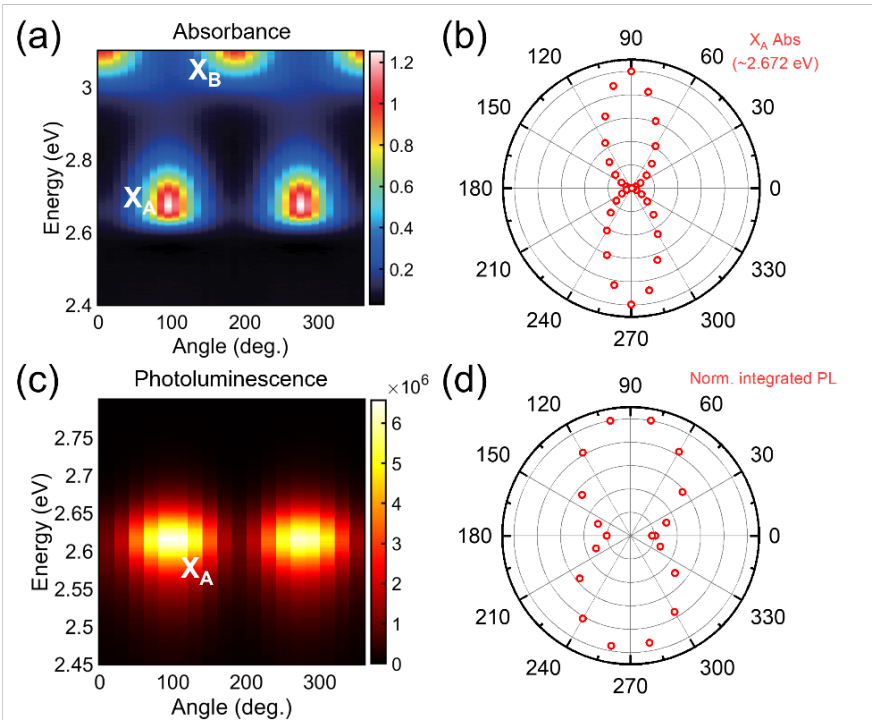

Figure 8.5 (a) 2D color plot showing absorption spectra of the exfoliated AgSePh-F_2(2,3) crystal as a function of polarization angle of incident light. (b) Polar plot showing intensities of the absorption peaks at 2.672 eV (X_A exciton) as a function of polarization of incident light. (c) 2D color plots showing PL spectra of the exfoliated AgSePh-F_2(2,3) crystal as a function of polarization angle of the emitted light. (d) Polar plot showing integrated PL intensities of the AgSePh-F_2(2,3) crystal as a function of polarization angle of the emitted light.

Figure 8.5a shows a 2D color plot of polarization-resolved absorption spectra of the exfoliated AgSePh-F_2(2,3) crystal. Two excitonic resonances at ~2.672 eV (X_A) and ~3.10 eV (X_B) both exhibited significant polarization dependence, with orthogonal polarization to each other: when the absorption intensity of the X_A exciton was highest, the intensity of X_B exciton was suppressed the most, and vice versa. To assess the extent of absorption anisotropy of the lowest

exciton (X_A) we extracted the absolute absorption intensity at ~2.672 eV as a function of the polarization angle. The polar plot clearly shows that the lowest exciton is strongly polarized parallel to the left edge of the crystal (Figures 8.3a and 8.5b).

The PL spectra of the exfoliated AgSePh-F_2(2,3) crystal also exhibited strong polarization dependence (Figure 8.5c), as expected from its strong absorption anisotropy. The polar plot of the integrated PL intensities shows that the PL centered at ~2.617 eV is polarized in the same direction as the lowest excitonic absorption resonance. Given this same polarization and small Stokes-shift (~55 meV), we attribute the origin of the PL to the recombination of the X_A exciton.

8.3.4 Comparison of the optical anisotropy between AgSePh and AgSePh-F_2(2,3)

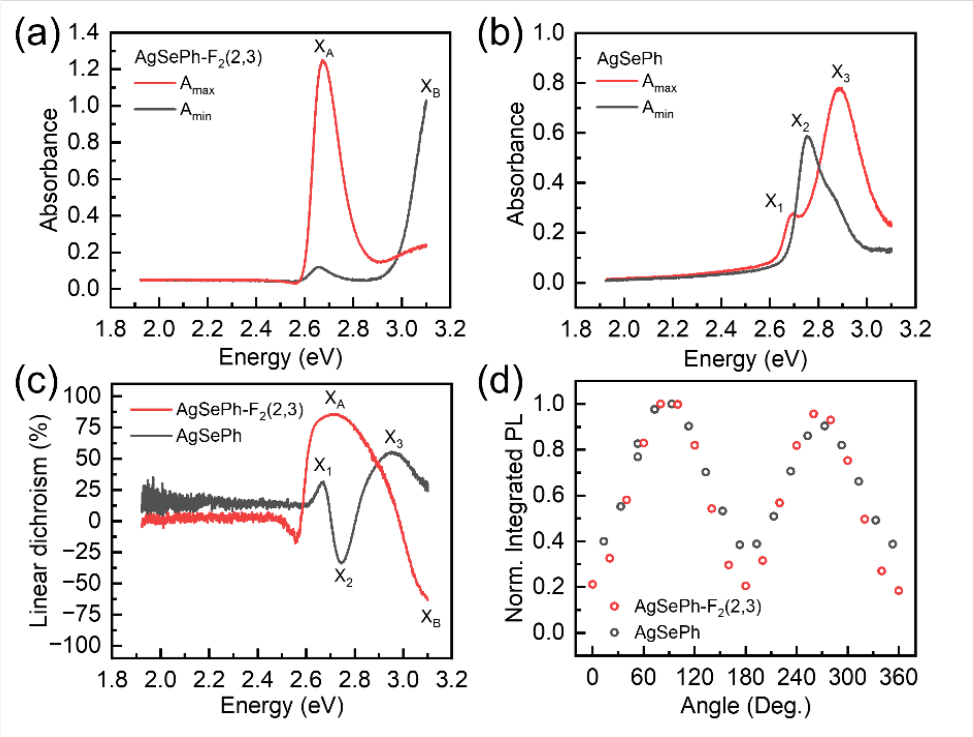

Figure 8.6 (a) Polarization-resolved absorption spectra of the AgSePh-F_2(2,3) crystal when X_A excitonic absorption is maximum (red) and minimum (black). (b) Polarization-resolved absorption spectra of the AgSePh crystal when X_1 excitonic absorption is maximum (red) and minimum (black). (c) Linear dichroism of AgSePh (black) and AgSePh-F_2(2,3) (red) as a function of photon energy. (d) Integrated PL intensities of AgSePh (black) and AgSePh-F_2(2,3) (red) as a function of polarization angle of the emitted light. The raw data for AgSePh in (d) was taken from Figure 7.10b.

To compare the optical anisotropy between AgSePh and AgSePh-F_2(2,3), we calculated the linear dichroism (LD) as a function of energy using the following equation:

$$\frac{A_{max} - A_{min}}{A_{max} + A_{min}} \tag{8.1}$$

where A_{max} and A_{min} correspond to the absorption intensity when the lowest excitonic transition [X_1 exciton for AgSePh and X_A exciton for AgSePh-F_2(2,3)] is at its maximum and minimum, respectively (Figure 8.6a,b). As expected from their strikingly different absorption spectra (Figure 8.2), AgSePh and AgSePh-F_2(2,3) exhibited different LD spectral shape (Figure 8.6c). Notably, AgSePh-F_2(2,3) showed much stronger LD (85% at ~2.714 eV and 63% at ~3.10 eV) compared to AgSePh (30% at ~2.664 eV, 33% at ~2.746 eV, and 55% at ~2.953 eV). In both cases, energies of peaks in the LD spectra are close to energies of excitonic transitions, indicating stronger excitonic anisotropy in AgSePh-F_2(2,3) compared to AgSePh. Additionally, the anisotropy in integrated PL intensities as a function of polarization is stronger in AgSePh-F_2(2,3) compared to AgSePh, further supporting this claim (Figure 8.6d).

8.3.5 Anisotropic electronic band structure of AgSePh-F_2(2,3)

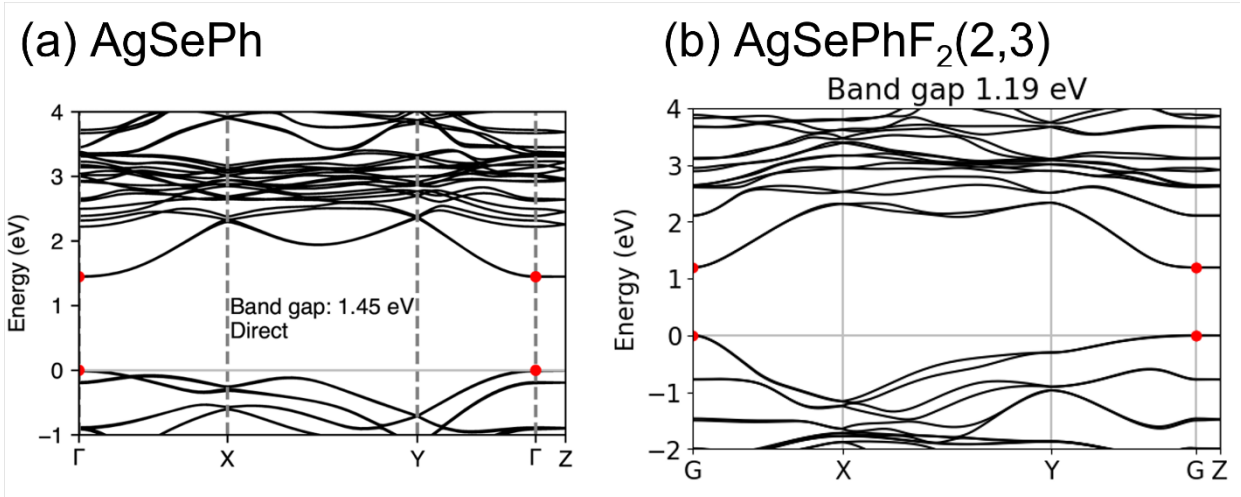

Figure 8.7 Electronic band structures of AgSePh in $P2_1/c$ and AgSePh-F_2(2,3) in $P2_1/n$, calculated with density functional theory.

The electronic band structures of AgSePh and AgSePh-F_2(2,3) were investigated using density functional theory (DFT) calculations (Figure 8.7). These calculations used the structures of AgSePh in $P2_1/c$ and AgSePh-F_2(2,3) in $P2_1/n$. AgSePh features a direct gap of 1.45 eV at Γ and AgSePh-F_2(2,3) has a direct gap of 1.19eV at Γ. For both, the bands exhibit negligible

dispersion along the out-of-plane direction (band extrema or Γ → Z), indicating confinement of electrons and holes within the 2D AgSe plane. Notably, AgSePh-F_2(2,3) shows more anisotropic valence band structure, with much stronger dispersion along Γ → X compared to Γ → Y, than AgSePh, which exhibits relatively similar dispersion along both directions.

8.3.6 The origin of divergent excitonic structure and anisotropy in 2D AgSePh-R

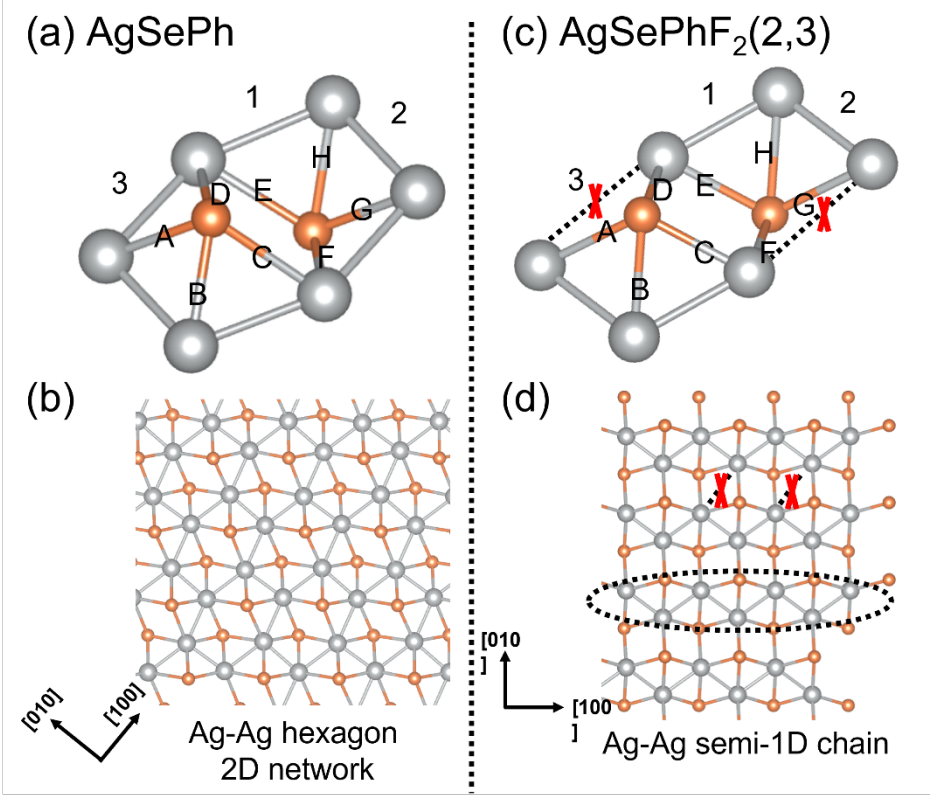

Figure 8.8 (a) Hexagonal shape of AgSe in AgSePh. (b) Top view of the AgSe layer in AgSePh, featuring a hexagonal 2D Ag-Ag network. (c) hexagonal shape of AgSe with a broken Ag-Ag bond marked by a red X in AgSePh-F_2(2,3). (d) Top view of the AgSe layer in AgSePh-F_2(2,3), featuring a semi-1D Ag-Ag chain due to broken Ag-Ag bond marked by red X.

The giant excitonic anisotropy in AgSePh-F_2(2,3) and its strikingly different absorption spectrum compared to AgSePh can be understood by the differences in their AgSe layer structures (Figure 8.8 and Table 8.1). AgSePh features hexagonal 2D networks of Ag-Ag bonds, where the three Ag-Ag bonds, labeled 1, 2, and 3 in the hexagon, have similar lengths of 2.986, 3.038, and 2.899 Å, respectively (Figure 8.8a,b). This can allow excitons to be formed, polarized, and delocalized along the direction parallel to Ag-Ag chain formed by the connection between Ag-Ag (1) and Ag-Ag (3). In contrast, the Ag-Ag (3) bond in AgSePh-F_2(2,3) is 3.925Å, too long to

support the formation or delocalization of an exciton along this direction. Instead, valence electron density in AgSePh-F_2(2,3) may be primarily distributed along the Ag-Ag chain formed by the connection between Ag-Ag (1) (2.959 Å) and Ag-Ag (2) (2.903 Å), which supports the formation and delocalization of the X_A exciton along this direction. Consequently, differences in electronic and excitonic structures arising from different inorganic structure leads to divergent absorption spectra between AgSePh and AgSePh-F_2(2,3). Furthermore, the semi-1D structure induced by the broken Ag-Ag (3) bond in AgSePh-F_2(2,3) may lead to much stronger excitonic anisotropy than in AgSePh, which has a hexagonal 2D Ag-Ag network. This finding can be generalized to other blue-emitting 2D AgSePh-R compounds (Table 8.1). AgSePh-*m*F and AgSePh-CH3, which has similar absorption spectra to AgSePh, exhibit similar bond lengths for Ag-Ag (1), Ag-Ag (2), and Ag-Ag (3), close to ~3 Å. In contrast, AgSePh-F_2(2,4) and AgSePh-F_2(2,5), which has similar absorption spectra to AgSePh-F_2(2,3) exhibit long bond lengths of Ag-Ag (3) [3.788 Å for AgSePh-F_2(2,4) and 3.815 Å for AgSePh-F_2(2,5)].

Table 8.1 Ag-Ag and Ag-Se bond lengths of 2D AgsePh-R. Bond labels are shown in Figure 8.8(a,c).

	Ag-Ag hexagonal 2D network			Ag-Ag semi-1D chain		
Bond (Å)	*m*F	H	CH_3	F_2(2,3)	F_2(2,4)	F_2(2,5)
1 (Ag-Ag)	3.1057	2.9866	2.9868	2.959	2.9413	2.9483
2 (Ag-Ag)	2.9434	3.0386	2.9868	2.903	2.8593	2.8796
3 (Ag-Ag)	2.8821	2.8995	2.8681	3.925	3.7888	3.8151
A (Ag-Se)	2.6772	2.7012	2.6909	2.701	2.6995	2.7117
B (Ag-Se)	2.6808	2.6993	2.7009	2.725	2.6985	2.6945
C (Ag-Se)	2.766	2.8155	2.6961	2.696	2.6978	2.7019
D (Ag-Se)	2.8821	2.6984	2.8797	2.794	2.76	2.768
E (Ag-Se)	2.6662	2.8596	2.6961	2.696	2.6978	2.7019
F(Ag-Se)	2.7906	2.7352	2.8797	2.794	2.76	2.768
G (Ag-Se)	2.7092	2.6885	2.6909	2.701	2.6995	2.7117
H (Ag-Se)	2.7023	2.6878	2.7009	2.725	2.6985	2.6945

8.4 Conclusion

In conclusion, we demonstrated the significant electronic and excitonic anisotropy of AgSePh-F_2(2,3) in comparison to AgSePh through polarization-resolved optical spectroscopy and density functional theory calculations. These observations were explained by their structural differences: the AgSePh-F_2(2,3) structure exhibits a significantly distorted Ag-Ag hexagon with

one bond length considerably longer than the others, resulting in semi-1D Ag-Ag chains. This causes an anisotropic electronic band structure, a distinct absorption spectrum, and strong excitonic anisotropy, compared to AgSePh, which has a hexagonal 2D Ag-Ag network. This correlation between Ag-Ag bond parameters and the absorption spectrum can be generalized to other 2D blue-emitting AgSePh-R compounds, resolving the divergence between the AgSePh-like and AgSePh-F_2(2,3)-like absorption spectra. This finding promotes future studies on anisotropic charge carrier or exciton transport in AgSePh-F_2(2,3), arising from its anisotropic electronic band structures and strong excitonic anisotropy.

8.5 Methods

Material synthesis. Diorganic diselenide ligands were synthesized via Grignard reactions, except for diphenyl diselenide which is commercially available. The AgSePh-R crystals were synthesized using the amine-assisted method. Detailed information about the synthesis of organic ligands and AgSePh-R crystals, as well as crystal structures of these crystals, will be reported in future publications authored by Tomoaki Sakurada and other co-workers including myself.

Experimental characterization. The details of diffuse-reflectance spectroscopy, polarized optical microscopy, polarization-resolved micro-absorption and photoluminescence spectroscopy, atomic force microscopy are described in Chapter 7.

Density functional theory (DFT) calculations. DFT calculations were conducted by Dr. Yeongsu Cho, a former postdoc in the Kulik group at MIT. Detailed information about the electronic band structure calculations of AgSePh-F_2(2,3) will be reported in future publications authored by Tomoaki Sakurada, Yeongsu Cho, and other co-workers including myself. Details of the electronic band structure calculation of AgSePh are described in Chapter 7.

8.6 References

(1) Lee, W. S.; Cho, Y.; Powers, E. R.; Paritmongkol, W.; Sakurada, T.; Kulik, H. J.; Tisdale, W. A. Light Emission in 2D Silver Phenylchalcogenolates. *ACS Nano* **2022**, *16* (12), 20318–20328. https://doi.org/10.1021/acsnano.2c06204.

(2) Paritmongkol, W.; Sakurada, T.; Lee, W. S.; Wan, R.; Müller, P.; Tisdale, W. A. Size and Quality Enhancement of 2D Semiconducting Metal–Organic Chalcogenolates by Amine Addition. *J Am Chem Soc* **2021**, *143* (48), 20256–20263. https://doi.org/10.1021/jacs.1c09106.

(3) Trang, B.; Yeung, M.; Popple, D. C.; Schriber, E. A.; Brady, M. A.; Kuykendall, T. R.; Hohman, J. N. Tarnishing Silver Metal into Mithrene. *J Am Chem Soc* **2018**, *140* (42), 13892–13903. https://doi.org/10.1021/jacs.8b08878.

(4) Schriber, E. A.; Popple, D. C.; Yeung, M.; Brady, M. A.; Corlett, S. A.; Hohman, J. N. Mithrene Is a Self-Assembling Robustly Blue Luminescent Metal–Organic Chalcogenolate Assembly for 2D Optoelectronic Applications. *ACS Appl Nano Mater* **2018**, *1* (7), 3498–3508. https://doi.org/10.1021/acsanm.8b00662.

(5) Veselska, O.; Demessence, A. D10 Coinage Metal Organic Chalcogenolates: From Oligomers to Coordination Polymers. *Coord Chem Rev* **2018**, *355*, 240–270. https://doi.org/10.1016/j.ccr.2017.08.014.

(6) Maserati, L.; Refaely-Abramson, S.; Kastl, C.; Chen, C. T.; Borys, N. J.; Eisler, C. N.; Collins, M. S.; Smidt, T. E.; Barnard, E. S.; Strasbourg, M.; Schriber, E. A.; Shevitski, B.; Yao, K.; Hohman, J. N.; Schuck, P. J.; Aloni, S.; Neaton, J. B.; Schwartzberg, A. M. Anisotropic 2D Excitons Unveiled in Organic–Inorganic Quantum Wells. *Mater Horiz* **2021**, *8* (1), 197–208. https://doi.org/10.1039/C9MH01917K.

(7) Yao, K.; Collins, M. S.; Nell, K. M.; Barnard, E. S.; Borys, N. J.; Kuykendall, T.; Hohman, J. N.; Schuck, P. J. Strongly Quantum-Confined Blue-Emitting Excitons in Chemically Configurable Multiquantum Wells. *ACS Nano* **2021**, *15* (3), 4085–4092. https://doi.org/10.1021/acsnano.0c08096.

(8) Khamlue, R.; Sakurada, T.; Cho, Y.; Lee, W. S.; Leangtanom, P.; Taylor, M. G.; Naewthong, W.; Sripetch, P.; Na Ranong, B.; Autila, T.; Rungseesumran, T.; Kaewkhao, J.; Sudyoadsuk, T.; Kopwitthaya, A.; Müller, P.; Promarak, V.; Kulik, H. J.; Tisdale, W. A.; Paritmongkol, W. Heterocyclic Modification Leading to Luminescent 0D Metal Organochalcogenide with Stable X-Ray Scintillating Properties. *Chemistry of Materials* **2024**, *36* (10), 5238–5240. https://doi.org/10.1021/acs.chemmater.4c00653.

(9) Sakurada, T.; Cho, Y.; Paritmongkol, W.; Lee, W. S.; Wan, R.; Su, A.; Shcherbakov-Wu, W.; Müller, P.; Kulik, H. J.; Tisdale, W. A. 1D Hybrid Semiconductor Silver 2,6-Difluorophenylselenolate. *J Am Chem Soc* **2023**, *145* (9), 5183–5190. https://doi.org/10.1021/jacs.2c11896.

Chapter 9

Conclusions and Outlooks

9.1 Conclusions

Metal organochalcogenolates (MOCs) are novel hybrid excitonic semiconductors that fundamentally differ from other low-dimensional semiconductors. They not only provide an excellent platform to explore exciton physics and many-body interactions but also have potential for advanced optoelectronic and photonic applications. However, we do not understand how their excitonic properties arise at a fundamental level. (Chapters 1-3)

This thesis paved the way to answer this question. In Chapter 4, we demonstrated the growth of up to millimeter-sized single crystalline 2D AgEPh (E = S, Se, Te), enabling their crystal structure determination via single crystal X-ray diffraction: AgSPh in $P2_1$, AgSePh in $P2_1/c$, and AgTePh in $P2_1/c$. In Chapter 5, we investigated the light emission mechanism in AgSePh and AgTePh thin films. Despite having the same crystal structure, AgSePh exhibited narrow blue emission and broad emission that only emerged at lower temperatures, whereas AgTePh exhibited single broad emission with large Stokes shift from 5K to room temperature. Through spectroscopic studies, we demonstrated that light emission in AgSePh is dominated by free-exciton emission and defect-derived emission, while in AgTePh it is dominated by self-trapped exciton emission. In Chapter 6, we showed that AgSePh-AgTePh forms homogeneous complete solid solution system, whereas AgSPh and AgSePh/AgTePh do not, which we explained by their crystal structures determined in Chapter 4. Additionally, we demonstrated dual emission in $AgSe_{1-n}Te_nPh$ alloys, where broad emission from self-trapped exciton recombination becomes dominant as the Te ratio increases, implying the important role of chalcogen in determining exciton-phonon coupling strength. In Chapter 8, we investigated excitonic anisotropy in single crystalline AgEPh, revealing multiple low-lying excitons with in-plane anisotropy in AgSePh and AgTePh. This showcases the richness of excitonic physics in these materials, which arises from their low-symmetry crystal structures. Finally, we demonstrated that the electronic and excitonic structure of AgSePh can be engineered by organic functionalization, resulting in giant excitonic anisotropy and completely different absorption spectrum of $AgSePhF_2(2,3)$ compared to AgSePh. This difference was

attributed to the semi 1D Ag-Ag chains in $AgSePhF_2$(2,3) compared to Ag-Ag hexagonal 2D network in AgSePh, which can be generalized to other blue-emitting 2D AgSePh-R compounds that exhibit either AgSePh-like or $AgSePhF_2$(2,3)-like absorption spectra.

In conclusion, this thesis advanced the understanding of the structure-composition-excitonic property relationships, paving the way for the future investigation in these emerging hybrid semiconductors.

9.2 Outlooks

When I started my Ph.D. in 2019 Fall, there were only four papers about AgSePh (Note that the first report of AgSePh was in 2002).[1–4] Five years later, there are now more than 30 papers on about AgSePh and its derivates. While the field is still small compared to halide perovskite or transition metal dichalcogenides, the MOC community is definitely growing, and I anticipate (and hope) that this field will grow more rapidly in the future. During my five years as a Ph.D. student, I tried to fill the existing knowledge gaps, but in the process, I also identified many new ones. Here, I conclude my thesis by briefly discussing future research directions.

Photostability. Although AgSePh and many other 2D blue-emitting MOCs are stable in air, they degrade quickly and significantly under photo-excitation, hindering spectroscopic studies as well as optoelectronic and photonic applications. Therefore, it is essential to identify how photo-excitation degrades the crystals and devise methods to prevent it.

Photoluminescence quantum yield (PLQY). One of the advantages of AgSePh is its narrow blue emission, but its PLQY is limited to less than 0.1% at room temperature. Identifying the origin of the low PLQY and improving it is essential for both fundamental studies and applications.

Device fabrication. Due to the two limitations mentioned above, the device applications of AgSePh have been limited. Even if its photostability and PLQY are improved, there will still be many steps to investigate and optimize for its practical applications, such as, metal-semiconductor contacts, dielectric-semiconductor contacts, and more.

Exfoliation.[5] While it is anticipated that the bandgap of MOCs is layer-independent, controlling its thickness is crucial because of its natural photonic structure. Additionally, thickness

control is essential for device fabrication. However, successful and reproducible exfoliation of MOCs down to monolayer limit has not yet been demonstrated.

Metal doping.[6] In this thesis, we demonstrated chalcogen substitution or alloying. In addition to chalcogen substitution, metal doping (substituting Ag with other metals) will be an interesting approach to controlling their properties.

Organic functionalization.[7,8] While there have been active studies on the organic functionalization of MOCs, given the vast diversity of organic ligands, this topic remains an area for further investigation.

Strain engineering.[9] Another effective approach to manipulate material properties is intentionally applying strain to the material. Given its soft lattice and strong exciton-lattice interactions, there may be a significant influence of strain on the properties of MOCs.

Anisotropy.[10,11] In this thesis, we demonstrated strong structural and excitonic anisotropy in MOCs. Investigation of anisotropic electrical, thermal and mechanical properties as well as anisotropic transport of phonon, photon, electrons (excitons) in these materials will be interesting topics for future research.

9.3 References

(1) Cuthbert, H. L.; Wallbank, A. I.; Taylor, N. J.; Corrigan, J. F. Synthesis and Structural Characterization of [Cu20Se4(M3-SePh)12(PPh3)6] and [Ag(SePh)]∞. *Z Anorg Allg Chem* **2002**, *628* (11), 2483–2488. https://doi.org/10.1002/1521-3749(200211)628:11<2483::AID-ZAAC2483>3.0.CO;2-U.

(2) Schriber, E. A.; Popple, D. C.; Yeung, M.; Brady, M. A.; Corlett, S. A.; Hohman, J. N. Mithrene Is a Self-Assembling Robustly Blue Luminescent Metal–Organic Chalcogenolate Assembly for 2D Optoelectronic Applications. *ACS Appl Nano Mater* **2018**, *1* (7), 3498–3508. https://doi.org/10.1021/acsanm.8b00662.

(3) Trang, B.; Yeung, M.; Popple, D. C.; Schriber, E. A.; Brady, M. A.; Kuykendall, T. R.; Hohman, J. N. Tarnishing Silver Metal into Mithrene. *J Am Chem Soc* **2018**, *140* (42), 13892–13903. https://doi.org/10.1021/jacs.8b08878.

(4) Popple, D. C.; Schriber, E. A.; Yeung, M.; Hohman, J. N. Competing Roles of Crystallization and Degradation of a Metal–Organic Chalcogenolate Assembly under Biphasic Solvothermal Conditions. *Langmuir* **2018**, *34* (47), 14265–14273. https://doi.org/10.1021/acs.langmuir.8b03282.

(5) Huang, Y.; Sutter, E.; Shi, N. N.; Zheng, J.; Yang, T.; Englund, D.; Gao, H.-J.; Sutter, P. Reliable Exfoliation of Large-Area High-Quality Flakes of Graphene and Other Two-Dimensional Materials. *ACS Nano* **2015**, *9* (11), 10612–10620. https://doi.org/10.1021/acsnano.5b04258.

(6) Veselska, O.; Dessal, C.; Melizi, S.; Guillou, N.; Podbevšek, D.; Ledoux, G.; Elkaim, E.; Fateeva, A.; Demessence, A. New Lamellar Silver Thiolate Coordination Polymers with Tunable Photoluminescence Energies by Metal Substitution. *Inorg Chem* **2019**, *58* (1), 99–105. https://doi.org/10.1021/acs.inorgchem.8b01257.

(7) Khamlue, R.; Sakurada, T.; Cho, Y.; Lee, W. S.; Leangtanom, P.; Taylor, M. G.; Naewthong, W.; Sripetch, P.; Na Ranong, B.; Autila, T.; Rungseesumran, T.; Kaewkhao, J.; Sudyoadsuk, T.; Kopwitthaya, A.; Müller, P.; Promarak, V.; Kulik, H. J.; Tisdale, W. A.; Paritmongkol, W. Heterocyclic Modification Leading to Luminescent 0D Metal Organochalcogenide with Stable X-Ray Scintillating Properties. *Chemistry of Materials* **2024**, *36* (10), 5238–5240. https://doi.org/10.1021/acs.chemmater.4c00653.

(8) Sakurada, T.; Cho, Y.; Paritmongkol, W.; Lee, W. S.; Wan, R.; Su, A.; Shcherbakov-Wu, W.; Müller, P.; Kulik, H. J.; Tisdale, W. A. 1D Hybrid Semiconductor Silver 2,6-Difluorophenylselenolate. *J Am Chem Soc* **2023**, *145* (9), 5183–5190. https://doi.org/10.1021/jacs.2c11896.

(9) Qi, Y.; Sadi, M. A.; Hu, D.; Zheng, M.; Wu, Z.; Jiang, Y.; Chen, Y. P. Recent Progress in Strain Engineering on Van Der Waals 2D Materials: Tunable Electrical, Electrochemical, Magnetic, and Optical Properties. *Advanced Materials* **2023**, *35* (12). https://doi.org/10.1002/adma.202205714.

(10) Zhao, S.; Dong, B.; Wang, H.; Wang, H.; Zhang, Y.; Han, Z. V.; Zhang, H. In-Plane Anisotropic Electronics Based on Low-Symmetry 2D Materials: Progress and Prospects. *Nanoscale Adv* **2020**, *2* (1), 109–139. https://doi.org/10.1039/C9NA00623K.

(11) Li, L.; Han, W.; Pi, L.; Niu, P.; Han, J.; Wang, C.; Su, B.; Li, H.; Xiong, J.; Bando, Y.; Zhai, T. Emerging In-plane Anisotropic Two-dimensional Materials. *InfoMat* **2019**, *1* (1), 54–73. https://doi.org/10.1002/inf2.12005.